EXPERIMENTAL TESTS OF TRIPLE REGGE THEORY

Thesis by

Rosemary Gillian Kennett

In Partial Fulfillment of the Requirements

for the Degree of

Doctor of Philosophy

California Institute of Technology

Pasadena, California

1980

(Submitted September 25, 1979)

ACKNOWLEDGEMENTS

I am grateful to the Fannie and John Hertz Foundation for financing my graduate studies at Caltech through a fellowship and thus enabling me to fulfill my desires to pursue research. I am also grateful to the Department of Energy who financed the experiment described herein and enabled such beautiful data to be collected and analyzed.

I am grateful to my advisor, Dr. Bob Walker, for supervising all the data-collecting and the analysis of this experiment. I am also grateful to my fellow graduate students, Alan Barnes, Frank Nagy and Kar Yung, for helping me to understand various facets of experimental physics. I also thank two undergraduate students, Bruce Cortez and Aileen Stone, for help with the data analysis, and three former members of the experimental group, Dave Hermeyer, Joel Mellema and Alvin Tollestrup, for help in setting up this experiment. I also thank the phenomenology group at Caltech, who initiated the experiment many years ago.

Finally, I should like to thank my husband, Geoffrey, for his patience and kindness during the many hours on which I worked on this thesis.

ABSTRACT

The results of measurements on the inclusive production of π^0 and η mesons from 100 GeV $\pi^{\pm}$, $K^{\pm}$, p and $\bar{p}$ beams in the triple Regge kinematic region are presented. Fits are made to the predictions of the triple Regge model which show that the model is successful. The ρ, A_2, K* and N Regge trajectories are extracted from the fits and they all agree with those found from exclusive processes at low -t. For -t above about 1.5 GeV^2, the ρ and A_2 trajectories both flatten off at a value of about -0.5. Evidence is seen for the wrong signature nonsense zero of the ρ. Results on the neutral final state production of π^0 and η mesons from π^- beams are also presented and the ρ and A_2 trajectories extracted using an extended triple Regge theory are in agreement with those from both the inclusive and exclusive processes. Comparisons with predictions from QCD are made.

CONTENTS

APPENDICES

CHAPTER 1

INTRODUCTION

Measurements of the inclusive production of π^0 and η mesons from hadron beams incident on a hydrogen target at Fermilab are described in this thesis. The cross sections were extracted in a kinematic region where triple Regge theory is expected to be valid and provided a clean and successful test of this theory together with some interesting results on the ρ, A_2, K* and N Regge trajectories.

Regge theory is a model to describe strong interactions in a certain kinematic region. There is an interesting experimental observation that the strongly-interacting particles having the same quantum numbers other than their spin, J, lie on a straight line when J is plotted against their mass-squared, m^2. In Regge theory these lines, $J = J(m^2)$, form the real, positive m^2, part of the Regge trajectories which are named after the lowest mass particles on them. The lines for differing quantum numbers have almost the same slope of about 0.9 GeV^{-2}, as shown on Figs. 1.1-3 for the trajectories which were measured in this experiment. A 2→2 body reaction of the form a + b → c + d is described in Regge theory by the exchange of virtual particles carrying the four-momentum-squared, t, which is observed to be transferred from a to c:

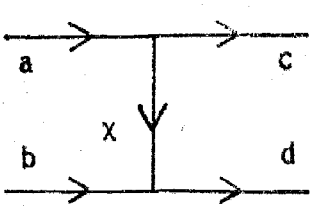

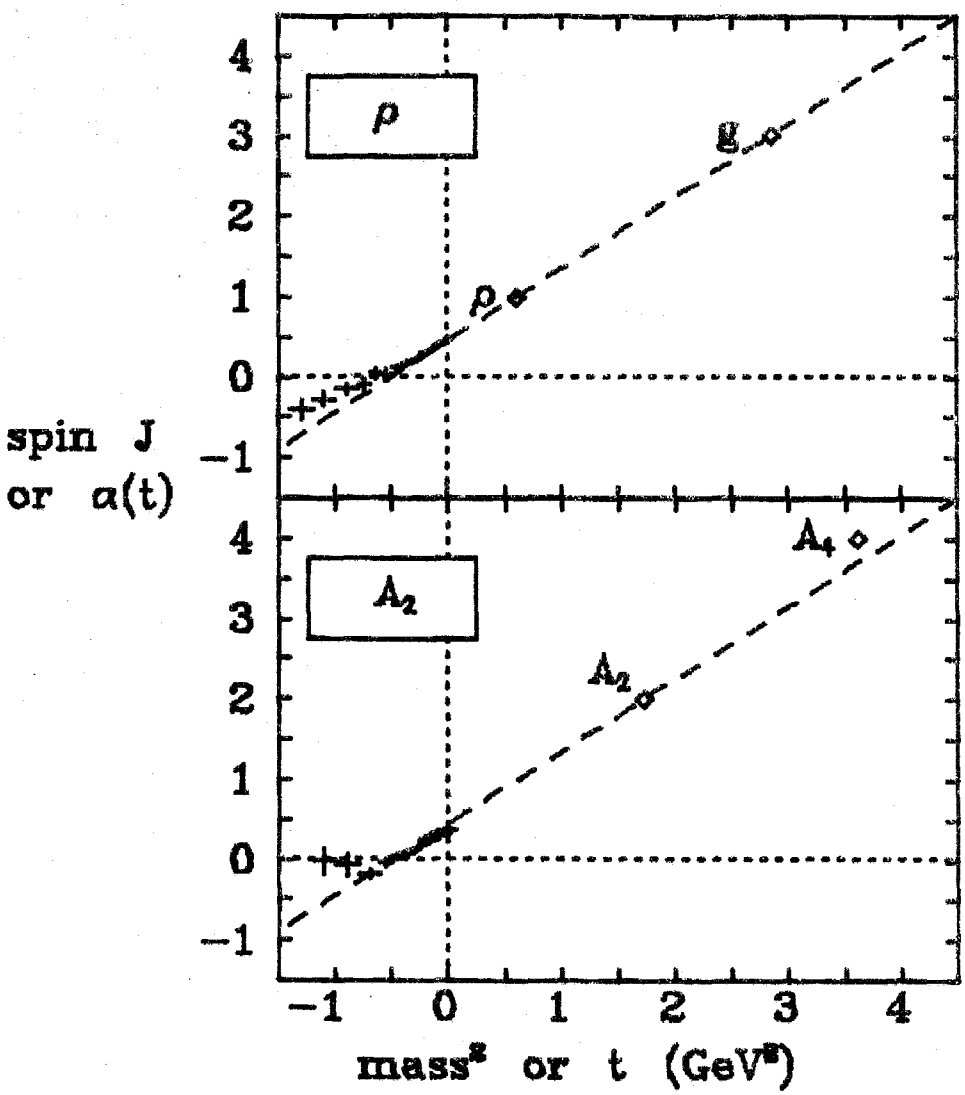

FIGURE 1.1 Non-strange meson trajectories: ρ trajectory from $\pi^- p \to \pi^0 n$ (Ba76) and A_2 trajectory from $\pi^- p \to \eta n$ (Da76) using data with $40 < s < 400$ GeV^2 and the physical particles lying on these trajectories (PD78). The straight lines shown have slopes of 0.9 GeV^{-2} and pass through the lowest mass particle on the trajectory.

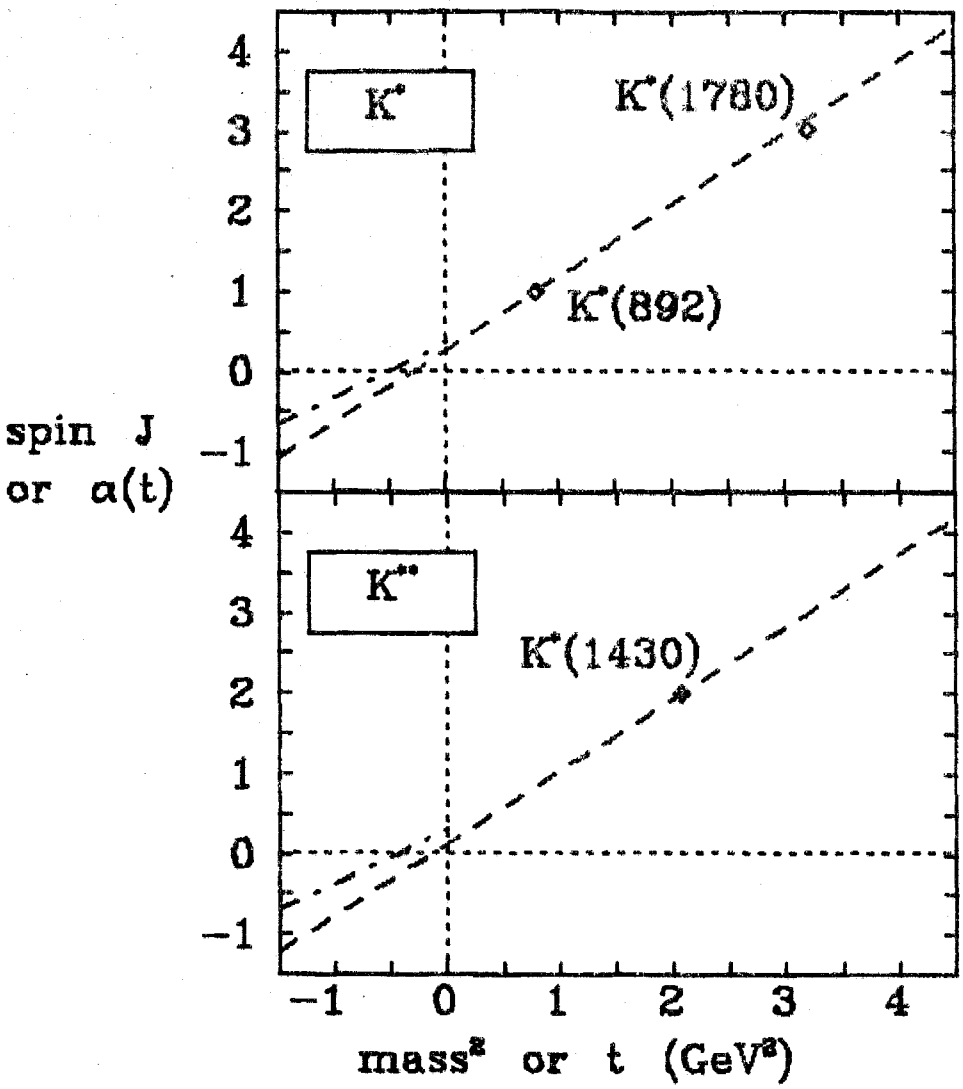

FIGURE 1.2 K* trajectories: K*(892) and K*(1430) trajectories determined for t < 0 using low energy data on exclusive reactions in Ref. (Na76) (dot-dashed lines) and the physical particles lying on these trajectories (PD78). The dashed lines have slopes of 0.9 GeV^{-2} and pass through the lowest mass particle on the trajectory.

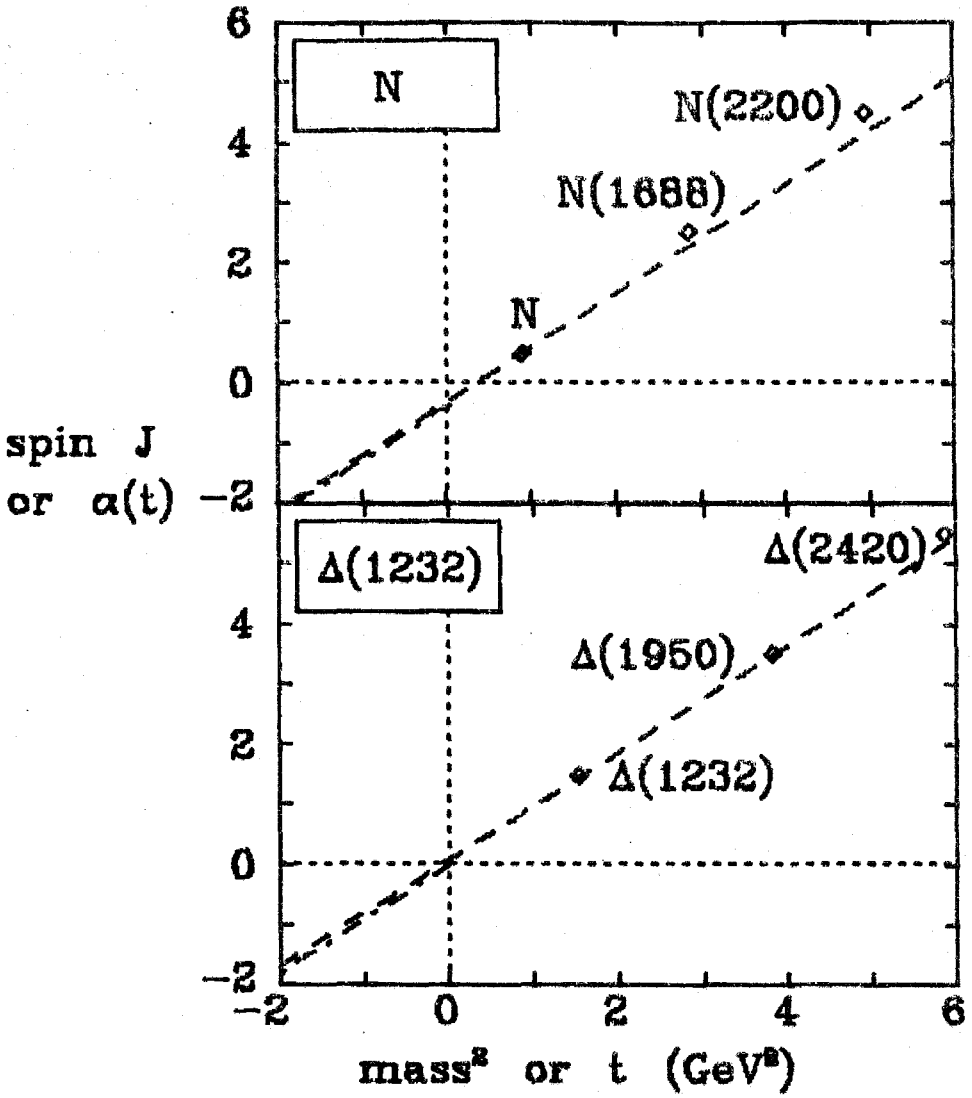

FIGURE 1.3 Baryon trajectories: The physical particles lying on the nucleon and Δ(1232) trajectories (PD78). The dashed lines have slopes of 0.9 GeV^{-2} and pass through the lowest mass particle on the trajectory. The dot-dashed lines are the trajectories used to fit low energy backward πN scattering data in Ref. (St75).

The exchanged particles have an angular momentum, α, which is a continuous complex function of t. This function is just the unphysical m^2 part of the Regge trajectory. When only one trajectory, χ, is exchanged, Regge theory predicts that the cross section for this process at high s is given by

$$\frac{d\sigma}{dt}(s,t) = G_{\chi}(t)s^{2\alpha_{\chi}(t)-2}, \qquad (1.1)$$

where s is the center of mass (c.m.) energy-squared, $\alpha_{\chi}(t)$ is the Regge trajectory of the particle χ and $G_{\chi}(t)$ is some function of t.

Hence for positive values of t, the trajectory α can only be experimentally determined when α is an integer, at which values t is given by the mass-squared of the various particles which differ in quantum numbers only in the spin. For negative t, the trajectory at a fixed value of t may be obtained from the differential cross sections for appropriate reactions by comparing the cross sections at that t for different values of s and using the prediction (1.1). Experimentally this has been done for various reactions by collecting data at different values of s, that is, at different beam momenta, and looking at the s-dependence of the cross section for different t bins to obtain the trajectory as a function of t. In practice, most reactions allow the exchange of more than one trajectory and thus it is not so simple to disentangle the trajectories. Some experimentally measured trajectories are shown in Figs. 1.1-3. For negative t, they are generally linear extensions of the straight lines on which

the particles lie. Regge theory is described in more detail in Chapter 4.

Triple Regge theory extends Regge theory to inclusive processes of the form a + b → c + X, where X means that anything may be produced. When only one exchange, χ, is possible then the amplitude is given in Regge theory by:

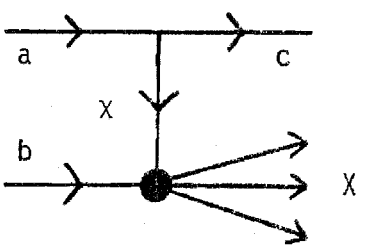

To form the cross section this amplitude is squared to give:

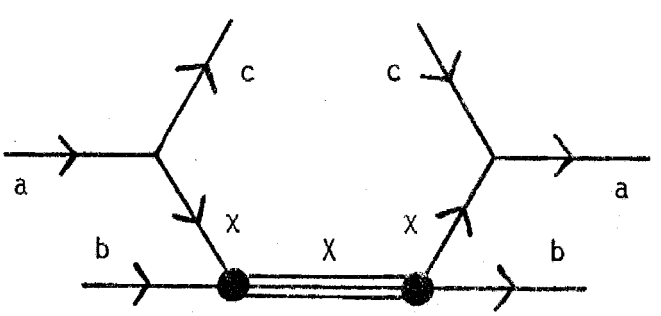

Summing over all the possibilities for X gives the total cross section for χb collisions which, by the optical theorem, is related to the χb forward amplitude. This is dominated by Pomeron (denoted P) exchange with t = 0, thus giving the "triple vertex" diagram:

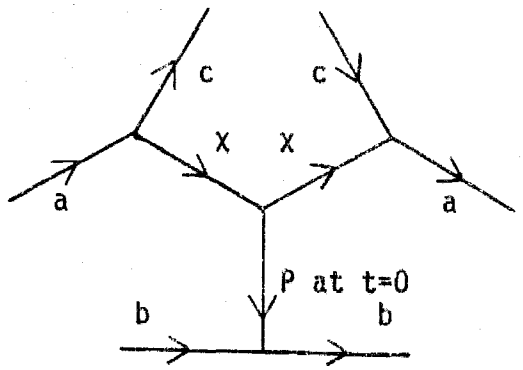

A third variable, x, is needed to describe this reaction. x is the fraction of longitudinal momentum given to c from a in the c.m. frame. Triple Regge theory predicts that the cross section for this process at high x, high s and low -t is given by

$$\frac{d^2\sigma}{dtdx}(x,t,s) = G_{\chi\chi P}(t)(1-x)^{\alpha_p(0) - 2\alpha_\chi(t)} s^{\alpha_p(0) - 1}, \quad (1.2)$$

where G(t) will be referred to as the "residue function" below and $\alpha(t)$ is the same trajectory function as used in the description of the exclusive processes above. Since t is generally negative for these processes, the symbol t_m is used below for -t. As in the exclusive case, the trajectories may be extracted from the cross sections using (1.2), but once again there may be several sets of trajectories exchanged for a single reaction.

Regge theory is only valid at high s and thus when Fermilab started an experiment, E111, was run by a Caltech-Lawrence Berkeley Laboratory collaboration to test its predictions (Ba76,Da76). The principal reactions chosen were

$$\pi^- + p \rightarrow \pi^0 + n \qquad (1.3a)$$

and

$$\pi^- + p \rightarrow \eta + n, \qquad (1.3b)$$

since only one trajectory, the ρ or A_2 trajectory respectively, can be exchanged in each reaction. By taking data at several beam momenta, the trajectories were obtained from (1.1) for t_m up to about 1 GeV^2, as shown on Fig. 1.1. For the experiment, E350, described here, whose purpose was to test triple Regge theory, the corresponding inclusive reactions,

$$\pi^{\pm} + p \rightarrow \pi^0 + X \qquad (1.4a)$$

and

$$\pi^{\pm} + p \rightarrow \eta + X, \qquad (1.4b)$$

were chosen because they are likewise dominated by single exchanges, namely those with ρ and A_2 mesons on the top two legs and the Pomeron on the bottom leg. There have been many previous experiments (Fi74,Bu76a,Al76) to test triple Regge theory but they have been mainly on diffractive reactions, such as $p + p \rightarrow p + X$, where many triple Regge terms can contribute and so a clean test of the theory was not possible.

In both sets of reactions, (1.3) and (1.4), it was necessary to detect a π^0 or η. Thus the detector built and used by E111 could be adapted for the latter experiment. The π^0 and η mesons were detected by their two-photon decay modes in a lead-scintillator sandwich

detector. The experimental setup of E350, described in Chapter 2, was simpler than that of E111, for which one also had to determine that only a neutron was present in the final state. However the analysis of the data, described in Chapter 3, was more complicated than that of E111 since it was necessary to identify the π^0 and η mesons in the presence of other particles produced in the inclusive reaction and to determine their energies and transverse momenta. The results on the production of π^0 and η mesons from pion beams are presented in Chapter 5. Results were also obtained on their production from kaon, proton and antiproton beams, enabling the K* and N trajectories to be found, as described in Chapter 7.

A modification of triple Regge theory describes subprocesses of the form

$$a + b \rightarrow c + X^0, \tag{1.5}$$

where X^0 means that only neutral particles may be present in the final state. This is referred to as the "neutral final state" or "NFS" below. Results from the data collected on the NFS production of π^0 and η mesons from a π^- beam are presented in Chapter 6. The ρ and A_2 trajectories are again exchanged and thus two independent determinations of each were made by this experiment.

In Table 1.1 on the following page, the cross sections for various π^- induced reactions are listed. Since the inclusive π^0 production in the triple Regge kinematic region has only 1% of the

TABLE 1.1. Comparison of cross sections for $\pi^- p$ reactions at 100 GeV.

Reaction	$-t$ (GeV^2)	x	cross section
$\pi^- p \to X$			24 mb
$\pi^- p \to \pi^- p$	< 1		3.3 mb
	> 1		16 nb
$\pi^- p \to \pi^0 n$	< 1		3 μb
	> 1		3 nb
$\pi^- p \to \pi^0 X$	< 1	> 0.7	340 μb
	> 1	> 0.7	30 μb
$\pi^- p \to \pi^0 X^0$	< 1	> 0.7	13 μb
	> 1	> 0.7	0.4 μb
$\pi^- p \to X^0$			40 μb

total cross section and the NFS π^0 production has only 0.01%, it was necessary to provide a "trigger" for the experiment which would select the desired events without having to record the numerous events from other processes. An additional advantage of measuring π^0 mesons was the ease with which both a clean energy trigger and a clean t trigger could be designed, so that most of the events recorded did include π^0 or η mesons at high x, as described in Chapter 3. The Peyrou plot in Fig. 1.4 shows the kinematic regions over which data were collected for the full inclusive and NFS production of π^0 mesons from pion beams.

It was found that the triple Regge model provided an excellent

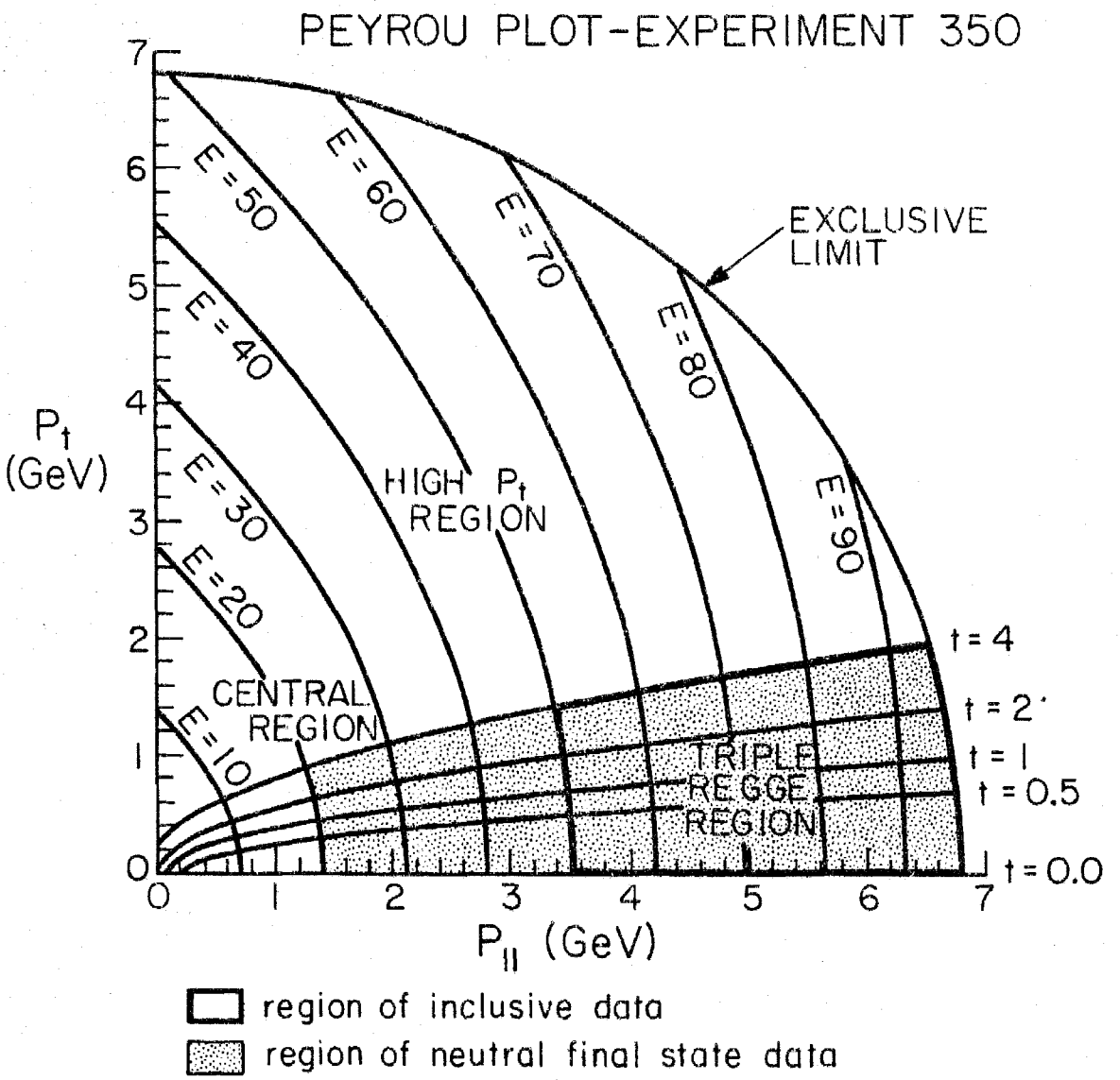

FIGURE 1.4 Peyrou plot showing the kinematic region in the center of momentum frame over which data were collected for the reactions $\pi^{\pm}p \rightarrow \pi^0 X$ and $\pi^- p \rightarrow \pi^0 X^0$. The curves of constant π^0 energy, E, (in GeV) and four-momentum-transfer-squared, t, (in GeV^2) in the laboratory frame are shown.

description of the data as a function of x and t at s = 200 GeV^2 and the extracted trajectories agreed with those obtained from the exclusive processes for $t_m \leq 1$ GeV^2. The inclusive cross sections are much larger than the exclusive cross sections and also fall much less sharply with t_m, as indicated in Table 1.1, and so it was possible to find the trajectories out to larger t_m than before. The ρ and A_2 trajectories both flattened off for t_m above 1.5 GeV^2 and assumed a value of about -0.5 at large t_m. This behavior may be due to some mechanism other than triple Regge becoming dominant at large t_m so that the apparant flattening may not be that of the trajectory itself.

The results presented in this thesis are from data collected at Fermilab with a 100 GeV incident beam during June and July 1976. Some of the results presented here have already been published in Refs. (Ba78a,b,c). Data were also collected with a 200 GeV incident beam during January and February 1977. It is assumed throughout this thesis that c = 1, $\hbar$ = 1 and the Regge scale factor, s_o, = 1 GeV^2.

CHAPTER 2

APPARATUS

2.1 GENERAL DESCRIPTION

The apparatus used in this experiment is shown in Fig. 2.1. The photon detector and target were the same as those used by E111 to measure exclusive π^0 production. The aim of E350 was to detect the two photons from the decay of a π^0 or η meson at high x with as small a background as possible and with a good energy and transverse momentum resolution in the presence of other photons, neutral particles and charged particles.

The beam interacted in the hydrogen target and any π^0 mesons produced and some η mesons produced would decay into photons immediately. The detector was set at a sufficient distance from the target, 20 m, for the two photons to produce distinguishable electromagnetic showers on hitting the detector. The magnet situated between the target and the detector was present to bend the non-interacting beam particles away from the detector and to bend any charged particles from interactions away from any photons produced. A charged particle counter with the same dimensions as the photon detector was placed immediately in front of the detector but was not used in either the trigger or in the analysis of the data presented here since it was found that charged particles did not create a problem. A small lead scintillator telescope was set behind the detector aligned with the direction of the bent beam

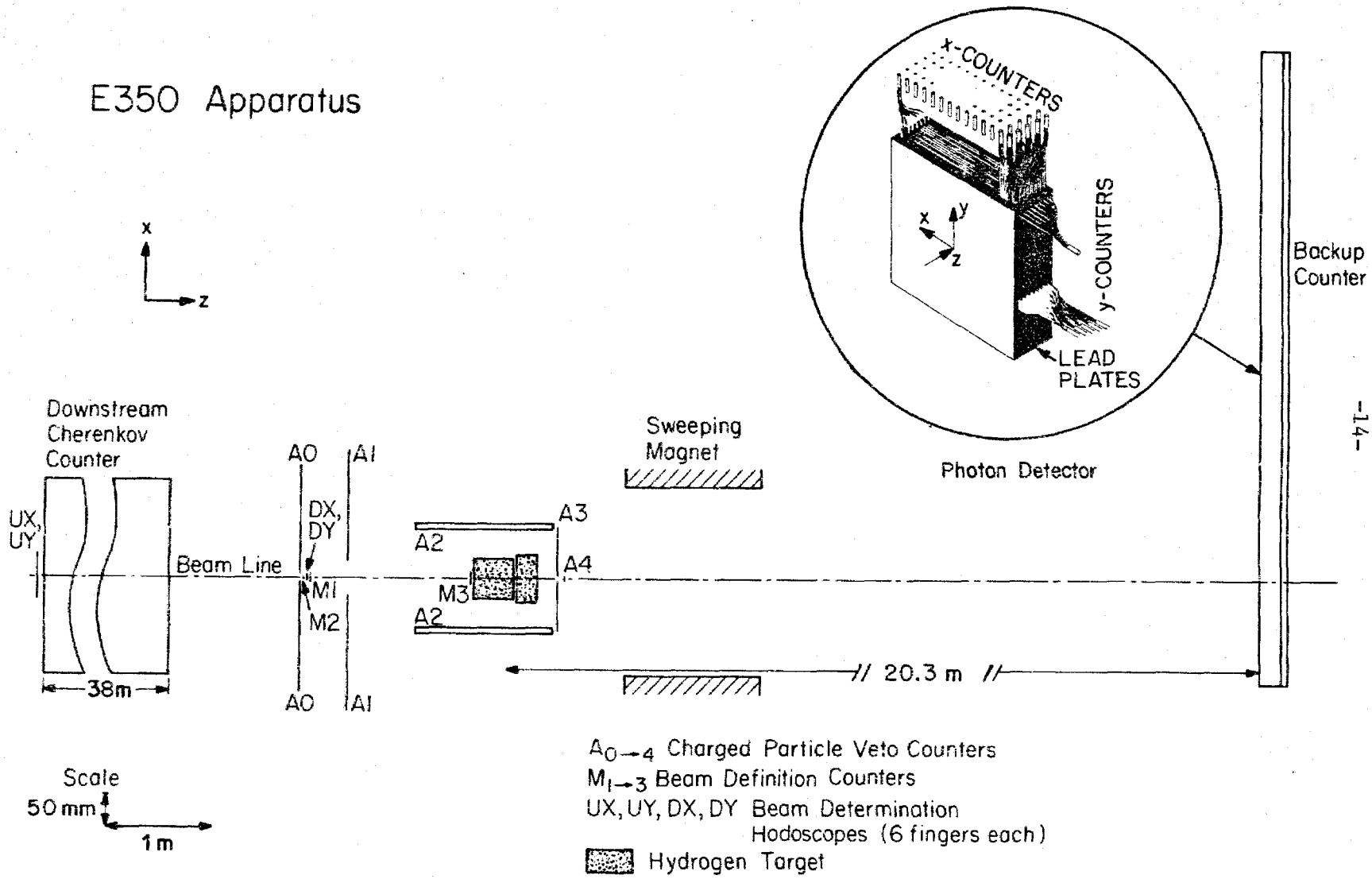

FIGURE 2.1 Schematic arrangement of the experimental apparatus. The inset shows the photon detector.

particles and was used to monitor the flux of electrons throughout the experiment. The scintillation counters around the target were used to distinguish the neutral final state events by the absence of charged particles. The two Cherenkov counters in the beam, of which only one is shown on the figure, were used to tell whether the incident particle was a pion, kaon or (anti)proton. The various parts of the apparatus are described in more detail below. Since this experiment was the third one to use the basic apparatus, many aspects of the design were determined by the earlier experiments, especially by the initial charge-exchange experiment, E111 (Da76, Jo75).

2.2 BEAM

The experiment was performed in the M2 secondary beam at Fermilab using 100 GeV hadrons produced by a 400 GeV Main-Ring proton beam incident on the meson laboratory target. The beam composition is given in Table 2.1, as determined by the methods described in Appendix 3.IX. A series of dipole bending magnets determined the

TABLE 2.1. Beam particle content (after electrons are absorbed).

	π	p	K
Negative beam	0.934	0.024	0.042
Positive beam	0.677	0.283	0.040

momenta of the beam particles and steered them onto the experiment's target whilst quadrupole magnets focused the beam on the target. The beam momentum distribution was approximately flat within a width determined by the width of a collimator. Most of the data were collected with a full width of 1.8 GeV except for the low -t data from pion beams which were collected with a full width of 0.5 GeV. Another collimator controlled the flux of particles and was set to give about 70,000 particles per spill for collecting the low -t pion data and 500,000 particles per spill for collecting the other data.

The direction of each beam particle was determined using two hodoscopes which each had six scintillator fingers in each of two orthogonal planes. One was placed at 61.6 m from the midpoint of the target and had 9.7 mm wide fingers and the second was at 1.8 m and had 1.6 mm wide fingers, as shown in Fig. 2.1.

A lead radiator was placed at the first beam focus to reduce the electron content of the beam. Its thickness was 9.5 mm for the low -t data and 3.2 mm for the high -t data. When a trigger requiring a kaon or (anti)proton was in use this radiator was removed because the Cherenkov counter would then veto the electrons.

2.3 CHERENKOV COUNTERS

To determine the beam particle type, two Cherenkov counters made from the beam vacuum pipes were used. The upstream one was 94.6 m long and the downstream one, shown on Fig. 2.1, was 58.0 m long and

both were 0.30 m in diameter. They were filled with helium gas at reduced pressure. The optical systems on the two counters were essentially identical and based on the fact that Cherenkov light from particles of different masses can be focussed onto rings of different radii. Hence at the downstream end of each counter there was a flat mirror placed at 45° to the axis of the beampipe which reflected the light onto a 0.32 m parabolic mirror of 2.34 m focal length. A small mirror of elliptical shape was placed so as to receive the central circle of light, containing the ring due to the kaons, and reflect it onto a photomultiplier tube, called the "inner" tube. The remaining light was collected by a second photomultiplier tube, called the "outer" tube. The pressure of the helium gas was adjusted so that the ring of light due to the on-axis pions was seen by this phototube. Protons and antiprotons were distinguished by the absence of Cherenkov light.

The pulses from the four photomultiplier tubes were integrated in charge-to-time converters and then digitized in 10-bit scalers. They were also discriminated so that light giving one photoelectron or more set a bit when the experiment was triggered. Particles satisfying the beam particle requirements (see Appendix 2.I) with bit patterns resembling pions, protons and kaons (see Appendix 3.IX) were added into three scalers. Since the Cherenkov counter efficiencies for the different particles varied, some off-line analysis, described in Appendix 3.IX, was necessary to distinguish

true pions, (anti)protons and kaons and to obtain the true pion, (anti)proton and kaon fluxes seen by the experiment.

2.4 HYDROGEN TARGET AND CHARGED PARTICLE VETO COUNTER

The target used for this experiment was the one constructed for E111 (Jo75). It consisted of two flasks, both of which were filled with liquid hydrogen for this experiment, giving a total length of 0.602 m when cold. The pressure was kept constant at 5 p.s.i. above atmosphere throughout the experiment.

In Fig. 2.1 is shown the charged particle veto counter surrounding the target, consisting of counters A1, A2, A3 and A4. The A1 counter covered the region upstream of the target except for a small hole for the beam. The A2 counter consisted of a box of four pieces of scintillator, each 1.32 m long, 0.18 m wide and 9.5 mm thick and viewed along the long edge by five light pipes equally spaced apart and leading into photomultiplier tubes. This counter surrounded the target. The A3 counter was downstream of the target and consisted of a large square piece of scintillator with a hole in the center and viewed by two photomultiplier tubes on opposite sides. A disc of 1.6 mm thick scintillator, viewed by one photomultiplier tube and called the A4 counter, covered the hole in the A3 counter. These counters were used for the NFS trigger (see Appendix 2.I). The hardware cuts on the pulse heights from the counters A2, A3 and A4 were less stringent than later imposed in the offline analysis

because the delta rays from the beam particles gave light which caused NFS events to be vetoed. Hence these photomultiplier tubes were pulse height analyzed and recorded in 11-bit scalers so that a cleaner NFS definition could be made later and so that the delta ray background could be estimated, as described in Appendix 6.I. A scaler counted the total number of successful beam particles which satisfied the NFS trigger requirement.

2.5 PHOTON DETECTOR

The photon detector is shown in the inset to Fig. 2.1. It was a square hodoscope containing 21 radiation lengths of lead scintillator sandwich. The lead consisted of nineteen 0.75 m x 0.75 m x 6.4 mm sheets. Each hodoscope counter was made of eight scintillation rods, each 10.5 mm wide, 0.7 mm thick (along the beam direction) and 0.735 m long. These eight rods were each tightly wrapped with aluminized mylar having graded reflectivity so as to minimize the light attenuation along the rod (Wa72) and were connected to a light pipe seen by one RCA4517 photomultiplier tube. There were seventy such counters in each of two orthogonal directions (x and y) perpendicular to the beam direction. The construction consisted of a plane of rods in the x direction, followed by a sheet of lead, another plane of rods in the y direction and a sheet of lead. This sequence was repeated eight times. There were also two sheets of lead in front of the first plane of rods and two behind the last set. Thus the energy deposited in the longitudinal direction was integrated optically and

the photon showers were seen in the two transverse directions.

In this experiment it was necessary not just to distinguish a π^0 meson but also to measure its energy well, for it was no longer constrained by the beam energy as it had been for the exclusive processes of E111. Not all the longitudinal shower of an incident 100 GeV particle was contained in the photon detector. Hence a subsidiary counter was attached to the back of the photon detector, which was called the "backup counter". It consisted of about four radiation lengths of lead-scintillator sandwich. The scintillator was divided into ten counters, each formed from three fingers, which were 70 mm wide and 0.70 m long and aligned vertically. The fingers were joined by lucite light pipes feeding into photomultiplier tubes. The method used to correct for the energy leakage using this backup counter is described in Appendix 3.III.

When an event was triggered, the pulses from the detector and the backup counter were integrated in charge-to-time converters, then digitized in 11-bit scalers and read out by a SAC data collection system to an XDS Sigma II computer (To76). To monitor the gains of the photomultiplier tubes and the pulse height analyzers, radioactive sources were placed between the lucite light pipes and the photomultiplier cathodes on both the photon detector and the backup counter. These consisted of Bi^{207} between two small discs of scintillator inserted into a disc of lucite with the same diameter as the cathodes. These sources were analyzed during the interval

between beam spills. The average and standard deviation within a predetermined pulse height window for each source were calculated and these, along with the total number of source triggers for each counter, were recorded about every 20 minutes (Ba75c). It was also necessary to monitor and record the zero level of every pulse height analyzer. This was done by taking a special pedestal collection at the start of each run (about every 20-60 minutes) and after each time that the gain information had been recorded on tape.

For the data presented here, the detector was placed at 20.32 m from the center of the hydrogen target. This distance was chosen so that the magnet did not aperture any photons produced and so that the acceptance for the two-photon decay mode of the etas was not too small. The detector was positioned laterally so that the unbent beam passed 0.174 m into the detector and the bent beam just missed the detector on the side away from the photomultiplier tubes. It was positioned vertically so that the beam went through the center.

2.6 TRIGGER

The cross section for the main reaction measured by this experiment, namely $\pi^- p \rightarrow \pi^0 X$ with $x > 0.7$, is only 1.5% of the total cross section for π^- on protons, as shown in Table 1.1, whilst that of the NFS reaction, $\pi^- p \rightarrow \pi^0 X^0$, is only 0.04%! The data acquisition and recording system was limited to recording only 80 events per

spill, which was far less than the 5000 interactions which occurred every spill. Thus various electronic triggers were designed so as to restrict the recorded data to the reactions of greatest interest without putting too great a bias on the type of data collected. These triggers were successful as one-sixth of the events recorded were included in the cross section determinations. The basic trigger required that a beam particle well isolated in time from other particles and directed close to the axis of the experiment be present, as described in Appendix 2.I. In addition to this, three other types of triggers were used in which

(i) the energy in some part of the detector had to be above some threshold

or

(ii) the beam particle had to be of a certain type

or

(iii) there had to be no light in the charged particle veto counter.

These triggers are discussed briefly below and described in detail in Appendix 2.I.

One of the main aims of this experiment was to obtain data on π^0 production at high x, that is, at a high energy relative to the beam energy. Since the energy deposited in the detector was measured, it was relatively simple to include an energy requirement in the trigger. Applying the energy requirement on the total energy

deposited provided the low t_m pion beam data. This was called trigger "A". A second trigger, called trigger "B", was designed to accept only the high t_m events by making the energy requirement on the region of the detector away from the beamline, as shown by the shaded region below:

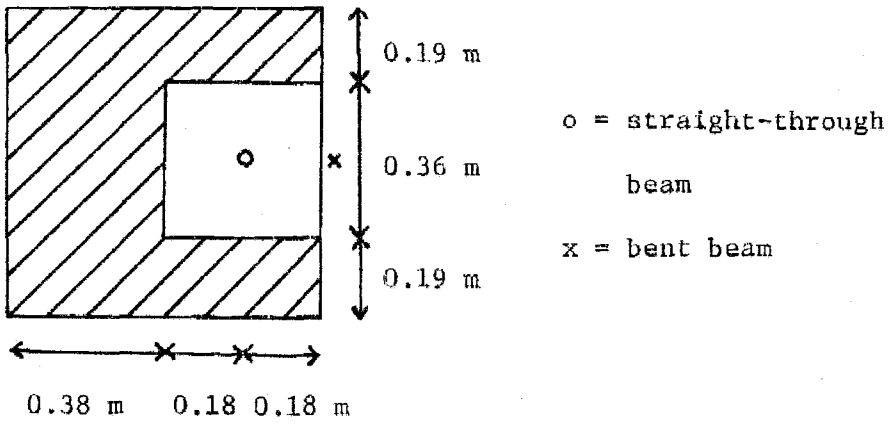

This trigger had a good acceptance for events with t_m above about 1 GeV^2, as described in Appendix 3.IX. Triggers A and B were run with three energy thresholds, called low, medium and high, and corresponding to cut-off energies of about 40, 60 and 70 GeV respectively. This was done to provide an adequate coverage of the high x region because the cross section fell rapidly with x (except at low t where it was flat). The data from triggers A and B were combined together to give the results presented in Chapter 5.

To obtain data on the reactions with incident kaon, antiproton and proton beams it was necessary to put a requirement on the

TABLE 2.2 Summary of triggers. All fluxes are divided by 10^7.

Trigger	Bias	Negative Beam flux		Positive beam flux	
		Full	Empty	Full	Empty
A	low	0.73	0.68	1.45	0.96
A	medium	10.44	8.05	5.16	3.17
B	low	4.62	4.78	0	0
B	medium	166.35	148.82	81.40	95.23
B	high	171.44	26.92	81.37	0
C	low	8.27	9.85	0	0
C	medium	180.75	104.10	34.18	11.82
C	high	47.33	18.27	0	0
K	medium	0	0	141.93	39.28
NFS	none	488.92	360.69	0	0

Cherenkov counters into the trigger since, as shown in Table 2.1, pions formed most of both the negative and positive polarity beams. Some of the data were collected requiring that either a kaon or an (anti)proton be present (called trigger "C") and some of the positive beam data were collected requiring that a kaon be present (called trigger "K"). An energy cut was imposed along with the beam particle requirement.

The trigger types are summarized in Table 2.2 above, which gives the total number of acceptable beam particles (called "flux") for which data were collected for each trigger. The empty target data

were collected for calculating the background from interactions with the target walls and the air, as described in Section 3.3.

CHAPTER 3

ANALYSIS OF THE DATA

3.1 INTRODUCTION

The main aim of the analysis of an event from this experiment was to identify the π^0 and η mesons present in the event and to calculate their energies and transverse momenta. The cross section was obtained as a function of energy and t by accumulating the identified particles in bins in energy and t and then correcting for any missing or misidentified particles. The raw data from the photon detector for an event consisted of seventy pulse heights in two orthogonal views. Each pulse height measured the energy deposited in a counter formed of eight scintillation rods, each 0.74 m long and 10.5 mm wide, which were aligned in depth and separated by lead, as described in Section 2.5.

A typical event is displayed in Fig. 3.1, where the beam is directed into the paper. Several showers of similar shape but different magnitudes are present and there are clearly at least four photons in the event. When a 100 GeV π^0 decayed into two photons at the target, they reached the detector 20 meters downstream separated by at least four counterwidths in one view, where a counterwidth is the width of a detector counter. The photons produced electromagnetic showers by pair production and bremsstrahlung interactions in the lead and the energy deposited was detected by the scintillation light. These showers had a F.W.H.M. in the transverse direction of

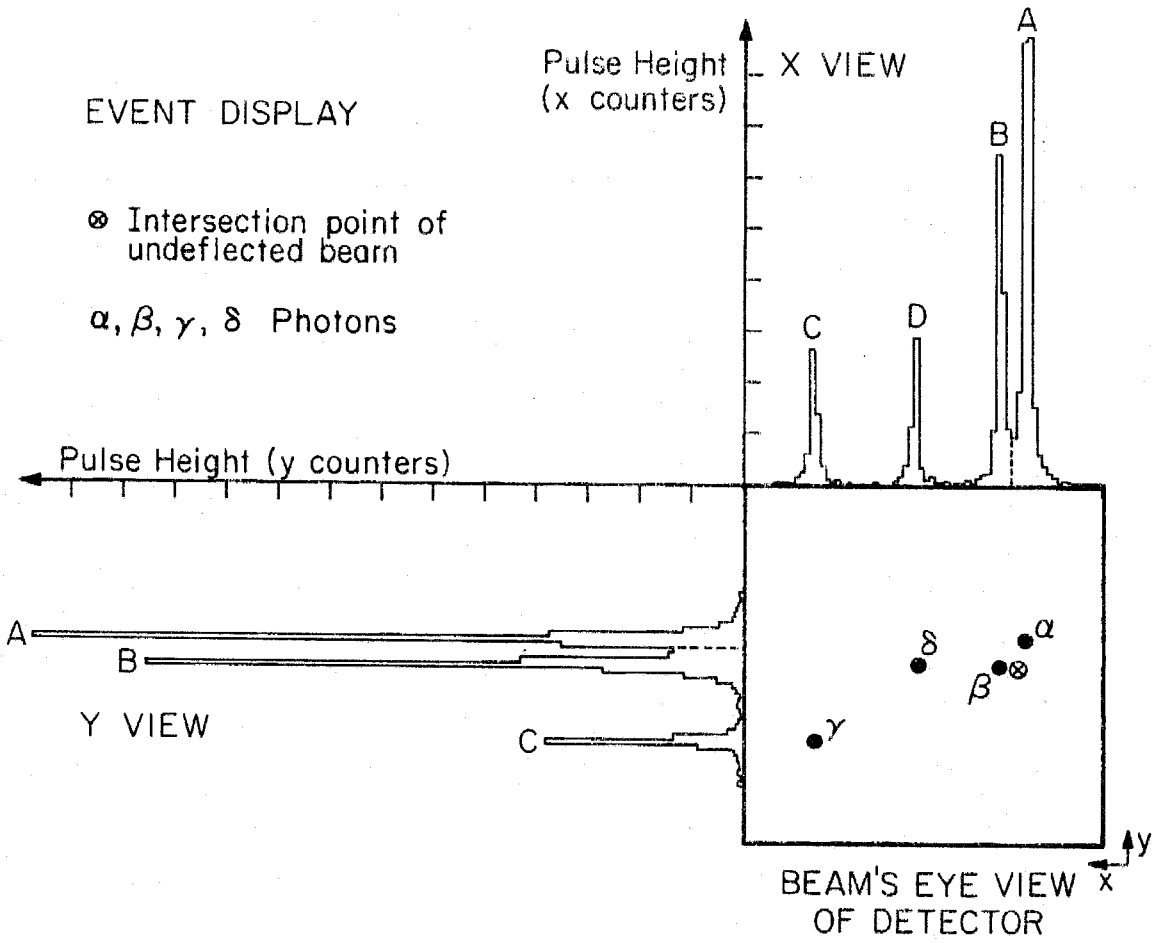

FIGURE 3.1 A typical event. A, B, C and D indicate the observed peaks in each view and α, β, γ and δ indicate the positions of the photons on the face of the detector. Photons α and β form the π^0 in the triple Regge region.

about one counterwidth, so the two photon showers from a π^0 were distinct in at least one view, but they were not necessarily separated from other photons in the event. In the example shown, two π^0 mesons were present with photons α and β belonging to the higher energy one and photons γ and δ to the other. In the x view, all the photons were distinct but in the y view the showers from β and δ merged. Most of the events were simpler to analyze than that shown because three-quarters of the events had only the two photons from the π^0 or η decay in the detector, as discussed in Appendix 3.VI.

For the analysis of E111, a simple moments method was possible (Jo75, Wa71) since only photons from the produced π^0 or η were present in the detector and also because there was no cause to measure the particles' energies because they were fixed by the beam momentum. In this experiment there was the possibility that other photons may have been present in the detector and also the energy of the particle had to be measured well. Thus a very different approach to the analysis was made, which both optimized the recognition of π^0 and η mesons in a multi-photon environment and tried to minimize the energy resolution. The analysis was based on the fact that the transverse development of an electromagnetic shower was subject to only small statistical fluctuations. The observed shape of a peak (labeled A - D in Fig. 3.1) was used both to tell if it was the projection of several photons whose showers had coalesced in one view and to improve the energy resolution. Later in the analysis

of an event all the pulse heights were fit to some hypothesis for the positions and energies of all the photons present in the event and the pairing of some two photons to give a particle. The main steps involved in the data analysis are summarized on Fig. 3.2 and are described in detail below.

3.2 PRELIMINARY CORRECTIONS

The 140 photomultiplier tubes and pulse height analyzers which measured the energy deposited in each counter had different gains and so it was necessary to equalize their responses. This was done both in the hardware, so as to make the energy cut-off of the trigger sharp, and in the off-line software, so as to improve the energy resolution. At the start of the experiment an 100 GeV electron beam was sent into each counter in turn and the pulse height responses were equalized by adjusting the voltages on the photomultiplier tubes, as described in Appendix 3.I and in Ref. (Ba75b). The gains were monitored throughout the experiment using the radioactive sources described in section 2.5.

For the off-line analysis an improved determination was made for the gains of each counter by using π^0 and η mesons which deposited a significant energy in that counter and comparing its pulse heights with those predicted from the shower shape distribution. Hence a counter whose gain was too low generally had less pulse height than predicted. This method was successful and is described in detail

DATA ANALYSIS SCHEME FOR EXPERIMENT 350

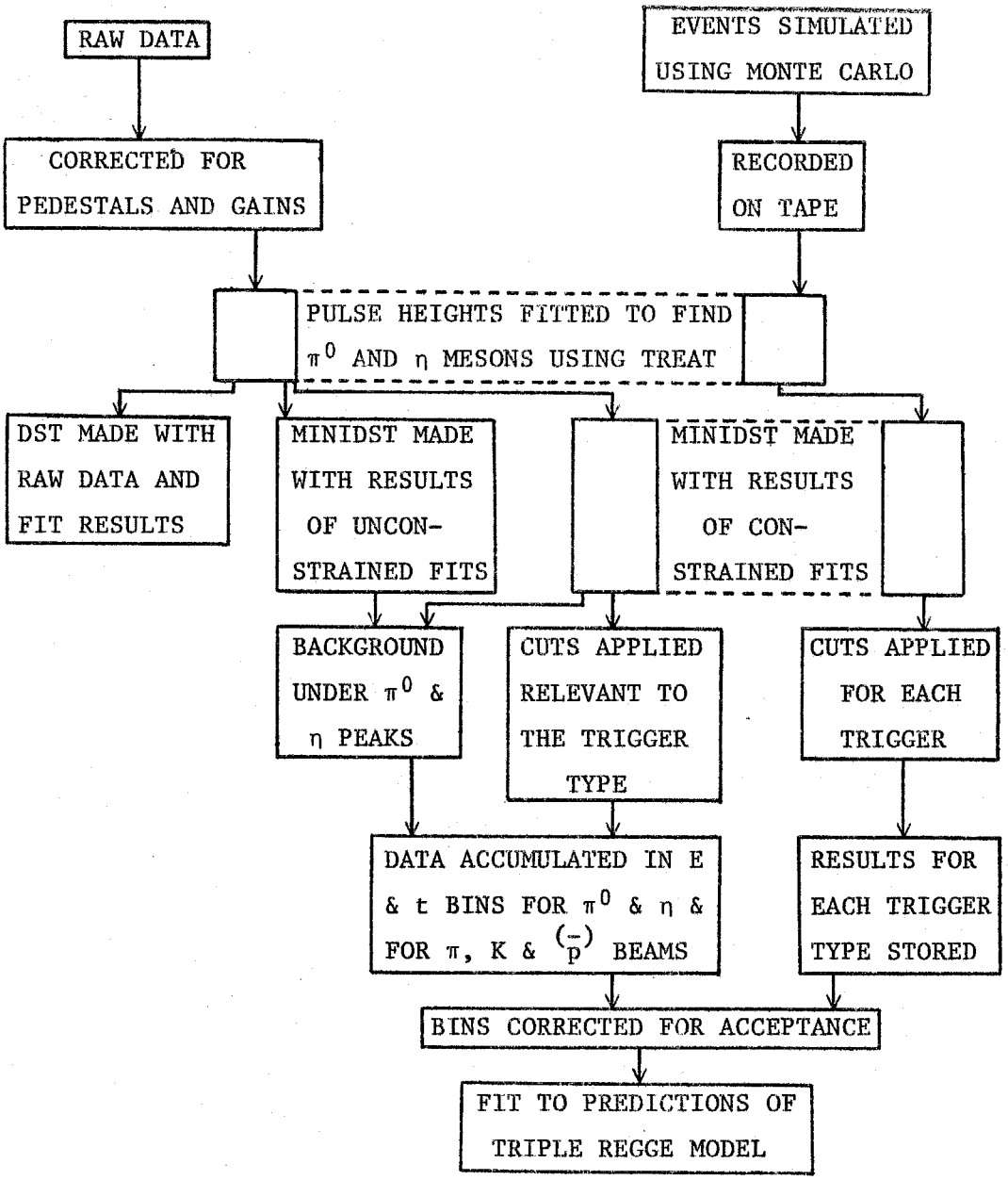

FIGURE 3.2 Flow chart to describe the data analysis.

in Appendix 3.I. Effects such as the attenuation along the counters and the differing sizes of the counters were ignored even though they contributed to the energy resolution.

Before doing the analysis it was necessary to know the shower shape distribution. This describes the energy deposited by a photon in a counter as a function of how far the counter is from the center of the shower and depends on the energy of the photon. It was obtained initially by looking at the shape of a large number of isolated showers of 45 GeV photons from 50 GeV π^0 and η mesons (Ba75a). The energy-dependence of this distribution was then found as a correction to this shape using a minimization technique similar to that used for the gains and described in Appendix 3.II.

It was necessary to know the calibration of the detector, that is, the correspondence between the pulse heights and the energy in GeV. This was determined by looking at a large number of events with only two photons present in the detector and calculating their mass by assuming that the two photons came from a particle at the midpoint of the target. The first large peak in the mass distribution is the π^0, as shown in Fig. 3.3. The various curves on this figure are explained later in the text. Fixing the center of this peak at the known π^0 mass (PD78) thus gave the calibration. A further check could be made by looking at the events in the region of the η and checking their mass distribution, as shown on Fig. 3.4.

It was also necessary to correct for the energy leakage in the

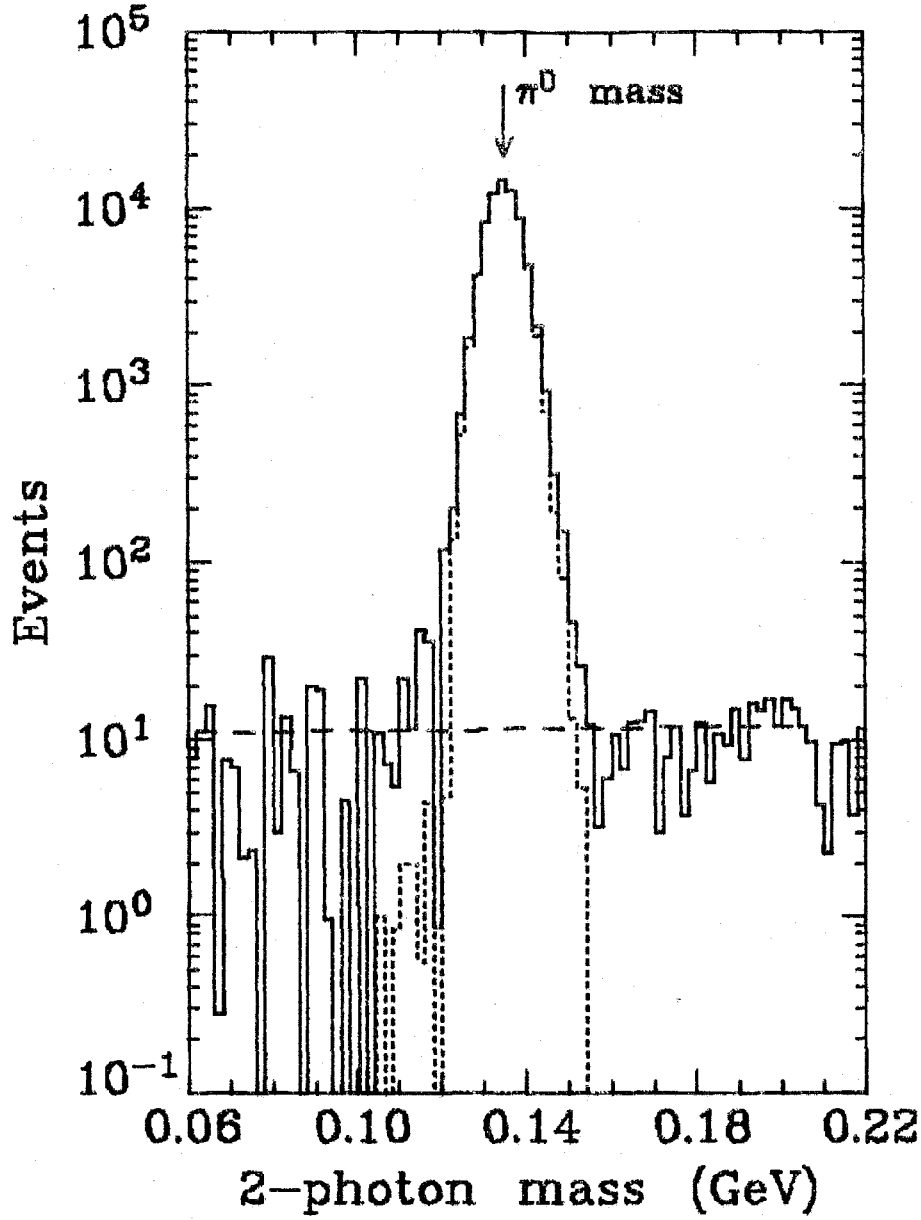

FIGURE 3.3 Mass spectrum for events with two photons in the detector in the π^0 region with energy above 60 GeV produced by an incident π^- beam and collected using trigger A. The empty target contribution has been subtracted. The curves are described in the text.

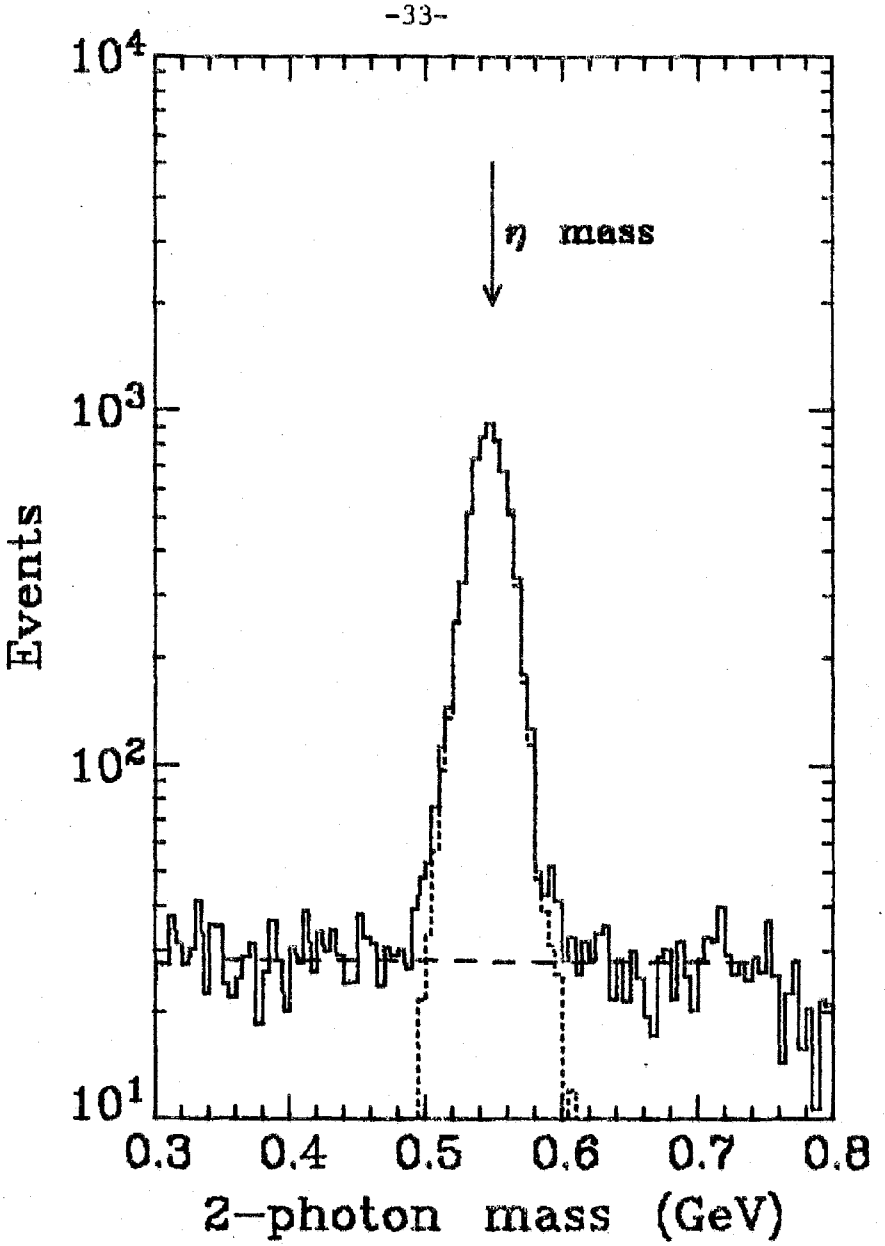

FIGURE 3.4 Mass spectrum for events with two photons in the detector in the η region with energy above 60 GeV produced by an incident π^- beam and collected using trigger A. The empty target contribution has been subtracted. The curves are described in the text.

longitudinal direction since the photon detector, which was 21 radiation lengths deep, was not long enough to contain an 80 GeV photon shower. The purpose of the backup counter, described in Section 2.5, was to sample the energy emerging from the back of the photon detector so that the energy deposited in the photon detector could be corrected for the leakage. The correction factor used the sum of the ten backup counter pulse heights as described in detail in Appendix 3.III.

The gains, shower shape distribution, calibration and leakage correction were determined iteratively by analyzing a small sample of events (about 100,000). The total data set was then analyzed to obtain the physics results.

3.3 EVENT ANALYSIS

In this section the method used to reconstruct photons and particles from the pulse heights is described. The procedure was to look at one data-taking run at a time in the off-line analysis. This corresponded to between 20 and 60 minutes of running time, depending on the trigger type and the target condition. Each event was then considered individually up to the stage of understanding the energies and transverse momenta of the particles present. A long summary tape, called a "DST", containing both the pulse heights and the results of the reconstruction analysis was produced along with two files, called "MINIDST"s, containing brief

descriptions of each event. The only cuts made during this analysis were ones to save unnecessary computing time and ones to deal with situations for which no algorithm existed. Cuts on the Cherenkov counters, quality of fit, etc., were made later, as discussed in the following section, so that the effects of these cuts could be investigated. One immediate cut was to require a hit in each plane of the two beam hodoscope counters, since this cut failed about one-fifth of the events before even looking at the pulse heights. All the data analysis was done using the CDC 7600 at L.B.L.

On each run the pedestal data had been collected and stored at the start of the file. The source data had also been stored on the tape approximately every 20 minutes. This had been used beforehand to obtain the counter gains by averaging over the source records on the file, or from the nearest source collection in time if none existed on the file, and dividing by the "ideal" value of each source, determined as described in Appendix 3.I. These were stored on a separate file for convenience (Ke77) and accessed before analyzing each file. For each event, the pedestal values were first subtracted from the 150 photon detector and backup counter pulse heights and each was divided by its gain. The energy deposited in each view was summed up and converted to GeV using the calibration discussed in section 3.2. A cut was made on the energy in each view at a value about 5 GeV below that required to trigger and at 10 GeV for the NFS trigger, which had no energy requirement.

It was also required that the ratio of the x and y total energies be between 0.5 and 2.0 so as to eliminate events where particles had interacted in the light pipes. It was found that few events failed these energy cuts except in the NFS case.

A detailed discussion of the event reconstruction algorithms is given in Appendix 3.IV so just a brief discussion will follow. The two views were searched for peaks and then matched together to find photons. In the example shown in Fig. 2.1, the peaks have been labeled A, B, C and D whereas the four photons have been labeled α, β, γ and δ. Pairings of these photons were searched to find π^0 and η mesons by looking at their masses. Possible photon and particle assignments were then checked by fitting the pulse heights to the shower shape distribution and finding the energies and positions of the photons. This was done either with no particle requirement (called an "unconstrained fit") or with the mass of the particle constrained in the fit ("constrained fit"). The constrained fits were made so as to improve the energy resolution and the results presented below come from these fits. The unconstrained fits were made on part of the data sample so that the background under the π^0 and η mesons could be calculated, as described in Appendix 3.VI. An unconstrained fit was also made on every event with only two photons present in the detector to provide a monitor of the detector calibration from the variation of the π^0 and η mass peaks with time. It was found that the calibration did not change. The results of these

fits were stored on the DST's. Separate MINIDST's containing the constrained and unconstrained fits for each event were also produced.

3.4 DATA SELECTION

The events for which successful fits with either a π^0 or an η present had been found were divided into two sets according to whether they came from the NFS trigger or an energy trigger (or both). Many cuts were now applied to these data. First a cut was made on the χ^2 of the fit and then energy cuts of 14 GeV, 34 GeV, 56 GeV and 64 GeV were applied for the NFS, low bias, medium bias and high bias triggers respectively. A cut was made using the pulse heights from the beam Cherenkov counters (see Appendix 3.IX) to eliminate ambiguous events and to divide the data into those from pion, kaon and (anti)proton beams. Since the energy resolution and reconstruction ability were poorer at large decay angles of the particle into two photons, the decay cosine was required to be less than 0.75. To eliminate edge effects, both photons in the particle were required to hit the detector more than two counterwidths from every edge. For the events from the NFS trigger, an additional cut was made on the pulse heights from the veto counter, as described in Appendix 6.I.

Corrections were made for a triggering effect which resulted in the amount of energy required to trigger an event depending on where the event occurred on the face of the detector. This happened because

the discriminator worked more on the peak pulse height than on the integral of the pulse height. The light reflected from the end of the counter and that coming directly from the event arrived at the photomultiplier tube at different times. For an event occurring at the end of the counter farthest from the photomultiplier tube both pulses arrived together and gave a larger signal than that from a similar event occurring near to the photomultiplier tube. So an event occurring far from a photomultiplier tube could trigger with less energy than one coming from near to a photomultiplier tube. If a uniform energy cut had been applied over the detector based on the highest energy required to trigger, then many of the events would have been eliminated, since the cross section falls rapidly with energy. Hence the variation of the threshold energy along each of the x and y planes was investigated for each trigger type, as described in Appendix 3.V, and a cut was applied at 5% above these values. Another unfortunate effect was due to the partial failure of the mixer covering most of the upper y counters. Events which triggered only in this mixer were eliminated.

Data were collected for every trigger with the target both full of hydrogen and empty. Both data sets were analyzed identically up to this stage. The number of events of any type which occurred from interactions with the hydrogen, N_p, was related to the number of events from the full and empty target data, N_{FULL} and N_{EMPTY}, by

$$N_p = N_{FULL} - \xi \frac{\text{Effective flux}_{FULL}}{\text{Effective flux}_{EMPTY}} N_{EMPTY}, \qquad (3.4.1)$$

where the "effective flux" is the number of beam particles effectively seen by the target once the beam counter requirements and the dead time of the electronics and the data collection system have been taken into account (see Appendix 3.IX). ξ is the fraction of the flux seen on average by the material outside the hydrogen target when the target is full. Its value was 0.985, 0.987 and 0.975 for the pion, kaon and (anti)proton beams respectively. This procedure eliminated the interactions occurring in the target walls and the beam counters and also the beam particle decays.

The subtraction varied from 4% to 59% of the full rate, as shown in Table 3.1. The values quoted are the ratios of the number of events satisfying the cuts described so far and weighted to correct for the background under the π^0 and η mass peaks, as described below. The lowest correction was for the NFS data due to the reduced cross section for π^0 and η production off heavy nuclei. The largest correction was for the kaon beam data and was due to the background from the decays $K^{\pm} \to \pi^{\pm}\pi^0$, $\mu^{\pm}\overset{(-)}{\nu}\pi^0$, $e^{\pm}\overset{(-)}{\nu}\pi^0$ and $\pi^{\pm}\pi^0\pi^0$. For most of the triggers the subtraction is about 14%, which is approximately that expected from calculating the interaction length of the material outside the hydrogen target and comparing it to the total material including the hydrogen. In the angular region with $0.006 \leqslant p_t/E \leqslant 0.010$, the empty target subtraction was found to be larger than

TABLE 3.1. Ratios, R, of the signals for π^0 and η production from the empty target data to those from the full target data.

Trigger	Bias	$-t$ (GeV^2)	Beam	$R(\pi^0)$	$R(\eta)$
A	low	< 1	$\pi^{\pm}$	0.151 ± 0.003	0.13 ± 0.01
A	medium	< 1	$\pi^{\pm}$	0.137 ± 0.001	0.124 ± 0.005
B	low	> 1	π^-	0.150 ± 0.007	0.20 ± 0.04
B	medium	> 1	$\pi^{\pm}$	0.139 ± 0.002	0.15 ± 0.01
B	high	> 1	$\pi^{\pm}$	0.15 ± 0.01	0.27 ± 0.08
A & C	low	all	p & $\bar{p}$	0.17 ± 0.01	0.21 ± 0.09
A & C	medium	all	p & $\bar{p}$	0.130 ± 0.006	0.15 ± 0.03
C	high	all	$\bar{p}$	0.16 ± 0.05	0.15 ± 0.15
A & C	low	all	$K^{\pm}$	0.55 ± 0.02	0.18 ± 0.03
A, C & K	medium	all	$K^{\pm}$	0.591 ± 0.006	0.14 ± 0.01
C	high	all	K^-	0.57 ± 0.02	0.18 ± 0.06
NFS	E > 40	all	π^-	0.035 ± 0.001	0.042 ± 0.003

usual and was due to beam particles which were partially bent by the sweeping magnet and then interacted with the air, thus attaining an artificially large transverse momentum.

The nature of the events satisfying all of the cuts is illustrated by the ratios in Table 3.2. These numbers are for the interactions of pion beams off hydrogen with the empty target contribution subtracted according to (3.4.1). About 80% of the accepted events had only two photons in the detector (called "2γ") and so the data are

TABLE 3.2. Nature of successful π^0 and η events from pion beams. All numbers have had the empty target contribution subtracted as described in the text.

		$2\gamma\ \pi^0$/Flux ($\times 10^7$)				
Trigger	Bias	- Beam	+ Beam	$2\gamma\ \eta/2\gamma\ \pi^0$	$m\gamma\ \pi^0/2\gamma\ \pi^0$	$m\gamma\ \eta/2\gamma\ \eta$
A	low	10172±136	9168±98	0.077±0.002	0.303±0.005	0.27 ±0.02
A	medium	5385± 24	5189±55	0.083±0.001	0.200±0.002	0.170±0.006
B	low	855± 14	-	0.044±0.004	0.216±0.008	0.19 ±0.04
B	medium	174± 1	163± 2	0.040±0.001	0.141±0.002	0.13 ±0.01
B	high	56± 1	51± 1	0.035±0.002	0.086±0.004	0.07 ±0.02
NFS	E > 40	165.7±0.6	-	0.096±0.001	0.484±0.003	0.378±0.008

fairly clean. The remaining events are called the "multiphoton" events ("$m\gamma$" in the table) and these generally had either three or four photons in the detector and were due mainly to the production of two π^0 mesons or to a π^0 and η combination. Later in the analysis these events were weighted to give the true signals, as described below, and this weighting suppressed the multiphoton signal relative to the two photon signal.

In the low bias and NFS data where a low energy cut was applied, there may have been several particles present in a single event. Thus each event was searched for photon pairs other than those in the fitted particle with masses suitable to be π^0 or η mesons. These additional particles were included in the cross section determination if they passed all the cuts, with a suitable weighting if several such pairs were present in an event.

One consequence of analyzing the data using constrained fits was that this gave a mass distribution with delta functions at the π^0 and η masses, so that the backgrounds under these signals could not be determined from this set of fits alone. Figures 3.3 and 3.4 show the mass distributions of all events with two photons in the detector from trigger A in the regions of the π^0 and η mesons using the unconstrained fits (solid curve). Also shown are the mass distributions for those events with a successful constrained fit (dotted curve). Clearly not all the tails of the mass peaks had successful constrained fits whilst some of the background arising from uncorrelated photons was successfully fitted. The mass distributions of the unconstrained fits on both sides of the π^0 and η mass peaks were fitted to polynomials, shown as dashed curves on the histograms, and from these the backgrounds were calculated and subtracted from the totals to give the magnitudes of the π^0 and η signals. The ratio of these signals to the number of events with constrained fits gave a weighting. This was determined as a function of the energy, the laboratory production angle, $\Omega = p_t/E$, the type of detected particle and the incident beam particle, as described in Appendix 3.VI. This correction was almost negligible for π^0 mesons in events with only two photons present but was very large for η mesons in events with three or more photons present.

The successful events from each incident and detected particle type combination were accumulated in bins in energy, E, and four-momentum transfer-squared, t, for each trigger type and beam polarity. For each bin, the weight, weight-squared and Ω for all the

contributing events were summed.

A correction was now made for the acceptance, that is, the probability of an event being detected once produced. This was calculated as a function of the energy and p_t/E of the particle and each bin was divided by the acceptance averaged over the energy and t ranges of the bin. This acceptance was determined by simulating two photon decays of π^0 and η mesons, fitting those events with both photons in the detector and passing those with successful fits through the same cuts as seen by the data. The scheme for combining the data and Monte Carlo results is presented in Fig 3.2 and the details of the Monte Carlo method for determining the acceptances and the results are presented in Appendix 3.VII. The acceptance was generally high and fairly uniform, varying for π^0 mesons from the maximum of 0.75 (due to the decay cosine cut) at zero p_t to about 0.2 at p_t = 2 GeV. A branching ratio into two photons of 0.9883 for the π^0 and 0.38 for the η (PD78) was included in the acceptance. Other corrections were made for the beam attenuation due to interactions occurring in the target which reduce the flux available to produce the desired interaction and for the possibility of two interactions taking place in the target with the second interaction producing the detected π^0 or η meson. This correction, which is described in Appendix 3.VIII, was about 3% at p_t = 1 GeV.

CHAPTER 4

THEORETICAL BACKGROUND

4.1 REGGE THEORY

In this section the application of Regge theory to obtain the cross section for 2-2 body scattering,

$$a + b \rightarrow c + d, \tag{4.1.1}$$

is described. This is an "exclusive reaction", in which all the particles produced are explicitly defined. The process (4.1.1) may be described in terms of two kinematic invariants, s and t, called the Mandelstam variables and defined by

$$s = (p_a + p_b)^2 \tag{4.1.2a}$$

$$t = (p_a - p_c)^2 \tag{4.1.2b}$$

where p is the four-momentum of the particle. Thus s is the square of the center of mass (c.m.) energy and t is the square of the four-momentum transferred between a and c. To observe the reaction (4.1.1), it is necessary that

$$s \geq s_{min} = \max\{(m_a + m_b)^2, (m_c + m_d)^2\}, \tag{4.1.3}$$

where m is the mass of the particle, and also that $t < t_{min}$ where t_{min} is the solution of the quadratic expression (Co77),

$$st_{min}u(t_{min}) - s(m_a^2m_b^2 + m_c^2m_d^2) - t_{min}(m_a^2m_c^2 + m_b^2m_d^2) - u(t_{min}) \times (m_a^2m_d^2 + m_b^2m_c^2) + 2m_a^2m_b^2m_c^2m_d^2(m_a^{-2} + m_b^{-2} + m_c^{-2} + m_d^{-2}) = 0 \tag{4.1.4a}$$

where the invariant u is defined as

$$u = (p_a - p_d)^2. \tag{4.1.4b}$$

When $m_a = m_c$ and $m_b = m_d$, this requirement becomes simply $t < 0$. The reaction (4.1.1) is assumed to be related to the "crossed" reactions,

$$a + \bar{c} \rightarrow \bar{b} + d \tag{4.1.5}$$

$$a + \bar{d} \rightarrow c + \bar{b}, \tag{4.1.6}$$

and the set (4.1.1,5,6) are referred to as the s, t and u channels of the process. If $\bar{s}$ and $\bar{t}$ are the invariants describing (4.1.5), then its amplitude, $\bar{A}(\bar{s},\bar{t})$, is assumed to be related to the amplitude, A(s,t), for (4.1.1) by

$$\bar{A}(\bar{s},\bar{t}) = A(\bar{t},\bar{s}) \tag{4.1.7}$$

Since the c.m. energy-squared, $\bar{s}$, for reaction (4.1.5) is t, the amplitude A(s,t) can be measured for positive t and negative s.

The specialized case with a, b, c and d all spinless is now considered for simplicity in the c.m. frame following the approach of Ref. (Co77). If the crossed reaction, (4.1.5), is considered, then the amplitude can be expanded as a series in the orbital angular momentum, ℓ, of a and $\bar{c}$ (or $\bar{b}$ and d) as follows,

$$A(s,t) = 16\pi \sum_{\ell=0}^{\infty} (2\ell + 1)A_\ell(t)P_\ell(\bar{z}(s,t)), \tag{4.1.8}$$

where P_ℓ is the Legendre polynomial of order ℓ and $\bar{z} = \cos\theta$, where

θ is the scattering angle between the directions of motion of the particles a and $\bar{b}$ in the c.m. frame.

The approach of Regge theory is to treat the angular momentum, ℓ, as a continuous complex variable, as described in Ref. (Co77) and in references therein. The series in (4.1.8) may diverge outside the t-channel physical region, but the amplitude may be rewritten using dispersion relations so as to be defined everywhere. Instead of using A_ℓ, partial waves, A_ℓ, of definite signature, $\tau = \pm 1$ (or "even" and "odd" signature), are defined. These satisfy

$$A_\ell^+(t) = A_\ell(t) \qquad \text{for } \ell = 0, 2, 4, \ldots, \qquad (4.1.9)$$

$$A_\ell^-(t) = A_\ell(t) \qquad \text{for } \ell = 1, 3, 5, \ldots, \qquad (4.1.10)$$

and the physical (unphysical) integer values of ℓ are called the "right (wrong) signature points". When there is no left-hand cut in the $\bar{z}$-plane then A_ℓ is bounded and $A_\ell^+ = A_\ell^- = A_\ell$, giving the phenomenon called "exchange degeneracy". This corresponds to the impossibility of the corresponding u-channel reaction occurring through the production of a single resonance. In potential scattering this means that there is no exchange force. A pair of exchange-degenerate trajectories, such as the ρ and A_2, have particles at all integral J.

Regge theory is based on the assumption that A_ℓ has only isolated singularities in ℓ and so can be analytically continued throughout the complex angular momentum plane. With this assumption,

a Sommerfeld-Watson transform applied to (4.1.8) gives

$$A^T(s,t) = 8\pi i \int_C (2\ell + 1) A^T_\ell(t) P_\ell(-\bar{z}) \operatorname{cosec}(\pi\ell) d\ell, \qquad (4.1.11)$$

where C encloses the non-negative integers and is closed at positive infinity, as shown below:

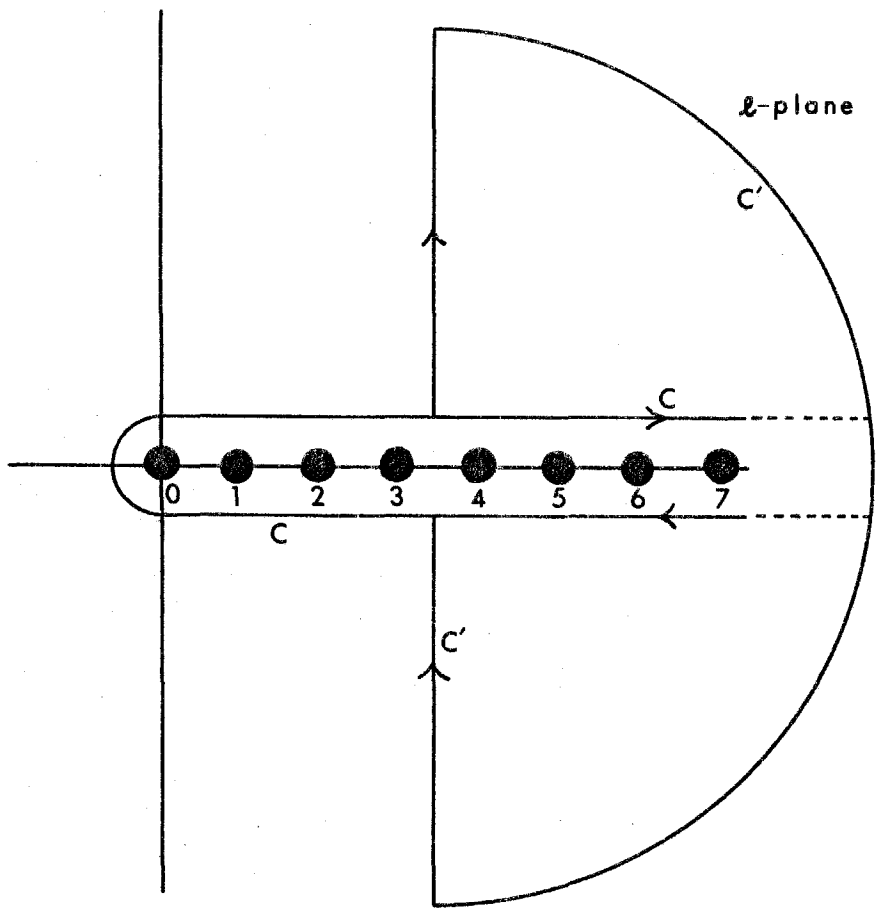

FIGURE 4.1 Contours, C and C', for the Sommerfeld-Watson transform.

P_ℓ can be defined for non-integral ℓ by expressing it in terms of the hypergeometric function, which gives $P_\ell(x) = F(-\ell,\ell + 1;1;(1 - x)/2)$. The contour integral is calculated by displacing C to the contour C', which is the line $\mathrm{Re}(\ell) = L$ together with a semi-circle at infinity,

and then moving the line $\mathrm{Re}(\ell) = L$ to the left. Then a pole at $\ell = \alpha(t)$ of the form $A_\ell(t) \sim \beta(t)/(\ell - \alpha(t))$, which is called a "Regge pole" or a "Regge trajectory" as it varies with t, gives a contribution,

$$A(s,t) = -16\pi^2(2\alpha(t) + 1)\beta(t)\mathrm{cosec}(\pi\alpha(t))(P_{\alpha(t)}(-\bar{z}) + \tau P_{\alpha(t)}(\bar{z})). \qquad (4.1.12)$$

The limit of high s is given by the limit of high z and results in the cross section,

$$\frac{d\sigma}{dt}(s,t) = B(t)|\xi(t)|^2 s^{2\alpha(t) - 2}, \qquad (4.1.13)$$

where $\xi(t)$ is the "signature factor" for the exchanged trajectory, defined by

$$\xi(t) = (e^{-i\pi\alpha(t)} + \tau)\mathrm{cosec}(\pi\alpha(t)). \qquad (4.1.14)$$

This factor ensures that a trajectory contributes a pole in t only when $\alpha(t)$ passes through a right-signature integer. The exact form of $B(t)$ is unimportant here, but it can be defined so that (4.1.13) also holds for particles with spin, being then a sum over several terms. (4.1.13) holds for the physical region $s > s_{min}$ and $t < t_{min}$.

The trajectory, $\alpha(t)$, may be experimentally determined from the cross section using the form (4.1.13) for $t < t_{min}$, where it is usually purely real. This trajectory lies on an analytic continuation of that observed for positive t whenever a physical particle

with the correct quantum numbers is present, as shown in the examples on Figs. 1.1-3. Since each Regge trajectory has a definite signature, the physical particles are separated by two units of angular momentum.

As an example of the application of Regge theory, consider the charge-exchange πN scattering process,

$$\pi^- + p \to \pi^0 + n. \qquad (4.1.15)$$

In this case the exchanged trajectory must have the quantum numbers $B = 0$, $S = 0$, $C = 0$, $I = 1$ and $G = +1$ and the only possibility is the ρ trajectory as shown below:

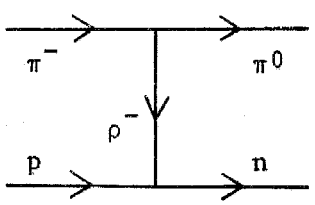

Figure 1.1 shows this trajectory as obtained from the s-dependence of the cross section for the process (4.1.15) as a function of t for $t < t_{min} \simeq 0$ by experiment E111. The crossed reaction,

$$\pi^- + \pi^0 \to \bar{p} + n \qquad (4.1.16)$$

may proceed by the production of the ρ and g particles, of spin 1 and 3 respectively, giving the two lowest mass particles on the trajectory. The trajectory determined from (4.1.15) at low t_m follows closely the line through the ρ and g.

Figure 1.1 also shows the A_2 trajectory, on which the A_4 also lies, which has the quantum numbers B = 0, S = 0, C = 0, I = 1 but G = -1, which gives it the opposite signature but otherwise the same quantum numbers as the ρ. It has been determined for negative t from the process

$$\pi^- + p \rightarrow \eta + n. \qquad (4.1.17)$$

Clearly the ρ and A_2 trajectories are almost coincident. For $t > 0$ they both correspond to the line

$$\alpha_\rho(t) \simeq \alpha_{A_2}(t) \simeq 0.5 + 0.9t. \qquad (4.1.18)$$

Such a pair of trajectories are called "exchange degenerate". The K*(892) and K*(1430) trajectories, shown on Fig. 1.2, are likewise exchange degenerate and lie for $t > 0$ on a line parallel to the ρ and A_2 trajectories given by

$$\alpha_{K^*(892)}(t) \simeq \alpha_{K^*(1430)}(t) \simeq 0.3 + 0.9t. \qquad (4.1.19)$$

However exchange degeneracy does not hold for the baryon trajectories, although they again have the universal slope of 0.9. The nucleon trajectory, shown on Fig. 1.3, is given by

$$\alpha_N(t) \simeq -0.37 + 0.9t \qquad (4.1.20)$$

whilst the Δ trajectory is given by

$$\alpha_{\Delta}(t) \simeq 0.0 + 0.9t. \qquad (4.1.21)$$

Elastic scattering processes, such as $\pi^- p \to \pi^- p$, may also be described in terms of Regge theory but it is found that $\sigma_{tot}(s) \simeq s^{\alpha(0)-1}$ is generally flat and thus $\alpha(0) \simeq 1$, whilst all the known trajectories have $\alpha(0) < 0.5$. Clearly this trajectory has the quantum numbers of the vacuum, namely B = 0, S = 0, C = 0, I = 0 and G = +1, and thus a new trajectory called the "Pomeron" and denoted P was invented (Ch61) to describe elastic scattering as a Regge process. This trajectory probably does not have any corresponding physical particles and may be a more complicated singularity than a simple pole. The other trajectories are collectively referred to as "Reggeons" and denoted R.

4.2 TRIPLE REGGE THEORY FOR ONE-PARTICLE INCLUSIVE PRODUCTION

In this section, Regge theory is extended to describe inclusive reactions of the form

$$a + b \rightarrow c + X, \tag{4.2.1}$$

where a is the incident beam particle, b is the target particle and c is the detected particle. X means that any other particles may be produced, making this a type of "inclusive reaction". The cross section is integrated over all possibilities for X and so it is a function of three kinematic variables. Here the variables s and t which were used in section 4.1 to describe exclusive reactions with Regge theory will again be used. The third variable used here is the Feynman variable (Fe69), x, which is defined as

$$x = \left(p_{\parallel c}/p_{\parallel c_{max}}\right)_{c.m.} \tag{4.2.2}$$

where $p_{\parallel c}$ is the scalar product $\underline{p}_c \cdot \hat{\underline{p}}_a$. In the case when the masses of a, b and c are negligible compared with s and t there is an approximation:

$$M^2 \simeq s(1 - x), \tag{4.2.3}$$

where M^2 is the mass-squared of X.

The integration over the unobserved particles, X, is done using a generalization of the optical theorem due to Mueller (Mu70) which relates the inclusive cross section for the production of particle c to the elastic $a\bar{c}b$ "forward" scattering amplitude (Bø74,Ho73), as

shown diagrammatically below:

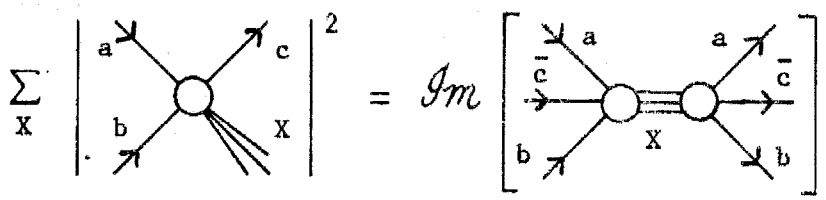

Here Mueller's theorem is applied to reaction (4.2.1) just for the particular kinematic region relevant for this experiment, namely high x and high s. Suppose first that s/M^2 becomes large with t and M^2 fixed. Then the reaction can be regarded as a sum of two-body scattering processes of the form a + b → c + X with X being a particle of mass M and the sum is over the various possibilities for the quantum numbers of X. Regge theory in this limit describes each such process by the exchange of singularities, χ, in the t-channel, shown schematically by:

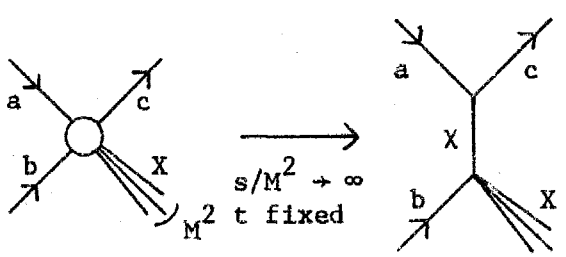

This amplitude is now squared to produce the cross section. Mueller's theorem says that the cross section is obtained by summing the amplitudes for reactions of the form

$$\chi + b \to \psi + b \qquad (4.2.4)$$

at zero momentum-transfer, where χ and ψ are the virtual exchanged particles. The c.m. energy for this process is M, which is now assumed to be large so that Regge theory can be invoked again to say that the cross section is given by the exchange of singularities, ζ, at zero momentum-transfer, as shown below:

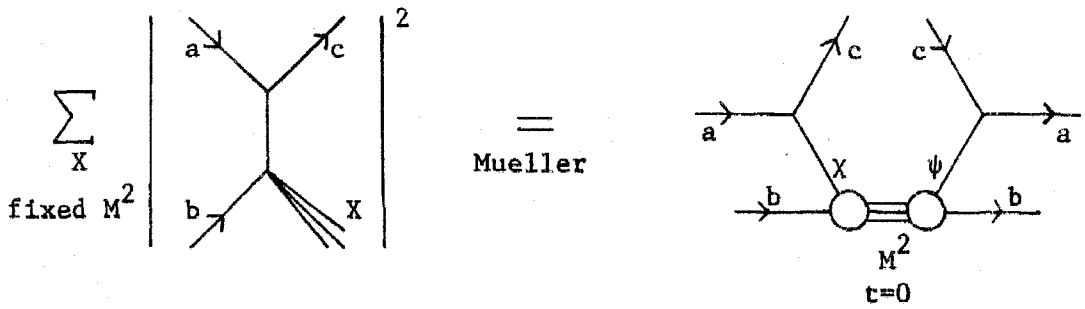

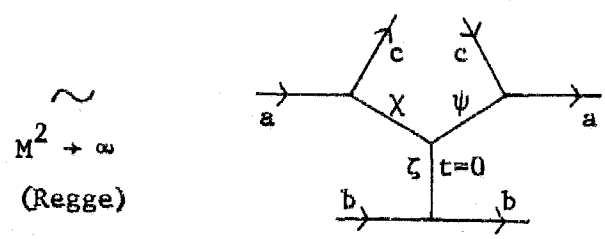

This gives the "triple vertex" diagram of triple Regge theory. The cross section from the contribution with the exchange of poles χ and ψ with four-momentum-squared t on the top two legs and the pole ζ on the bottom leg is, using the approximation (4.2.3), given by:

$$\frac{d^2\sigma}{dtdx}(x,t,s) = G_{\chi\psi\zeta}(t)(1-x)^{\alpha_\zeta(0)-\alpha_\chi(t)-\alpha_\psi(t)} s^{\alpha_\zeta(0)-1} \qquad (4.2.5)$$

where $G_{\chi\psi\zeta}(t)$ is the product of the residues of the exchanged particles together with the coupling of the three exchanged particles. This is referred to as the "residue function" below and is defined as

$$G_{\chi\psi\zeta}(t) = \gamma_{ac\chi}(t)\gamma_{ac\psi}(t)\gamma_{bb\zeta}(0)\gamma_{\chi\psi\zeta}(t)\mathrm{Re}[\xi_\chi(t)\xi^*_\psi(t)], \quad (4.2.6)$$

where $\xi(t)$ is the signature factor defined by (4.1.14) and γ_{abc} is the coupling at the abc vertex, chosen to be real here with no loss of generality. The definition (4.2.6) holds providing a and c are spinless particles since only the spin non-flip amplitude for b is important in the triple Regge region. For particles with spin, G is a sum over the helicity states. The leading triple Regge term usually has χ and ψ being the same trajectory and ζ being the Pomeron, which was described in the previous section. Since the intercept of the Pomeron trajectory, $\alpha_P(0)$, is close to unity, the terms with Pomeron exchange on the bottom leg have cross sections which are almost independent of s, that is, they "scale", whilst the contributions with other particles (Reggeons) on the bottom leg have cross sections which fall rapidly with s since it is observed that $\alpha(0) \leqslant 0.5$ for all known particle trajectories.

A useful concept in this kinematic region is the "Finite Mass Sum Rule" or "FMSR", obtained by averaging the subprocess (4.2.4)

over the resonance region of M. To do this it is necessary to integrate over both the reactions,

$$a + b \rightarrow c + X \tag{4.2.7a}$$

$$c + b \rightarrow a + X, \tag{4.2.7b}$$

which correspond to positive and negative M^2 respectively. For convenience, the integration variable used is

$$\nu = p_2 \cdot (p_1 - p_3) = \frac{1}{2}(M^2 - t - m_b^2) \tag{4.2.8}$$

and, instead of just averaging, the n^{th} moment can be taken to give

$$\int_0^N \nu^n d\nu \left(\frac{d^2\sigma}{dtdM^2}(ab\rightarrow cX) + (-1)^{n+1} \frac{d^2\sigma}{dtdM^2}(cb\rightarrow aX) \right) =$$

$$\sum_{\chi\psi\zeta} \frac{G_{\chi\psi\zeta}(t)}{32\pi^2} s^{\alpha_\chi(t) + \alpha_\psi(t) - 2} \frac{N^{\alpha_\zeta(0)-\alpha_\chi(t)-\alpha_\psi(t)+n+1}}{\alpha_\zeta(0)-\alpha_\chi(t)-\alpha_\psi(t)+n+1}, \tag{4.2.9}$$

where n = 0, 2, 4, ... for odd signature ζ trajectories and n = 1, 3, 5, ... for even signature ζ trajectories and N is some sufficiently large number.

The finite mass sum rules can be used rigorously as they stand in relation (4.2.9). They have also led to the approximation called "two-component duality" for the processes where χ and ψ are Reggeons, which is the case for this experiment. Each side of relation (4.2.9) is divided into two halves and equated to each

other. The left-hand side is divided into the integral over the resonances in M^2, which is equated to the sum over the processes where ζ is a Reggeon, and the integral over the non-resonant background, which is equated to the processes where ζ is the Pomeron. This duality concept was used in making estimates of cross sections.

4.3 TRIPLE REGGE THEORY FOR INCLUSIVE π^0 AND η PRODUCTION

The results of section 4.2 are now specialized to the reactions measured in this experiment. The basic reaction was

$$\pi^- + p \rightarrow \pi^0 + X, \tag{4.3.1}$$

whose main contribution at high x is given by the exchange of two ρ mesons and a Pomeron (P) at $t = 0$, as shown pictorially in Fig. 4.2. Also shown, for comparison, is the corresponding NFS reaction, which is described in the following section. Using (4.2.5), the cross section due to this exchange is given by

$$\frac{d^2\sigma}{dtdx}(x,t,s) = G_{\rho\rho P}(t)(1 - x)^{1-2\alpha_\rho(t)}, \tag{4.3.2}$$

where the Pomeron intercept has been assumed to be $\alpha_P(0) = 1.0$. This assumption is valid in the kinematic region covered by this experiment since the total cross sections are flat at these values of M^2 (PD78). The cross section (4.3.2) also gives the leading contribution to the reaction

$$\pi^+ + p \rightarrow \pi^0 + X \tag{4.3.3}$$

and so the cross sections for (4.3.1) and (4.3.3) should be similar.

The other terms which contribute significantly to the high x cross section are shown in Fig. 4.3. The ρp elastic scattering part of the model may also take place through ρ, f and f' exchange. The

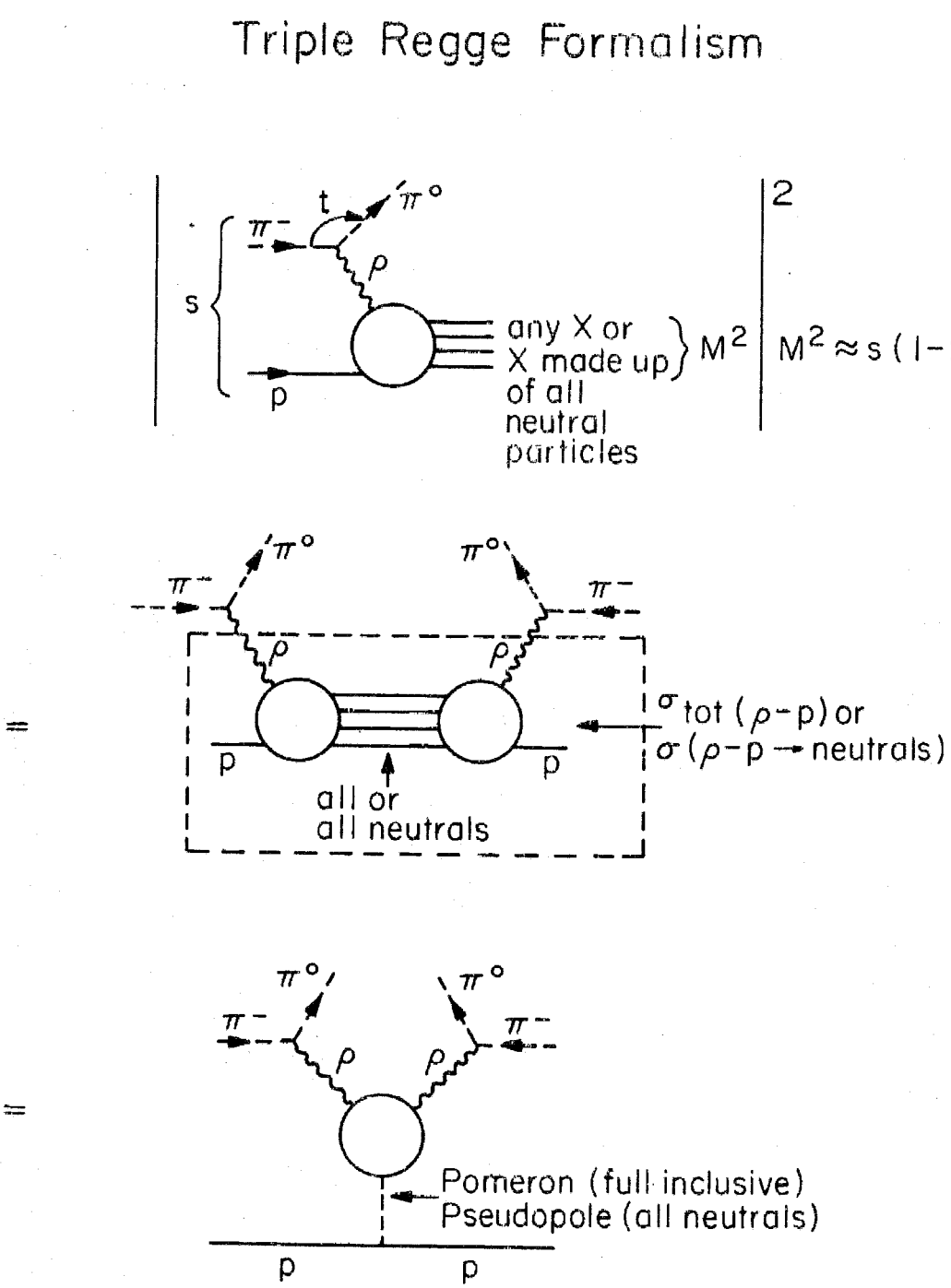

FIGURE 4.2 Triple Regge formalism explained diagrammatically for the main terms contributing to $\pi^- p \to \pi^0 X$ and $\pi^- p \to \pi^0 X^0$.

CONTRIBUTIONS TO $\pi^{\pm}$ p → π^0X

A: DOMINANT TRIPLE REGGE TERM

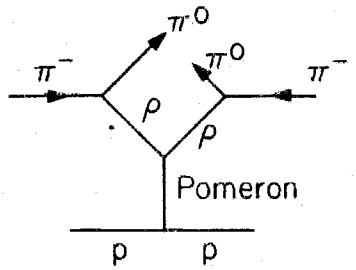

π^+ beam ≡ π^- beam

B: (SMALL) TRIPLE REGGE CORRECTION

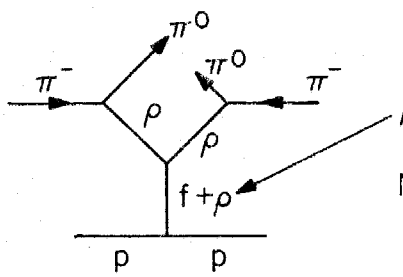

ρ changes sign for π^+ beam

Net $(f+\rho)\big|_{\pi^+} \sim 0.65\,(f+\rho)\big|_{\pi^-}$

C: LOW MASS CONTRIBUTIONS

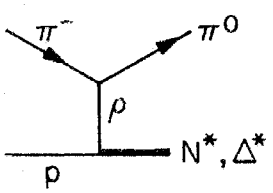

By Duality

Total resonances$\big|_{\pi^+} \sim 0.65$ Total resonances$\big|_{\pi^-}$

D: I=2 CONTRIBUTIONS

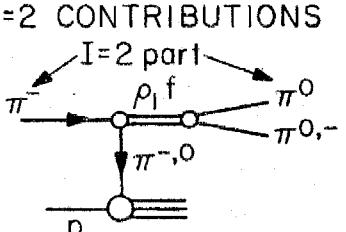

or

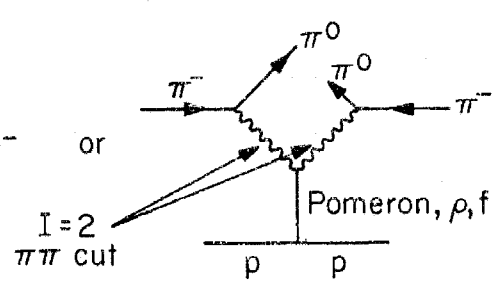

FIGURE 4.3 The four terms which contribute to $\pi^{\pm}p \to \pi^0X$ in the triple Regge region.

f' has been observed to be mainly $s\bar{s}$ in the quark model and thus, by Zweig's rule, does not couple to either the $\rho\rho$ vertex or the $p\bar{p}$ vertex, so it is ignored here. Isospin conservation at the ρ and p vertices shows that only the linear combinations $f_{\pm} = (\sqrt{2}f \mp \sqrt{3}\rho)/\sqrt{5}$ can be exchanged for the $\pi^{\pm}$ beams respectively. Their contributions to the cross sections for $\pi^{\pm}$ incident beams are given by

$$\frac{d^2\sigma}{dtdx}(x,t,s) = G_{\rho\rho f_{\pm}}(t)s^{-0.5}(1 - x)^{0.5-2\alpha_{\rho}(t)}, \qquad (4.3.4)$$

where the intercepts of the f and ρ trajectories have been taken to be $\alpha_{\rho}(0) = \alpha_{f}(0) = 0.5$. In Appendix 4.I it is shown that at low -t

$$G_{\rho\rho f_{+}}(t) \approx 0.65 G_{\rho\rho f_{-}}(t) \qquad (4.3.5)$$

and an estimation of this normalization is made using the FMSR. The $s^{-0.5}$ factor in (4.3.4) helps to make this contribution small at the beam energy of 100 GeV used here. The f dominates over the ρ because the $fp\bar{p}$ coupling is much larger than the $\rho p\bar{p}$ coupling as is shown by comparing the non-diffractive part of πp elastic scattering (f and ρ exchange) to the charge-exchange process $\pi^- p \to \pi^0 n$ (Ir78).

At high x, above the triple Regge region, there are contributions from the production of resonances of low mass, as shown in Fig. 4.3C, which were included in the interpretation of the data because the energy resolution caused them to contribute at lower energies. The exclusive neutron production has been measured at 60, 100 and 150 GeV but the $\Delta(1232)$ production has been measured at low s only

whilst the production of higher mass Δ and N* baryons has not been measured. Using duality arguments it can be shown that the ratio of the contribution of these resonances to the π^+ cross section to their contribution to the π^- cross section is that given by (4.3.5), namely 0.65. The modeling of this term is described in Appendix 4.II and its success is discussed in section 5.1. These duality arguments apply only to the averages over the resonances but, due to the finite energy resolution of 1.5 GeV, this averaging has essentially been done by the detector itself. The triple Regge terms were truncated at the mass of 1.4 GeV, above the Δ(1232) production.

If the isospins of the incident and detected particles are considered, then

$$|\langle\pi^{\pm}|T|\pi^0\rangle|^2 = \frac{1}{2}|T_1|^2 + \frac{1}{2}|T_2|^2 \pm \mathrm{Re}(T_1 T_2^*) \qquad (4.3.6)$$

where T_1 and T_2 are the amplitudes for the isospin I = 1 and 2 exchanges respectively. The $|T_1|^2$ part is just the ρ exchange considered already. The remaining I = 2 exchange and the interference terms had to be included separately. For most reactions they give a negligible contribution but in this case they can be produced by double π exchange, as shown in Fig. 4.3D, which is large at small t_m because of the low mass of the π. This term was calculated explicitly using a model described in Appendix 4.III and subtracted from the data before fitting for the I = 1 exchange processes. It is slightly different for the π^+ and π^- reactions because of the

different s-dependence of the total cross sections, $\sigma_{tot}(\pi^{\pm}p)$, and because of the different sign of the interference term in (4.3.6).

The production of η mesons by the reactions,

$$\pi^{\pm} + p \to \eta + X, \tag{4.3.7}$$

is dominated by A_2A_2P exchange, which has a cross section given by

$$\frac{d^2\sigma}{dtdx}(x,t,s) = G_{A_2A_2P}(t)(1 - x)^{1-2\alpha_{A_2}(t)}. \tag{4.3.8}$$

Again there are smaller contributions from the $A_2A_2\mathcal{P}$ exchange and the low mass resonance production. Since the η is an isoscalar, the triple Regge exchanges are pure isospin 1.

The reactions with incident kaon beams, namely

$$K^{\pm} + p \to \pi^0 + X \tag{4.3.9}$$

$$K^{\pm} + p \to \eta + X, \tag{4.3.10}$$

are dominated by the K*K*P and K**K**P exchanges, where K* and K** are used to denote the K*(892) and K*(1430) trajectories respectively. These are exchange degenerate, just like the ρ and A_2 trajectories. With the reactions $\pi^{\pm} + p \to \pi^0 + X$ and $\pi^{\pm} + p \to \eta + X$, only one of the two trajectories is exchanged in each case because the G-parity quantum number has to be conserved. This quantum number is not defined for strange particles, so both the K* and K** trajectories can be exchanged in each of π^0 and η production from

kaon beams. It is however possible to estimate the content of the exchanges in the two cases using assumptions from SU_3. In the SU_3 classification scheme, the K* and K** belong to different octets (vector, V, and tensor, T, respectively), whose neutral members (e.g. ρ and A_2 respectively) have charge conjugation, C, of -1 and +1 respectively. This results in a different SU_3 coupling and hence different proportions of the two trajectories are exchanged in π^0 and η production. The vector-pseudoscalar(P_1)-pseudoscalar(P_2) coupling (from $Tr[V(P_1P_2-P_2P_1)]$) and tensor-pseudoscalar-pseudoscalar coupling (from $Tr[T(P_1P_2+P_2P_1)]$ are conventionally denoted by F and D respectively. A further complication is that the η is a mixture of the octet member, $\eta_8 = (u\bar{u} + d\bar{d} - 2s\bar{s})/\sqrt{6}$, and the singlet member, $\eta_1 = (u\bar{u} + d\bar{d} + s\bar{s})/\sqrt{3}$, The mixing angle, θ, between the η and η' is defined so that $\eta = -\sin\theta\eta_1 + \cos\theta\eta_8$ and $\eta' = \cos\theta\eta_1 + \sin\theta\eta_8$ and has a value of about -11° (PD78). The singlet member, S, together with a pseudoscalar does not couple to a vector, since $Tr[V(SP-PS)]$ vanishes, but does couple to a tensor (from $Tr[T(SP+PS)]$), with a coupling denoted by D' below. The resulting cross sections are

$$\frac{d^2\sigma}{dtdx}(K^{\pm}p\to\pi^0X)\Big|_P = \frac{1}{2}\gamma_{\bar{p}pP}(0)\left[\gamma_{K^*K^*P}(t)\left|\xi_{K^*}(t)\right|^2F^2(t)\right.$$
$$\times\ (1-x)^{1-2\alpha_{K^*}(t)} + \gamma_{K^{**}K^{**}P}(t)\left|\xi_{K^{**}}(t)\right|^2$$
$$\left.\times\ D^2(t)(1-x)^{1-2\alpha_{K^{**}}(t)}\right] \qquad (4.3.11)$$

$$\frac{d^2\sigma}{dtdx}(K^{\pm}p\to\eta X)\Big|_P = \gamma_{p\bar{p}P}(0)\left[\frac{3}{2}\gamma_{K^*K^*P}(t)\left|\xi_{K^*}(t)\right|^2F^2(t)\cos^2\theta\right.$$
$$\times\ (1-x)^{1-2\alpha_{K^*}(t)} + \gamma_{K^{**}K^{**}P}(t)\left|\xi_{K^{**}}(t)\right|^2$$
$$\left.\times\ \left[\frac{2}{\sqrt{3}}\sin\theta D'(t) + \frac{1}{\sqrt{6}}\cos\theta D(t)\right]^2(1-x)^{1-2\alpha_{K^{**}}(t)}\right. \tag{4.3.12}$$

where γ_{abc} is the coupling at the abc vertex and ξ_a is the signature factor. For the pion beam reactions, the Pomeron term in π^0 production is due solely to the F coupling whilst the η production is due to the D and D' couplings. Thus the corresponding cross sections are

$$\frac{d^2\sigma}{dtdx}(\pi^{\pm}p\to\pi^0X)\Big|_P = 2\gamma_{p\bar{p}P}(0)\gamma_{\rho\rho P}(t)\left|\xi_\rho(t)\right|^2F^2(t)(1-x)^{1-2\alpha_\rho(t)} \tag{4.3.13}$$

$$\frac{d^2\sigma}{dtdx}(\pi^{\pm}p\to\eta X)\Big|_P = \gamma_{p\bar{p}P}(0)\gamma_{A_2A_2P}(t)\left|\xi_{A_2}(t)\right|^2\frac{1}{3}[-2\sin\theta D'(t) +$$
$$\sqrt{2}\cos\theta D(t)]^2(1-x)^{1-2\alpha_{A_2}(t)}\ . \tag{4.3.14}$$

Thus the kaon beam reactions may be related to the pion beam reactions. A comparison of the data is shown and discussed in Chapter 7.

There are no low mass resonances for the reactions with K^+ beams since no particles exist with B = 1 and S = 1. For the reactions with K^- beams both Λ and Σ baryons may be produced. Duality argu-

ments suggest that the exchanges with Reggeons on the bottom leg would exist only for the K^- reactions. This is further shown by the total cross section, $\sigma_{tot}(K^+p)$, which is flat at the values of s relevant to this experiment (PD78). As with the pion beams, the P on the bottom leg may be replaced by the ρ, f or f'. Since there is no longer any G-parity restriction, the corresponding particles with the opposite G-parity, the A_2, ω and ϕ, may also be exchanged. Again, by Zweig's rule, the f' and ϕ couple only weakly to the $p\bar{p}$ and are ignored here. Now the reactions $K^+ + n \to \pi^0 + X$ and $K^+ + p \to \pi^0 + X$ both have no low mass resonance contributions and so the I = 1 (ρ and A_2) and I = 0 (f and ω) parts must independently vanish for the K^+ beam. Hence the f and ω exchanges must contribute equally to the K^- beam and likewise the ρ and A_2 must contribute equally. Again the f dominates over the ρ. Isospin considerations show that the contributions are from the linear combination $(f + \rho + \omega + A_2)/2$.

Considering the isospins of the incident and detected particles in reactions (4.3.9) gives

$$|\langle K^{\pm}|T|\pi^0\rangle|^2 = \frac{1}{3}|T_{1/2}|^2 + \frac{2}{3}|T_{3/2}|^2 \mp \frac{2\sqrt{2}}{3}\,\mathrm{Re}(T_{1/2}T^*_{3/2}). \quad (4.3.15)$$

The I = 1/2 contribution, $T_{1/2}$, corresponds to the K* and K** exchanges discussed above. The terms involving the I = 3/2 amplitude, $T_{3/2}$, were calculated by assuming that they were due to π exchange with the production of an additional unobserved kaon, as

described in Appendix 4.III. Again the η reaction is pure I = 1/2 exchange.

The production of π^0 mesons with incident proton and antiproton beams,

$$\overset{(-)}{p} + p \rightarrow \pi^0 + X, \qquad (4.3.16)$$

is assumed to be dominated by the NNP (with I = 1/2) and $\Delta\Delta P$ (with I = 3/2) exchanges, in the ratio 1:2 given by (4.3.15) with $\overset{(-)}{p}$ replacing $K^{\pm}$. Here N and Δ are used to denote the four I = 1/2 and I = 3/2 trajectories respectively having different signatures and parities and the radial excitations of these. The dominant trajectories are expected to be the highest ones in the Chew-Frautschi plot. These are the nucleon (or N_α) trajectory and the N(1520) (or N_γ) trajectory for the I = 1/2 set and the Δ(1232) (or Δ_γ) trajectory for the I = 3/2 set. Studies of πN backward scattering have shown that the amplitude for the nucleon trajectory dominates over that for the N(1520) trajectory (Be71). The dominant trajectories are shown on Fig. 1.3. The interference terms where one leg is N exchange and one leg is Δ exchange is small because the Pomeron can no longer be exchanged on the bottom leg.

For reactions from a proton beam, no low mass resonances can be produced because there are no particles with B = 2 and so, by duality, there are no exchanges with Reggeons on the bottom leg. With the antiproton beam reactions such as $\bar{p} + p \rightarrow \pi^0 + \pi^0$ are possible and and thus exchanges with Reggeons on the bottom leg exist and lead to

a larger antiproton cross section, as shown in Section 7.3. The f, ρ, ω and A_2 are exchanged, as described above for the K^- beam. In this case the f and ω terms dominate even more over the ρ and A_2 because there are now two $p\bar{p}$Reggeon couplings instead of one.

4.4 PSEUDO REGGE THEORY FOR NEUTRAL FINAL STATE REACTIONS

"Pseudo Regge theory" is an extension of Regge theory based on the multiperipheral model. It was applied to triple Regge theory to describe some test data on π^0 mesons produced with only neutral particles taken by E111 and used to test the feasibility of the present experiment (E374, Fo74). The basic idea of the multiperipheral model is that the dominant production mechanisms are chains of particles with each one produced at a small momentum transfer with respect to the adjacent particle, that is, "peripherally", as shown diagrammatically below:

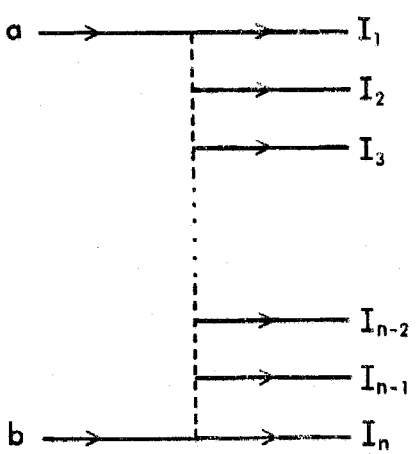

In the application considered here, the exchanges (shown by dashed lines) are due to Reggeons and the intermediate states, I_j, are preferentially clusters of particles instead of single particles, as this model is only valid when the center of mass energy of adjacent particles, I_j and I_{j+1}, is much larger than $\sqrt{s_o}$ = 1 GeV for all j.

The total cross section for

$$a + b \to X \tag{4.4.1}$$

is obtained by summing the squares of these diagrams over all combinations of n particles, for all multiplicities n, and gives the result (Ho73),

$$\sigma(ab \to X) \sim p_{lab}^{\alpha_p(0)-1}, \tag{4.4.2}$$

for the dominant contribution at high p_{lab}, where p_{lab} is the momentum of a when b is at rest and $\alpha_p(0)$ is the Pomeron intercept. Pseudo Regge theory extends this idea to the case when all the intermediate states, $I_1,\ldots,I_n$, satisfy some restrictive property, Q, and thus explains reactions of the form,

$$a + b \to X_Q, \tag{4.4.3}$$

where X_Q means that all the particles obey the property Q. The cross section for (4.4.3) is shown diagrammatically as a "ladder diagram":

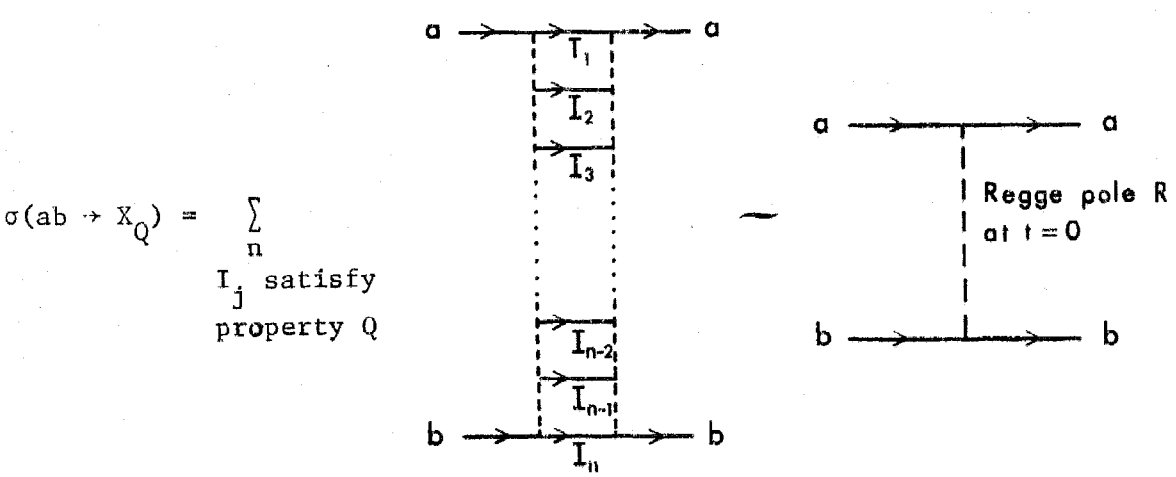

The cross section is given by

$$\sigma(ab \to X_Q) \sim p_{lab}^{\alpha_R(0)-1}, \qquad (4.4.4)$$

where the nature of the Regge pole, R, and hence the value of its intercept, $\alpha_R(0)$, depends on the property Q.

For the neutral final state (NFS) trigger used in this experiment, the requirement, Q, is that all the final state particles be neutral. Just as the total cross section is described in terms of the exchange of a Pomeron at t = 0, the cross section for producing a neutral final state may described by the exchange of a "Pseudopole", $\mathcal{P}$, at t = 0 (Fo74, Ba78b). Hence

$$\sigma(ab \to X^0) \sim p_{lab}^{\alpha_{\mathcal{P}}(0)-1}, \qquad (4.4.5)$$

where X^0 means that only neutral particles are produced. In Section 6.1, it is shown that (4.4.5) is verified experimentally and $\alpha_{\mathcal{P}}(0)$ is determined.

For reactions of the form,

$$a + b \to c + X^0, \qquad (4.4.6)$$

where c is a neutral particle, the summation over X for the full inclusive process in the triple Regge model described in Section 4.2 is replaced by a summation over neutral particles using a ladder diagram as shown above. The resulting cross section is given by

$$\frac{d^2\sigma}{dtdx}(x,t,s) = G_{\chi\psi\mathcal{P}}(t)(1-x)^{\alpha_{\mathcal{P}}(0)-\alpha_\chi(t)-\alpha_\psi(t)} s^{\alpha_{\mathcal{P}}(0)-1} \qquad (4.4.7)$$

in analogy with (4.2.5). For the reaction,

$$\pi^- + p \rightarrow \pi^0 + X^0, \qquad (4.4.8)$$

the χ and ψ in (4.4.7) are the ρ, as shown in Fig. 4.1, whilst for the reaction,

$$\pi^- + p \rightarrow \eta + X^0, \qquad (4.4.9)$$

the χ and ψ are both the A_2. For both these reactions, the production of low mass resonances contributes at high x and their cross section is not included in (4.4.7) which is invalid for x near unity. The estimation of their cross sections is described in Appendix 4.II.

4.5 MODELS FOR HADRON PRODUCTION AT HIGH TRANSVERSE MOMENTA

The last four sections have described Regge theory, which was developed about a decade ago as a model for understanding the strong interaction. More recently a greater understanding of the constituents of hadrons (quarks and gluons) has developed and the scattering of quarks and gluons can be calculated using the theory of Quantum Chromodynamics (QCD). Much work has been done in recent years on developing models to explain the abundance of particles and jets found experimentally at large transverse momenta (p_t). Most of the effort in applying these models has concentrated on explaining large p_t phenomena at $x \approx 0$, where the cross section is largest. However some of these models are also valid for x near unity and it is hoped that they can explain the large t behavior of the effective Regge trajectories, presented in Chapters 5-7, and the t-dependence of the cross sections. The description of the models presented here follows the approach of two review articles, references (Si76) and (Ja78).

Only the hard-scattering models are considered here and just the inclusive reaction,

$$a + b \rightarrow c + X, \qquad (4.5.1)$$

is discussed. In these models, some part, A, of the beam particle, a, interacts with some part, B, of the target particle, b, and two particles, C and D, are produced at a wide angle in the c. m. frame, as shown diagrammatically below:

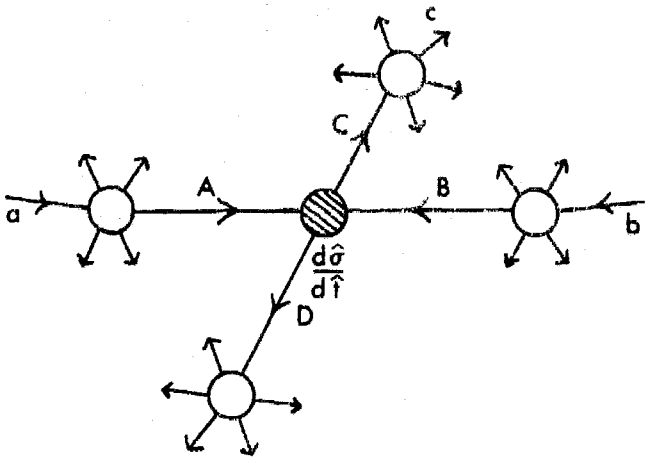

The hadrons in the undetected part, X, are formed from the fragments of a, b, C and D by a mechanism which has yet to be understood. Since some of the scattered particles, A, B, C and D may be quarks, with fractional charges, it is clear that some fragments from one of these will join with fragments from others to form particles. At high p_t, the hard (that is, energetic) fragments from each of C and D create "jets" along the general direction of their parent particles.

Using this model, the cross section for reaction (4.5.1) is

$$E_c\frac{d^3\sigma}{dp_c^3} = \frac{1}{\pi}\int \sum_A \sum_B \sum_C \sum_D d^2p_{t_A} d^2p_{t_B} d^2p_{t_C} dx_A dx_B G_{A/a}(x_A,p_{t_A}) G_{B/b}(x_B,p_{t_B})$$

$$x \frac{1}{x_c} F_{c/C}(x_c,p_{t_c}) \frac{d\hat{\sigma}}{d\hat{t}}(\hat{s},\hat{t})\Big|_{AB \to CD}, \qquad (4.5.2)$$

where $G_{Y/y}(x_Y,p_{t_Y})$ is the probability distribution for finding the constituent Y in y with longitudinal momentum $x_Y|\vec{p}_y|$ and momentum p_t transverse to the direction of y and $F_{c/C}(x_c,p_{t_c})$ is the number

distribution for the fragmentation of C into the hadron c with longitudinal momentum $x_c|\vec{p}_C|$ and transverse momentum p_{t_c}. The distributions G and F both have to be found empirically as there is little theoretical understanding of the processes of hadron disintegration and formation. $\hat{s}$ and $\hat{t}$ are the square of the c. m. energy and the square of the four-momentum-transfer respectively for the subprocess AB → CD and are given by

$$\hat{s} = x_A x_B s \tag{4.5.3a}$$

$$\hat{t} = x_A t/x_c, \tag{4.5.3b}$$

where s and t describe reaction (4.5.1).

There are various models of high p_t phenomena and they differ mainly in their choice of the subprocess AB → CD. In the constituent interchange model (CIM) it is supposed that the dominant contributions to wide-angle scattering are from quark-hadron subprocesses such as the subprocess,

$$M_i + q_i \rightarrow M_f + q_f, \tag{4.5.4}$$

where M_i and M_f are quark-antiquark systems and q_i and q_f are quarks (Si76). Thus for the pion and kaon beam reactions,

$$\pi^{\pm} + p \rightarrow (\pi^0,\eta) + X, \tag{4.5.5}$$

$$K^{\pm} + p \rightarrow (\pi^0,\eta) + X, \tag{4.5.6}$$

the incident and detected particles are already mesons and so (4.5.2) is used with A = a and C = c and gives, on neglecting the transverse

momentum of B,

$$E_c \frac{d^3\sigma}{dp_c^3} = \frac{1}{\pi} \frac{sx_{Bj}}{s+u} \sum_{q_i} G_{q_i/p}(x_{Bj}) \left. \frac{d\hat{\sigma}}{d\hat{t}}(\hat{s},\hat{t}) \right|_{aq_i \to cq_f}, \qquad (4.5.7)$$

where the fractional longitudinal momentum, x_{Bj}, of the quark, q_i, in the proton (called the "Bjorken scaling variable") is given by

$$x_{Bj} = \frac{-t}{s+u}, \qquad (4.5.8)$$

and where $\hat{s} = x_{Bj}s$ and $\hat{t} = t$.

At high x_{Bj}, the main contribution to the cross section is from the valence quarks in the proton, that is, the uud system, whilst the cross section at low x_{Bj} is dominated by scattering off the quarks and antiquarks in the sea of quark-antiquark pairs surrounding the proton. x_{Bj} is related to the Feynman scaling variable, x, defined by relation (4.2.2) as follows:

$$x_{Bj} \simeq \frac{-t}{s(1-x)-t}. \qquad (4.5.9)$$

Since $s \simeq 200$ GeV^2 in this experiment, x_{Bj} is unity at $x = 1$ and then decreases very rapidly to 0.14 at $x = 0.97$ and 0.05 at $x = 0.9$ for $-t \simeq 1$ GeV^2 and then remains at a value near 0.02 for x down to 0.7. The x-range used for the fits described in Chapters 5-7 was 0.71 - 0.97 and -t was under 4 GeV^2 and so the definition of the triple Regge kinematic region used here corresponds to small x_{Bj} and hence the interactions occur off the sea quarks in the proton. Only at much higher values of -t will the interactions off the valence

quarks be important in the triple Regge region. The distributions of u and d quarks and antiquarks in the sea are about equal (ignoring effects due to Pauli statistics) and so π^0 and η mesons should be produced at the same rate from meson beams of opposite polarity, according to this model. If the valence quarks were being probed, then the production of π^0 mesons would be higher from a π^- beam than from a π^+ beam, for example, because the reactions would be caused by the subprocesses,

$$\pi^- + u \to \pi^0 + d, \tag{4.5.10}$$

$$\pi^+ + d \to \pi^0 + u, \tag{4.5.11}$$

respectively and there are two u quarks and only one d quark in the proton and a higher probability of finding the u quark at high x_{Bj} than the d quark.

The cross section for a subprocess, A + B → C + D, of the form (4.5.4) is obtained from some dimensional counting arguments which have now been justified by QCD (Br79b) and these show that in leading order the cross section is

$$\frac{d\hat{\sigma}}{dt}(\hat{s},\hat{t}) \sim \hat{s}^{-n_A-n_B-n_C-n_D+2} f(\hat{\theta}(\hat{s},\hat{t})), \tag{4.5.12}$$

where n_H is the number of valence quarks and antiquarks in the hadron H and f is some function of the c. m. scattering angle, $\hat{\theta}$. Substituting (4.5.12) into (4.5.7) shows that the t-dependence of the cross sections for processes of the form (4.5.5,6) has the form,

$$\left.\frac{d^2\sigma}{dtdx}\right|_{x \text{ fixed}} \sim t^{-4}. \qquad (4.5.13)$$

For the reactions $\overset{(-)}{p}p \to \pi^0 X$, the cross section behaves like t^{-5}.

A further contribution of the CIM model is a prediction of the form of $f(\hat{\theta})$ in (4.5.12), which gives (B174a),

$$\frac{d\hat{\sigma}}{d\hat{t}}(\hat{s},\hat{t}) \sim \frac{1}{\hat{s}\hat{u}^3}. \qquad (4.5.14)$$

This predicts an x-dependence of the form $(1 - x)^3$ for reactions (4.5.5,6). For $\overset{(-)}{p}p \to \pi^0 X$, the x-dependence is predicted to be $(1 - x)^4$. An integer exponent is predicted for any reaction which can be considered as an exchange of an elementary particle in a crossed channel. For example, the reaction (4.5.10) may be considered as the exchange of a d quark in the u channel:

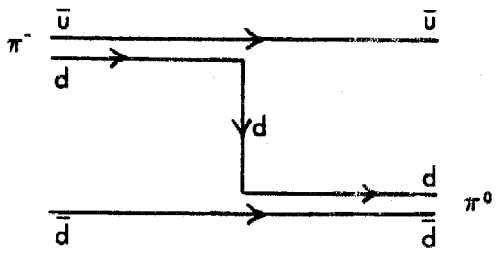

It is now believed (Fa79) that the prediction (4.5.14) is not derivable from quark exchanges in QCD and so the predictions for the exponents will be changed, although an odd integer is predicted for the meson exchanges and an even integer is predicted for the baryon exchanges. The oddness or evenness of the integer arises from the fact

that Born diagrams such as that shown above can only give rise to poles or logarithmic terms and not to square root cuts in the amplitude. The normalization of the reactions can also be calculated (B178, Fa79) using the form (4.5.14) and the result is compared with the data in the following chapters.

In terms of QCD, the dominant CIM mechanism for the process $\pi^- p \to \pi^0 X$ at high t_m consists of the exchange of a ρ meson (a coherent quark-antiquark pair) and the exchange of gluons carrying large momenta between the two valence quarks in the pion, for example,

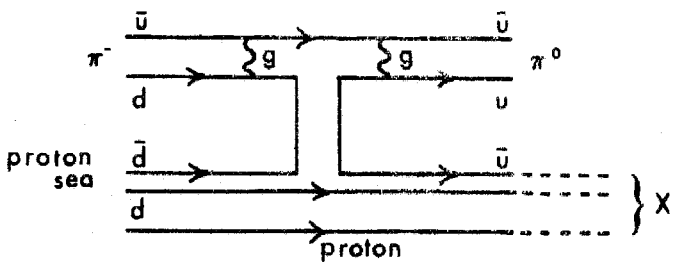

A second contribution to wide-angle scattering is from gluon exchange or gluon annihilation between a constituent of the incident pion and a constituent of the proton (Fi79). There are eight such subprocesses. These are the scattering of quarks and antiquarks, $qq \to qq$, $\bar{q}q \to \bar{q}q$ and $\bar{q}\bar{q} \to \bar{q}\bar{q}$, the scattering of gluons off quarks and antiquarks, $gq \to gq$ and $g\bar{q} \to g\bar{q}$, the annihilation processes, $gg \to \bar{q}q$ and $\bar{q}q \to gg$, and gluon scattering, $gg \to gg$. For the processes (4.5.5,6) in the triple Regge region, the dominant contributions are from the scattering of a quark in the incident particle off a gluon

or a quark in the target proton. The cross sections for these processes may be calculated using QCD and substituted into (4.5.2) and the integral is then calculated using the quark distribution function within the pion, the quark and gluon distribution functions within the proton and the quark fragmentation functions into π^0 and η mesons. The transverse momenta of the quarks and gluons are incorporated using a "smearing" process which has to assume values for the mean transverse momenta of quarks and gluons inside hadrons. Unfortunately this calculation has yet to be done using the latest pion distribution function.

CHAPTER 5

INCLUSIVE π^0 AND η PRODUCTION FROM PION BEAMS

5.1 ρ TRAJECTORY AND RESIDUE FUNCTION FROM INCLUSIVE π^0 PRODUCTION

In this section, the results from the reactions,

$$\pi^- + p \rightarrow \pi^0 + X \tag{5.1.1}$$

and

$$\pi^+ + p \rightarrow \pi^0 + X, \tag{5.1.2}$$

are presented in the context of the triple Regge model and the ρ trajectory and residue function are extracted. From Section 4.3, it is seen that this model predicts that the cross sections for reactions (5.1.1) and (5.1.2) are given by

$$\frac{d^2\sigma}{dtdx}(x,t,s)\Big|_{\pi^{\pm}p \rightarrow \pi^0 X} = G_{\rho\rho P}(t)(1-x)^{1-2\alpha_\rho(t)} +$$

$$G_{\rho\rho f_{\pm}}(t)s^{-0.5}(1-x)^{0.5-2\alpha_\rho(t)} + (I = 2 \text{ exchanges})$$

$$+ (\text{low mass resonances}). \tag{5.1.3}$$

The data were thus accumulated in t bins as a function of the energy of the π^0, E, as found from the constrained fits described in Chapter 3, for the various trigger types and for the two beam polarities. The measurements in each energy bin were corrected for the acceptance and for the effects of multiple scattering and beam attenuation in the target using the energy at the midpoint of the

bin and the mean p_t/E for the bin. The calculations of these corrections are described in Appendices 3.VII and 3.VIII. The data were corrected by overall factors for the inefficiency of the pion definition, as described in Appendix 3.IX, and for the loss of π^0 mesons due to photon conversions, as described in Appendix 6.I. Figure 5.1 shows the data with all the corrections applied but with purely statistical errors. The theoretical curves are described below.

FIGURE 5.1 Data on $\pi^{\pm}p \to \pi^0 X$ as a function of the energy of the π^0, E, in different t bins. The results of fits to the π^- and π^+ data simultaneously over the energy range 80 - 96 GeV are shown. The resulting values for α are shown on Fig. 5.2 and listed in Table 5.1. The various terms contributing to the cross section are shown independently and are described in the key.

KEY

—— Final fit, that is, total theoretical cross section smeared with the energy resolution and the beam momentum distribution

---- ppP triple Regge contribution

—— ppf triple Regge contribution

..... Low mass resonances (estimated)

-·-· I = 2 π exchange (estimated)

⬍ ⬍ Limits of fit

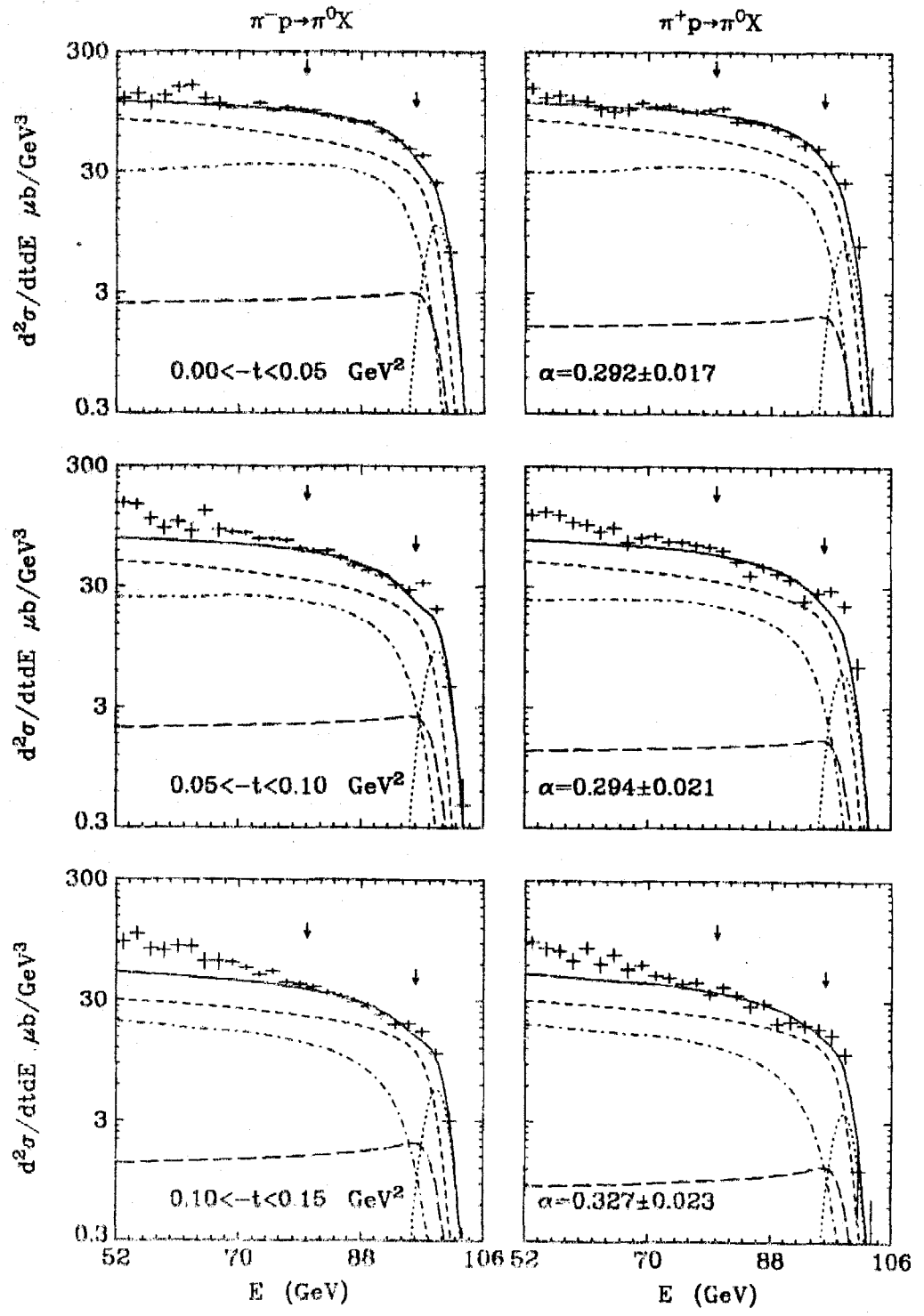
$\pi^-p\to\pi^0X$
$\pi^+p\to\pi^0X$
$d^2\sigma/dtdE$ $\mu b/GeV^3$
300
30
3
0.3
$0.00<-t<0.05$ GeV^2
$\alpha=0.292\pm0.017$
$0.05<-t<0.10$ GeV^2
$\alpha=0.294\pm0.021$
$0.10<-t<0.15$ GeV^2
$\alpha=0.327\pm0.023$
52
70
88
106
E (GeV)

FIGURE 5.1(a)

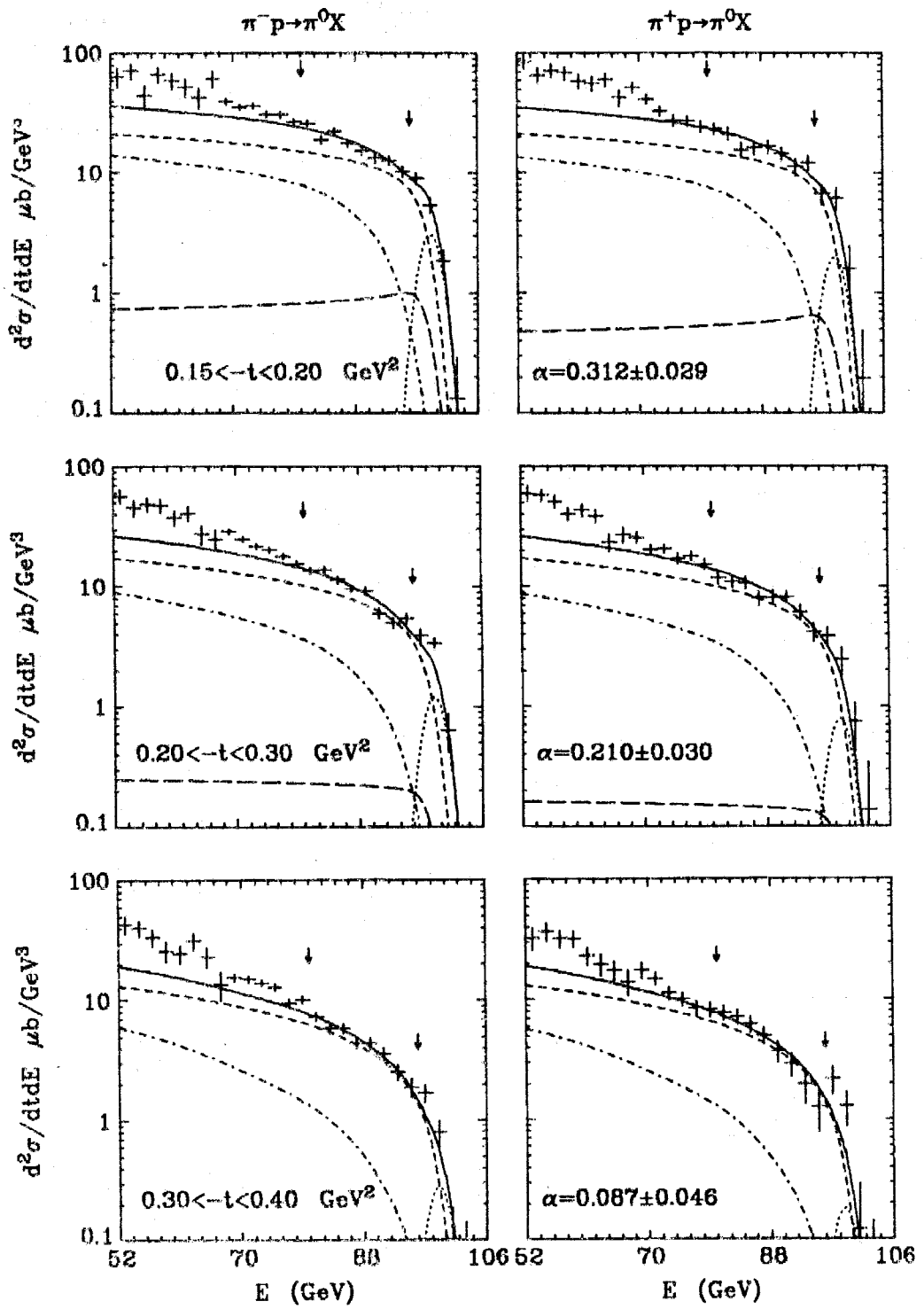
$\pi^- p \to \pi^0 X$
$\pi^+ p \to \pi^0 X$
$d^2\sigma/dtdE$ $\mu b/GeV^3$
100
10
1
0.1
$0.15 < -t < 0.20$ GeV^2
$\alpha = 0.312 \pm 0.029$
$0.20 < -t < 0.30$ GeV^2
$\alpha = 0.210 \pm 0.030$
$0.30 < -t < 0.40$ GeV^2
$\alpha = 0.087 \pm 0.046$
52
70
88
106
E (GeV)

FIGURE 5.1(b)

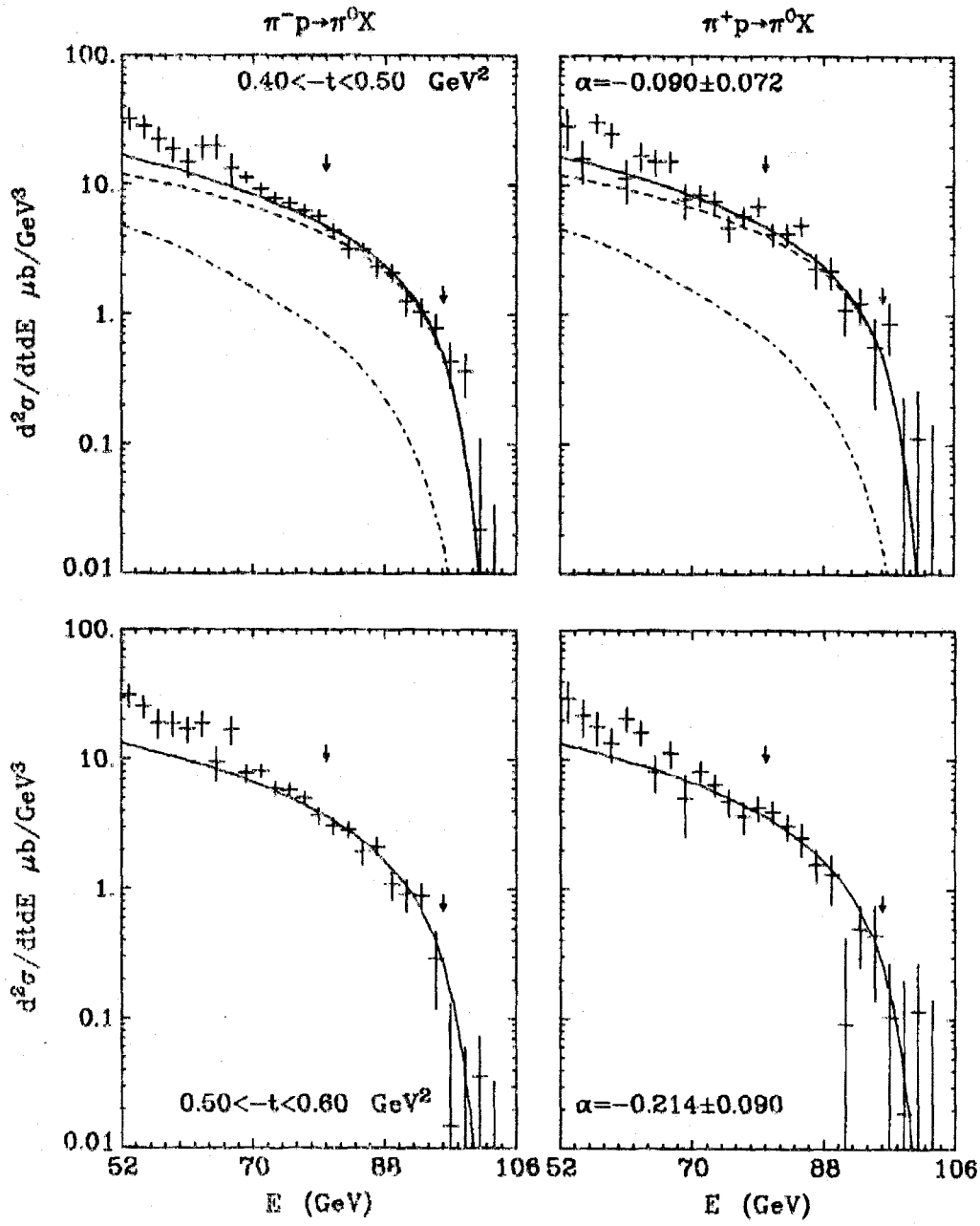
$\pi^-p\to\pi^0X$
$\pi^+p\to\pi^0X$
0.40<−t<0.50 GeV²
α=−0.090±0.072
0.50<−t<0.60 GeV²
α=−0.214±0.090
$d^2\sigma/dtdE$ μb/GeV³
E (GeV)
100.
10.
1.
0.1
0.01
52
70
88
106

FIGURE 5.1(c)

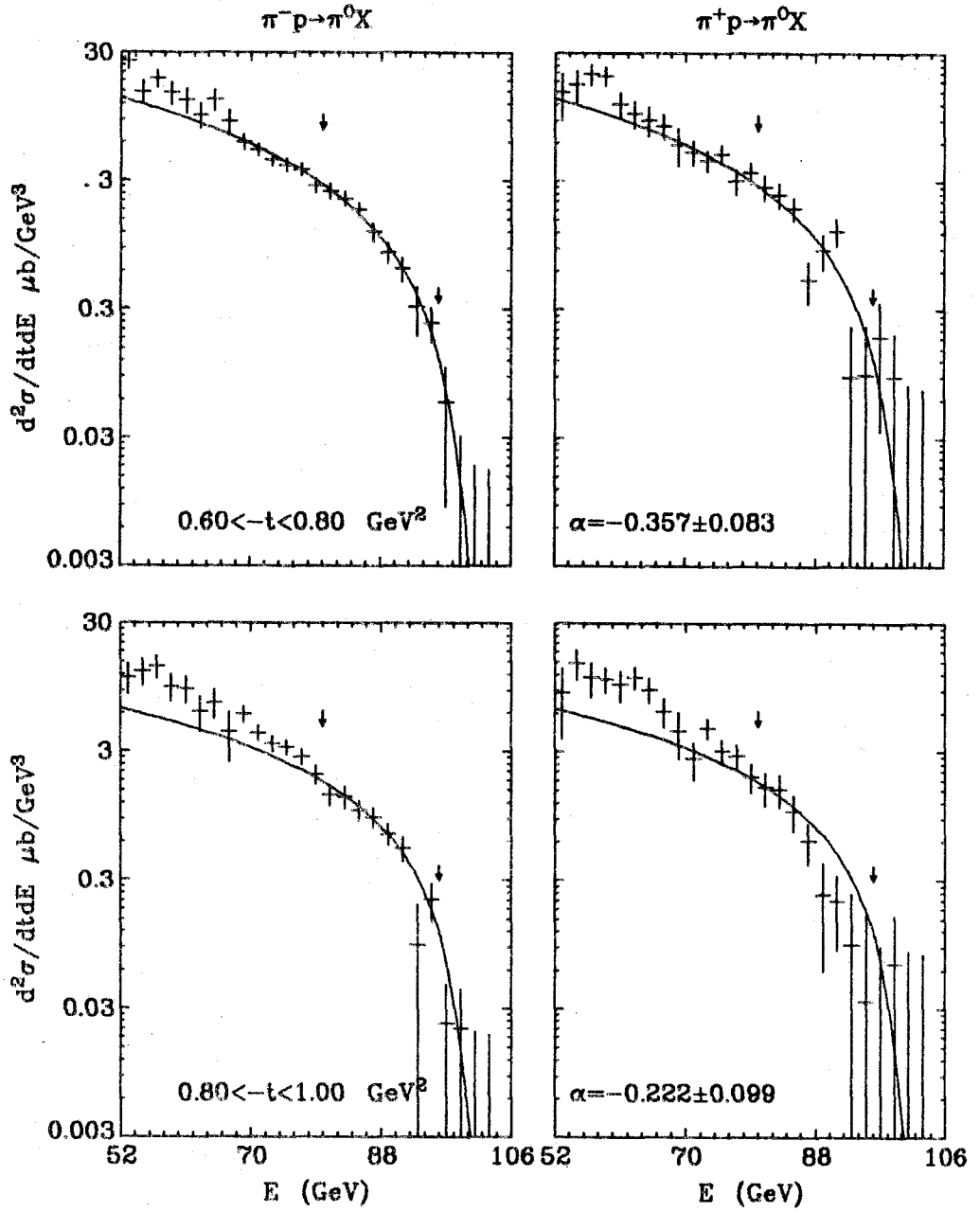
$\pi^-p\to\pi^0X$
$\pi^+p\to\pi^0X$
$d^2\sigma/dtdE$ μb/GeV³
30
3
0.3
0.03
0.003
0.60<−t<0.80 GeV²
α=−0.357±0.083
0.80<−t<1.00 GeV²
α=−0.222±0.099
52
70
88
106
E (GeV)

FIGURE 5.1(d)

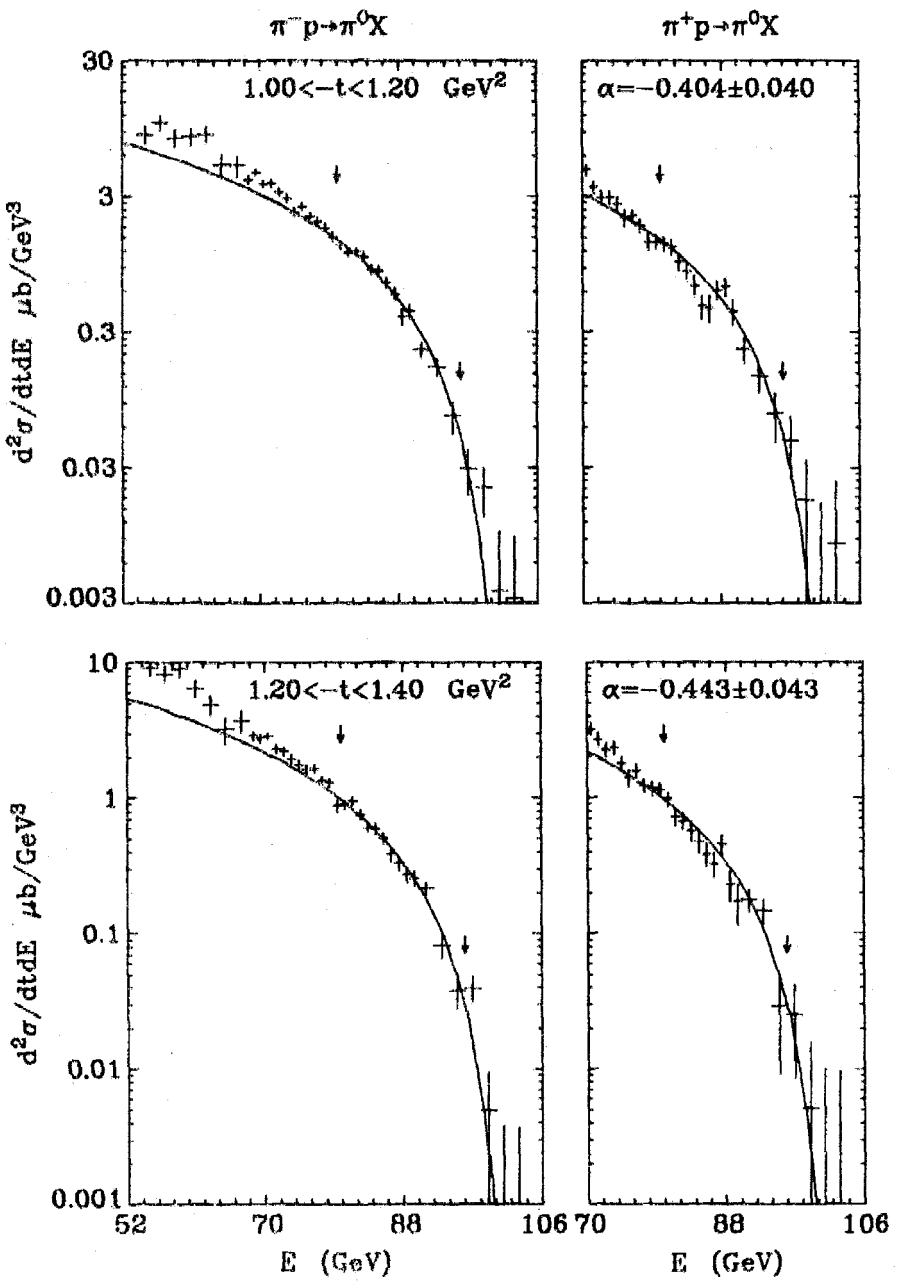
$\pi^- p \to \pi^0 X$
$\pi^+ p \to \pi^0 X$
1.00<−t<1.20 GeV²
α=−0.404±0.040
1.20<−t<1.40 GeV²
α=−0.443±0.043
$d^2\sigma/dtdE$ μb/GeV³
E (GeV)
30
3
0.3
0.03
0.003
10
1
0.1
0.01
0.001
52
70
88
106

FIGURE 5.1(e)

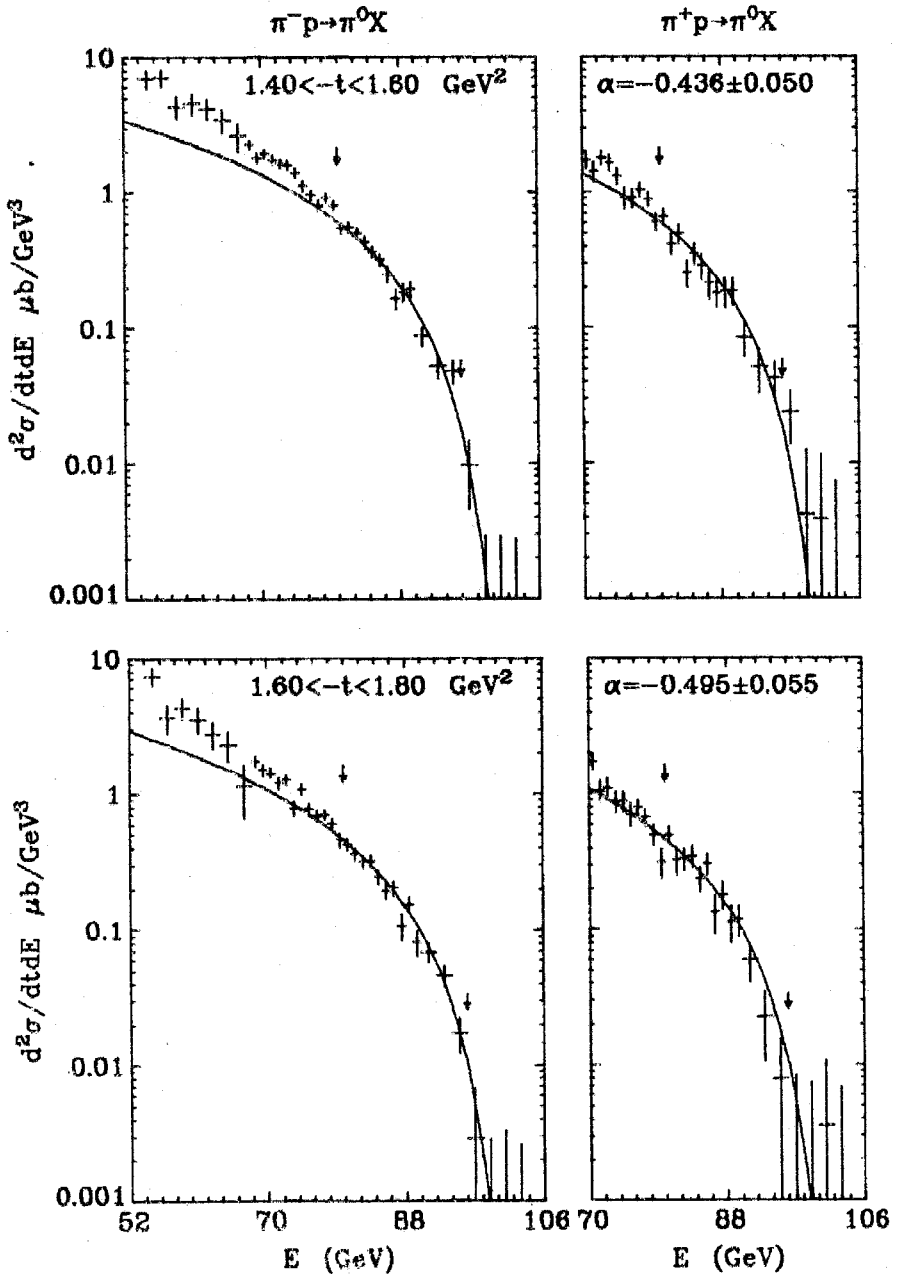
π⁻p→π⁰X
π⁺p→π⁰X
1.40<-t<1.60 GeV²
α=-0.436±0.050
1.60<-t<1.80 GeV²
α=-0.495±0.055
d²σ/dtdE μb/GeV³
10
1
0.1
0.01
0.001
52
70
88
106
E (GeV)

FIGURE 5.1(f)

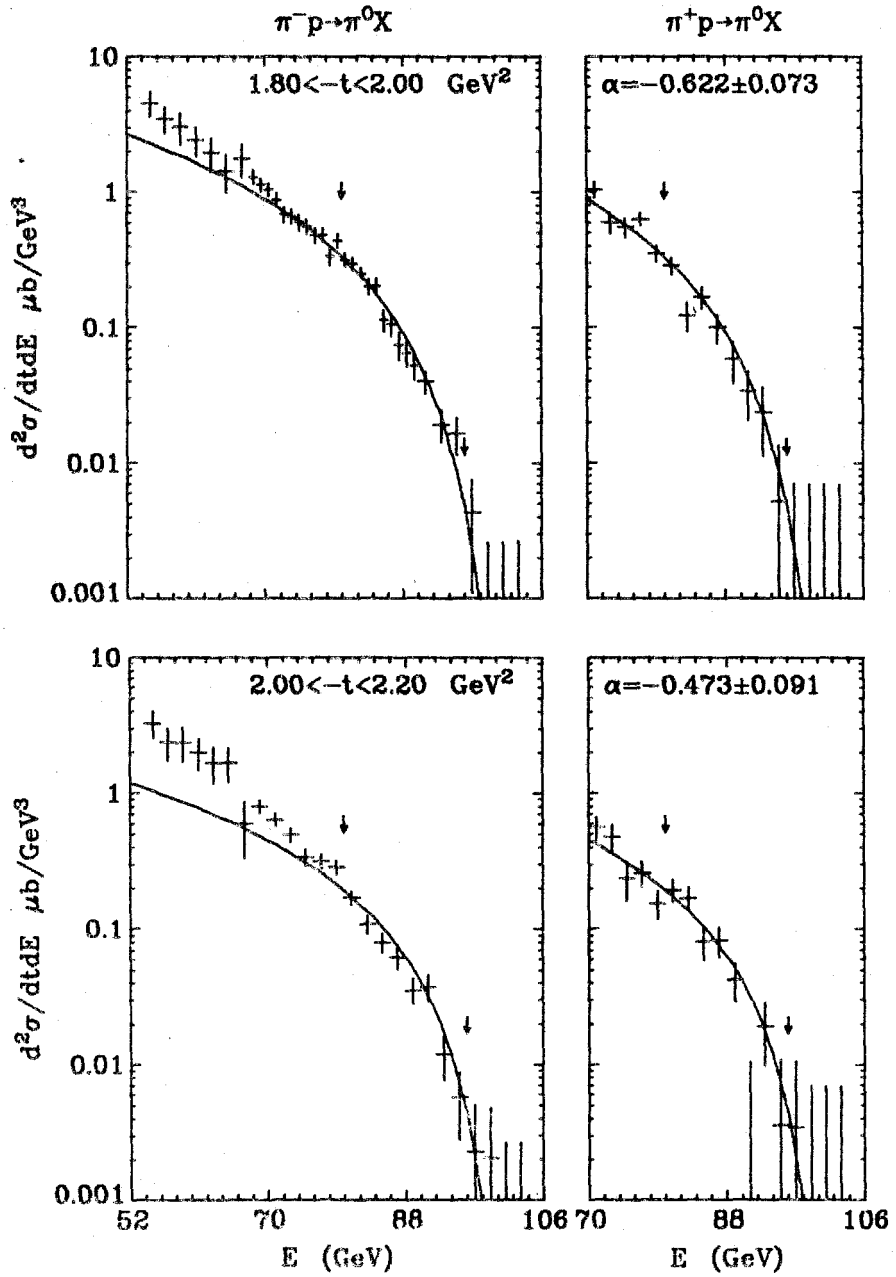
$\pi^-p\to\pi^0X$
$\pi^+p\to\pi^0X$
1.80<−t<2.00 GeV²
α=−0.622±0.073
2.00<−t<2.20 GeV²
α=−0.473±0.091
$d^2\sigma/dtdE$ μb/GeV³
10
1
0.1
0.01
0.001
52
70
88
106
E (GeV)

FIGURE 5.1(g)

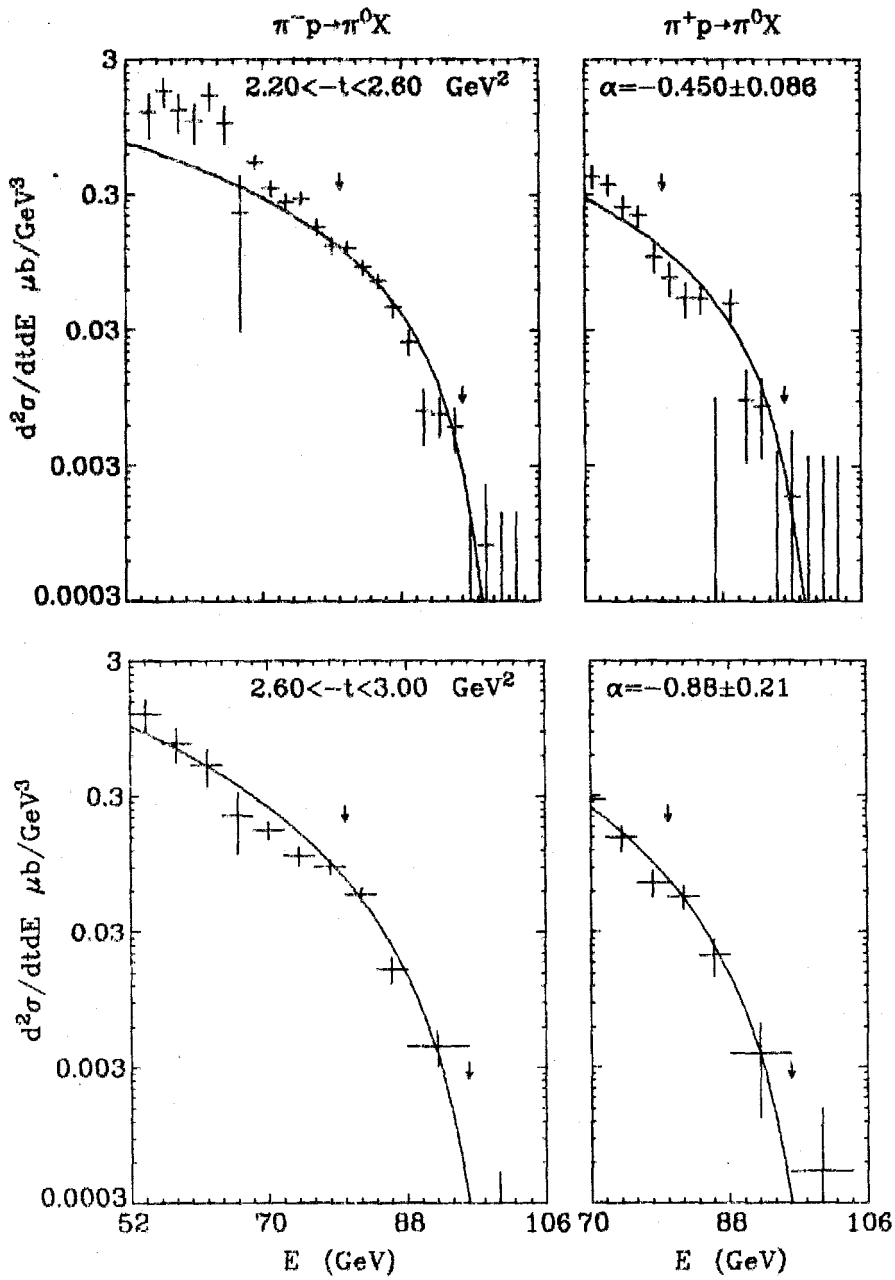
π⁻p→π⁰X
π⁺p→π⁰X
2.20<-t<2.60 GeV²
α=-0.450±0.086
2.60<-t<3.00 GeV²
α=-0.88±0.21
d²σ/dtdE μb/GeV³
3
0.3
0.03
0.003
0.0003
52
70
88
106
E (GeV)

FIGURE 5.1(h)

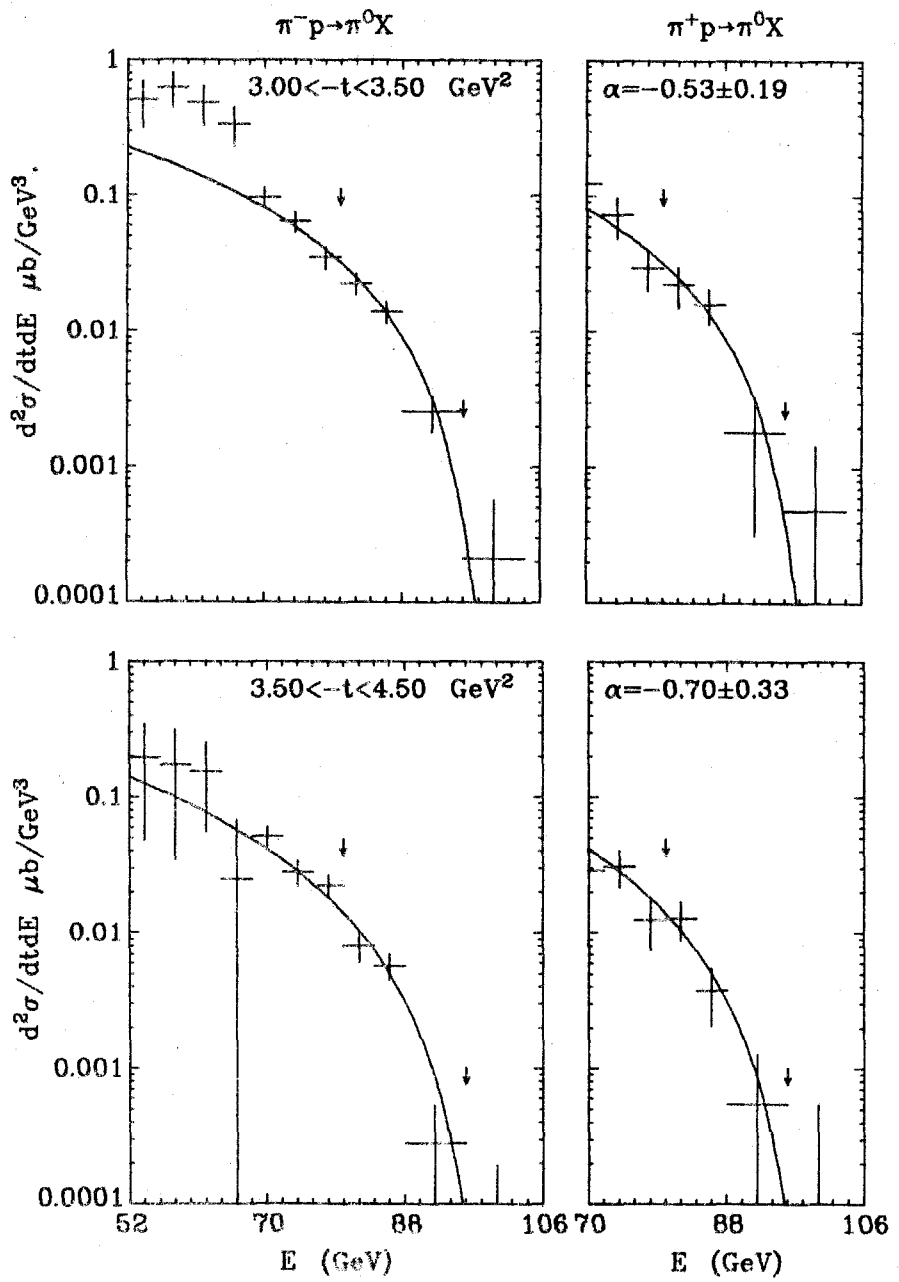
$\pi^-p\to\pi^0X$
$\pi^+p\to\pi^0X$
3.00<-t<3.50 GeV^2
α=-0.53±0.19
3.50<-t<4.50 GeV^2
α=-0.70±0.33
$d^2\sigma/dtdE$ μb/GeV^3
1
0.1
0.01
0.001
0.0001
52
70
88
106
E (GeV)

FIGURE 5.1(i)

To apply (5.1.3) to the data, it was smeared with the energy resolution, which was found to be Gaussian with a σ of 1.6 GeV for a 100 GeV π^0, as described in Appendix 5.I, and with the beam momentum distribution, described in Section 2.2. It was also necessary to integrate (5.1.3) over the energy range of each bin. It was supposed that the t bins were sufficiently large that the t resolution could be ignored but sufficiently small that the energy-dependence of the data within each bin could be described by (5.1.3) with one value of α_ρ, $G_{\rho\rho P}$ and $G_{\rho\rho f}$. x was defined by (4.2.2) and was determined using E, p_t/E and the beam momentum, whose determination is described in Appendix 5.II. For the fits shown in Fig. 5.1 and later in this thesis, the beam momentum may be considered to be 99.2 GeV.

There are some particles which decay electromagnetically or weakly to π^0 mesons. Their contributions to the π^0 cross section should be subtracted from the data before the fits are done. The ω meson may be produced by ρ or B exchange and its two-body decay, $\omega \to \pi^0\gamma$, produces π^0 mesons. The π^0 cross section cannot be calculated since the cross section for inclusive ω production has not been measured. It is expected to be small as the cross section for exclusive ω production, $\pi^- p \to \omega n$, with the $\omega \to \pi^0\gamma$ decay mode (Da77) is about two orders of magnitude smaller than the cross section for exclusive π^0 production, $\pi^- p \to \pi^0 n$, (Ba76). The three-body decays, $\eta \to \pi^0\pi^0\pi^0$, $\eta \to \pi^0\pi^+\pi^-$, $\omega \to \pi^0\pi^+\pi^-$ and $\eta' \to \pi^0\pi^0\eta$, give π^0 mesons with energies less than 74%, 72%, 87% and 47% respectively of the energy of their

parent particle and so can be largely ignored at high x.

There were two important contributions which had to be subtracted from the data before the ρ trajectory and residue function could be extracted from the ρρP and ρρf exchange cross sections. The isospin, I, = 2 exchanges were subtracted out using a calculation based on a π exchange model described in Appendix 4.III and smearing this with the energy resolution. The low mass resonance contributions were likewise subtracted, using the estimated cross sections described in Appendix 4.II. The normalizations of the ρρf terms, $G_{\rho\rho f_{\pm}}(t)$, were determined using results from the analysis of the reaction pp → pX in Ref. (Fi74) to obtain $G_{\rho\rho f_-}(0)$, the FMSR, described in Section 4.3, to obtain the t-dependence, $G_{\rho\rho f_-}(t)/G_{\rho\rho f_-}(0)$, and SU_3 to obtain $G_{\rho\rho f_+}(0)/G_{\rho\rho f_-}(0)$, as described in Appendix 4.I. Thus the theoretical prediction, (5.1.3), contained only two unknown functions of t, $\alpha_\rho(t)$ and $G_{\rho\rho P}(t)$. Hence a fit to the data in each t bin could be made to solve for α_ρ and $G_{\rho\rho P}$.

The technique used for the fit was to minimize the χ^2 using Marquardt's method. However it was found that α and G had a correlation coefficient of about -0.99 and so any fluctuations in α caused fluctuations in G. Hence the fits actually solved for α and the cross section, C(t), for the ρρP term, integrated between the limits of the fit, that is

$$C(t) = G_{\rho\rho P}(t)\int_{x_1}^{x_2} (1 - x)^{1-2\alpha(t)}dx, \qquad (5.1.4)$$

where the fit was made over the region $x_1 < x < x_2$. It was found that α and C had a correlation coefficient of about -0.8. The χ^2 per degree of freedom was close to unity for every t bin, indicating that the parameterization of the data predicted by the triple Regge model, (5.1.3), was successful.

The data from the different bias triggers were fitted simultaneously and it was checked that their cross sections agreed with each other in the overlap regions. In the displays of the data, results from these different triggers have been averaged together except for those from the low bias triggers which had lower statistics and were only included for energies below the medium bias triggers. The data for t_m below and above 1 GeV^2 are from triggers A and B respectively and were taken with the biases listed in Table 2.2. For each trigger type, the empty target data were subtracted out before the fit was performed. The data are presented over a wider range of energy than used for the fits since the data were collected in this wider energy interval in order to obtain an idea of the range in x over which the triple Regge model is valid. The fits shown were made below 96 GeV so as to preclude the low mass resonance region corresponding to missing masses below about 2 GeV, or E > 97 GeV, where the triple Regge model is not valid, as discussed in Section 4.3. The I = 2 term was subtracted out from the cross section for $t_m < 0.5$ GeV^2, above which it could not be calculated, and the low mass resonance contribution and the $\rho\rho f$ terms

were included for $t_m < 0.4$ GeV^2, above which they both gave negligible contributions to the cross sections. The π^- and π^+ data were fit simultaneously after ascertaining that both agreed independently with the triple Regge model.

From Fig. 5.1 it is seen that the energy-dependence of the cross section changes dramatically with t, just like the "shrinkage" effect seen in the s-dependence of the corresponding exclusive reaction,

$$\pi^- + p \to \pi^0 + n, \qquad (5.1.5)$$

by E111 (Ba76). Figure 5.2 and Table 5.1 show the values of $\alpha_\rho(t)$ arising from the fits shown on Fig. 5.1, together with the errors from the fit. At low t_m, where it has been possible to remove the I = 2 contribution arising from π exchange, the resulting trajectory lies just below the E111 results, as shown in more detail on Fig. 5.3, which shows just the low t_m region. The latter measurement of the ρ trajectory was obtained from data on the corresponding exclusive reaction, (5.1.5), taken at high energies by using Regge theory and fitting the s-dependence of the cross section, as described in Section 4.1. The disagreement in the lowest t bins, $t_m < 0.1$ GeV^2, may be due to the presence of π^0 mesons from another source.

From Fig. 5.1(a,b) it is seen that the low mass resonance term may have been slightly underestimated. This is expected because the cross section was estimated by assuming that only the $\Delta(1232)$ was present in the π^+p reaction, as described in Appendix 4.II, whereas there are higher mass Δ baryons which typically decay to many charged

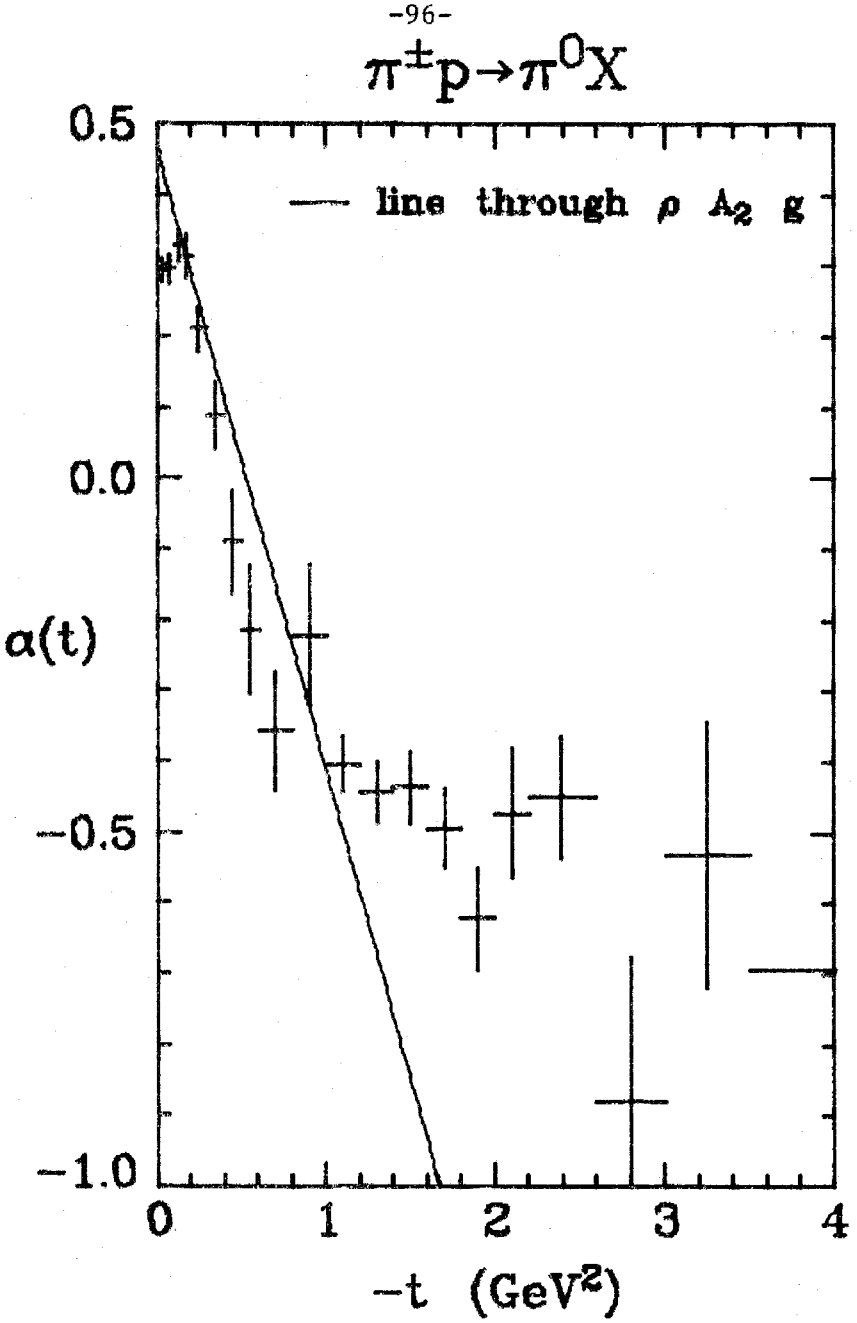

FIGURE 5.2 $\alpha_\rho(t)$ from the fits to $\pi^{\pm}p \rightarrow \pi^0 X$ over the range 80 - 96 GeV as shown in Fig. 5.1. The I = 2 contribution has been subtracted for $-t < 0.5$ GeV^2. The values for α are listed in Table 5.1.

TABLE 5.1(a). ρ Regge trajectory, $\alpha_\rho(t)$, and residue function, $G_{\rho\rho P}(t)$, from fits to $\pi^{\pm}p \to \pi^0 X$ data from trigger A over the energy ranges 80 - 96 GeV and 70 - 96 GeV. In the latter case, the I = 2 contribution has only been subtracted for $t_m < 0.50$ GeV^2.

	Fits over 80 - 96 GeV				Fits over 70 - 96 GeV	
	I = 2 ignored		I = 2 subtracted			
-t range	α	G (mb/GeV^2)	α	G (mb/GeV^2)	α	G (mb/GeV^2)
0.00 - 0.05	0.259±0.011	21.35±0.23	0.292±0.017	11.52 ±0.20	0.272±0.011	12.23 ±0.15
0.05 - 0.10	0.216±0.016	13.09±0.19	0.294±0.021	6.08 ±0.14	0.202±0.014	9.20 ±0.14
0.10 - 0.15	0.229±0.019	9.15±0.16	0.327±0.023	4.16 ±0.11	0.238±0.016	7.09 ±0.13
0.15 - 0.20	0.213±0.025	6.59±0.15	0.312±0.029	3.055±0.098	0.212±0.020	5.67 ±0.12
0.20 - 0.30	0.126±0.027	4.60±0.10	0.210±0.030	2.408±0.068	0.096±0.020	4.495±0.085
0.30 - 0.40	0.035±0.043	3.45±0.11	0.087±0.046	2.372±0.089	-0.046±0.029	3.771±0.093
0.40 - 0.50	-0.141±0.067	2.95±0.14	-0.090±0.072	2.57 ±0.14	-0.150±0.042	3.11 ±0.11
0.50 - 0.60	-0.214±0.090	3.69±0.21			-0.304±0.051	3.74 ±0.13
0.60 - 0.80	-0.357±0.083	4.53±0.23			-0.373±0.045	4.10 ±0.13
0.80 - 1.00	-0.222±0.099	4.25±0.28			-0.397±0.056	4.79 ±0.19

TABLE 5.1(b). ρ Regge trajectory, $\alpha_\rho(t)$, and residue function, $G_{\rho\rho P}(t)$, from fits to $\pi^{\pm}p \to \pi^0 X$ data from trigger B over the energy ranges 80 - 96 GeV and 70 - 96 GeV.

	Fits over 80 - 96 GeV		Fits over 70 - 96 GeV	
-t range	α	G (mb/GeV^2)	α	G (mb/GeV^2)
1.00 - 1.20	-0.404 ± 0.040	3.314 ± 0.077	-0.551 ± 0.020	5.262 ± 0.071
1.20 - 1.40	-0.443 ± 0.043	2.207 ± 0.055	-0.622 ± 0.021	4.542 ± 0.066
1.40 - 1.60	-0.436 ± 0.050	1.409 ± 0.041	-0.697 ± 0.025	3.572 ± 0.060
1.60 - 1.80	-0.495 ± 0.055	1.019 ± 0.034	-0.695 ± 0.029	2.722 ± 0.054
1.80 - 2.00	-0.622 ± 0.073	0.690 ± 0.028	-0.750 ± 0.036	1.956 ± 0.049
2.00 - 2.20	-0.473 ± 0.091	0.440 ± 0.025	-0.795 ± 0.050	1.296 ± 0.045
2.20 - 2.60	-0.450 ± 0.086	0.286 ± 0.015	-0.727 ± 0.048	0.806 ± 0.027
2.60 - 3.00	-0.88 ± 0.21	0.135 ± 0.012	-0.879 ± 0.086	0.1593 ± 0.0091
3.00 - 3.50	-0.53 ± 0.19	0.0721 ± 0.0076	-0.81 ± 0.10	0.0789 ± 0.0059
3.50 - 4.50	-0.70 ± 0.33	0.0262 ± 0.0038	-0.83 ± 0.14	0.0328 ± 0.0031

TABLE 5.2. Effect on the extracted ρ Regge trajectory, $\alpha_\rho(t)$, of doubling the cross section for low mass resonance production (case A) and of halving (case B) and doubling (case C) the $\rho p f$ residue function, $G_{\rho p f}$.

-t range	standard α	α (case A)	α (case B)	α (case C)
0.00 - 0.05	0.292±0.017	0.289±0.017	0.299±0.018	0.279±0.016
0.05 - 0.10	0.294±0.021	0.290±0.021	0.303±0.022	0.277±0.020
0.10 - 0.15	0.327±0.023	0.323±0.023	0.337±0.024	0.308±0.022
0.15 - 0.20	0.312±0.029	0.308±0.029	0.321±0.030	0.294±0.027
0.20 - 0.30	0.210±0.030	0.209±0.031	0.213±0.031	0.203±0.030
0.30 - 0.40	0.087±0.046	0.086±0.046	0.088±0.047	0.086±0.046

pions (PD78). These contribute to the full inclusive cross section much more than to the NFS cross section and thus the effect of omitting them would be more pronounced in the former case. The low mass resonances contribute only for $1 \leqslant M^2 \leqslant 2$ GeV^2, which corresponds to x above 0.99, and the data were fit for $x < 0.97$, so the fit was not too sensitive to the low mass terms. The effect on α of doubling the low mass resonance cross section is to reduce it by less than 0.005, as shown in Table 5.2.

At higher t values, it was not possible to subtract the I = 2 contribution which, as seen in Fig. 5.1(c), is not negligible and contributes about 12% of the cross section at $t_m \simeq 0.4$ GeV^2 compared to about 35% at $t_m \simeq 0$ GeV^2 for energies between 80 and 96 GeV. The

difference made by its subtraction at low t_m is shown in Table 5.1(a) and in Fig. 5.3. The data points shown by crosses are the same as those on Fig. 5.2, whilst those shown with diamonds are from fits made without subtracting the I = 2 term. Since the I = 2 term falls off faster with energy than the ρρP triple Regge term, the effective α becomes smaller when it is not removed. It is believed that the correct results are given by the fits where it has been subtracted. The difference in α is about 0.1 at low t_m and about 0.05 at $t_m \approx 0.4$ GeV^2. A similar change in α may be expected at higher t_m.

For $t_m < 1$ GeV^2, the trajectory almost everywhere lies just below the E111 results and the straight line passing through the ρ, A_2 and g mesons (see Fig. 1.1). Then the trajectory curves dramatically away from this line, as shown on Fig. 5.2, and flattens off at about -0.5, implying that the cross section behaves like $(1 - x)^2$ here. This behavior may be due to the ρ trajectory changing slope or to another physical mechanism, such as some hard-scattering contribution as described in Section 4.5, swamping the triple Regge contribution. Its interpretation is discussed in Chapter 8 after the other data have been presented.

Table 5.1 also lists the results from fits with 70 < E < 96 GeV. The resulting trajectory is 0.1 lower than that from the fits over 80 - 96 GeV for $t_m \leq 1$ GeV^2 and 0.2 lower at higher t_m, so that the cross section falls more steeply with energy at lower energies. It should be noted that the lower energies, between 70 and 80 GeV, have larger statistics than the higher energies, above 80 GeV, and so the

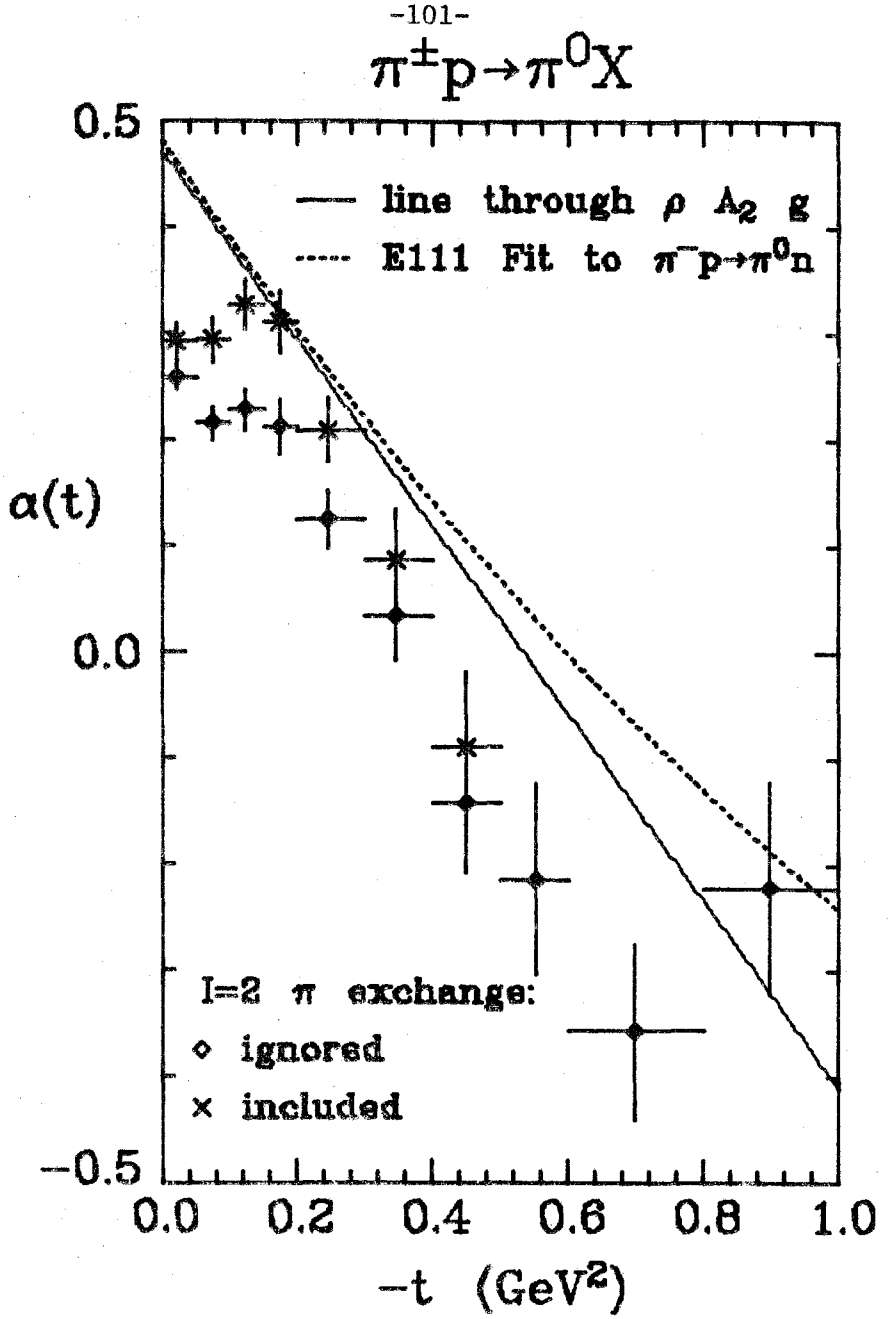

FIGURE 5.3 $\alpha_\rho(t)$ from fits to $\pi^{\pm}p \rightarrow \pi^0 X$ over the range 80 - 96 GeV for $-t < 1$ GeV^2. For $-t < 0.5$ GeV^2 the results from fits with the I = 2 exchange ignored and included are shown.

results are weighted towards the lower energies. This change in slope of the cross section with energy can be seen clearly in Fig. 5.1. At the lower energies, between 52 and 70 GeV, the fitted curve clearly lies well below the data. However triple Regge theory is only expected to be valid at high x and at lower x the "central region" (Ho73) is approached, where other mechanisms for producing π^0 mesons exist. Thus it is seen that the predictions of the triple Regge model only hold for rather high x, probably above the lower limit of these fits, x = 0.79, since the extracted trajectory is lower by about 0.1 from what was predicted from the exclusive results.

The sensitivity of the low t_m results to the $\rho\rho f$ parameterization was investigated by doubling and halving its normalization, $G_{\rho\rho f}$, and refitting the data. The results are shown in Table 5.2 and it is seen that α is changed by at most 0.02, as might have been expected since the cross section due to the $\rho\rho f$ term is small.

The sensitivity of the results to the determination of the beam momentum and the energy resolution have been tested and the results are shown in Table 5.3. Increasing or decreasing the beam momentum by 0.5% caused a decrease or increase of α by an amount varying from 0.03 at low t_m to 0.10 at high t_m. Since the beam momentum is known to about 0.2%, ignoring uncertainties in the calibration constant, as described in Appendix 5.II, this gives a systematic error in α whose magnitude is t-dependent and varies from about 0.01 at low t_m

TABLE 5.3. Effect on the extracted ρ Regge trajectory, $\alpha_\rho(t)$ of increasing (case A) and decreasing (case B) the beam momentum by 0.5% and of increasing the standard deviation of the energy resolution by 30% (case C) for sample t bins of the $\pi^{\pm}p \to \pi^0 X$ data.

-t range	standard α	α (case A)	α (case B)	α (case C)
0.00 - 0.05	0.292±0.017	0.262±0.019	0.320±0.015	0.293±0.017
0.20 - 0.30	0.210±0.030	0.187±0.033	0.229±0.028	0.209±0.031
0.40 - 0.50	-0.090±0.072	-0.127±0.076	-0.061±0.069	-0.095±0.073
0.80 - 1.00	-0.222±0.099	-0.29 ±0.10	-0.214±0.096	-0.25 ±0.10
1.20 - 1.40	-0.443±0.043	-0.494±0.045	-0.397±0.041	-0.453±0.044
2.00 - 2.20	-0.473±0.091	-0.596±0.097	-0.423±0.088	-0.550±0.094
3.00 - 3.50	-0.53 ±0.19	-0.70 ±0.20	-0.47 ±0.18	-0.65 ±0.19

to 0.05 at high t_m. Increasing the standard deviation of the energy resolution by 30% caused little change in α, as shown in Table 5.3.

To obtain the residue function, $G_{\rho\rho P}(t)$, a separate fit was made. This was done because it was found that fluctuations in α caused fluctuations in G, as discussed earlier. Thus the resulting trajectories from the initial sets of fits were parameterized as functions of t of the form,

$$\alpha_\rho(t) = A + Be^{Ct + Dt^2}. \qquad (5.1.6)$$

For the "standard" case, with the data fit between 80 and 96 GeV and the I = 2 term subtracted for $t_m < 0.5$ GeV^2, a fit to the form (5.1.6) for $0 < t_m < 2$ GeV^2 gave

$$A = -0.448, \quad B = 0.718, \quad C = -1.19, \quad D = -5.8. \qquad (5.1.7)$$

When no subtraction of the I = 2 term was made, the resulting values were

$$A = -0.460, \quad B = 0.716, \quad C = 0.06, \quad D = -2.92. \qquad (5.1.8)$$

When the data were fit between 70 and 96 GeV with the I = 2 term subtracted for $t_m < 0.5$ GeV^2, the resulting values were

$$A = -0.721, \quad B = 1.011, \quad C = 0.62, \quad D = -1.00. \qquad (5.1.9)$$

In each of the above cases a second fit to the data was performed to solve for $G_{\rho\rho P}$ alone, which used the trajectory given by (5.1.6) with the corresponding values of A, B, C and D. The resulting values for $G_{\rho\rho P}$ are shown in Fig. 5.4 and listed in Table 5.1. There is naturally a significant difference depending on whether or not the I = 2 term was subtracted.

The residue function falls rapidly with t_m until $t_m \approx 0.4$ GeV^2, rises until 0.7 GeV^2 and then falls again. The dip is coincident with the place at which the trajectory passes through zero. It is also at the same t value as the dip seen in the angular cross section $d\sigma/dt$ for the exclusive reaction, (5.1.5), over a wide range of s (St65, S066, Wa68, Ba76). There are several explanations for this dip. If the residue function is separated out from $G_{\rho\rho P}(t)$, it may be expressed, using (4.2.6) with (4.1.4), as

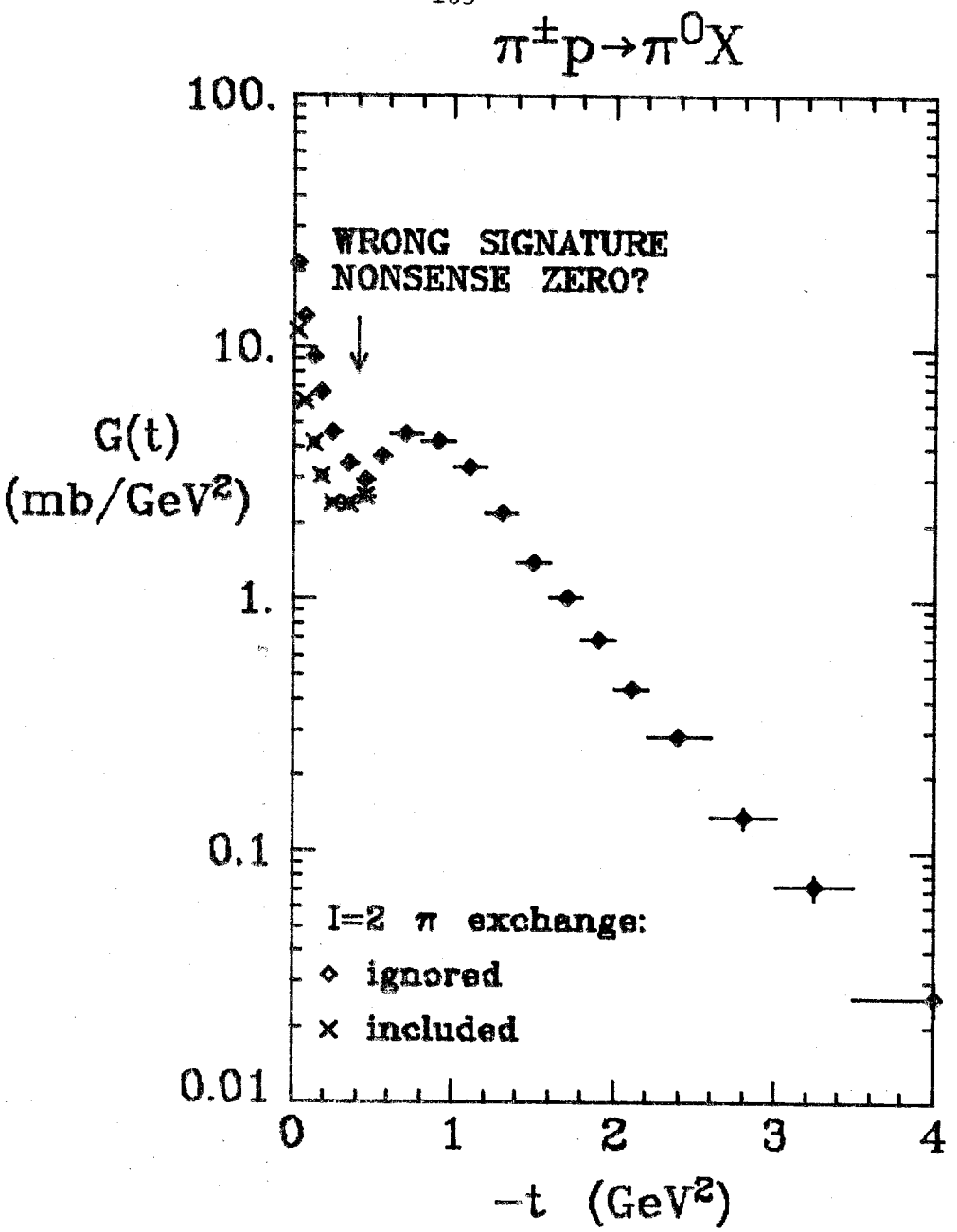

FIGURE 5.4 $G_{\rho\rho P}(t)$ from the fits to $\pi^{\pm}p \rightarrow \pi^{0}X$ over the range 80 - 96 GeV described in the text. The values for G are listed in Table 5.1.

$$G_{\rho\rho P}(t) = G(t)\left|e^{-i\pi\alpha_\rho(t)} - 1\right|^2 \mathrm{cosec}^2(\pi\alpha_\rho(t))$$

$$= G(t)\sec^2(\pi\alpha_\rho(t)/2), \qquad (5.1.10)$$

where

$$G(t) = \gamma^2_{\pi\pi\rho}(t)\gamma_{ppP}(0)\gamma_{\rho\rho P}(t). \qquad (5.1.11)$$

Since the secant-squared in (5.1.10) has a minumum at $\alpha_\rho(t) = 0$, with a value half that at $\alpha_\rho(t) = \pm 0.5$, which occurs at $t_m \simeq 0$ and 1 GeV^2, this dip will be present for any smooth form of $G(t)$ near the zero of $\alpha_\rho(t) = 0$.

A second explanation of the dip is that it is the "wrong signature nonsense zero" present because the ρ and A_2 trajectories are strongly exchange degenerate and is due to a zero in $G(t)$ at $\alpha = 0$. To understand this, consider the process,

$$K^+ + K^0 \to K^0 + K^+, \qquad (5.1.12)$$

which has no resonances, since there are no strangeness S = 2 mesons in the quark model, and so, by duality, the imaginary part of its amplitude for Reggeon exchange vanishes. This exchange is pure isospin I = 1 and mediated by the ρ and A_2 and so these contributions must cancel giving, since $Im(\xi_\rho(t)) = Im(\xi_{A_2}(t)) = 1$, that

$$\gamma^2_{KK\rho}(t) = \gamma^2_{KKA_2}(t). \qquad (5.1.13)$$

Now the A_2 amplitude is given by

$$A(K^+K^0 \to K^0K^+)\big|_{A_2} \propto \gamma^2_{KKA_2}(t)(1 + e^{-i\pi\alpha_{A_2}(t)})\mathrm{cosec}(\pi\alpha_{A_2}(t))$$

$$\sim 2\gamma^2_{KKA_2}(t)/(\pi\alpha), \qquad (5.1.14)$$

for $\alpha = \alpha_{A_2}(t) \sim 0$. For this to be finite requires that

$$\gamma_{KKA_2}(t) \sim \sqrt{\alpha} \quad \text{for } \alpha \sim 0. \tag{5.1.15}$$

From (5.1.13) it follows that

$$\gamma^2_{KK\rho}(t) \sim \alpha \quad \text{for } \alpha \sim 0 \tag{5.1.16}$$

and then SU_3 arguments give, since the couplings in a given multiplet are related, that

$$G(t) \sim \gamma^2_{\pi\pi\rho}(t) \sim \alpha \text{ for } \alpha \sim 0. \tag{5.1.17}$$

Hence a zero is present in $G_{\rho\rho P}(t)$ when α is zero as well as the dip present from the residue function. This explanation of the dip has assumed that the contribution from cuts is small.

An explanation of the dips seen in $d\sigma/dt$ for $\pi^- p \to \pi^0 n$ was provided by the absorption model (Ka76, Co77, Fo72). This was an attempt to incorporate cuts in the ℓ-plane as well as poles into the Regge theory picture. Whereas a pole corresponds to the exchange of a single resonance and its effect can be parameterized by the trajectory, $\alpha(t)$, and the residue, $\beta(t)$, in (4.1.2) at any given t, a cut corresponds to the exchange of two or more particles. Its effect is parameterized by the discontinuity across the cut and this is a function at any given t, and thus it is much harder to incorporate cuts into a model.

In the absorption model, the spin of the initial (p) and final (n) states is included explicitly and so the analogy of (4.1.8) for the s-channel for a specific helicity state, H, is used. This is

$$A_H(s,t) = 16\pi \sum_{J=M}^{\infty} (2J + 1)A_{HJ}(s)d^J_{\mu\mu'}(z(s,t)), \qquad (5.1.18)$$

where $z = \cos\theta$, with θ the scattering angle between the π^- and the π^0 in the c.m. frame, μ and μ' are the helicities of the p and n respectively, $M = \max(|\mu|,|\mu'|)$ and $d^J_{\mu\mu'}$ is the rotation matrix (Ed60). For large $s >> t$ and large J,

$$d^J_{\mu\mu'}(z) \simeq J_N(2J\sqrt{-t/s}) \qquad (5.1.19)$$

where $N = |\mu - \mu'|$ and J_N is the Bessel function of the first kind of order N. Defining b as the classical impact parameter for a particle passing a target with angular momentum J, $b = 2J/\sqrt{s}$, replacing the summation over J by an integral over b and replacing $A_{HJ}(s)$ by $A(s,b)$ gives

$$A_H(s,t) = 8\pi s\int_0^{\infty} bA(s,b)J_N(b\sqrt{-t})db. \qquad (5.1.20)$$

The model now assumes that at short ranges, that is, $b \simeq 0$, there is a pole-cut interference which eliminates the scattering amplitude in this region, the effect which gives the model its name, and the predominant part of the scattering amplitude is at the peripheral region at a range $b \simeq 1$ fm $= 5$ GeV^{-1}. Approximating $A(s,b)$ by a delta function at $b = B$ gives

$$A_H(s,t) \sim J_N(B\sqrt{-t}). \qquad (5.1.21)$$

This amplitude has a zero when $B\sqrt{-t}$ passes through a zero of J_N. For $B = 5$ GeV^{-1}, the first zeroes are at $t = -0.2$, -0.55 and -1.2 GeV^2

for N = 0, 1 and 2 respectively. This clearly explains the dip seen in $d\sigma/dt$ for $\pi^- p \to \pi^0 n$ since this is dominated by the spin-flip amplitude, N = 1, as shown by the forward dip in the cross section. However the reaction, $\pi^- p \to nn$, would then be expected to have a similar behavior in this model and yet no dip is observed (Gu65, Wa68, Sh76, Da76), even though it is again dominated by the spin-flip amplitude. Thus it was necessary to modify this model to explain the lack of a dip in the η production.

When this model is applied to the inclusive reaction, $\pi^- p \to \pi^0 X$, the value of N will be large because the unmeasured part, X, is a sum of many particles and so has a large orbital angular momentum. Thus the amplitude is a sum over several terms of the form (5.1.21) at high N and so no zero is predicted by this model for the inclusive case. Later it is seen that the explanations due to the Regge model are confirmed by the lack of structure in both the full inclusive and NFS η production cross sections and by a dip seen at the same t value in the NFS π^0 production cross sections.

Some new results on the exclusive process $\pi^- p \to \pi^0 n$ with $30 < s < 80$ GeV^2 using the NICE detector at Serpukhov (Ap79b) have recently been published. The extracted trajectory for -t between 0 and 2 GeV^2 is in good agreement with the straight line through the ρ and g mesons and shows no curvature for t_m above 1 GeV^2, as was found by Ell1. This difference in behavior between the determinations of the ρ trajectory from the exclusive and the inclusive reactions may be

consistent with the hard-scattering processes described in Section 4.5. A coherent process such as the CIM model describes the exclusive processes at high t_m and probably it does not dominate over the Regge process until t_m is larger than 2 GeV^2, whereas an incoherent process such as the QCD parton model describes the inclusive processes and its effects start to dominate over the triple Regge process at t_m near 1 GeV^2.

5.2 A_2 TRAJECTORY AND RESIDUE FUNCTION FROM INCLUSIVE η PRODUCTION

In this section, the results from the reactions,

$$\pi^- + p \to \eta + X \tag{5.2.1}$$

and

$$\pi^+ + p \to \eta + X, \tag{5.2.2}$$

with the η detected by its decay into two photons, are presented. The A_2 trajectory and residue function are extracted using the predictions of the triple Regge model. From Section 4.3, it is seen that the cross sections are given by

$$\left.\frac{d^2\sigma}{dtdx}(x,t,s)\right|_{\pi^\pm p \to \eta X} = G_{A_2A_2P}(t)(1-x)^{1-2\alpha_{A_2}(t)} +$$

$$G_{A_2A_2f}(t)s^{-0.5}(1-x)^{0.5-2\alpha_{A_2}(t)} +$$

$$\text{(low mass resonances)} \tag{5.2.3}$$

The reaction with η production should provide a cleaner test of triple Regge theory than the π^0 reaction since it has no complications from I = 2 exchanges and also the η is less likely to result from the decay of another particle. The main background is from $\eta' \to \eta\pi^0\pi^0$ decays, which produce η mesons with up to 87% of the energy of the η'. However the statistics are lower both because of the branching ratio of the η into two photons of 0.38 and because of the lower acceptance of the detector due to the greater opening angle, as discussed in Appendix 3.VII.

The data were accumulated in t bins and corrected in the same

manner as described for π^0 mesons in the previous section. One additional correction was made. Since the η meson has a larger mass than the incident charged pion, the four-momentum-transfer-squared, t, at energy E is restricted to lie below a certain value, $t_{min}(E)$, which corresponds to the η carrying off no transverse momentum. This effect was corrected for using a parameterization of the low t_m cross section of the form,

$$\frac{d^2\sigma}{dtdE}(E,t) = A(E)e^{B(E)t}, \qquad t < t_{min}(E). \qquad (5.2.4)$$

A and B were found by fitting the data as a function of t in various energy bins, as presented in the following section. It was then assumed that the data behave like (5.2.4) for $t > t_{min}$ and thus the data with energy E in a bin ranging from t_1 to t_2 with $t_1 < t_{min} < t_2$ were multiplied by the factor δ, where

$$\delta = \frac{e^{B(E)t_2} - e^{B(E)t_1}}{e^{B(E)t_{min}} - e^{B(E)t_1}}. \qquad (5.2.5)$$

Most of the t bins were fit over an energy range of 70 to 96 GeV, but the first three bins were fit above higher energies because of the t_{min} effect; only energy bins with at least half of the t-range kinematically available were used in the fits. Fitting the entire data set over an energy range of 80 to 96 GeV, as was used for the π^0 data set, was not feasible because the statistics were too low.

Figure 5.5 shows the data with all the corrections applied

but with purely statistical errors. To extract the A_2 trajectory, the A_2A_2f exchange terms and the low mass resonances were subtracted from the data using the estimates of their cross sections discussed in Appendices 4.I and 4.II respectively. Fits were performed for each t bin which solved for the A_2 trajectory, $\alpha_{A_2}(t)$, and the cross section of the A_2A_2P exchange term. This fit used the π^+ and π^- beam data simultaneously. The resulting cross sections are shown by the solid curves on Fig. 5.5 and the various terms contributing are shown by the broken curves.

FIGURE 5.5 Data on $\pi^{\pm}p \to \eta X$ as a function of the energy of the η, E, in different t bins. The results of fits to the π^- and π^+ data simultaneously are shown using the energy ranges indicated by the arrows. The resulting values for α are shown on Fig. 5.6 and are listed in Table 5.4.

KEY

—— Final fit, that is, total theoretical cross section smeared with the energy resolution and the beam momentum distribution

--- A_2A_2P triple Regge contribution

— — A_2A_2f triple Regge contribution

····· Low mass resonances (estimated)

⬇ ⬇ Limits of fit

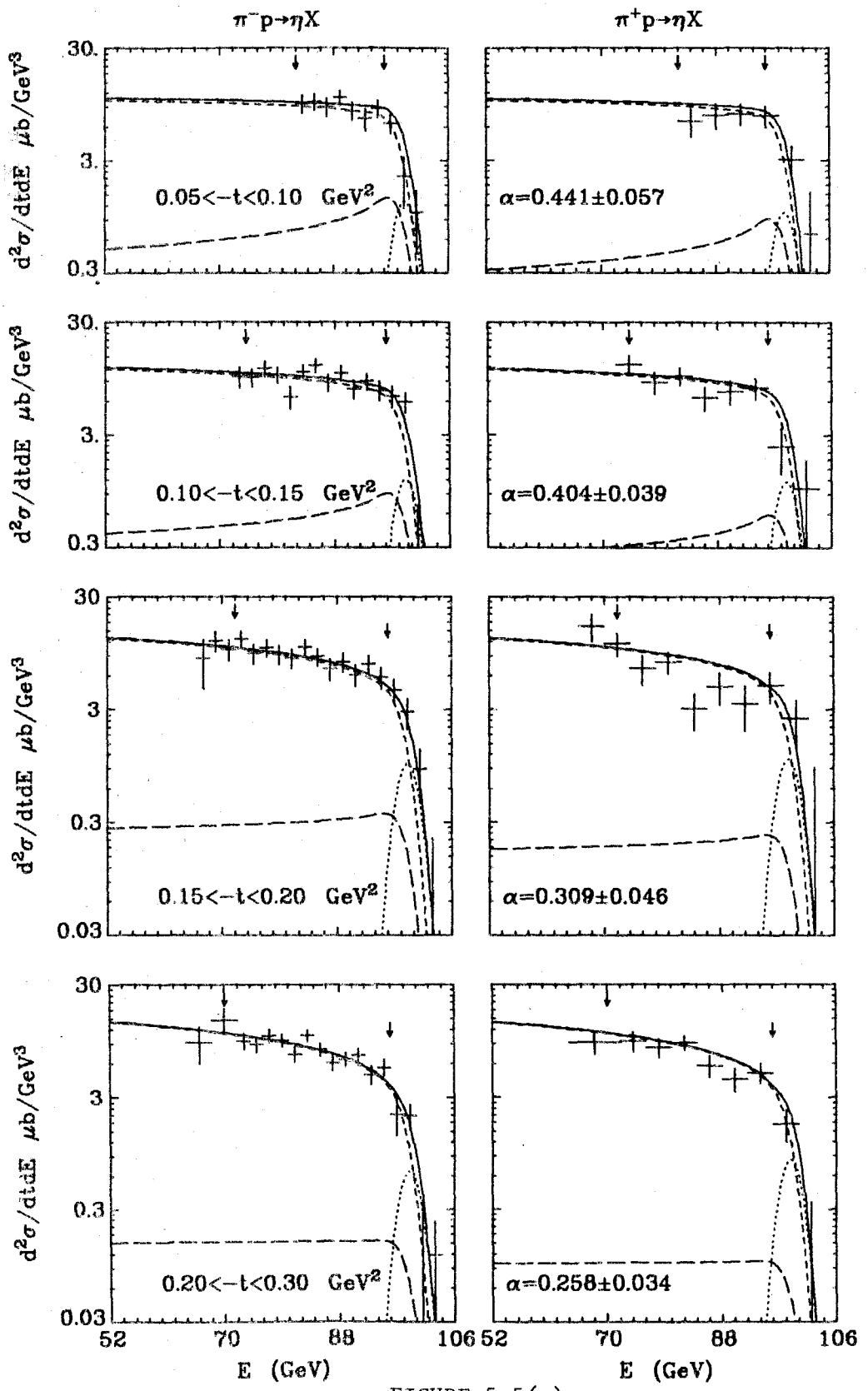
$\pi^-p\to\eta X$
$\pi^+p\to\eta X$
$d^2\sigma/dtdE$ μb/GeV³
30.
3.
0.3
0.05<−t<0.10 GeV²
α=0.441±0.057
0.10<−t<0.15 GeV²
α=0.404±0.039
30
3
0.3
0.03
0.15<−t<0.20 GeV²
α=0.309±0.046
0.20<−t<0.30 GeV²
α=0.258±0.034
52
70
88
106
E (GeV)

FIGURE 5.5(a)

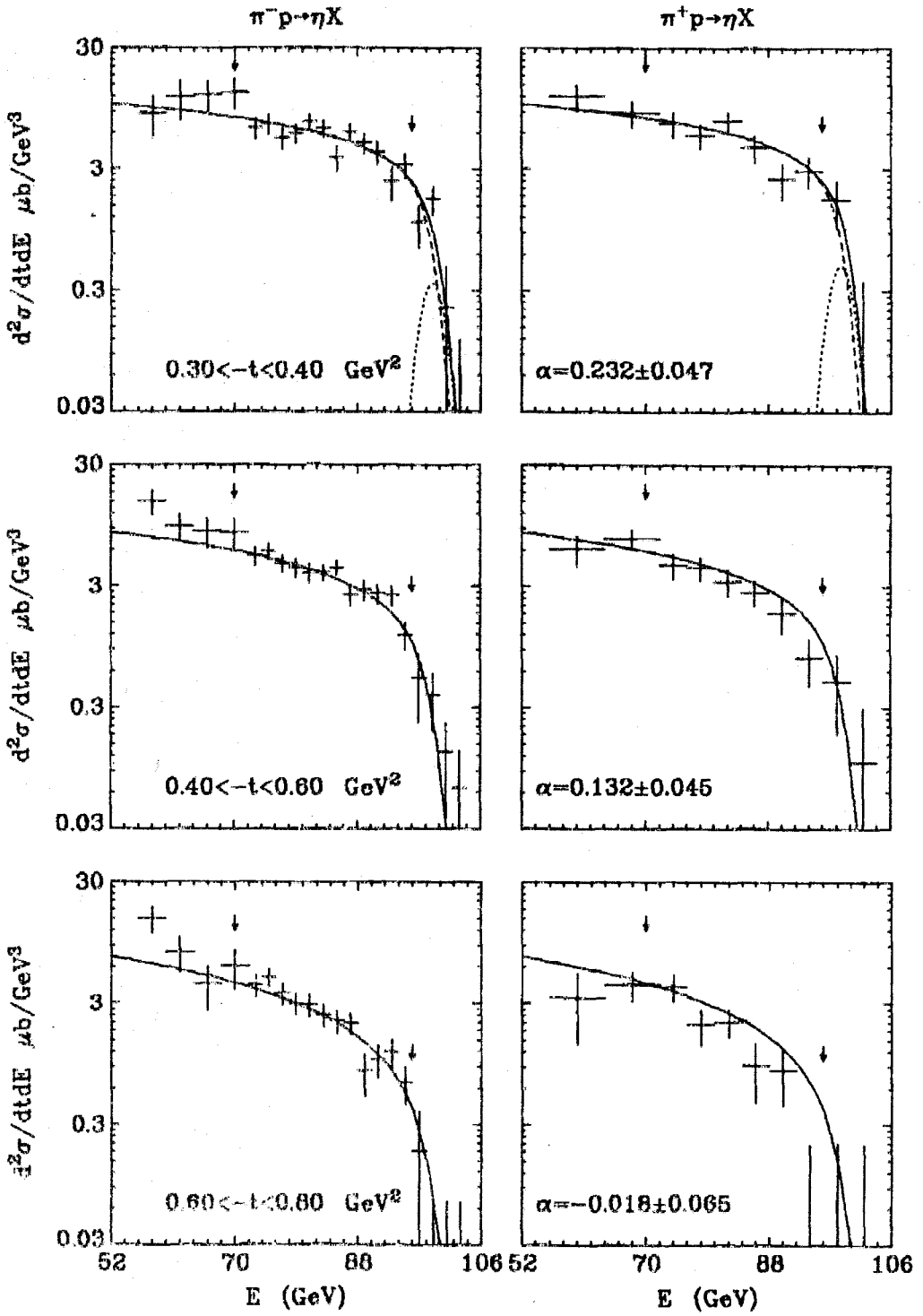
$\pi^-p\to\eta X$
$\pi^+p\to\eta X$
$d^2\sigma/dtdE$ μb/GeV^3
30
3
0.3
0.03
0.30<−t<0.40 GeV^2
α=0.232±0.047
0.40<−t<0.60 GeV^2
α=0.132±0.045
0.60<−t<0.80 GeV^2
α=−0.018±0.065
52
70
88
106
E (GeV)

FIGURE 5.5(b)

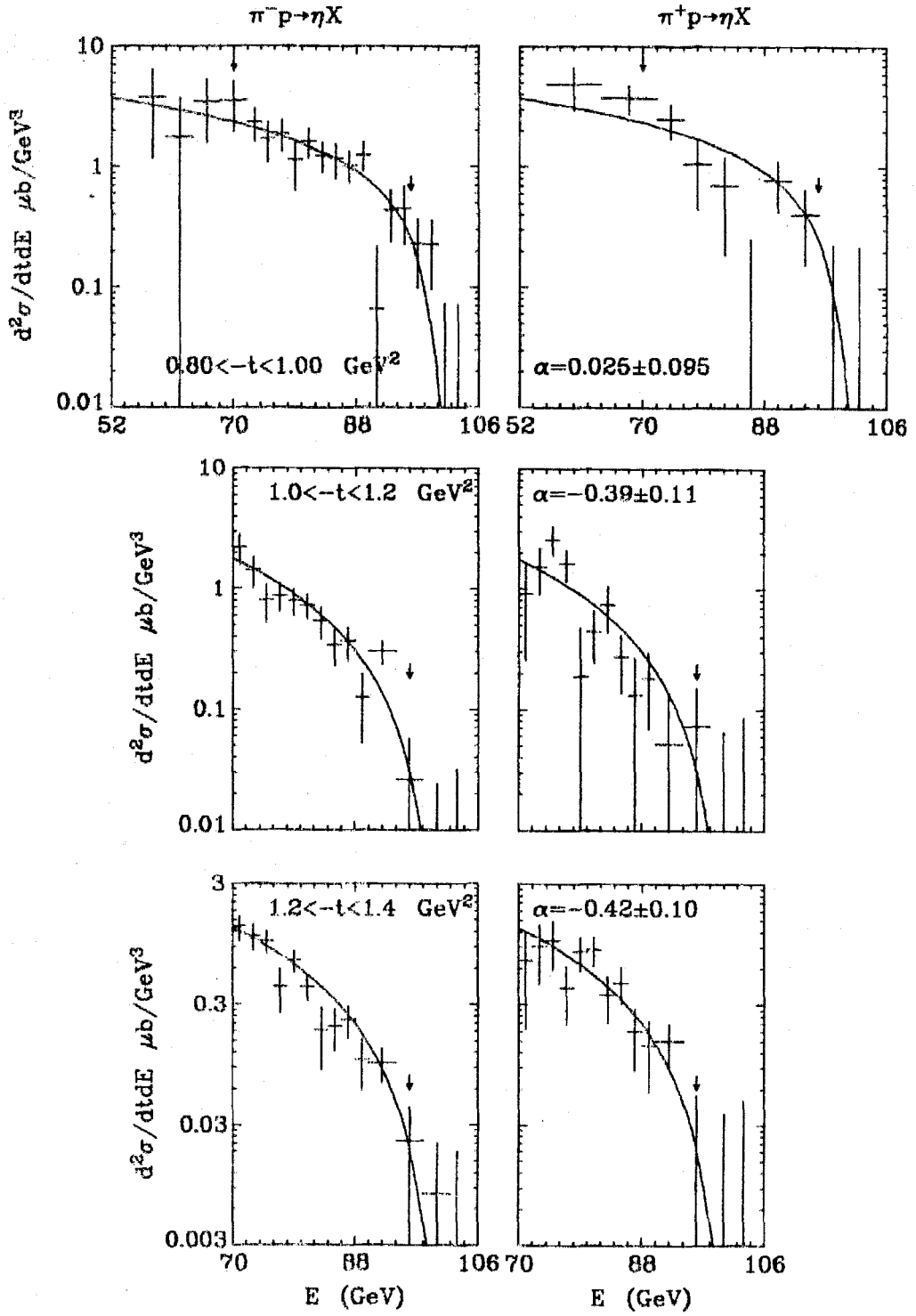
$\pi^-p\to\eta X$
$\pi^+p\to\eta X$
$d^2\sigma/dtdE$ $\mu b/GeV^3$
0.80<-t<1.00 GeV^2
α=0.025±0.095
1.0<-t<1.2 GeV^2
α=-0.39±0.11
1.2<-t<1.4 GeV^2
α=-0.42±0.10
E (GeV)

FIGURE 5.5(c)

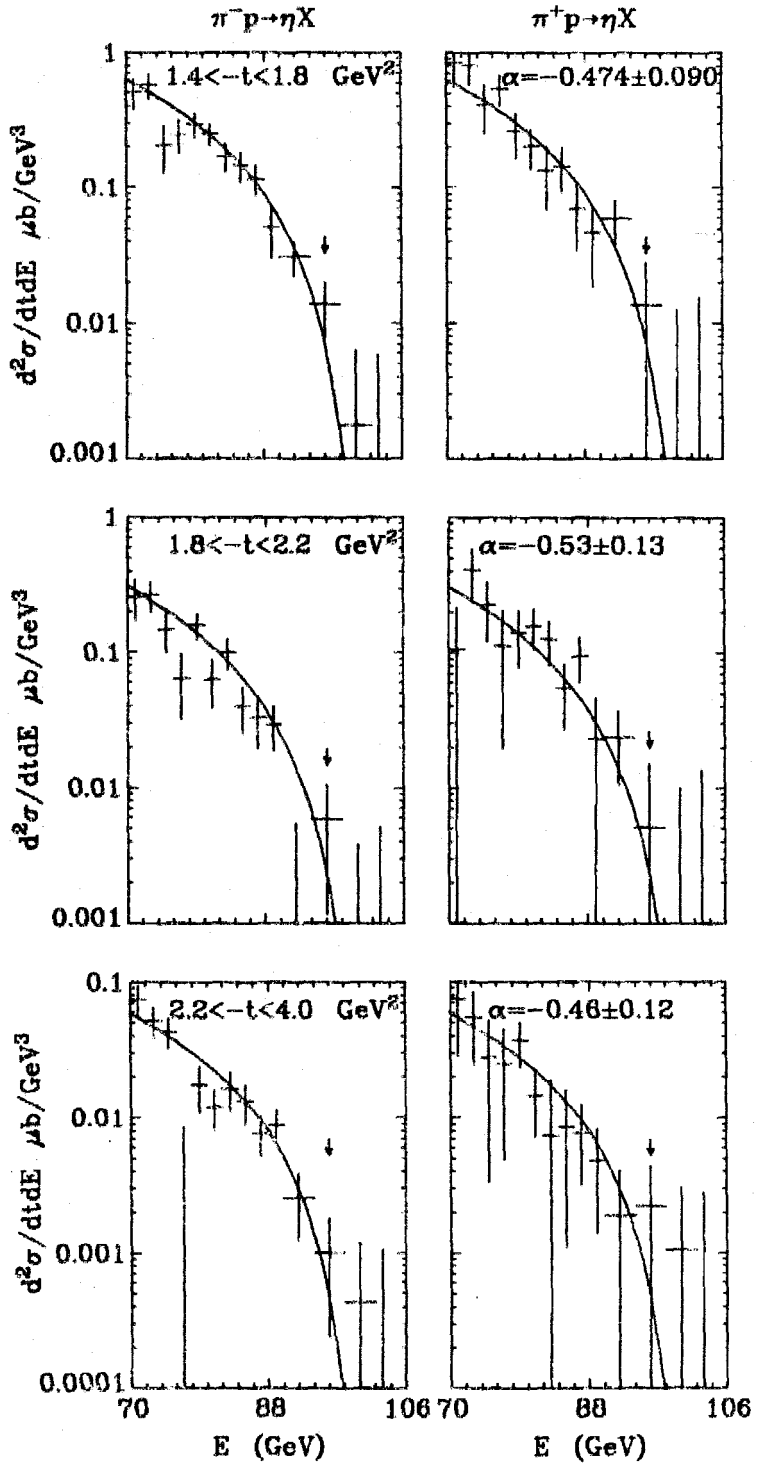
$\pi^-p\to\eta X$
$\pi^+p\to\eta X$
1.4<−t<1.8 GeV²
α=−0.474±0.090
1.8<−t<2.2 GeV²
α=−0.53±0.13
2.2<−t<4.0 GeV²
α=−0.46±0.12
d²σ/dtdE μb/GeV³
1
0.1
0.01
0.001
0.0001
70
88
106
E (GeV)

FIGURE 5.5(d)

TABLE 5.4. A_2 Regge trajectory, $\alpha_{A_2}(t)$, and residue function, $G_{A_2A_2P}(t)$, from fits to the $\pi^{\pm}p \to \eta X$ data over the energy range E' - 96 GeV, where E' is listed in Column 2.

-t range	E'	α	G (mb/GeV^2)
0.05 - 0.10	82	0.441 ± 0.057	1.160 ± 0.075
0.10 - 0.15	74	0.404 ± 0.039	1.421 ± 0.067
0.15 - 0.20	72	0.309 ± 0.046	1.465 ± 0.075
0.20 - 0.30	70	0.258 ± 0.034	1.769 ± 0.064
0.30 - 0.40	70	0.232 ± 0.047	1.685 ± 0.077
0.40 - 0.60	70	0.132 ± 0.045	1.560 ± 0.067
0.60 - 0.80	70	-0.018 ± 0.065	1.583 ± 0.089
0.80 - 1.00	70	0.025 ± 0.095	1.33 ± 0.12
1.00 - 1.20	70	-0.39 ± 0.11	0.921 ± 0.074
1.20 - 1.40	70	-0.42 ± 0.10	0.890 ± 0.067
1.40 - 1.80	70	-0.474 ± 0.090	0.597 ± 0.040
1.80 - 2.20	70	-0.53 ± 0.13	0.417 ± 0.037
2.20 - 4.00	70	-0.46 ± 0.12	0.144 ± 0.014

The resulting A_2 trajectory is shown on Fig. 5.6 and its values are listed in Table 5.4. At low t_m, the trajectory lies about 0.1 higher than the E111 result obtained from the s-dependence of the corresponding exclusive reaction (Da76),

$$\pi^- + p \to \eta + n, \qquad (5.2.6)$$

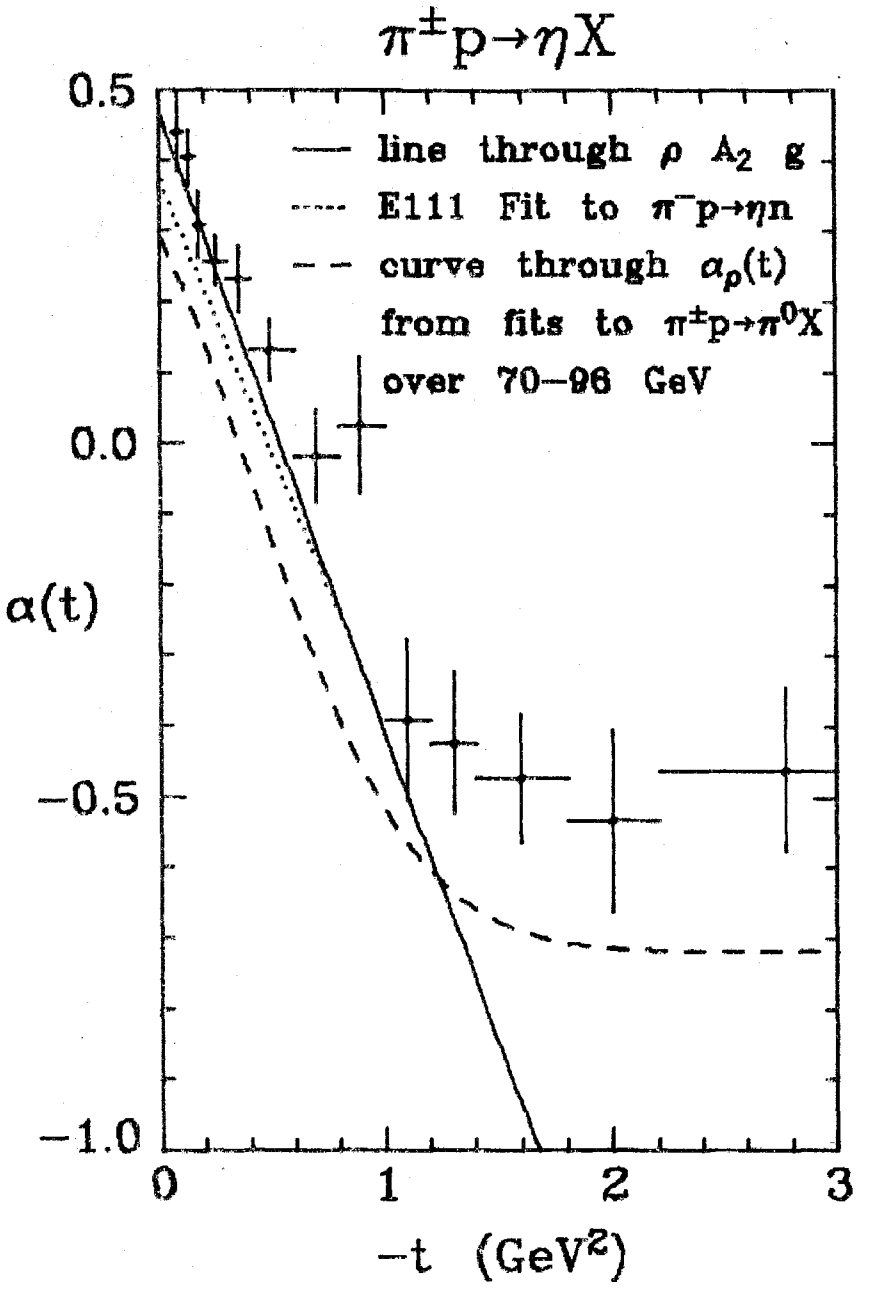

FIGURE 5.6 $\alpha_{A_2}(t)$ from the fits to $\pi^{\pm}p \to \eta X$ shown in Fig. 5.5 and performed over the energy ranges given in Table 5.4. The curve through $\alpha_\rho(t)$ from the fits to the $\pi^{\pm}p \to \pi^0 X$ data over 70 - 96 GeV given by (5.1.6,9) is shown for comparison.

measured over $40 < s < 400$ GeV^2. It lies everywhere about 0.2 higher than the ρ trajectory obtained from the fits to the full inclusive π^0 production data, $\pi^{\pm}p \to \pi^0 X$, over the same energy range, 70 - 96 GeV. The curve through $\alpha_\rho(t)$ with $0 < t_m < 2$ GeV^2 given by (5.1.6,9) is shown on Fig. 5.6 for comparison. Just as found for the ρ trajec-trajectory, the A_2 trajectory is parallel to the straight line through the ρ, A_2 and g particles until $t_m \simeq 1$ GeV^2 and then curves away from it and may level off at a value of α near -0.5.

A second fit was performed to extract the residue function, $G_{A_2A_2P}(t)$. $\alpha_{A_2}(t)$ was constrained by fitting a curve to the results shown on Fig. 5.6 with $t_m < 2.2$ GeV^2. This gave

$$\alpha_{A_2}(t) = -0.98 + 1.48e^{0.63t}. \qquad (5.2.7)$$

A second fit was performed and the resulting residue function is shown on Fig. 5.7 and is listed in Table 5.4. Except for the first three points, which were obtained from fits over limited energy ranges, the residue function falls with t_m. It clearly has no dip at $t_m \simeq 0.5$ GeV^2, like the corresponding ρ residue function, which is shown on Fig. 5.7 for comparison. A peak is expected at the place where $\alpha_{A_2}(t)$ is zero, at around 0.6 GeV^2, from the form (4.2.6) since the A_2 has even signature and thus the contribution of $\xi_{A_2}(t)$ to $G_{A_2A_2P}(t)$ would be infinite when $\alpha_{A_2}(t) = 0$. Unfortunately there are too few data points to tell whether the dip expected from the signature factor, (4.1.14), is present. This would be located at

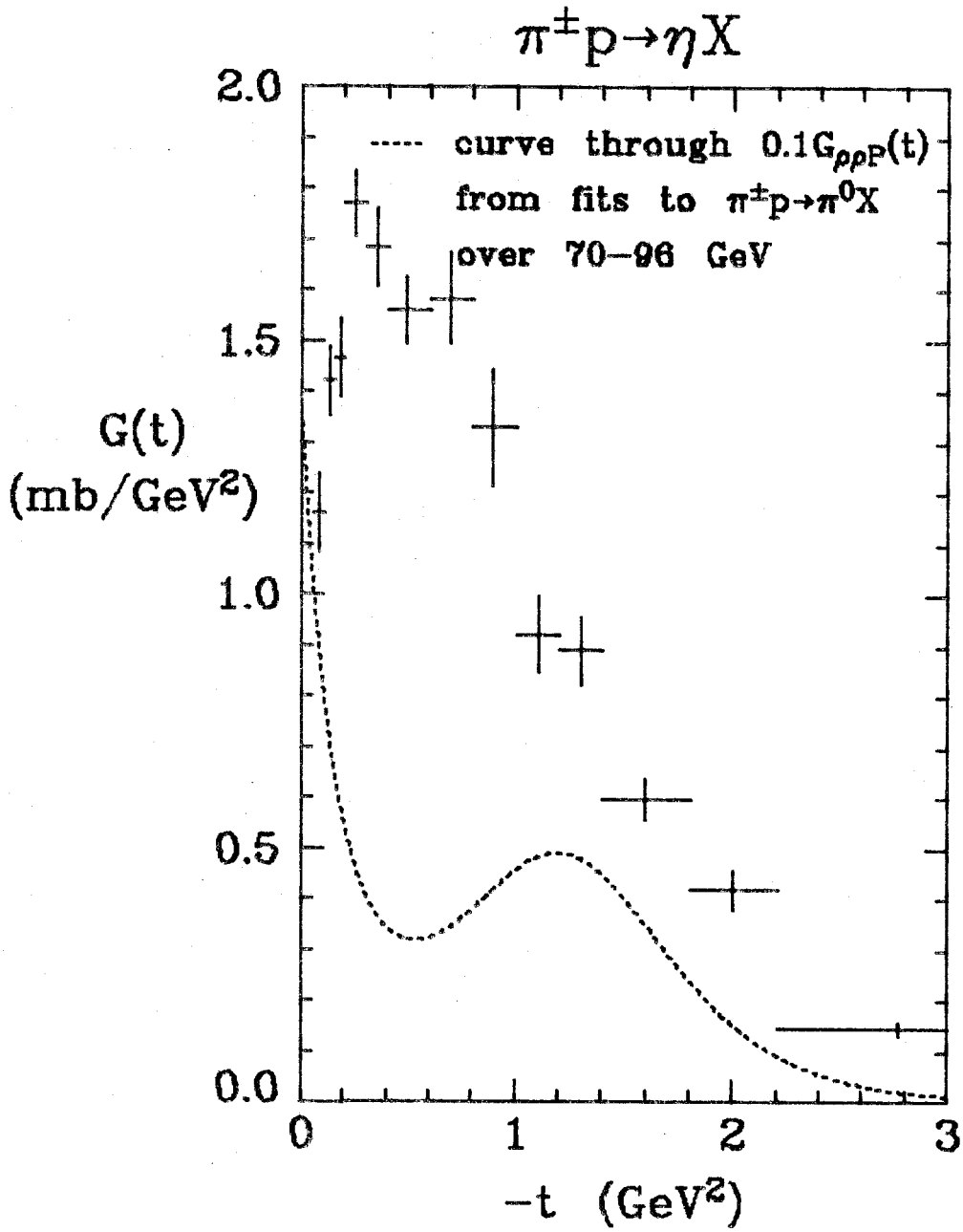

FIGURE 5.7 $G_{\Lambda_2 A_2 P}(t)$ from the fits to $\pi^{\pm}p \rightarrow \eta X$ described in the text and performed over the energy ranges listed in Table 5.4. A curve through $0.1G_{\rho\rho P}(t)$ from the fits to $\pi^{\pm}p \rightarrow \pi^0 X$ over 70 - 96 GeV is shown for comparison.

the place where $\alpha = -1$, which would be at $t_m \simeq 1.5$ GeV^2 if the trajectory were a straight line. This dip has been seen in the cross sections for the exclusive reactions, $\pi^- p \to \eta n$ and $\pi^+ p \to \eta \Delta^{++}$ (see for example the review in Ref. (Fo71)). If such a dip were present then it would show the presence of the triple Regge term and suggest that the flattening off of the trajectories may be due to some other mechanisms dominating at high t_m.

5.3 CROSS SECTIONS FOR INCLUSIVE π^0 AND η PRODUCTION

In this section, the data presented in Sections 5.1 and 5.2 for π^0 and η production from pion beams are shown as a function of t for various energy intervals. In Figs. 5.8 and 5.9 are shown the cross sections for $\pi^- p \to \pi^0 X$ and $\pi^+ p \to \pi^0 X$ in 10 GeV energy bins starting at 60 GeV. Any points consistent with zero cross section (that is, points with larger error than value) have been omitted from these plots and all future cross section plots. In all the energy bins, there is a dramatic change of slope whose location varies from $t_m \simeq 0.4$ GeV^2 at the lower energies to 0.6 GeV^2 at the higher energies. This is the place where the ρ trajectory, $\alpha_\rho(t)$, passes through zero (Figs. 5.2,3) and the place where a dip is present in $G_{\rho\rho P}(t)$, as shown on Fig. 5.4.

The cross sections for $t_m > 1.5$ GeV^2 have been fit to the exponential form

$$\int_{E_1}^{E_2} \frac{d^2\sigma}{dtdE}(t,E)dE = ABe^{(t + 1.5)B}, \qquad (5.3.1)$$

where A is the cross section integrated over the energy range $E_1 - E_2$ and over t_m above 1.5 GeV^2. The fit allowed A to vary for the different energy bins but constrained the slope parameter, B, to be the same for all the bins. The best fits gave $B = 1.83 \pm 0.03$ GeV^{-2} for the π^- beam data and $B = 1.76 \pm 0.06$ GeV^{-2} for the π^+ beam data. The resulting curves are shown by the dotted lines on Figs. 5.8,9 and are seen to describe the data well. However other forms may fit the

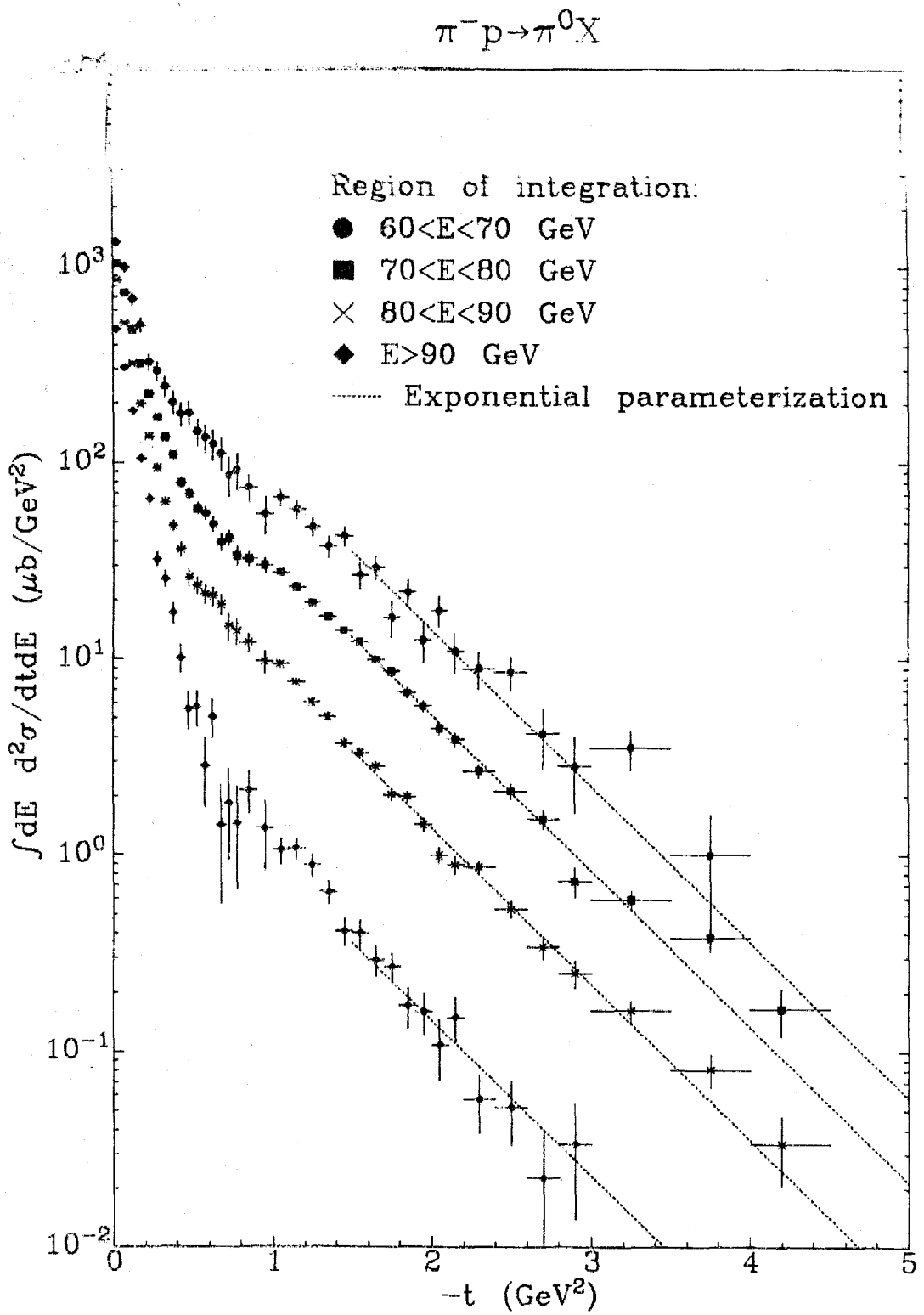

FIGURE 5.8 The t-dependence of the cross sections for $\pi^- p \to \pi^0 X$ integrated over 10 GeV ranges in the π^0 energy, E.

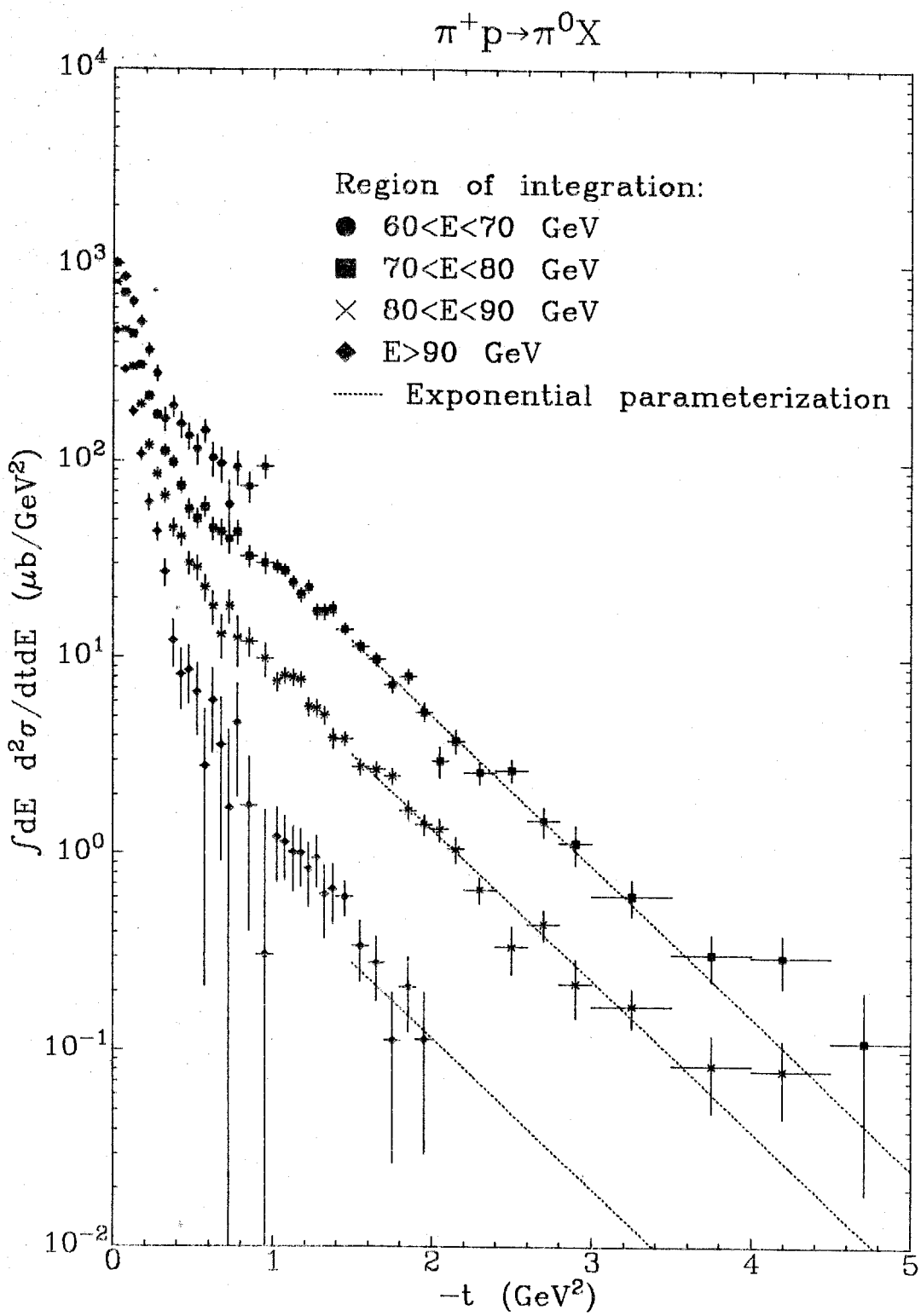

FIGURE 5.9 The t-dependence of the cross sections for $\pi^+ p \rightarrow \pi^0 X$ integrated over 10 GeV ranges in the π^0 energy, E.

data just as well. Clearly the slopes are very similar for the two beam polarities. The ratios of the values of A for the π^+ beam to the values for the π^- beam are 0.97 ± 0.04, 0.97 ± 0.04 and 0.8 ± 0.2 for the energy bins 70 - 80 GeV, 80 - 90 GeV and above 90 GeV respectively. These are all a little below unity, but nevertheless consistent with unity, which is the value expected at high t_m, as discussed below.

These cross sections may be compared with the theoretical predictions from the hard-scattering models described in Section 4.5. For the CIM model, the cross section has been estimated in Ref. (Fa79) using QCD to calculate the $\pi q \rightarrow \pi q$ scattering due to the exchange of gluons carrying large transverse momenta. The resulting cross section for $\pi^- p \rightarrow \pi^0 X$ is only about 1% of the measured cross section at $t_m = 2$ GeV^2 and about 2% at $t_m = 4$ GeV^2. Although there are some uncertainties in this calculation, it does seem implausable that the CIM model is the dominant mechanism in this kinematic region. The parton model, also described in Section 4.5, may well describe this region. Some rough calculations were in agreement and now more refined calculations are being made. There have been several measurements in other kinematic regions and of other processes which also disagree with the CIM predictions. The E268 data on $\pi^- p \rightarrow \pi^0 X$ at 90° in the c.m. (Do78b) are in poor agreement, as described in Ref. (Fa79). The E260 data on the ratio of the production of π^+ trigger particles to the production of π^- trigger particles from a

200 GeV π^+ beam with $1 < p_t < 4$ GeV (Br79a) agree with the parton model prediction from Ref. (Fi77) but its value of about 2 is about one unit lower than that predicted from the CIM model as interpreted in Ref. (Ch78). The ratio is high for the CIM model because of the difficulty in producing π^- mesons. As described in Ref. (Fa79), these earlier calculations of the CIM processes may be incorrect, but it is still difficult to understand how a significantly lower ratio could result.

The ratio of the cross section for the production of π^0 mesons from a π^+ beam to that from a π^- beam is shown in Fig. 5.10 as a function of t. Both cross sections have been integrated over energies above 70 GeV. The ratio is close to unity for t_m above 0.2 GeV^2 as expected from the dominance of the $\rho\rho P$ triple Regge term. For t_m below 0.2 GeV^2, the cross section from the π^+ beam is about 95% of that from the π^- beam. A value below unity is expected because both the low mass resonance production cross section and the Reggeon exchange cross section are larger for the π^- beam. At high t_m, the observed value of unity would be predicted from most hard-scattering models, such as the QCD-parton model and the CIM model, and so this ratio does not provide a good test of these models.

The cross section for η production from a π^- beam, $\pi^- p \to \eta X$, is shown in Fig. 5.11. The cross sections fall almost exponentially with t_m for all the energy bins and show no dramatic change of structure as was found for the π^0 production cross sections around 1 GeV^2.

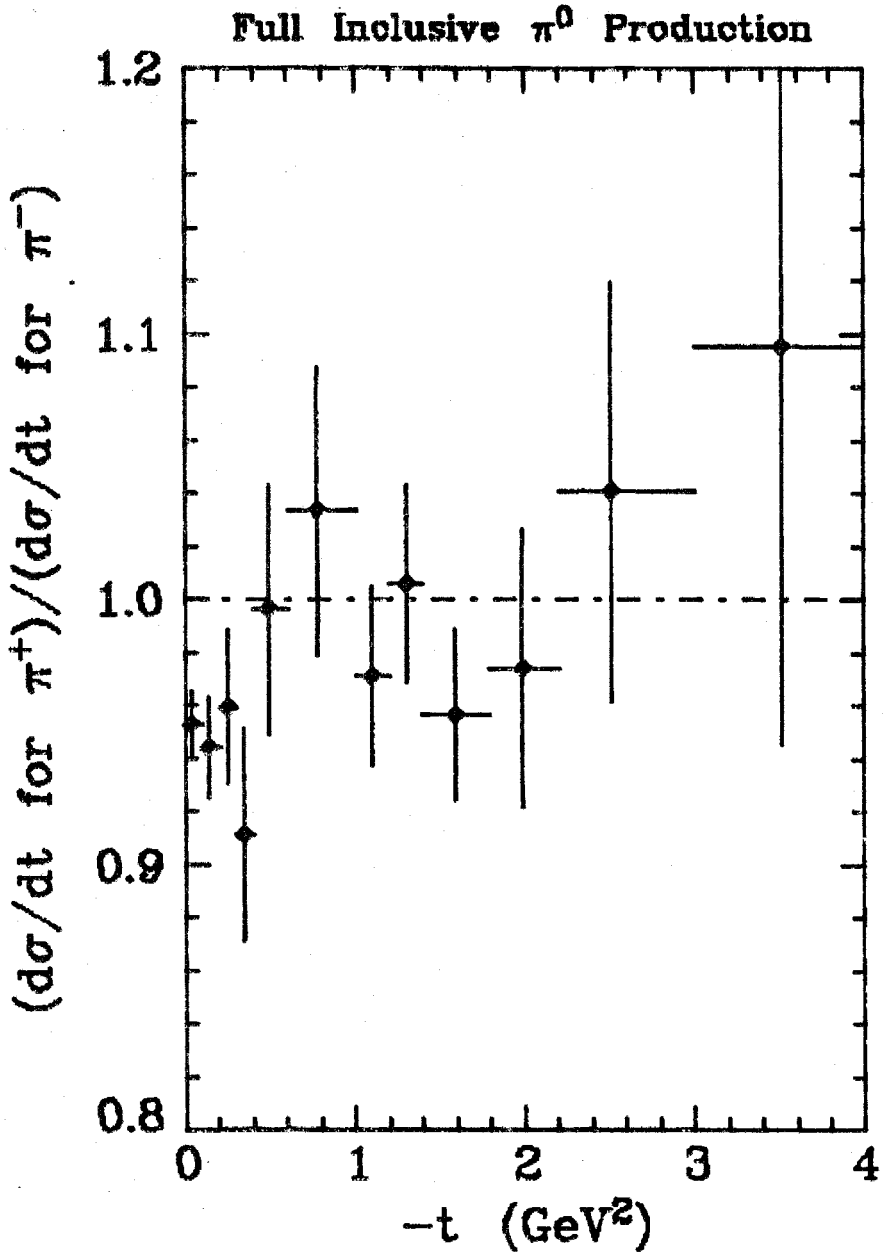

FIGURE 5.10 t-dependence of the ratio of the cross section for the inclusive production of π^0 mesons from a π^+ beam to that from a π^- beam. Both cross sections are integrated over energies above 70 GeV.

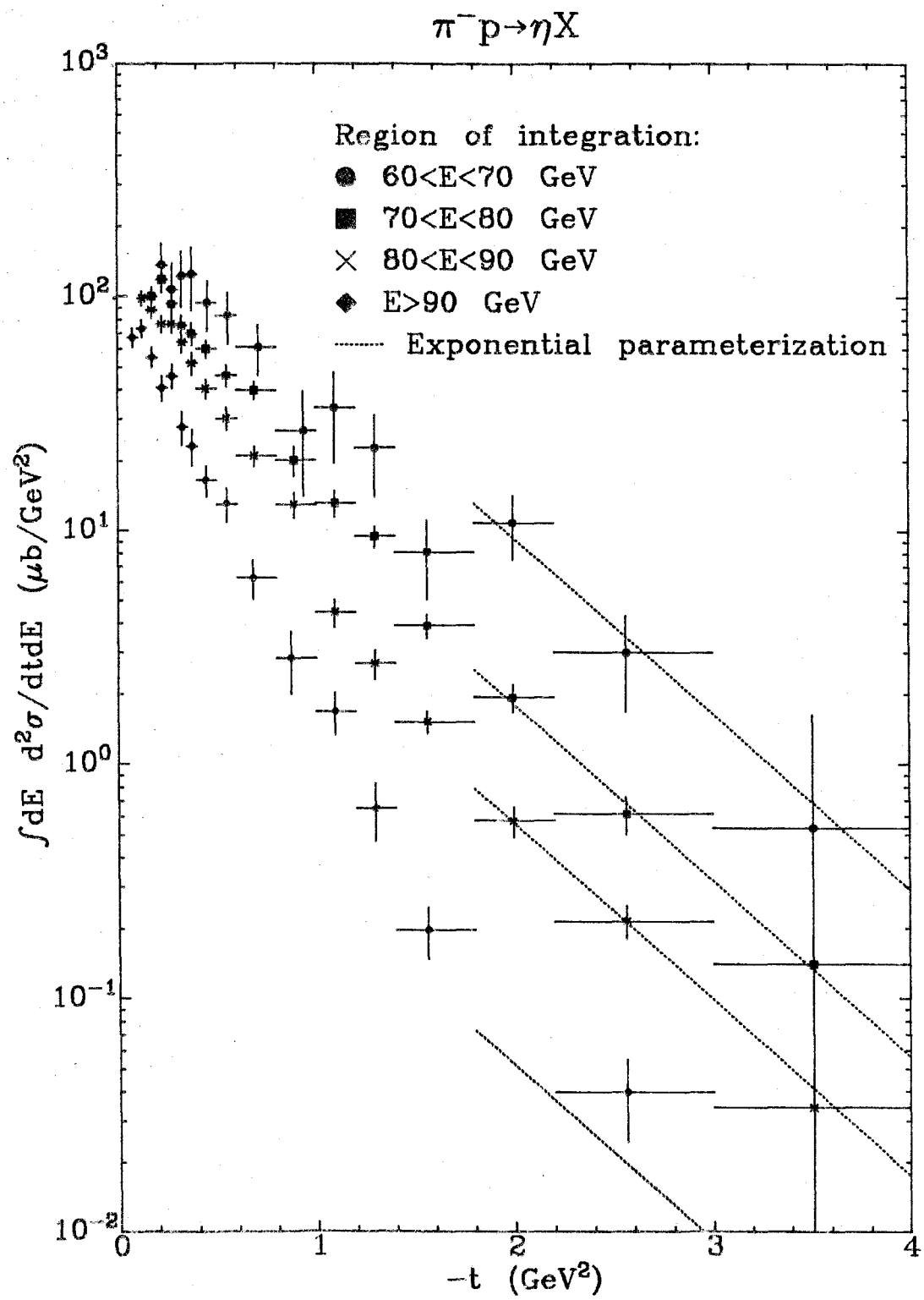

FIGURE 5.11 The t-dependence of the cross sections for $\pi^- p \to \eta X$ integrated over 10 GeV ranges in the η energy, E.

Exponentials of the form (5.3.1) have again been fit to the data with t_m above 1.8 GeV^2 and the best fit gave $B = 1.7 \pm 0.2$ GeV^{-2}, which is a similar slope to that found for π^0 production. The ratios of the values of A for η production from a π^- beam to π^0 production from a π^- beam are 0.7 ± 0.2, 0.34 ± 0.04, 0.41 ± 0.05 and 0.4 ± 0.2 for the energy bins 60 - 70 GeV, 70 - 80 GeV, 80 - 90 GeV and above 90 GeV respectively.

The ratio of the cross section for η production from a π^- beam, integrated above 70 GeV, to that for π^0 production is shown in Fig. 5.12. At high t_m, the ratio is about 0.4, which is close to the prediction of 0.5 from the naïve argument that only the $u\bar{u}$ and $d\bar{d}$ content of the π^0 and η are important and that $\eta = \frac{1}{\sqrt{2}}s\bar{s} + \frac{1}{2}(u\bar{u} - d\bar{d})$. This prediction assumes that the $u\bar{u}$ and $d\bar{d}$ terms contribute incoherently. It is certainly not valid at $x = 1$ since in Regge theory, which works for the corresponding exclusive scattering processes out to $t_m \simeq 2$ GeV^2, the $u\bar{u}$ and $d\bar{d}$ parts of the η interfere destructively at $t_m \simeq 1.5$ GeV^2, where the A_2 has its wrong signature nonsense zero, as described in Section 5.2. However it was shown above that the magnitude of the measured π^0 cross section rules out the coherent CIM mechanism and suggests that the incoherent quark-quark scattering processes may dominate. Thus the η cross sections also suggest that this mechanism dominates. This ratio is similar to those measured at low x and high p_t. Using the same photon detector, a ratio of 0.44 ± 0.05 was obtained by E268 for $2 < p_t < 4$ GeV (Do78a). Two ISR

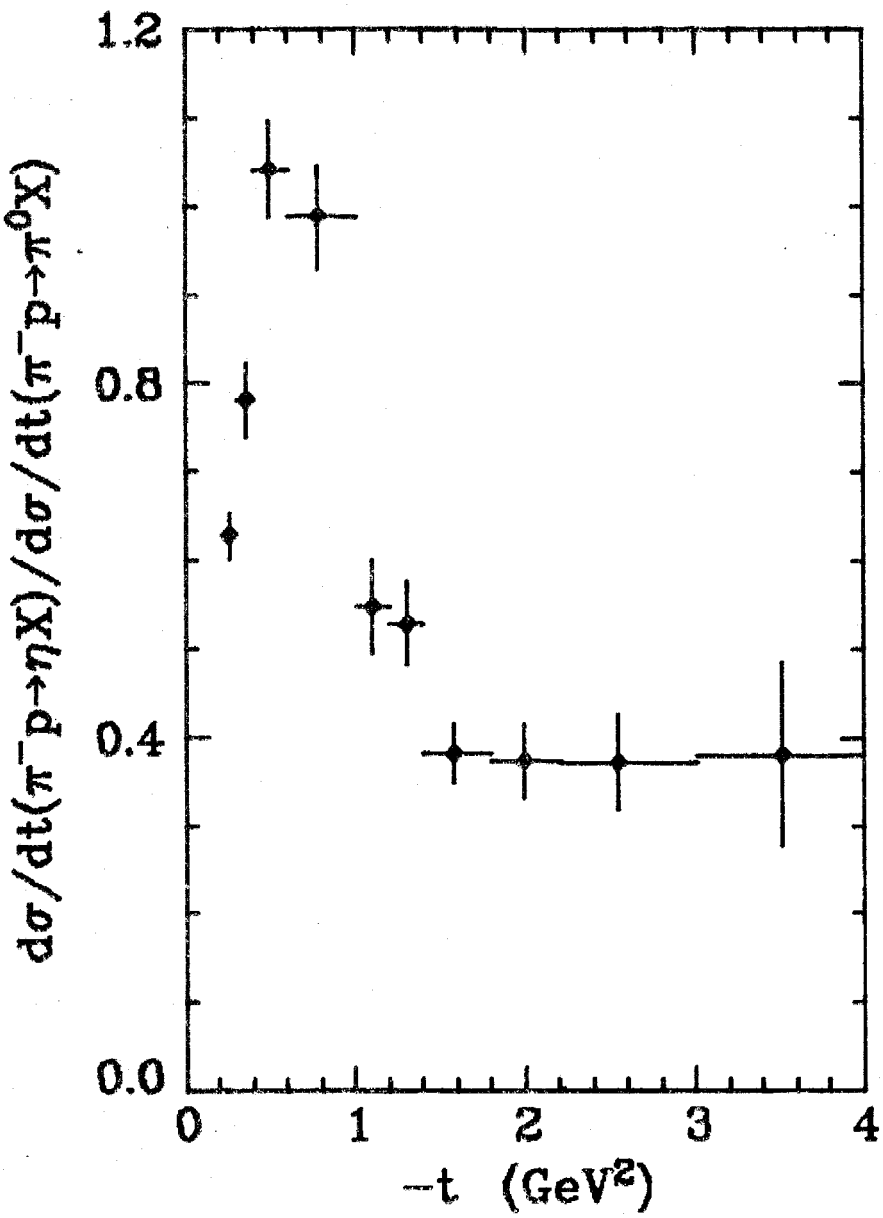

FIGURE 5.12 t-dependence of the ratio of the cross section for the full inclusive production of η mesons from a π^- beam to that for π^0 mesons. Both cross sections are integrated over energies above 70 GeV.

experiments have measured proton-induced π^0 and η production for s between 1000 and 4000 GeV^2 and have obtained ratios of 0.55 ± 0.10 for $3 < p_t < 5$ GeV (Bu76b) and 0.57 ± 0.08 for $3 < p_t < 7$ GeV (Ko79). In all cases the ratio was fairly constant over the entire p_t range.

The ratio of the cross section for the production of η mesons from a π^+ beam to that from a π^- beam is shown in Fig. 5.13. This ratio is about 0.8 at low t_m, where the Reggeon term is present, and consistent with unity at higher t_m, as expected from the dominance of the Pomeron exchange term and also from the hard-scattering models.

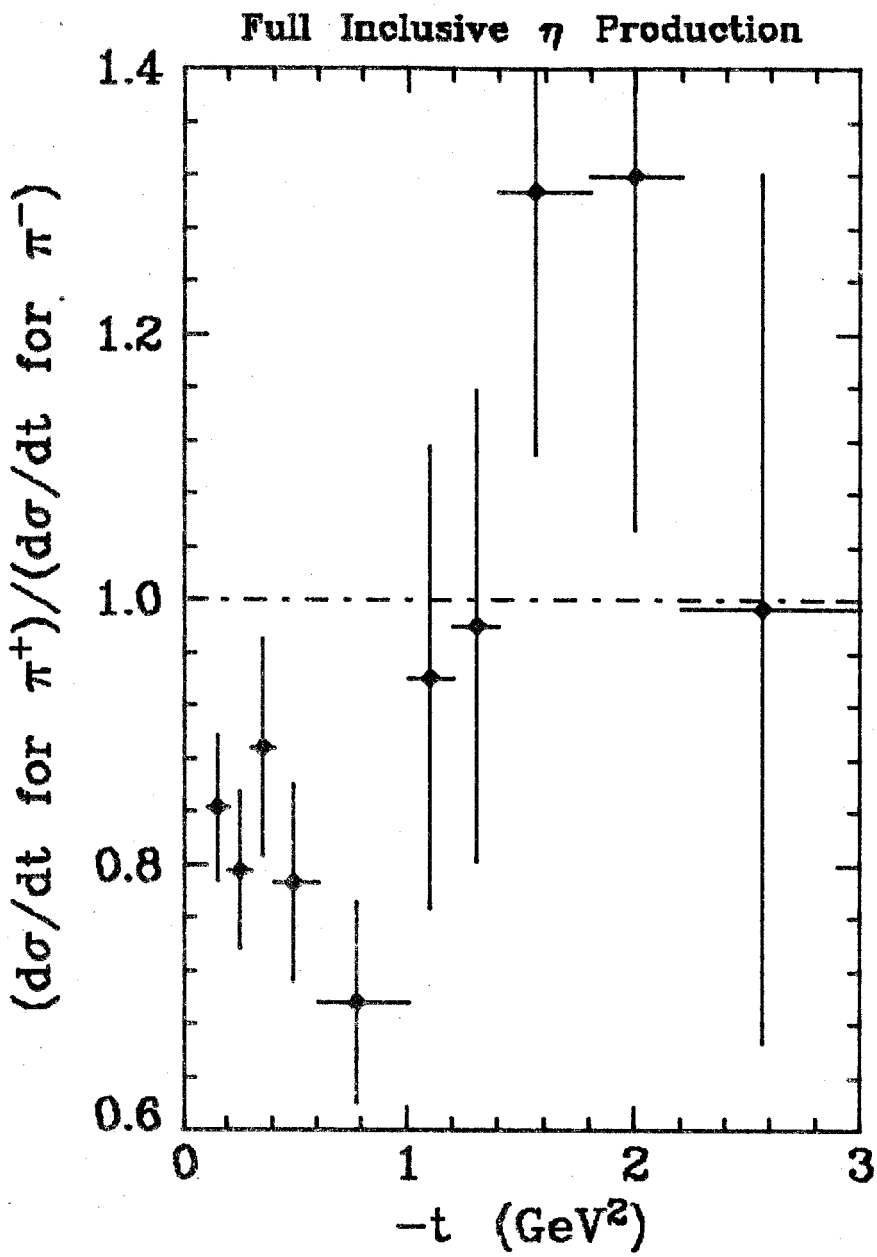

FIGURE 5.13 t-dependence of the ratio of the cross section for the inclusive production of η mesons from a π^+ beam to that from a π^- beam. Both cross sections are integrated over energies above 70 GeV.

CHAPTER 6

RESULTS FROM NEUTRAL FINAL STATE REACTIONS

6.1 PSEUDOPOLE TRAJECTORY INTERCEPT FROM TOTAL NFS CROSS SECTION

In Section 4.4 it was shown that the cross section for Neutral Final State (NFS) π^0 and η production depends on the intercept of the "pseudopole trajectory", $\alpha_{\varphi}(0)$. To determine this, (4.4.5) is used to show that the cross section for the NFS reaction,

$$\pi^- + p \to X^0, \tag{6.1.1}$$

at high beam momentum, p_{lab}, is

$$\sigma_{NFS}(p_{lab}) \sim A p_{lab}^{\alpha_{\varphi}(0)-1} . \tag{6.1.2}$$

Measurements of the total NFS cross section were made by this experiment at p_{lab} = 49 and 99 GeV. Software cuts were applied to the veto counters, as described in Appendix 6.I, and to the Cherenkov counters which required that a PION signal be present, as described in Appendix 3.IX. The same Cherenkov cuts were applied to the data from FLUX runs taken under the same beam conditions in order to find the PION content of the beam. This gave the uncorrected cross sections,

$$\sigma^U_{NFS}(49) = 60.17 \pm 0.54 \ \mu b \tag{6.1.3}$$

$$\sigma^U_{NFS}(99) = 25.66 \pm 0.21 \ \mu b. \tag{6.1.4}$$

The corrections for the biases in the hardware trigger, discussed in Appendix 6.I, and the beam attenuation, discussed in Appendix

3.VIII, were now applied to these cross sections and the empty target cross sections were similarly corrected and subtracted. This gave the final cross sections,

$$\sigma_{NFS}(49) = 90 \pm 10 \ \mu b \qquad (6.1.5)$$

$$\sigma_{NFS}(99) = 38.4 \pm 5.3 \ \mu b, \qquad (6.1.6)$$

where the errors are mainly systematic and due to the uncertainty in correcting for events producing charged particles through electromagnetic or weak decays. These results are compared to other measurements using zero-prong events in bubble chamber experiments, taken from Refs. (Ap73), (Br72), (Cr68), (Po75) and (Wh76), in Fig. 6.1. A fit to (6.1.2) with

$$\alpha_{\mathcal{P}}(0) = -0.08 \qquad (6.1.7)$$

is shown and it is seen that (6.1.2) provides a good representation of the data. Since the data from all these experiments have been corrected for some of the effects discussed in Appendix 6.I and the systematic errors have been treated in different ways, it is estimated that the error in this determination of $\alpha_{\mathcal{P}}(0)$ is about 0.2.

If the corrections to the 49 and 99 GeV measurements are assumed to be the same, then (6.1.3) and (6.1.4), which involve only statistical errors, may be used to give

$$\alpha_{\mathcal{P}}(0) = -0.21 \pm 0.02, \qquad (6.1.8)$$

where the error has been calculated using the statistical errors and assuming that the beam momenta are known to 0.3 GeV. If instead of

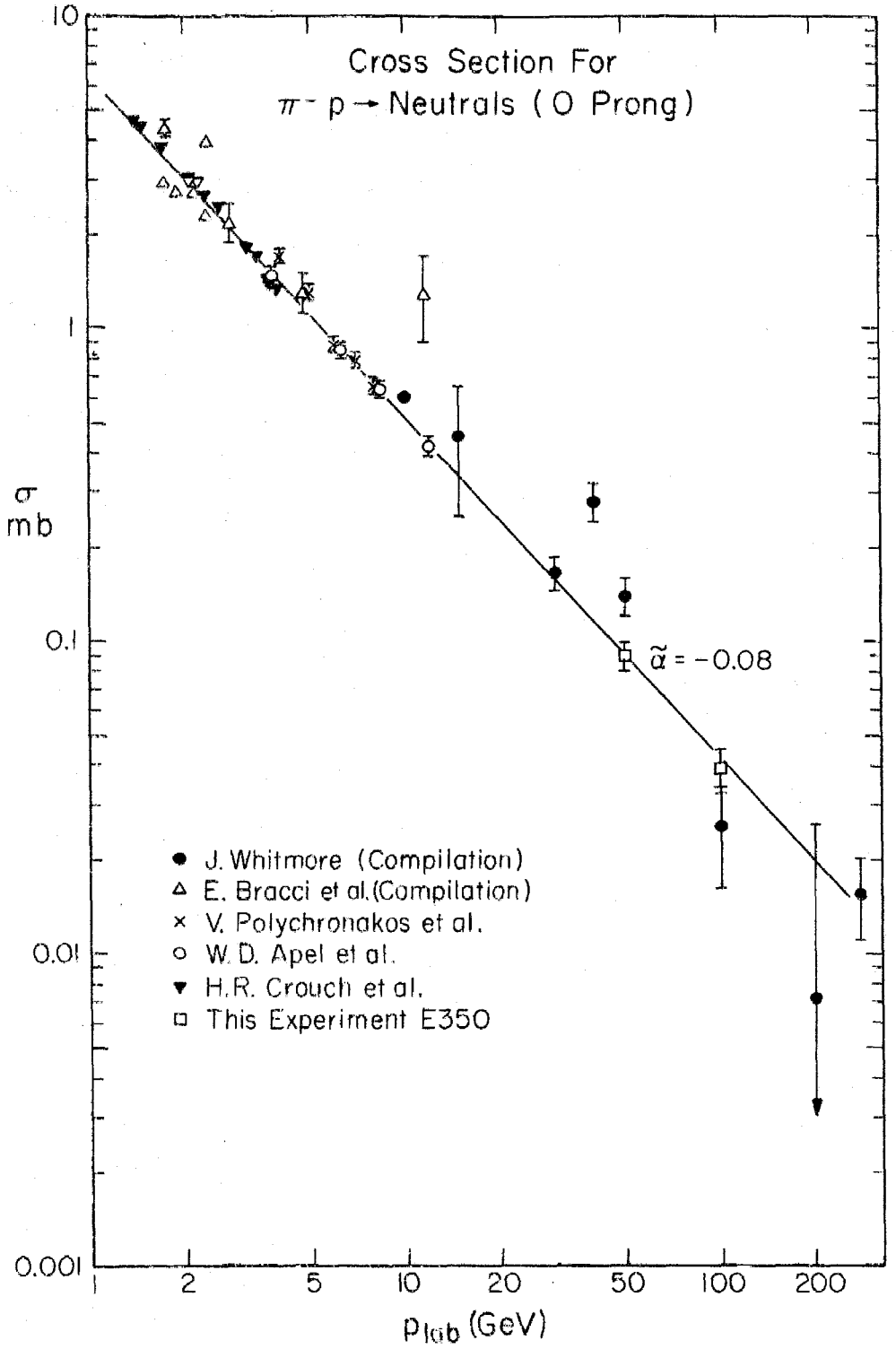

FIGURE 6.1 A compilation of data on $\pi^- p$ to all neutrals from Refs. (Ap73), (Br72), (Cr68), (Po75) and (Wh76) and from this experiment. The line corresponding to (6.1.1) with $\alpha_{\mathcal{P}}(0) = -0.08$ is shown.

supposing that the corrections are equal for the two beam momenta it is assumed that the NFS events at 49 GeV contain one less π^0 on average than the 99 GeV events, (6.1.3) would become 56.0 ± 0.5 μb and the extracted value of $\alpha_{\mathcal{P}}(0)$ would be

$$\alpha_{\mathcal{P}}(0) = -0.11 \pm 0.02. \qquad (6.1.9)$$

Thus an error of 0.1 in $\alpha_{\mathcal{P}}(0)$ can be assumed just from the lack of knowledge of the content of NFS events. It was decided to use the value (6.1.7) for the results presented in this chapter because it provides a good representation of the data with $p_{lab} < 30$ GeV, which is the appropriate region for M^2 here, and because the published results (Ba78b) used this value. Using the value given by (6.1.8) would decrease α by 0.06 everywhere.

The near-zero value of α has interesting implications because it means that the couplings in the ladder diagrams, described in Section 4.4, between the exchanged Reggeons and the clusters produced are small, as shown in Ref. (Ba78b). This shows that the multiperipheral model has greater validity for the NFS reaction than for the full inclusive reactions and so the former reactions may be theoretically preferred as a test of the theory. However the NFS trigger used in this experiment was rather biased, as described in Appendix 6.I, and so the cross sections for these reactions were harder to derive from the data.

6.2 ρ AND A_2 TRAJECTORIES AND RESIDUE FUNCTIONS FROM NFS REACTIONS

In this section, the results from the reactions,

$$\pi^- + p \to \pi^0 + X^0, \tag{6.2.1}$$

$$\pi^- + p \to \eta + X^0, \tag{6.2.2}$$

where X^0 means that only neutral particles are produced, are presented in the context of the pseudo-triple Regge model discussed in Section 4.4. The definition of the neutral final state (NFS) is given in Appendix 6.I. Reaction (6.2.1) will be discussed first. Supposing that the intercept of the pseudopole trajectory in (4.4.7) is given by (6.1.7), the cross section for reaction (6.2.1) is predicted to be given by

$$\frac{d^2\sigma}{dtdx}(x,t,s) = G_{\rho\rho\mathscr{P}}(t)s^{-1.08}(1-x)^{-0.08 - 2\alpha_\rho(t)} + (\text{low mass resonances}). \tag{6.2.3}$$

Hence a second determination of $\alpha_\rho(t)$ together with a determination of $G_{\rho\rho\mathscr{P}}(t)$ could be made.

The data were accumulated in t bins as described in Section 5.1 for the full inclusive case. The corrections due to events failed erroneously by the hardware trigger, which are described in Appendix 6.I, were applied using the values estimated for the exclusive reaction, $\pi^- p \to \pi^0 n$. The other corrections described in Section 5.1 were applied, except that no correction was made for the multiple

scattering in the target, which is negligible because the events produced in all the scatters have to be neutral. However an overall factor was applied for the beam attenuation. An additional correction was made for the t_{min} effect at low t_m and low energies, using the approach described for η production in Section 5.2 and using exponential parameterizations of the t-dependence of the NFS π^0 cross sections, which are presented in the following section.

The data are shown in Fig. 6.2 with all the corrections applied but with purely statistical errors. The data were collected for all π^0 energies but are shown only for energies above 26 GeV because the acceptance was small at the lower energies, as shown in Appendix 3.VII, and because the background under the π^0 was large, as shown in Appendix 3.VI. The solid curves on Fig. 6.2 are the results of fits to (6.2.3) using energies between 70 and 96 GeV. The data were

---

FIGURE 6.2 Data on $\pi^- p \to \pi^0 X^0$ as a function of the energy of the π^0, E, in different t bins. The results of fits over 70 - 96 GeV are shown. The resulting values are shown on Fig. 6.3 and in Table 6.1.

KEY

—— Final fit

--- $\rho\rho\varphi$ triple Regge contribution

..... Low mass resonances (estimated)

⬍ ⬍ Limits of fit

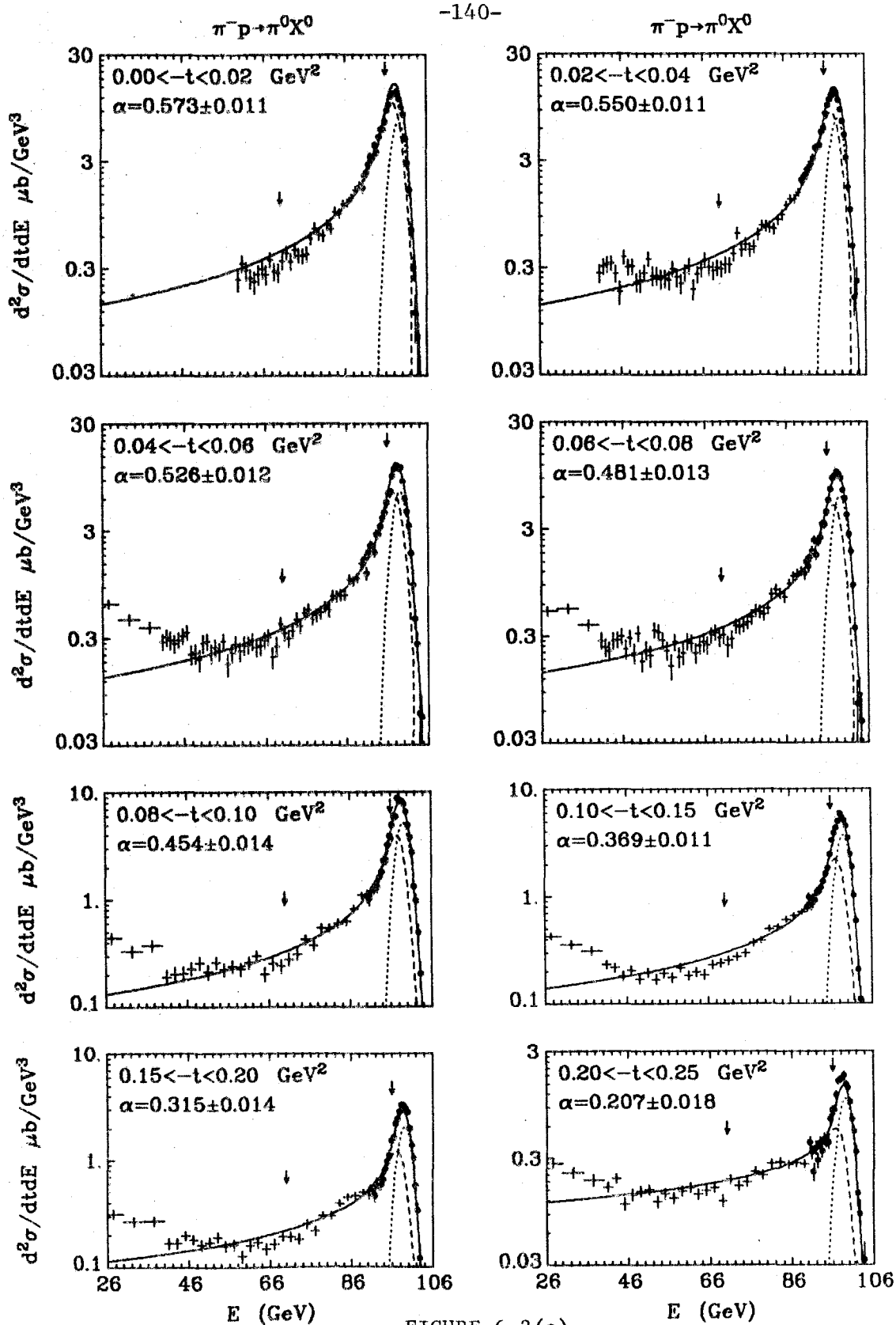
π⁻p→π⁰X⁰
0.00<−t<0.02 GeV²
α=0.573±0.011
0.02<−t<0.04 GeV²
α=0.550±0.011
0.04<−t<0.06 GeV²
α=0.526±0.012
0.06<−t<0.08 GeV²
α=0.481±0.013
0.08<−t<0.10 GeV²
α=0.454±0.014
0.10<−t<0.15 GeV²
α=0.369±0.011
0.15<−t<0.20 GeV²
α=0.315±0.014
0.20<−t<0.25 GeV²
α=0.207±0.018
d²σ/dtdE μb/GeV³
E (GeV)

FIGURE 6.2(a)

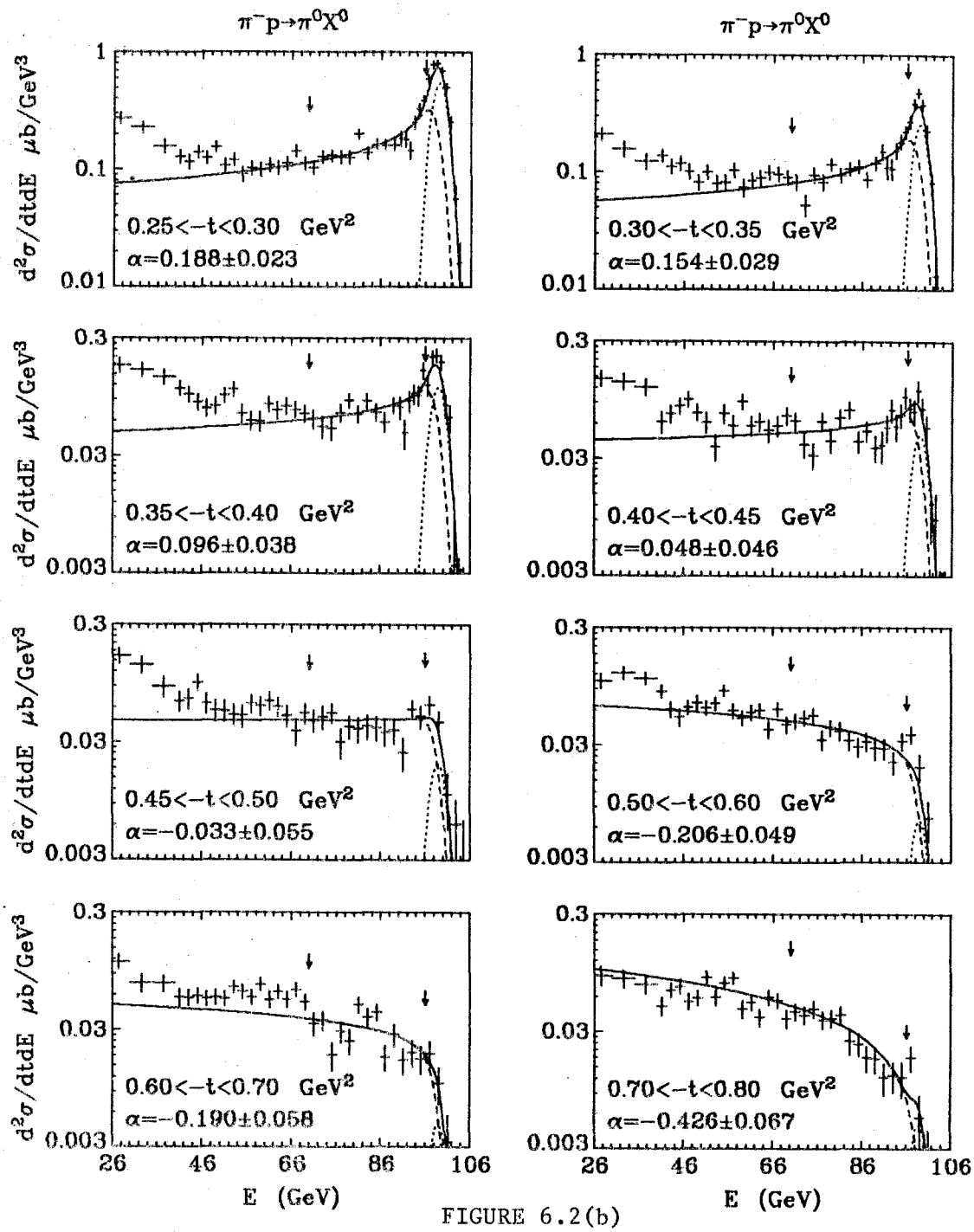
$\pi^-p\to\pi^0X^0$
$\pi^-p\to\pi^0X^0$
$d^2\sigma/dtdE$ μb/GeV³
0.25<−t<0.30 GeV²
α=0.188±0.023
0.30<−t<0.35 GeV²
α=0.154±0.029
0.35<−t<0.40 GeV²
α=0.096±0.038
0.40<−t<0.45 GeV²
α=0.048±0.046
0.45<−t<0.50 GeV²
α=−0.033±0.055
0.50<−t<0.60 GeV²
α=−0.206±0.049
0.60<−t<0.70 GeV²
α=−0.190±0.058
0.70<−t<0.80 GeV²
α=−0.426±0.067
1
0.1
0.01
0.3
0.03
0.003
26
46
66
86
106
E (GeV)

FIGURE 6.2(b)

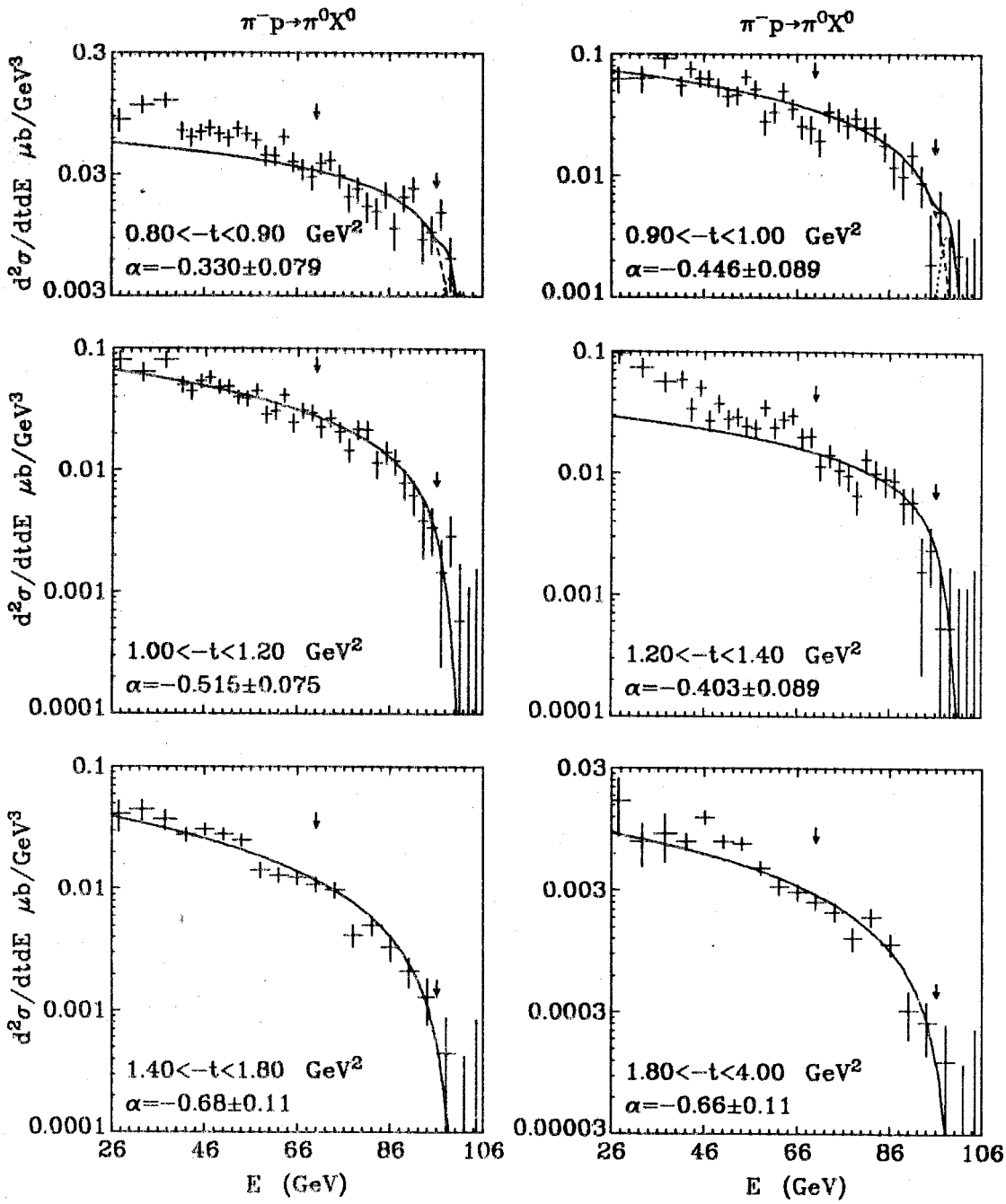
$\pi^-p\to\pi^0X^0$
$d^2\sigma/dtdE$ $\mu b/GeV^3$
0.80<−t<0.90 GeV²
α=−0.330±0.079
0.90<−t<1.00 GeV²
α=−0.446±0.089
1.00<−t<1.20 GeV²
α=−0.515±0.075
1.20<−t<1.40 GeV²
α=−0.403±0.089
1.40<−t<1.80 GeV²
α=−0.68±0.11
1.80<−t<4.00 GeV²
α=−0.66±0.11
E (GeV)

FIGURE 6.2(c)

fit in 0.5 GeV energy bins for $t_m < 0.25$ GeV^2 and 1 GeV bins for $t_m > 0.25$ GeV^2. Some of the energy bins have been combined together in Fig. 6.2 for display purposes.

The two terms in (6.2.3) are shown separately on Fig. 6.2. At low t_m and high x, both terms are important but only 3% of the cross section for the low mass resonance term is included in the energy range of the fit. Since the triple Regge term peaks at x = 1 at low t_m, it was not possible to distinguish the two terms and find the cross section for low mass resonance production from these data. Hence its cross section was estimated by including just the neutron and the $\pi^0 n$ decay mode of the $\Delta^0(1232)$ and estimating these using the results of E111 (Ba76) for the neutron production and the lower energy data on the $\Delta^{++}(1232)$ production (B174b), as described in Appendix 4.II. This term was included for $t_m < 1.0$ GeV^2 and the triple Regge term was used only for masses above 1.4 GeV^2.

There is a very striking change in the shape of the energy spectrum as t_m increases. At low t_m, as shown on Fig. 6.2(a), the triple Regge term peaks at high x, whilst at medium t_m values it becomes flat (Fig. 6.2(b)) and then assumes a shape whose fall with energy is independent of t (Fig. 6.2(c)). This shrinkage effect is similar to that observed in the full inclusive case but the shape at a given value of t is different because of the extra $(1 - x)^{-1.08}$ term in the cross section. The triple Regge cross section at low t_m and high x falls faster with t than the cross section for low mass

resonance production, as shown on Figs. 6.2(a,b) and Fig. 6.7. The latter term contributes less than half of the cross section under the peak at low t_m whilst at $t_m \simeq 0.25$ GeV^2 it contributes most of the peak. The $\pi^- p \to \pi^0 n$ and $\pi^- p \to \pi^0 \Delta^0$ processes are dominated by the spin-flip amplitudes and so their cross sections are flatter at t_m near zero and fall slower with t_m than the cross sections due to the non spin-flip amplitude.

The fits shown on Fig. 6.2 solved for the trajectory, $\alpha_\rho(t)$, and the cross section for the $\rho\rho\mathcal{P}$ term integrated over the energy range of the fit. The resulting values for $\alpha_\rho(t)$ are shown on Fig. 6.3 and are listed in Table 6.1. The trajectory lies about 0.1 higher than the straight line through the ρ, A_2 and g particles at very low t_m and then crosses it and lies below it by about 0.05 until $t_m \simeq 1$ GeV^2 where it starts to flatten off at a value of about -0.7, so that the cross section behaves like $(1 - x)^{1.3}$. This determination of the ρ trajectory agrees well with that determined from the full inclusive data fit over 80 - 96 GeV, shown by the dashed curve on Fig. 6.3, for $0.3 < t_m < 1$ GeV^2. It lies about 0.3 higher at t_m near zero and 0.2 lower for $t_m > 1.5$ GeV^2.

Fits were also made over the energy range 50 - 96 GeV and the resulting values for α are listed in Table 6.1. α has about the same values as in the 70 - 96 GeV fit for $t_m < 0.1$ GeV^2, is higher by about 0.02 until $t_m \simeq 0.25$ GeV^2 and then falls to lie about 0.08 lower for $t_m \gtrsim 0.35$ GeV^2. However the difference between these two

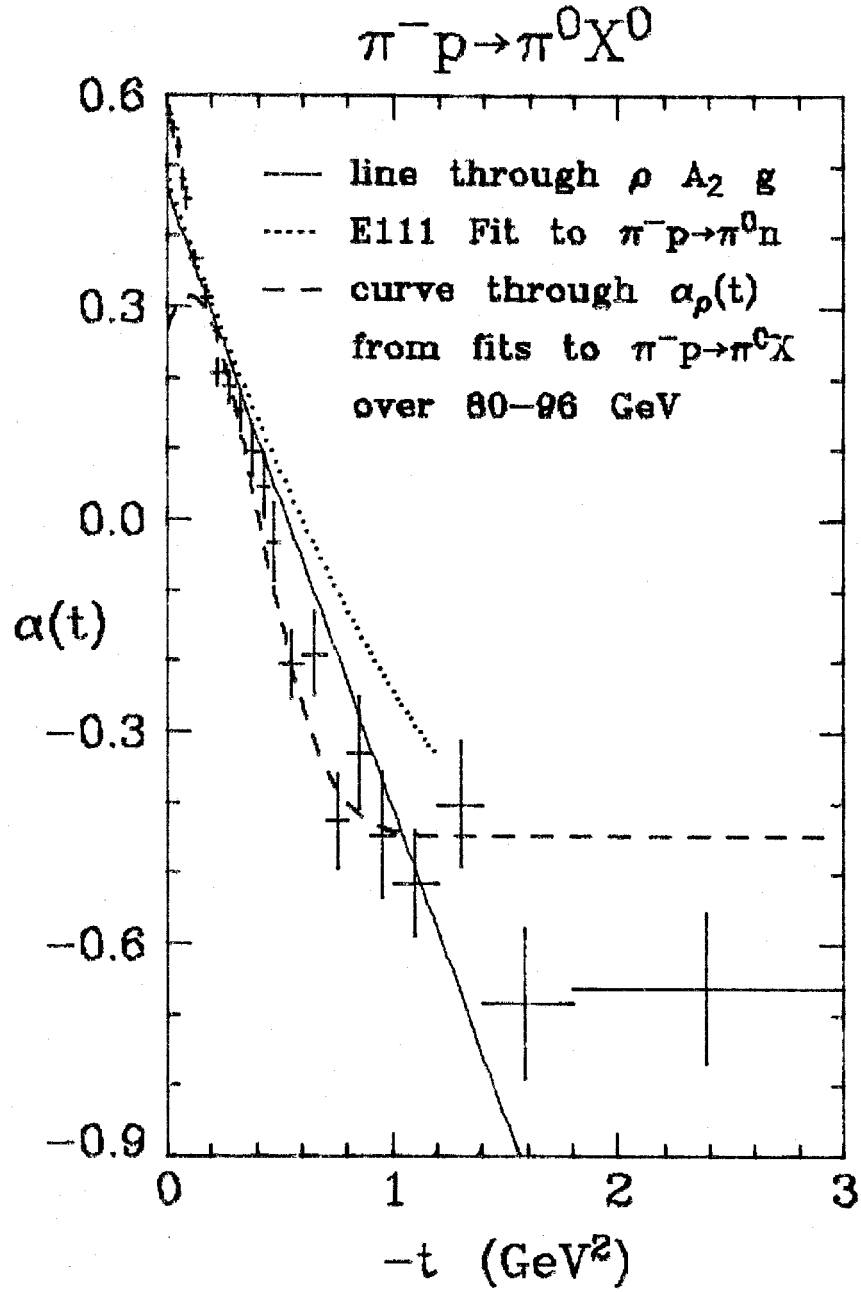

FIGURE 6.3 $\alpha_\rho(t)$ from the fits to $\pi^- p \to \pi^0 X^0$ over 70 - 96 GeV shown on Fig. 6.2. The values for α are listed in Table 6.1. The curve through the ρ Regge trajectory extracted from the fits to the full inclusive π^0 production data from pion beams over 80 - 96 GeV is shown for comparison.

TABLE 6.1(a). ρ Regge trajectory, $\alpha_\rho(t)$, and residue function, $G_{\rho p \bar{p}}(t)$, from fits to $\pi^- p \to \pi^0 X^0$ data with $-t < 0.40$ GeV^2 over the energy ranges 70 - 96 and 50 - 96 GeV. The two-term fits, which are described in the text, are over the energy range 70 - 96 GeV.

	Fits over 70 - 96 GeV		Fits over 50 - 96 GeV		Two-term fits	
-t range	α	G (μb/GeV^2)	α	G (μb/GeV^2)	α	a
0.00 - 0.02	0.573 ± 0.011	9.01 ± 0.15	-	-	0.66 ± 0.03	0.34 ± 0.06
0.02 - 0.04	0.550 ± 0.011	9.45 ± 0.16	0.5510 ± 0.0088	9.18 ± 0.15	0.65 ± 0.03	0.35 ± 0.06
0.04 - 0.06	0.526 ± 0.012	9.73 ± 0.18	0.5221 ± 0.0094	9.39 ± 0.16	0.58 ± 0.03	0.49 ± 0.06
0.06 - 0.08	0.481 ± 0.013	10.04 ± 0.20	0.484 ± 0.010	9.62 ± 0.18	0.58 ± 0.04	0.44 ± 0.08
0.08 - 0.10	0.454 ± 0.014	10.13 ± 0.22	0.447 ± 0.011	9.79 ± 0.19	0.50 ± 0.04	0.56 ± 0.08
0.10 - 0.15	0.369 ± 0.011	9.72 ± 0.15	0.3908 ± 0.0081	9.30 ± 0.13	0.44 ± 0.03	0.47 ± 0.07
0.15 - 0.20	0.315 ± 0.014	9.22 ± 0.18	0.323 ± 0.010	9.05 ± 0.16	0.39 ± 0.03	0.64 ± 0.08
0.20 - 0.25	0.207 ± 0.018	8.55 ± 0.21	0.225 ± 0.013	8.76 ± 0.18	0.19 ± 0.04	0.48 ± 0.11
0.25 - 0.30	0.188 ± 0.023	6.98 ± 0.22	0.166 ± 0.016	7.59 ± 0.20	0.13 ± 0.05	0.42 ± 0.16
0.30 - 0.35	0.154 ± 0.029	6.10 ± 0.24	0.099 ± 0.021	7.04 ± 0.22		
0.35 - 0.40	0.096 ± 0.038	5.32 ± 0.26	0.004 ± 0.026	6.64 ± 0.25		

TABLE 6.1(b). ρ Regge function, $\alpha_\rho(t)$, and residue function, $G_{\rho p \bar{p}}(t)$, from fits to $\pi^- p \to \pi^0 X^0$ data with $-t > 0.40$ GeV^2 over the energy ranges 70 - 96 GeV and 50 - 96 GeV.

	Fits over 70 - 96 GeV		Fits over 50 - 96 GeV	
-t range	α	G (μb/GeV^2)	α	G (μb/GeV^2)
0.40 - 0.45	0.048 ± 0.046	5.09 ± 0.30	-0.050 ± 0.032	6.61 ± 0.28
0.45 - 0.50	-0.033 ± 0.055	5.07 ± 0.34	-0.111 ± 0.037	6.70 ± 0.33
0.50 - 0.60	-0.206 ± 0.049	5.42 ± 0.28	-0.264 ± 0.031	7.82 ± 0.28
0.60 - 0.70	-0.190 ± 0.058	5.94 ± 0.38	-0.338 ± 0 035	9.75 ± 0.37
0.70 - 0.80	-0.426 ± 0.067	8.06 ± 0.49	-0.436 ± 0.039	12.03 ± 0.46
0.80 - 0.90	-0.330 ± 0.079	7.18 ± 0.57	-0.487 ± 0.048	11.07 ± 0.50
0.90 - 1.00	-0.446 ± 0.089	8.30 ± 0.64	-0.456 ± 0.051	11.03 ± 0.54
1.00 - 1.20	-0.515 ± 0.075	7.78 ± 0.50	-0.523 ± 0.041	10.49 ± 0.40
1.20 - 1.40	-0.403 ± 0.089	5.83 ± 0.49	-0.559 ± 0.052	7.96 ± 0.38
1.40 - 1.80	-0.68 ± 0.11	4.42 ± 0.36	-0.725 ± 0.059	5.26 ± 0.26
1.80 - 4.00	-0.66 ± 0.11	1.31 ± 0.12	-0.767 ± 0.064	1.36 ± 0.07

trajectories is nowhere much larger than one standard deviation. The difference in the behavior for $t_m \gtrsim 0.35$ GeV^2 can be seen from Figs. 6.2(b,c) since the data points between 50 and 70 GeV generally lie below the extrapolation of the curve from the fit over 70 - 96 GeV. For the fits over 50 - 96 GeV, the trajectory flattens off at a value of about -0.75 for large t_m, so that the cross section behaves like $(1 - x)^{1.4}$, compared with $(1 - x)^{1.3}$ for the higher energy fits. This change in the energy-dependence of the cross section may not be real, since the corrections due to the biases in the trigger were only calculated at x near unity. It is expected that the multiplicative correction should increase as the energy decreases, thus giving an improved agreement with the predictions. As described in Appendix 6.I, it is hard to calculate the corrections with any confidence away from x = 1 because the structure of the events is not understood. There is also a systematic error of 0.06 everywhere in the trajectories determined from the NFS data due to the error in the determination of $\alpha_{\mathcal{P}}(0)$, as discussed in the previous section. As with the full inclusive case, it is believed that the fits over the higher energy region describe the triple Regge contribution best since other physical mechanisms enter at lower energies. In the NFS case it is possible that the pseudo-Regge theory works down to lower x than the ordinary theory because a smaller central region would be present due to the small size of the coupling involved, as discussed in Section 6.1.

The fits shown on Fig. 6.2 describe the data well between 70 and 96 GeV but at higher energies, near x = 1, the extrapolation of the fitted curve lies below the data for $0.10 < t_m < 0.40$ GeV^2. To investigate this effect and to attempt to isolate the triple Regge term from the effects of the parameterization of the low mass resonance term, a second fit was performed in which the triple Regge term was truncated at an upper energy of 92.5 GeV. A second term, parameterized as a function of x of the form $(1 - x)^{-0.08 - 2a}$ was included above 92.5 GeV. Its normalization and a were allowed to vary. This parameterization was chosen to provide a convenient comparison with the triple Regge term. The resulting values of α and a from fits over the energy range 70 - 96 GeV are listed in Table 6.1(a), where they are labeled as "two-term fits". For $t_m \leq 0.1$ GeV^2, the resulting trajectory, α, is about 0.1 higher than that from the corresponding one-term fits, whilst for $t_m \approx 0.2$ GeV^2 the trajectories are about equal. The value of a is lower than α for t_m below 0.8 GeV^2, indicating that the cross section rises slower with x at high x.

To find the residue functions, $G_{\rho\rho\mathcal{P}}(t)$, a second set of fits was performed, as described in Section 5.1. The trajectory, $\alpha_\rho(t)$, resulting from the initial set of fits was parameterized in the form (5.1.6) and the resulting values for the coefficients were

$$A = -0.691, \quad B = 1.29, \quad C = 1.40, \quad D = -0.22, \quad (6.2.4)$$

for the fits over 70 - 96 GeV and

$$A = -0.675, \quad B = 1.275, \quad C = 1.277, \quad D = -1.03, \quad (6.2.5)$$

for the fits over 50 - 96 GeV. The resulting values for $G_{\rho\rho\mathcal{P}}$ are listed in Table 6.1 and are shown on Fig. 6.4 for the fits over 70 - 96 GeV. As with the full inclusive case, a definite dip is present at $t_m \simeq 0.45$ GeV^2, where G falls to almost half of its values at $t_m \simeq 0.05$ and 1 GeV^2, where it has maxima. This dip is coincident with the place where the trajectory passes through zero. For the fits over 50 - 96 GeV the dip is even more pronounced and occurs at $t_m \simeq 0.4$ GeV^2, which is again coincident with the place where the trajectory passes through zero. The probable explanations for this dip are the same as those discussed for the full inclusive case in Section 5.1.

Curves through $G_{\rho\rho P}(t)$ found from fits to $\pi^{\pm}p \to \pi^0 X$ over 70 - 96 GeV and 80 - 96 GeV are shown on Fig. 6.4 for comparison. At low t_m $G_{\rho\rho\mathcal{P}}$ has a forward dip, which is very different from the behavior of $G_{\rho\rho P}$, which falls sharply with t_m. In fact the cross sections integrated between energies of 70 and 96 GeV for the two cases have a very similar t-dependence for $t_m < 0.25$ GeV^2, as shown in the following section. The difference in the residue functions arises from the difference in the x-dependence for the two cases, which leads to a t-dependence of the form,

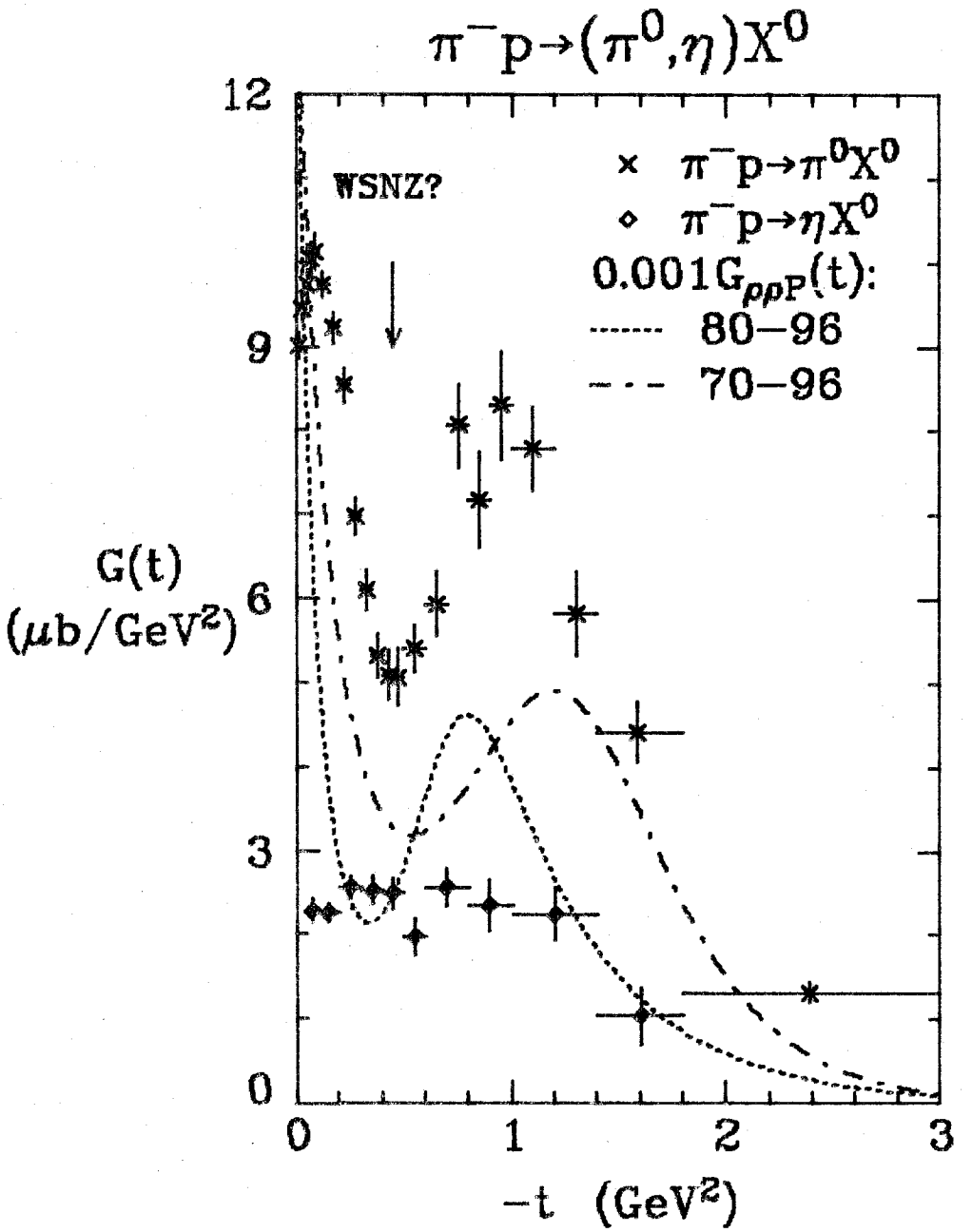

FIGURE 6.4 $G_{\rho\rho\mathscr{P}}(t)$ from the fits to $\pi^- p \to \pi^0 X$ over 70 - 96 GeV and $G_{A_2A_2\mathscr{P}}(t)$ from the fits to $\pi^- p \to \eta X^0$ over 70 - 96 GeV. The fits had the relevant trajectory constrained as described in the text. Also shown are curves through $G_{\rho\rho P}(t)$ determined from fits to the $\pi^{\pm} p \to \pi^0 X$ data over 70 - 96 GeV and 80 - 96 GeV.

$$G_{\rho\rho P}(t) \approx \frac{1 + \alpha_P(0) - 2\alpha_\rho(t)}{1 + \alpha_\theta(0) - 2\alpha_\rho(t)} G_{\rho\rho\theta}(t). \qquad (6.2.6)$$

Since the denominator vanishes when $\alpha_\rho(t) = 0.46$ for $\alpha_\theta(0) = -0.08$, $G_{\rho\rho P}(t)$ is large at $t \simeq 0$ GeV^2 and then falls rapidly with t_m compared with the behavior of $G_{\rho\rho\theta}(t)$. At large t_m, above 1 GeV^2, the behavior of $G_{\rho\rho\theta}(t)$ is similar to that of $G_{\rho\rho P}(t)$ and falls approximately exponentially with t_m.

The results from NFS η production, (6.2.2), are now presented. The data are shown in Fig. 6.5 for the different t bins and they have been fit to the form (6.2.3) with the ρ replaced by the A_2 and with the low mass resonance term estimated as described in Appendix 4.II. The fits were performed over the energy ranges indicated by

---

FIGURE 6.5 Data on $\pi^- p \to \eta X^0$ as a function of the energy of the η, E, in different t bins. The results of fits over the energy ranges E' - 96 GeV, where E' is listed in Column 2 of Table 6.2, are shown. The resulting values for α_{A_2} are shown on Fig. 6.6 and are listed in Table 6.2.

KEY

—— Final fit

– – – $A_2 A_2 \theta$ triple Regge contribution

····· Low mass resonances (estimated)

⬇ ⬇ Limits of fit

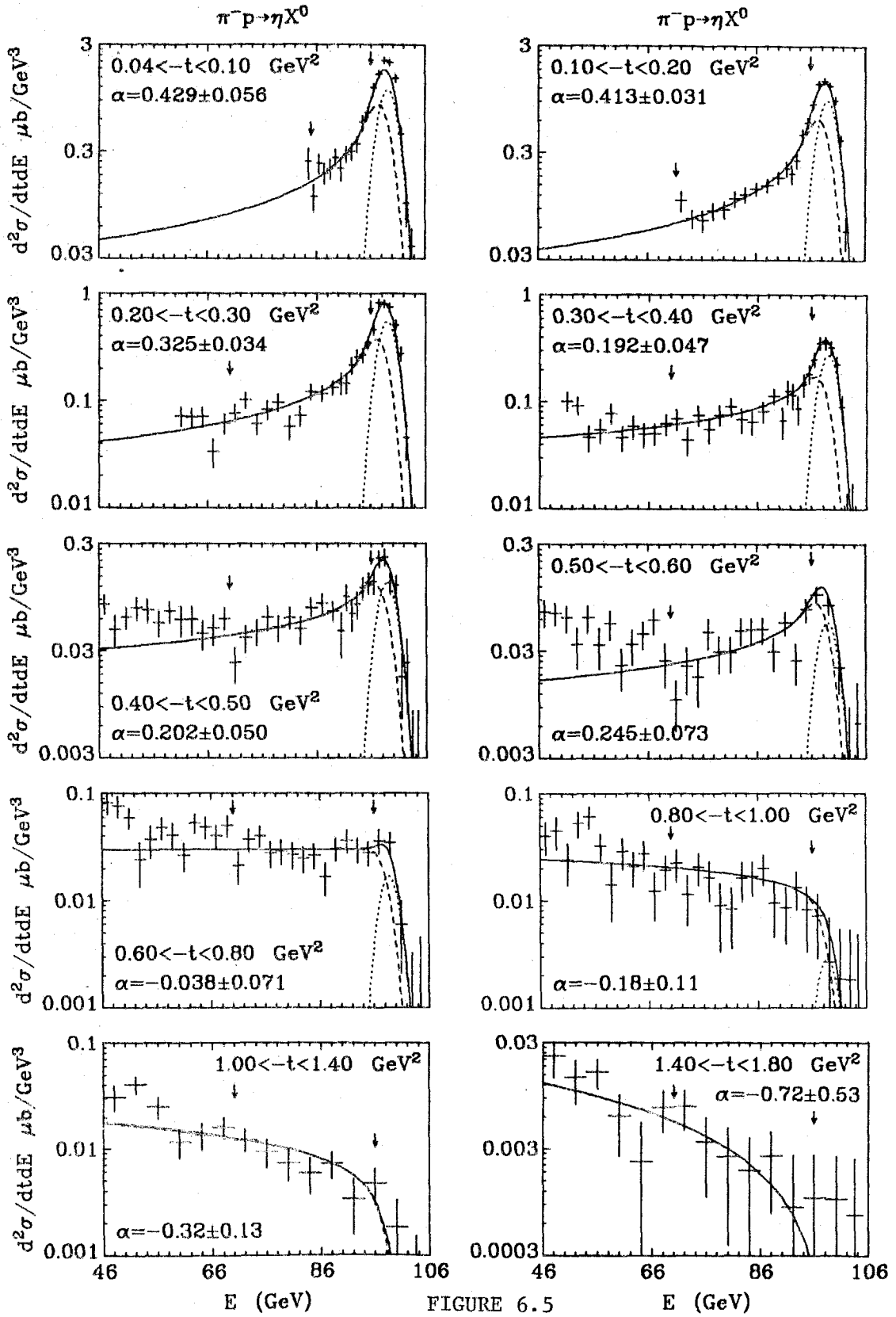
π⁻p→ηX⁰
0.04<−t<0.10 GeV²
α=0.429±0.056
0.10<−t<0.20 GeV²
α=0.413±0.031
0.20<−t<0.30 GeV²
α=0.325±0.034
0.30<−t<0.40 GeV²
α=0.192±0.047
0.40<−t<0.50 GeV²
α=0.202±0.050
0.50<−t<0.60 GeV²
α=0.245±0.073
0.60<−t<0.80 GeV²
α=−0.038±0.071
0.80<−t<1.00 GeV²
α=−0.18±0.11
1.00<−t<1.40 GeV²
α=−0.32±0.13
1.40<−t<1.80 GeV²
α=−0.72±0.53
d²σ/dtdE μb/GeV³
E (GeV)

FIGURE 6.5

TABLE 6.2. A_2 Regge trajectory, $\alpha_{A_2}(t)$, and residue function, $G_{A_2A_2\mathcal{P}}$, from fits to $\pi^- p \to \eta X^0$ data over the energy ranges listed.

		Fits over E' - 96 GeV		Fits over 50 - 96 GeV	
-t range	E'	α	G (μb/GeV^2)	α	G (μb/GeV^2)
0.04 - 0.10	85	0.429±0.056	2.30±0.14	-	-
0.10 - 0.20	71	0.413±0.031	2.27±0.10	-	-
0.20 - 0.30	70	0.325±0.034	2.57±0.12	-	-
0.30 - 0.40	70	0.192±0.047	2.54±0.16	0.161±0.032	3.92±0.33
0.40 - 0.50	70	0.202±0.050	2.50±0.18	0.079±0.038	4.27±0.42
0.50 - 0.60	70	0.245±0.073	1.98±0.21	0.075±0.058	2.55±0.37
0.60 - 0.80	70	-0.038±0.071	2.57±0.22	-0.183±0.050	5.55±0.54
0.80 - 1.00	70	-0.18 ±0.11	2.36±0.30	-0.292±0.077	4.36±0.61
1.00 - 1.40	70	-0.32 ±0.13	2.26±0.32	-0.570±0.093	5.88±0.82
1.40 - 1.80	70	-0.72 ±0.53	1.04±0.35	-0.68 ±0.26	2.32±0.73

the arrows and the resulting A_2 trajectory, $\alpha_{A_2}(t)$, is listed in Table 6.2 and shown on Fig. 6.6. As found for the full inclusive case in Section 5.2, the A_2 trajectory determined from the NFS data lies above the ρ trajectory determined from the NFS data, which is shown for comparison on Fig. 6.6. It is consistent with being a straight line, which lies just above that through the ρ and A_2, but is also consistent with a curve which flattens off at $t_m \approx 1$ GeV^2, as found for the other trajectories. Unfortunately the statistics on this reaction are rather limited. Fits were also performed over

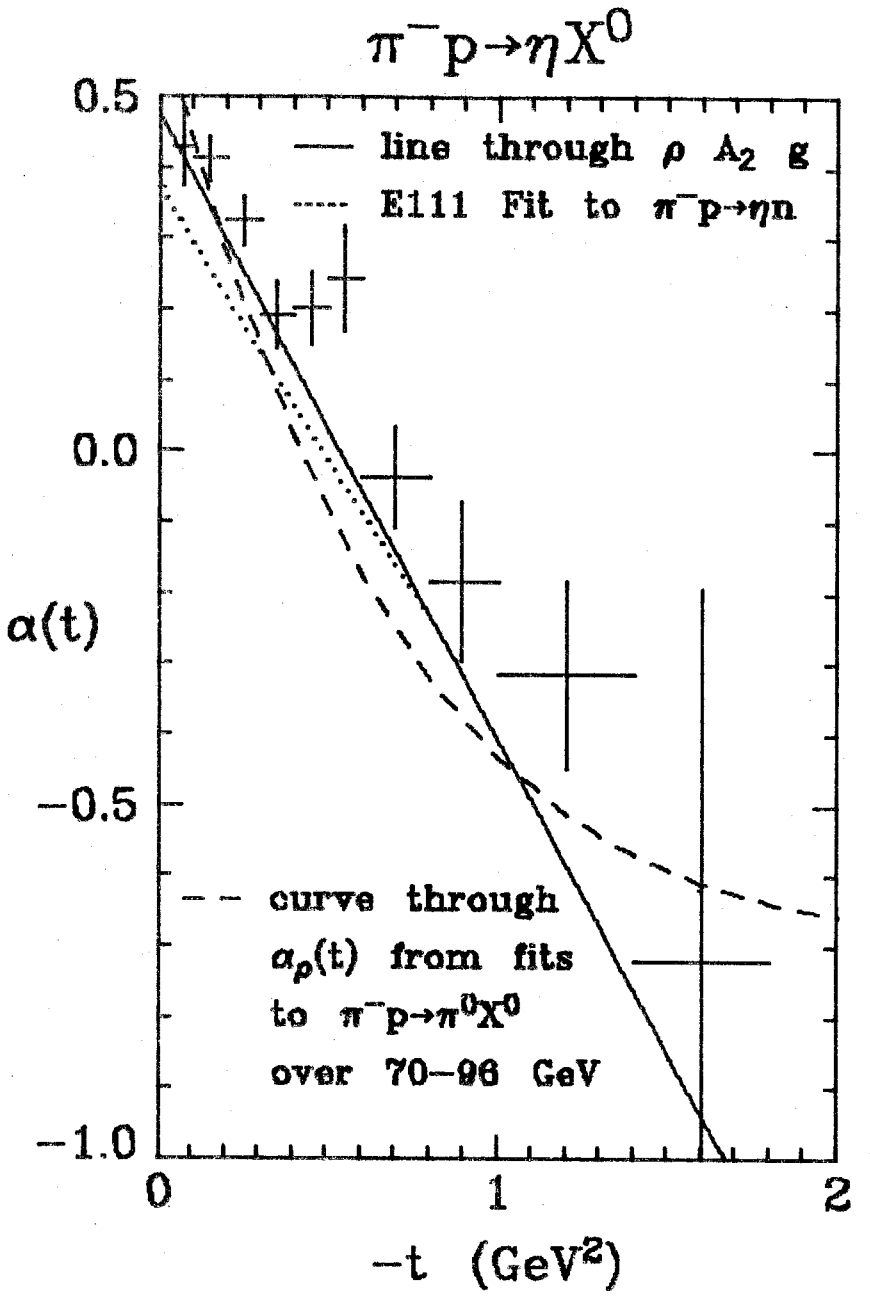

FIGURE 6.6 $\alpha_{A_2}(t)$ from fits to $\pi^- p \to \eta X^0$ over the energy ranges E' - 96 GeV, where E' is listed in Column 2 of Table 6.2. The curve through $\alpha_\rho(t)$ from NFS π^0 production, Fig. 6.3, given by (5.1.6) with (6.2.4) is shown for comparison.

the larger energy range, 50 - 96 GeV, and the results are listed in Table 6.2. It is seen that these fits gave a trajectory which is about 0.15 lower than that found from the fits over the higher energy range and this trajectory is in good agreement with the line through the ρ and A_2.

To find the residue function, $G_{A_2A_2\mathcal{P}}(t)$, from the data with 70 - 96 GeV, a second set of fits was again performed with the A_2 trajectory resulting from the first set of fits parameterized in the form (5.1.6) with

$$A = -0.50, \quad B = 0.98, \quad C = 0.49, \quad D = -0.69. \quad (6.2.7)$$

The resulting values for the residue function are shown on Fig. 6.4 and listed in Table 6.2. It is fairly flat and has no structure at the place where $G_{\rho\rho\mathcal{P}}(t)$ has its dip. For the fits over 50 - 96 GeV, the value for G listed in Table 6.2 is that arising from the same fits as solved for the trajectory. This residue function is higher but has no definite structure.

6.3 CROSS SECTIONS FOR NFS π^0 AND η PRODUCTION

In this section, the data presented in Section 6.2 for the NFS production of π^0 and η mesons from a π^- beam are shown as a function of t for various energy intervals. In Fig. 6.7 is shown the t-dependence of the cross sections for π^0 production, $\pi^- p \to \pi^0 X^0$, integrated over 10 GeV ranges in the π^0 energy, E, starting at 20 GeV. For clarity, the cross sections have been multiplied by powers of ten: 10, 10^2, 10^3, 10^4, 10^5, 10^6 and 10^7 for the energy ranges 80 - 90, 70 - 80, 60 - 70, 50 - 60, 40 - 50, 30 - 40 and 20 - 30 GeV respectively. For all the energy ranges, the cross sections peak at low t_m, although the peak becomes sharper with increasing energy. The cross section for energies above 90 GeV initially falls even faster with t_m than the cross section for the exclusive reaction, $\pi^- p \to \pi^0 n$, which is shown on Fig. 6.7 for comparison. In every energy bin there is also a distinct break of slope around $t_m \simeq 0.6$ GeV^2. Its location appears to increase slightly with energy. Unfortunately the t resolution and the lack of statistics prevent one from seeing any fine structure. For t_m above about 0.6 GeV^2, the cross sections become much flatter. The cross sections with $t_m < 1.5$ GeV^2 for the energy bins starting at 30 GeV were fit to the form (5.3.1) and the resulting value for the slope, B, was 1.47 ± 0.09 GeV^{-2}, which is a little flatter than that found for the full inclusive cross sections above 60 GeV. However it appears from Fig. 6.7 that all the energy bins agree with this universal slope, which

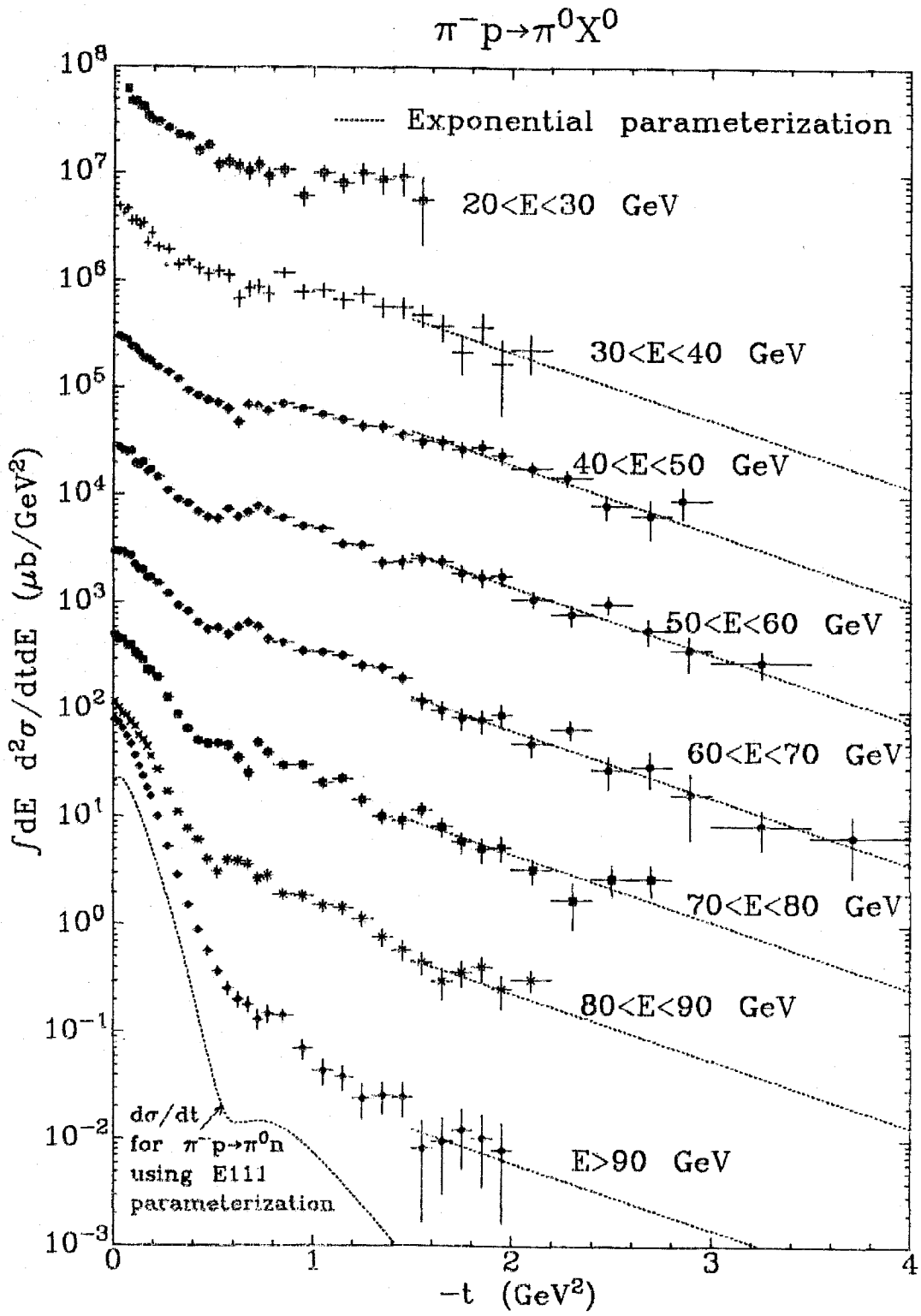

FIGURE 6.7 The t-dependence of the cross sections for $\pi^- p \to \pi^0 X^0$ over 10 GeV energy ranges. The text describes the presentation.

corresponds to triple Regge theory with a flat trajectory fitting all energies above 30 GeV, which is far larger than the expected range of the theory!

The t-dependence of the $\pi^- p \to \eta X^0$ cross sections are shown in Fig. 6.8. These are integrated over 10 GeV ranges in the η energy, E, starting at 50 GeV. Again the cross sections have been multiplied by powers of ten: 10, 10^2, 10^3 and 10^4 for the energy ranges 80 - 90, 70 - 80, 60 - 70 and 50 - 60 GeV respectively. The t-dependence is nearly exponential for every bin and there is no break of slope as found for the π^0 cross sections. The slope is similar for the four lowest energy bins but is steeper for the bin integrated over energies above 90 GeV. This bin has a slope similar to that of the cross section for $\pi^- p \to \eta n$, which is shown on Fig. 6.8 for comparison, but it is about four times its size.

The t-dependence of the NFS η/π^0 production ratio from pion beams is shown on Fig. 6.9. Two sets of points are shown: the points with diamonds and solid error bars are for the two cross sections integrated above 50 GeV and the points with crosses and dotted error bars are for the two cross sections integrated above 70 GeV. There is a peak at $t_m \simeq 0.5$ GeV^2 in both cases, which corresponds to the break in the slope of the π^0 cross section. The position of the peak moves from $t_m \simeq 0.4$ GeV^2 for the cross sections integrated above 50 GeV to 0.5 for those integrated above 70 GeV and this shift corresponds to the change in location of the break of slope in the cross

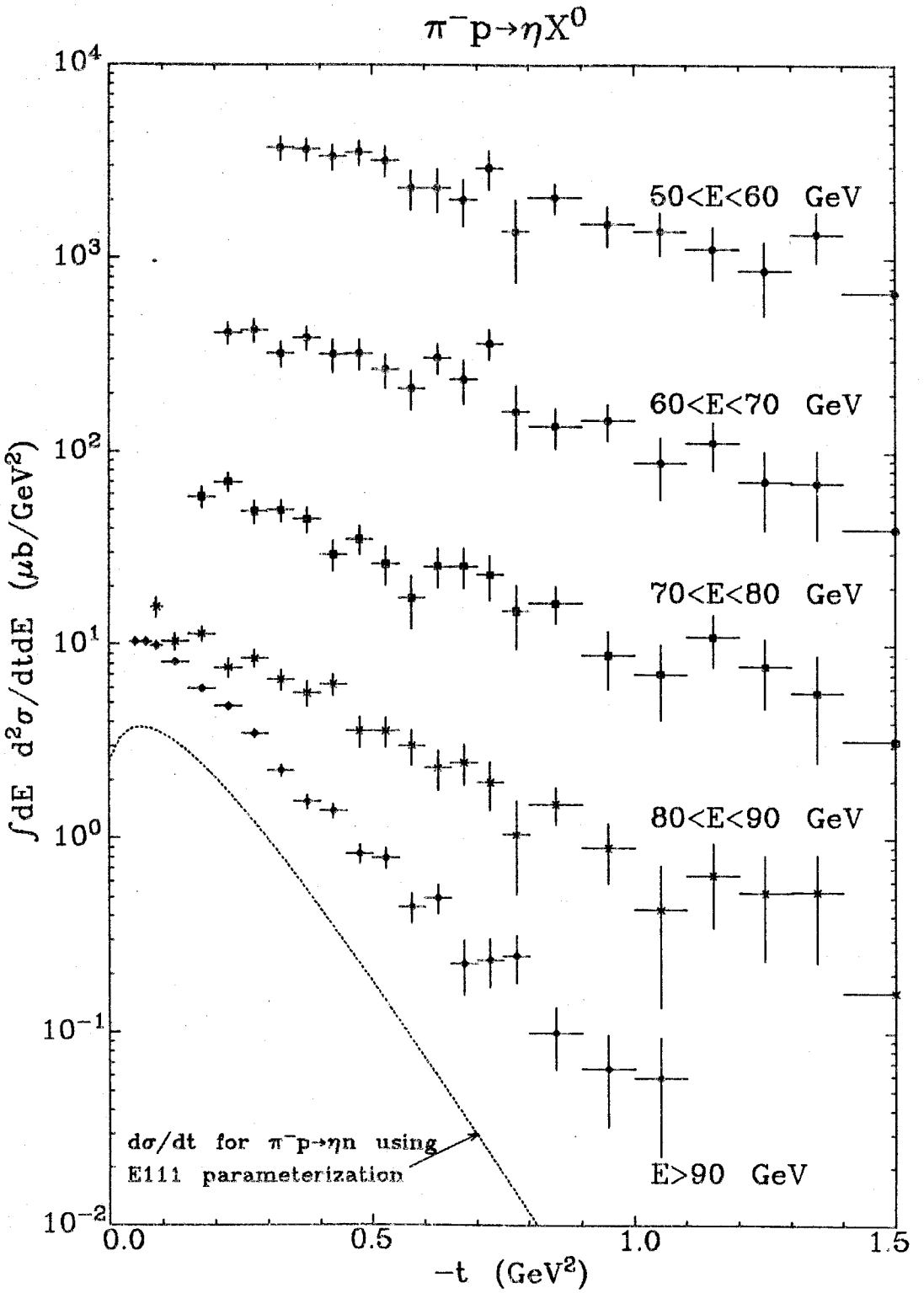

FIGURE 6.8 The t-dependence of the cross sections for $\pi^- p \to \eta X^0$ over 10 GeV energy ranges. The text describes the presentation.

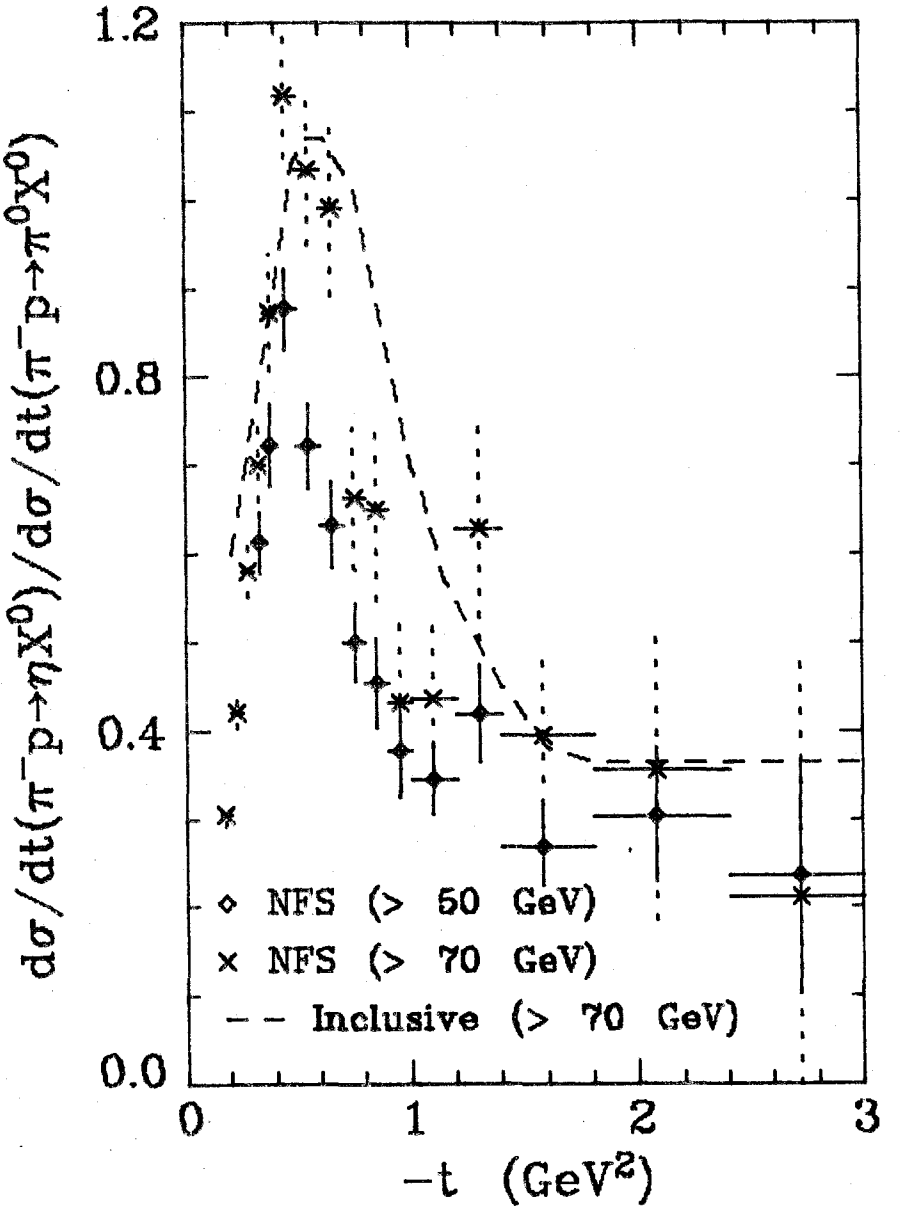

FIGURE 6.9 The ratio of the cross section for the NFS production of η mesons from a π^- beam to that for π^0 mesons integrated above energies of 50 GeV and 70 GeV. A curve representing the ratio of η to π^0 production from the full inclusive data with a π^- beam for energies above 70 GeV is shown for comparison.

sections shown on Fig. 6.7. A curve through the full inclusive η/π^0 ratio from a π^- beam for cross sections integrated above 70 GeV (from Fig. 5.9) is also shown on Fig. 6.9. The peak is wider than in the NFS case but otherwise the ratio is rather similar. For t_m above 1.5 GeV^2 the ratio is fairly flat with a value of about 0.3, which is a little lower than found for the full inclusive case.

The t-dependence of the ratio of the cross sections for NFS π^0 production to the cross sections for full inclusive π^0 production is shown in Fig. 6.10. The ratios for the cross sections integrated above energies of 60, 70, 80 and 90 GeV are shown separately. In all cases the ratio is fairly flat at low t_m and then falls rapidly until $t_m \simeq 0.5$ GeV^2, beyond which all the ratios are fairly flat. The ratio clearly decreases with the energy, as expected from the x-dependence predicted by the triple Regge model.

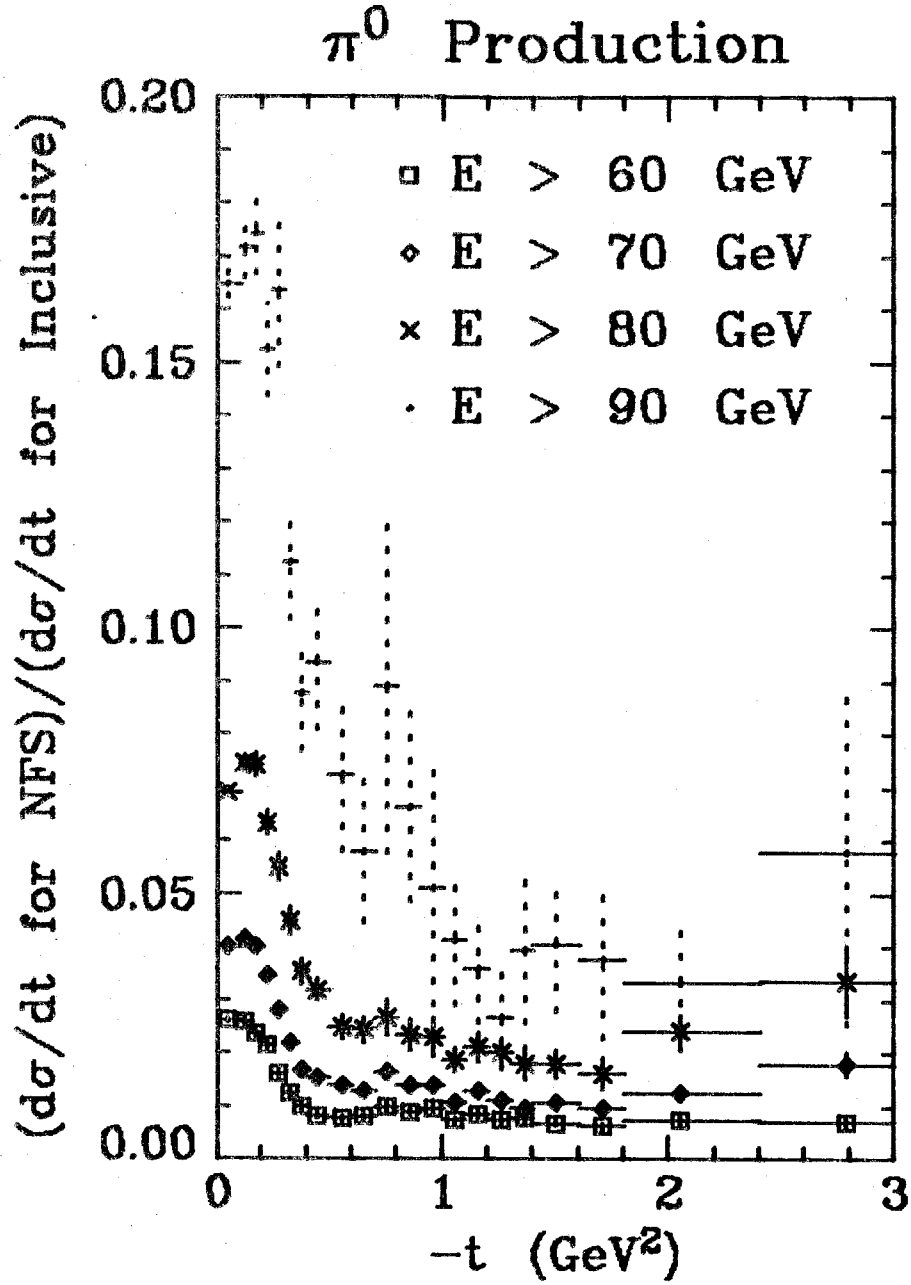

FIGURE 6.10 The t-dependence of the ratios of the cross section for the NFS production of π^0 mesons from a π^- beam, $\pi^- p \to \pi^0 X^0$, to the full inclusive production of π^0 mesons from a π^- beam, $\pi^- p \to \pi^0 X$, for the cross sections integrated above energies of 60, 70, 80 and 90 GeV.

CHAPTER 7

RESULTS FROM KAON, PROTON AND ANTIPROTON BEAMS

7.1 K* TRAJECTORIES AND RESIDUE FUNCTIONS

In this section, the results from the reactions,

$$K^- + p \to \pi^0 + X, \tag{7.1.1}$$

$$K^+ + p \to \pi^0 + X, \tag{7.1.2}$$

$$K^- + p \to \eta + X, \tag{7.1.3}$$

$$K^+ + p \to \eta + X, \tag{7.1.4}$$

are presented in the context of the triple Regge model. The acceptance-corrected data for π^0 production, (7.1.1,2), are shown in Fig. 7.1 as a function of the energy of the π^0, E, for different t bins. The energy-dependences of the K^- and K^+ data were fitted simultaneously for each t bin to the predictions of triple Regge theory, as discussed in Section 4.3. The isospin, I, = 3/2 exchange cross sections were subtracted out using the estimation based on a π exchange model described in Appendix 4.III. The low mass resonance term, which is present only for reaction (7.1.1), was subtracted out using an estimation of its cross section based on the lower energy data on Λ, $\Sigma(1192)$ and $\Sigma(1385)$ production in Ref. (Ch76), as described in Appendix 4.II.

Analyses of exclusive reactions have shown that the K*(892) trajectory, denoted K*, and the K*(1430) trajectory, denoted K**, are close together for negative t, as discussed later in this section, and so it was assumed that the effect of the K* and K** exchanges

could be summed into the exchange of one effective trajectory. If α_{K^*} denotes this trajectory, then the cross section due to its exchange is given by

$$\frac{d^2\sigma}{dtdx}(x,t,s) = G^{\pi}_{K^*K^*P}(t)(1-x)^{1-2\alpha_{K^*}(t)} + G^{\pi}_{K^*K^*R}(t)s^{-0.5}(1-x)^{0.5-2\alpha_{K^*}(t)}. \quad (7.1.5)$$

The first term in (7.1.5) describes exchanges with the Pomeron on the bottom leg of the triple vertex diagram and the second term describes exchanges with Reggeons, R, such as the f, ρ, ω and A_2 on the bottom leg. The form of $G^{\pi}_{K^*K^*P}$ in terms of the K* and K**

FIGURE 7.1 Data on $K^{\pm}p \to \pi^0 X$ as a function of the energy of the π^0, E, in different t bins. The results of fits to the K^- and K^+ data simultaneously over the energy range 80 - 96 GeV are shown. The resulting values for α are shown on Fig. 7.2 and are listed in Table 7.1.

KEY

—— Final fit

– – – K*K*P triple Regge contribution

— — K*K*R triple Regge contribution

····· Low mass resonances (estimated)

-·-·- I = 3/2 π exchange (estimated)

⬇ ⬇ Limits of fit

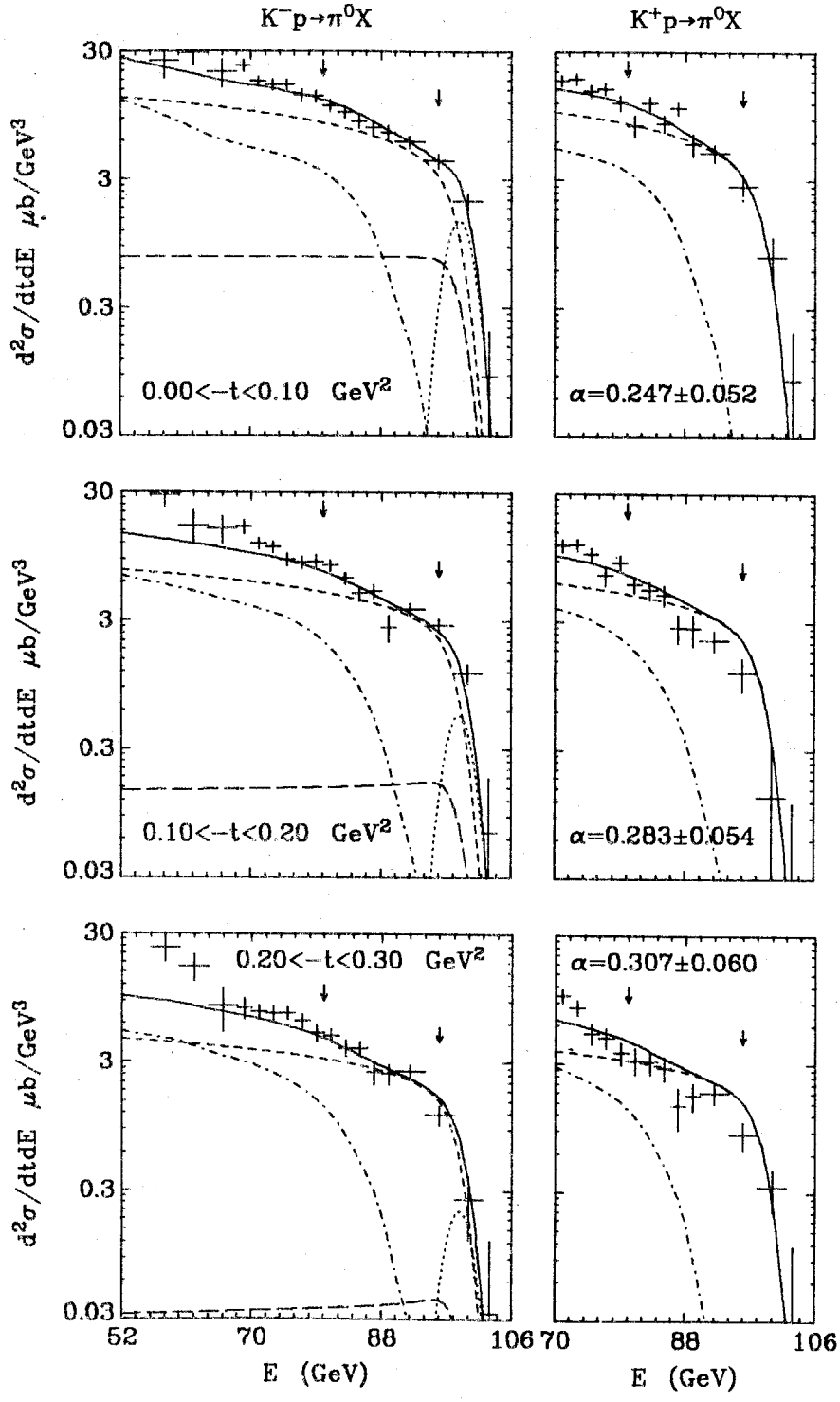
K⁻p→π⁰X
K⁺p→π⁰X
d²σ/dtdE μb/GeV³
30
3
0.3
0.03
0.00<−t<0.10 GeV²
α=0.247±0.052
0.10<−t<0.20 GeV²
α=0.283±0.054
0.20<−t<0.30 GeV²
α=0.307±0.060
52
70
88
106
E (GeV)

FIGURE 7.1(a)

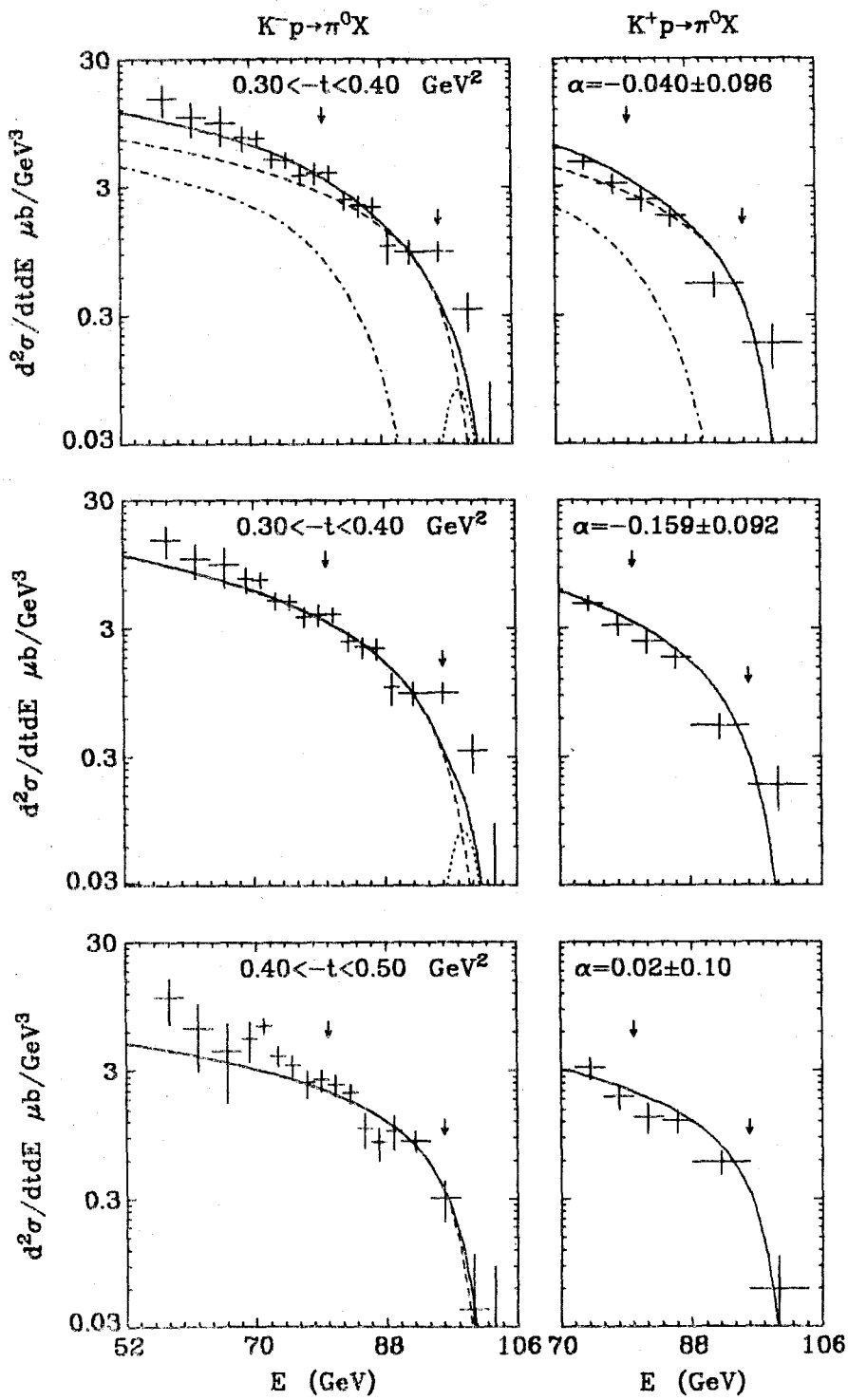
K⁻p→π⁰X
K⁺p→π⁰X
0.30<-t<0.40 GeV²
α=-0.040±0.096
0.30<-t<0.40 GeV²
α=-0.159±0.092
0.40<-t<0.50 GeV²
α=0.02±0.10
d²σ/dtdE μb/GeV³
30
3
0.3
0.03
52
70
88
106
E (GeV)

FIGURE 7.1(b)

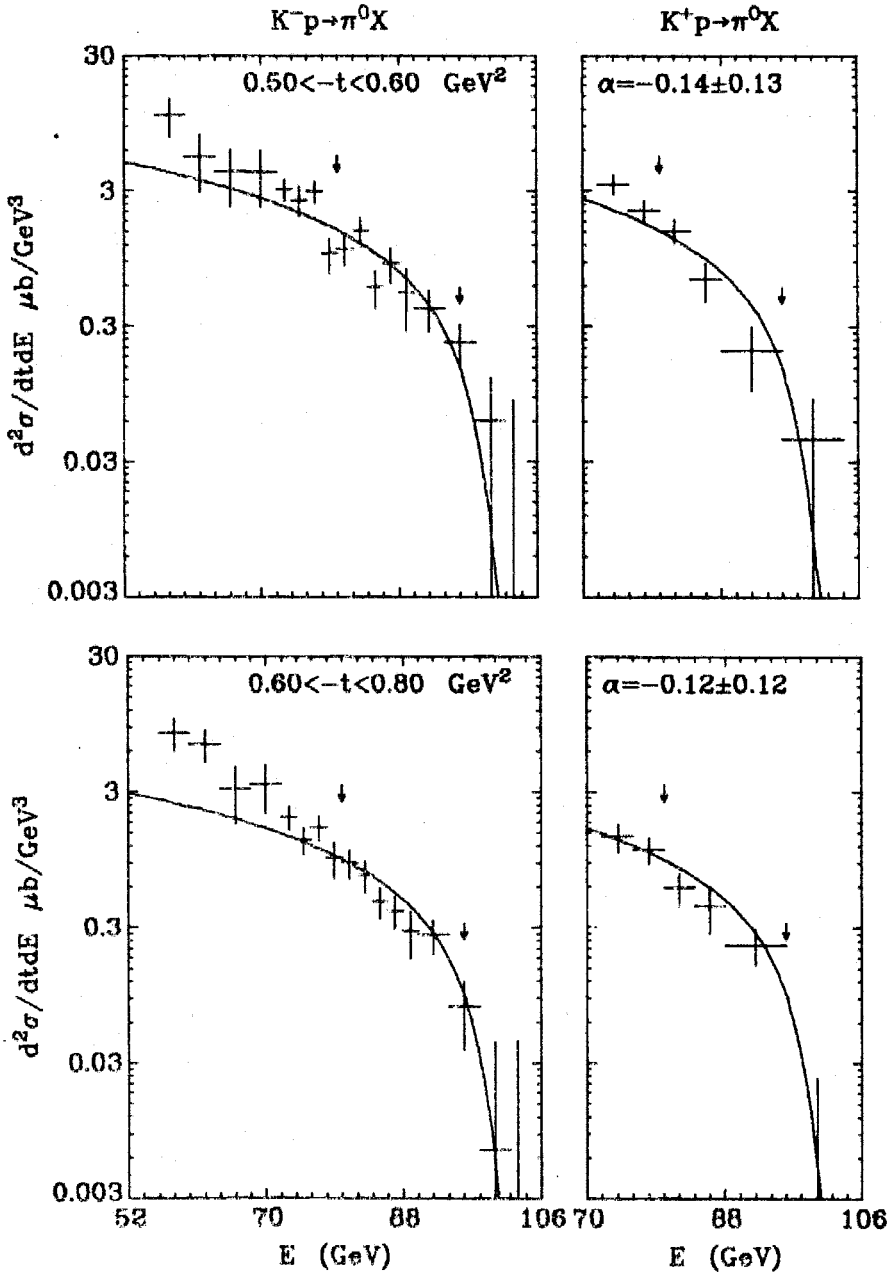
K⁻p→π⁰X
K⁺p→π⁰X
0.50<-t<0.60 GeV²
α=-0.14±0.13
0.60<-t<0.80 GeV²
α=-0.12±0.12
d²σ/dtdE μb/GeV³
30
3
0.3
0.03
0.003
52
70
88
106
E (GeV)

FIGURE 7.1(c)

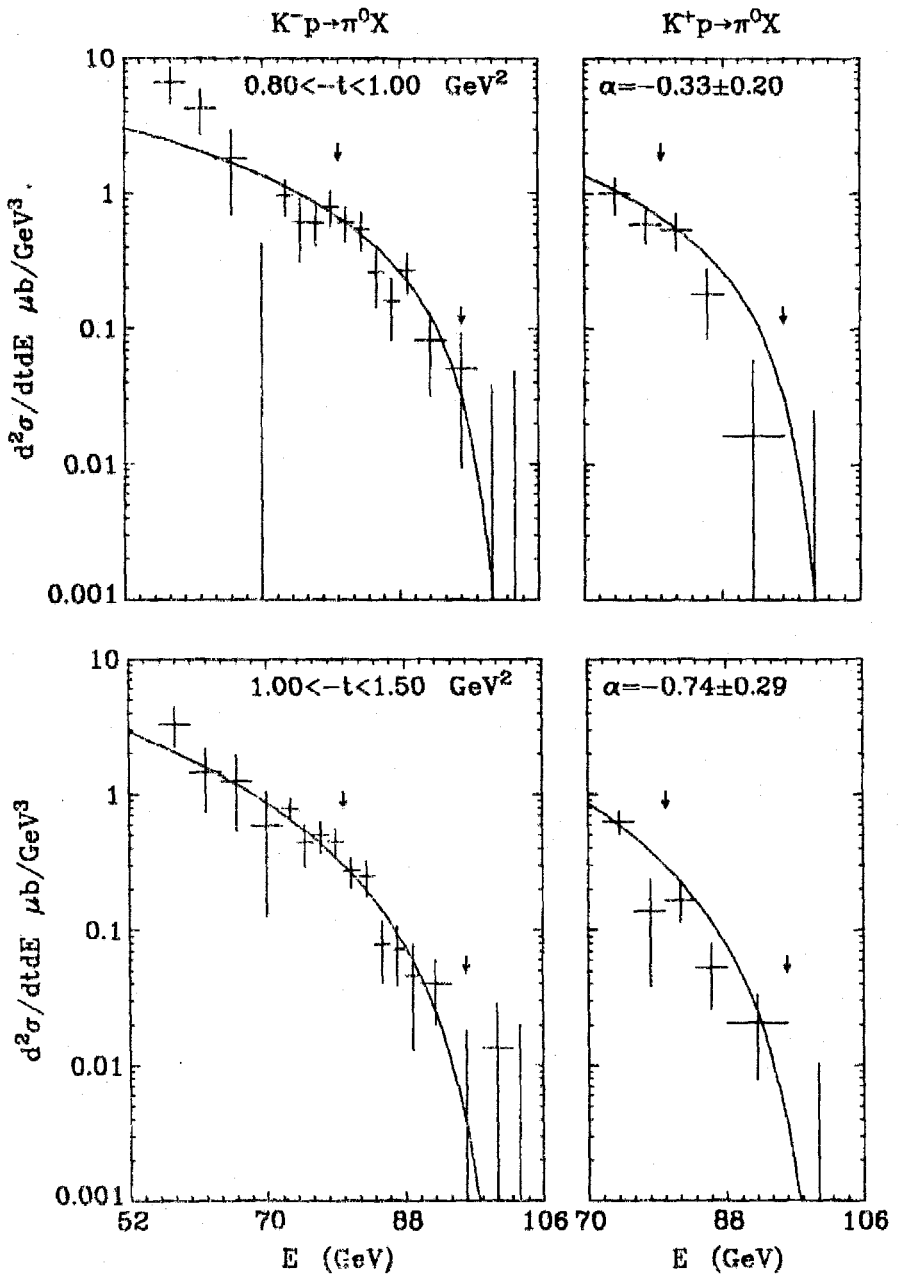
K⁻p→π⁰X
K⁺p→π⁰X
0.80<-t<1.00 GeV²
α=-0.33±0.20
1.00<-t<1.50 GeV²
α=-0.74±0.29
d²σ/dtdE μb/GeV³
10
1
0.1
0.01
0.001
52
70
88
106
E (GeV)

FIGURE 7.1(d)

couplings is clear from (4.3.11) and $G^{\pi}_{K^*K^*R}$ has an analogous expression with the Pomeron replaced by Reggeons. The Reggeon term is present only for the negative polarity beam, reaction (7.1.1), and in the fits $G^{\pi}_{K^*K^*R}$ was fixed using an estimation discussed in Appendix 4.I and was included only for $t_m < 0.5$ GeV^2 as its contribution becomes negligible at higher t_m.

The fits solved for the effective trajectory, $\alpha_{K^*}(t)$, and for the integrated cross section, as described in Section 5.1. They were performed over the energy range 80 - 96 GeV but the data at lower energies are shown on Fig. 7.1 for comparison. The results for the trajectory are shown on Fig. 7.2 as a function of t and the values are listed in Table 7.1. The I = 3/2 term has been subtracted from the data only for $t_m < 0.4$ GeV^2, since it was not known how to calculate it at higher t_m. For the bin with $0.3 < t_m < 0.4$ GeV^2, the results of fits without its subtraction are presented for comparison.

The three lowest mass K* mesons do not lie on a straight line on the Chew-Frautschi plot (Fig. 1.2) and so two lines are shown for comparison with the results on Fig. 7.2: the straight line through the K*(892) and the K*(1430), which has a slope of 0.8 GeV^{-2}, and the straight line through the K*(892) with a slope of 0.9 GeV^{-2}. The results agree better with the former line. Also shown on Fig. 7.2 are the K* and K** trajectories from the analysis in Ref. (Na76) of measurements of the exclusive processes, $\pi^- p \to K^0\Sigma^0$, $\pi^- p \to K^0\Lambda$, $\pi^+ p \to K^+\Sigma^+$, $K^- n \to \pi^-\Lambda$, $K^- p \to \pi^0\Lambda$ and $K^- p \to \pi^-\Sigma^+$ with $6 < s < 34$ GeV^2 and $0 < t_m < 1.5$ GeV^2. In this fit the trajectories were assumed to

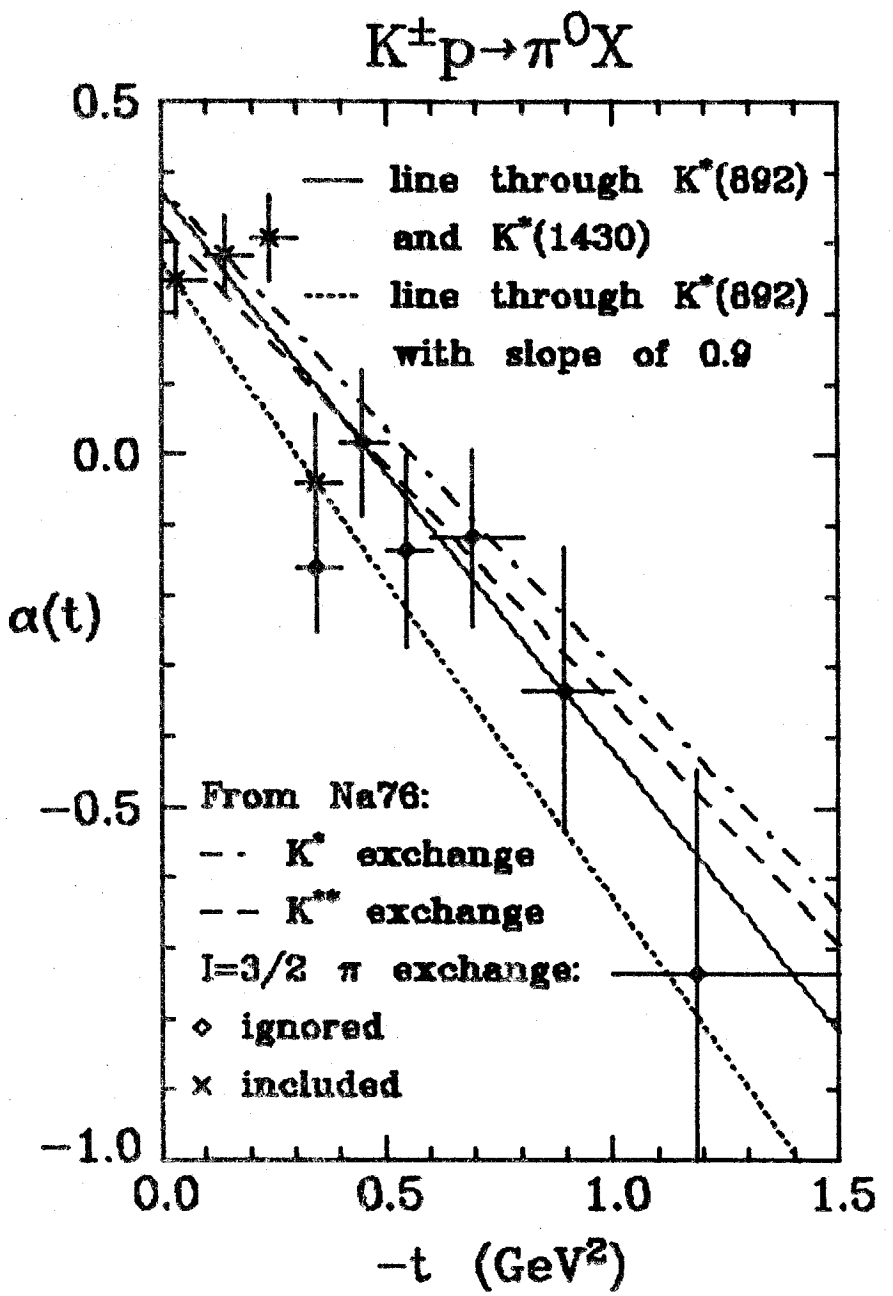

FIGURE 7.2 The effective trajectory, $\alpha_{K^*}(t)$, determined from the fits to $K^+p \rightarrow \pi^0 X$ over the energy range 80 - 96 GeV shown on Fig. 7.1. This is a combination of the K* and K** Regge trajectories, as described in the text. The various lines shown on the figure are also described in the text.

TABLE 7.1. Effective Regge trajectory, $\alpha_{K^*}(t)$, and residue function, $G^{\pi}_{K^*K^*p}(t)$, from fits to $K^{\pm}p \to \pi^0 X$ data over the energy ranges 80 - 96 GeV and 70 - 96 GeV. The I = 3/2 contribution has been subtracted from the first four entries.

	Fits over 80 - 96 GeV				Fits over 70 - 96 GeV	
	Standard		With Reggeon term doubled		Standard	
-t range	α	G (mb/GeV^2)	α	G (mb/GeV^2)	α	G (mb/GeV^2)
0.0 - 0.1	0.247±0.052	1.335±0.064	0.222±0.051	1.98 ±0.18	0.173±0.032	2.66 ±0.14
0.1 - 0.2	0.283±0.054	1.236±0.061	0.277±0.053	1.016±0.093	0.180±0.037	1.65 ±0.10
0.2 - 0.3	0.307±0.060	1.152±0.067	0.307±0.059	0.593±0.067	0.194±0.041	1.039±0.078
0.3 - 0.4	-0.040±0.096	0.955±0.071	-0.038±0.096	1.57 ±0.19	-0.034±0.061	1.52 ±0.14
0.3 - 0.4	-0.159±0.092	1.088±0.071	-0.158±0.092	2.91 ±0.29	-0.191±0.055	3.32 ±0.22
0.4 - 0.5	0.02 ±0.10	1.075±0.082	0.02 ±0.10	1.00 ±0.13	-0.187±0.066	2.40 ±0.21
0.5 - 0.6	-0.14 ±0.13	0.975±0.099			-0.340±0.092	2.93 ±0.29
0.6 - 0.8	-0.12 ±0.12	1.004±0.096			-0.201±0.079	1.07 ±0.11
0.8 - 1.0	-0.33 ±0.20	1.14 ±0.15			-0.31 ±0.12	0.94 ±0.14
1.0 - 1.5	-0.74 ±0.29	0.97 ±0.14			-0.83 ±0.15	2.58 ±0.34

be linear and to have the same slopes but different intercepts. The resulting trajectories were

$$\alpha_{K^*}(t) = 0.375 + 0.678t, \qquad (7.1.6a)$$

$$\alpha_{K^{**}}(t) = 0.322 + 0.678t. \qquad (7.1.6b)$$

More recent results on the reaction $\pi^+ p \to K^+\Sigma^+$ with $s = 140$ GeV^2 (Ar78) agreed with this analysis. The lines (7.1.6a,b) are close to the straight line through the K*(892) and K*(1430) for $0 < t_m < 1.5$ GeV^2. Thus the data from the present experiment are also in agreement with these trajectories.

A second fit was performed to extract the residue function, $G^{\pi}_{K^*K^*P}(t)$. $\alpha_{K^*}(t)$ was constrained by fitting a straight line to the results shown on Fig. 7.2, which gave

$$\alpha_{K^*}(t) = 0.350 + 0.79t. \qquad (7.1.7)$$

The resulting residue function is shown on Fig. 7.3 and its values are listed in Table 7.1. It falls slightly at low t_m but then becomes flat.

The sensitivity of these results to the Reggeon exchange contributions, namely the K*K*R and K**K**R triple Regge terms, was tested by doubling their normalization and refitting the data. The results are presented in Table 7.1. In this case the same fits solved for both the trajectory and the residue function. It is seen that the changes in α are generally small compared with the statistical errors. Fits were also performed over the energy range 70 - 96 GeV and the results are presented in Table 7.1. The resulting trajectory

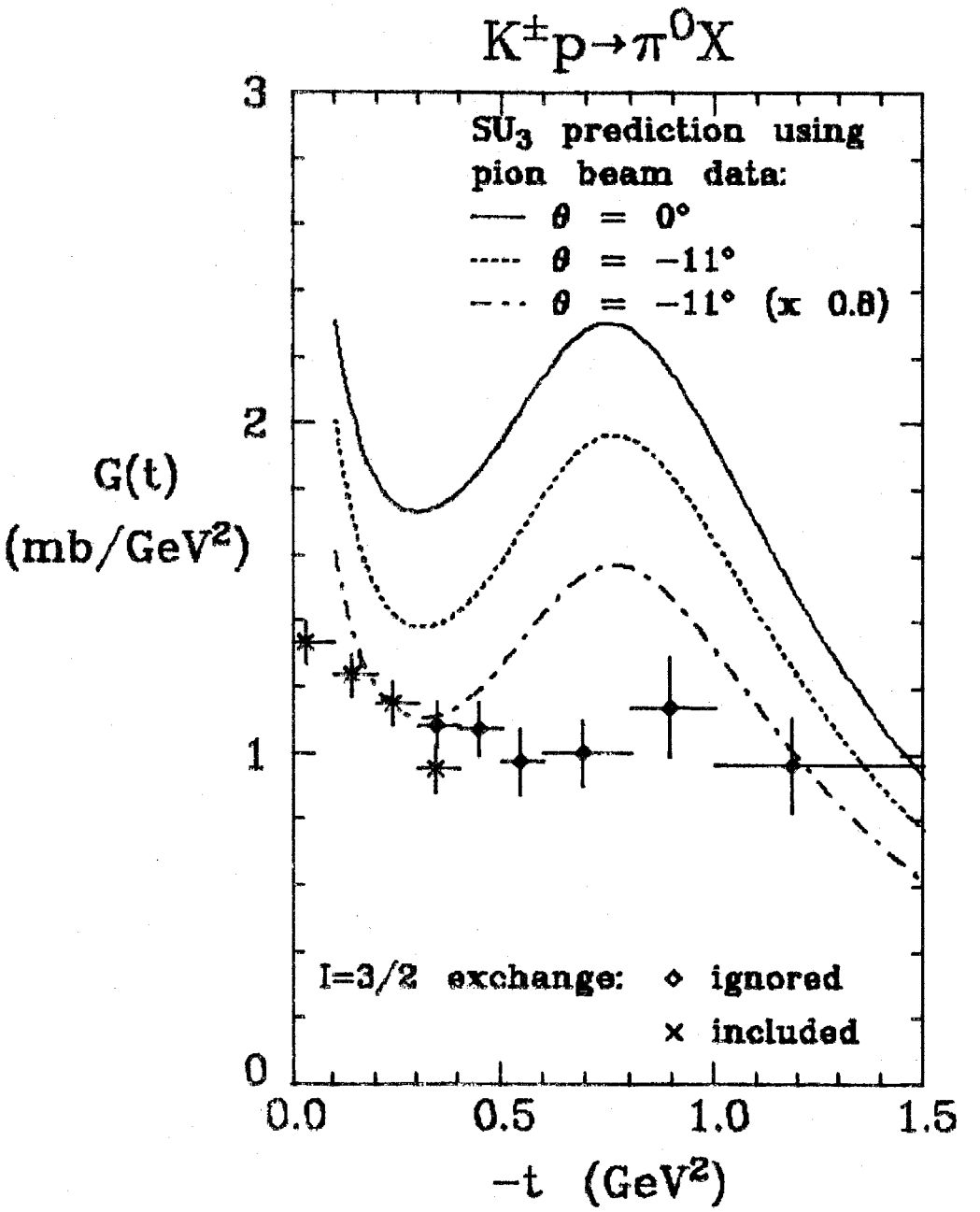

FIGURE 7.3 $G^{\pi}_{K^*K^*p}(t)$ from the fits to $K^{\pm}p \rightarrow \pi^0 X$ over 80 - 96 GeV described in the text. The curves are predictions made from the pion beam data on π^0 and η production with assumptions from SU_3 as explained in the text.

is up to 0.2 lower than that from the fits over 80 - 96 GeV and is generally about 0.1 lower. However it is seen from Figs. 7.1(a,b) that a large contribution to the cross section at low t_m for energies between 70 and 80 GeV comes from the I = 3/2 exchanges and so the trajectory may not be as well determined from these fits as suggested by the statistical errors alone.

It was difficult to obtain the normalizations for the kaon beam data, as discussed in Appendix 3.IX. In Table 3.IX.4 it is shown that the KAON beam fraction was only determined to 2% for the negative polarity beam and to 5% for the positive polarity beam. To test the sensitivity of α to these uncertainties in the normalizations, four additional sets of fits were performed, with the normalizations of the negative and positive polarity beam data changed by ±2% and ±5% respectively. In all cases and for all t bins, the change in α was much less than the statistical error. However it was found that the KAON fraction changed considerably with time (Ke79) and so each trigger type had to be normalized individually in practice, resulting in a much larger error than the 2% which arose from the total data set.

The data and the theoretical fits for η production from kaon beams, reactions (7.1.3) and (7.1.4), are shown in Fig. 7.4. The low mass resonance cross section due to the reaction $K^- p \to \eta\Lambda$ was subtracted out using an estimate of its cross section derived from the lower energy data, as described in Appendix 4.II. The remaining cross section was fit to the form (7.1.5) with the superscript π

replaced by an η and $\alpha_{K^*}(t)$ and the integrated cross section were solved for. The fits were performed over the energy range 70 - 96 GeV as there were insufficient data above 80 GeV. The resulting trajectory is shown on Fig. 7.5 and listed in Table 7.2. Again the extracted trajectory agrees well with the straight line through the K*(892) and the K*(1430) and with the results in Ref. (Na76).

A second fit was performed to extract the residue function, $G^{\eta}_{K^*K^*P}(t)$. $\alpha_{K^*}(t)$ was constrained by fitting a straight line to the results shown on Fig. 7.5. This gave

$$\alpha_{K^*}(t) = 0.377 + 0.63t. \qquad (7.1.8)$$

The resulting residue function is shown on Fig. 7.6 and its values are listed in Table 7.2. It falls with t_m for $t_m < 1$ GeV^2.

FIGURE 7.4 Data on $K^+p \to \eta X$ as a function of the energy of the η, E, in different t bins. The results of fits to the K^- and K^+ data simultaneously over 70 - 96 GeV are shown. The resulting values for α are shown on Fig. 7.5 and are listed in Table 7.2.

KEY

—— Final fit

– – – K*K*P triple Regge contribution

— — — K*K*R triple Regge contribution

····· Low mass resonances

⬇ ⬇ Limits of fit

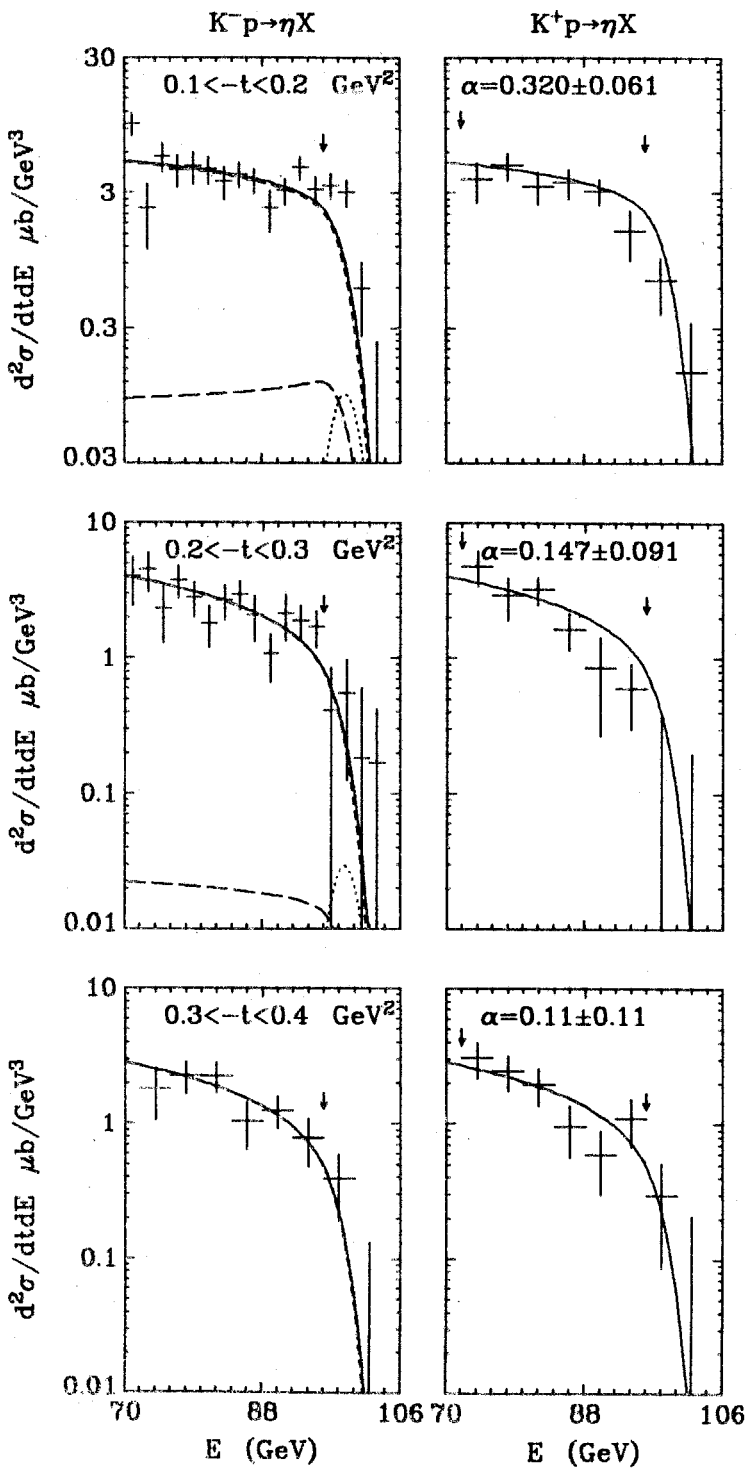
K⁻p→ηX
K⁺p→ηX
0.1<-t<0.2 GeV²
α=0.320±0.061
0.2<-t<0.3 GeV²
α=0.147±0.091
0.3<-t<0.4 GeV²
α=0.11±0.11
d²σ/dtdE μb/GeV³
30
3
0.3
0.03
10
1
0.1
0.01
70
88
106
E (GeV)

FIGURE 7.4(a)

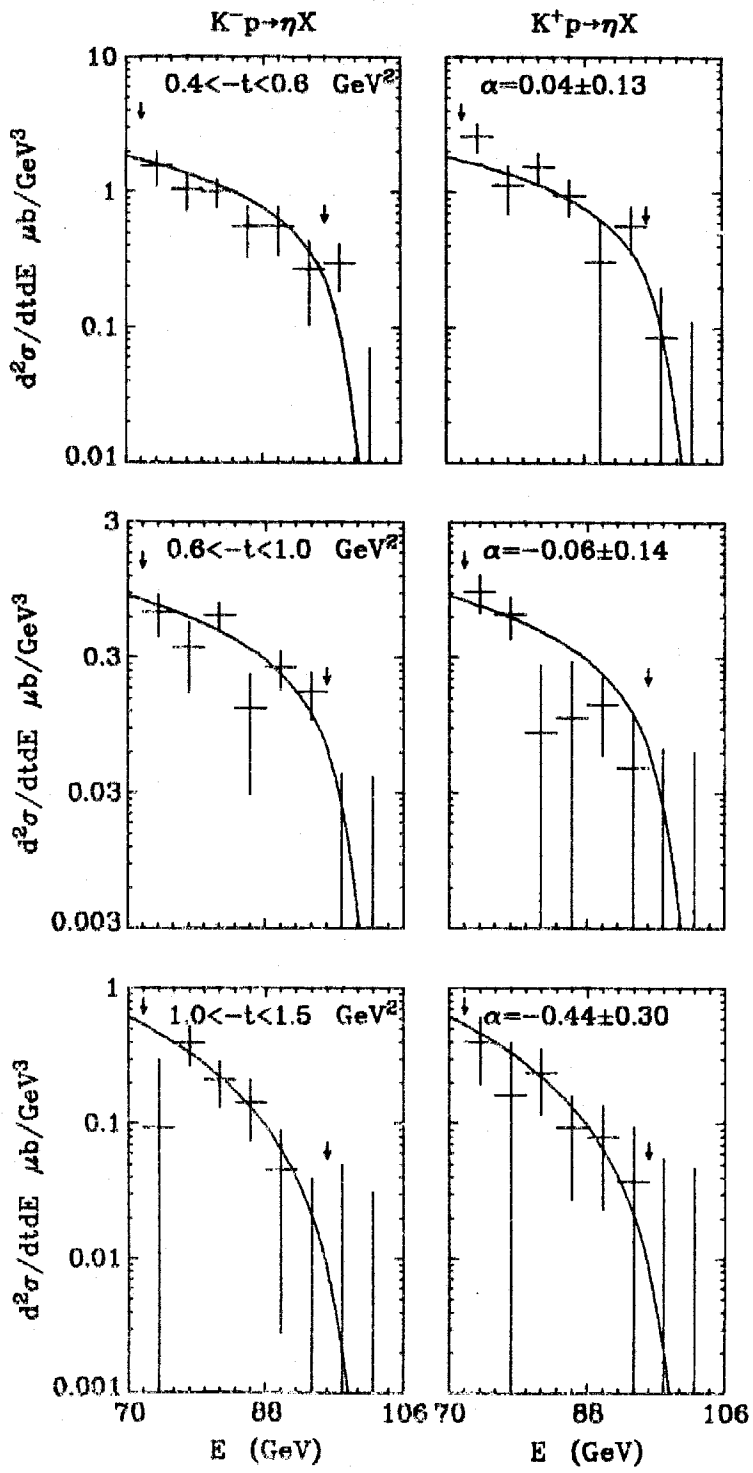
K⁻p→ηX
K⁺p→ηX
0.4<-t<0.6 GeV²
α=0.04±0.13
0.6<-t<1.0 GeV²
α=-0.06±0.14
1.0<-t<1.5 GeV²
α=-0.44±0.30
d²σ/dtdE μb/GeV³
E (GeV)
10
1
0.1
0.01
3
0.3
0.03
0.003
1
0.1
0.01
0.001
70
88
106

FIGURE 7.4(b)

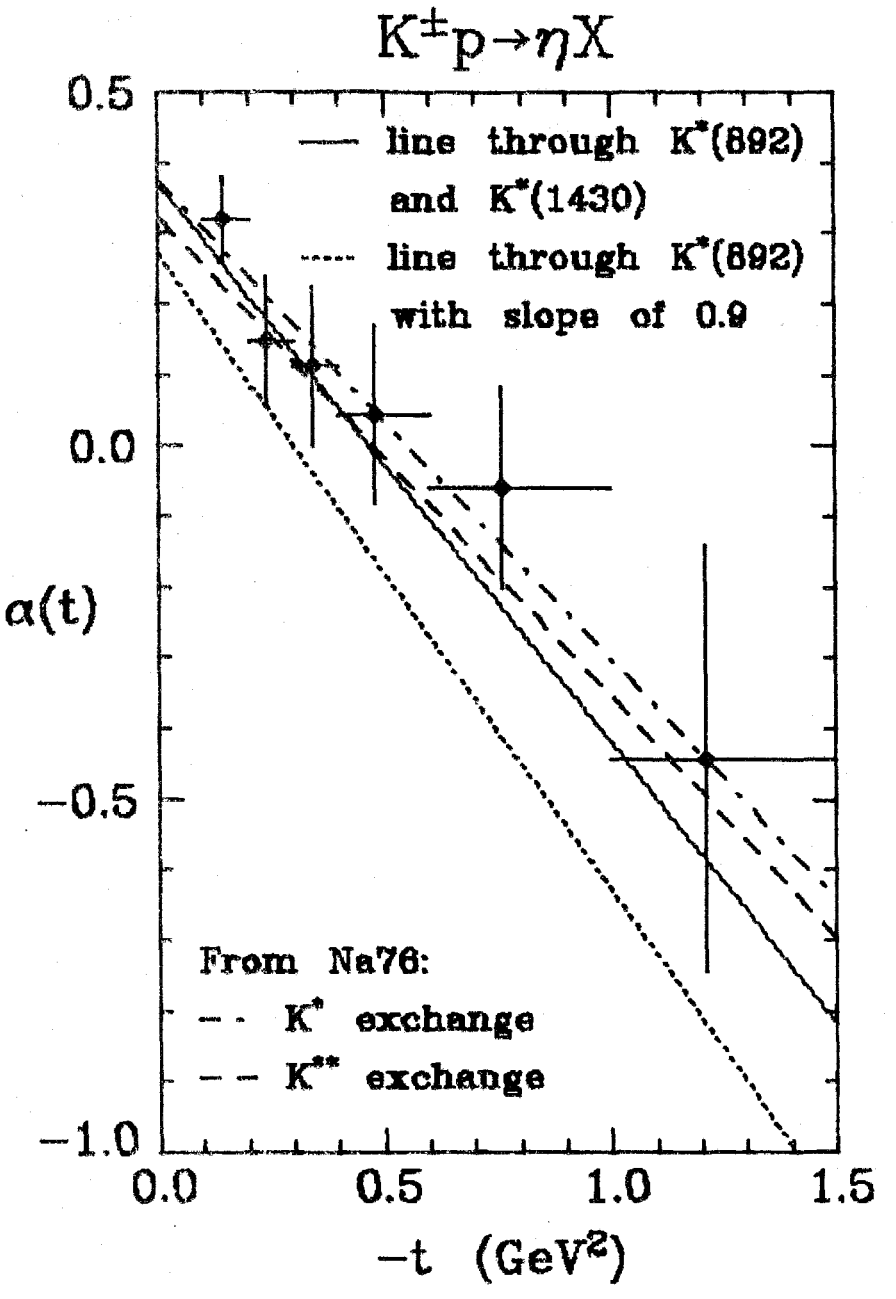

FIGURE 7.5 The effective trajectory, $\alpha_{K^*}(t)$, determined from the fits to $K^{\pm}p \rightarrow \eta X$ over the energy range 70 - 96 GeV shown on Fig. 7.4. This is a combination of the K* and K** Regge trajectories, as described in the text. The various lines shown on the figure are also described in the text.

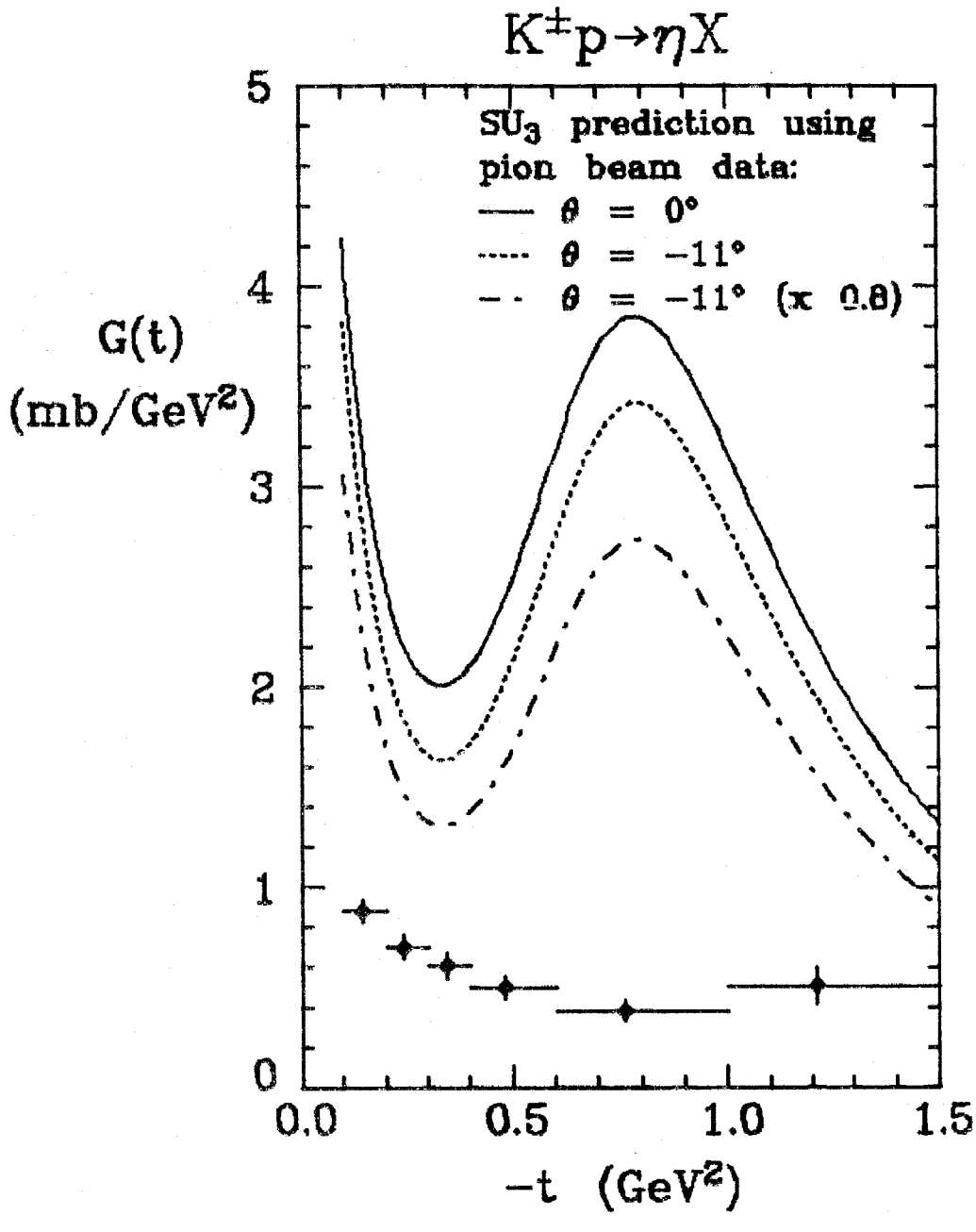

FIGURE 7.6 $G^{\eta}_{K*K*P}(t)$ from the fits to $K^{\pm}p \rightarrow \eta X$ over 70 - 96 GeV described in the text. The curves are predictions made from the pion bea beam data on π^0 and η production with assumptions from SU_3 as explained in the text.

TABLE 7.2. Regge trajectory, $\alpha_{K^*}(t)$, and residue function, $G^{\eta}_{K^*K^*P}(t)$, from fits to the $K^+p \to \eta X$ data over the energy range 70 - 96 GeV.

-t range	α	G (mb/GeV^2)
0.1 - 0.2	0.320 ± 0.061	0.886 ± 0.055
0.2 - 0.3	0.147 ± 0.091	0.704 ± 0.058
0.3 - 0.4	0.11 ± 0.11	0.606 ± 0.062
0.4 - 0.6	0.04 ± 0.13	0.501 ± 0.052
0.6 - 1.0	-0.06 ± 0.14	0.383 ± 0.051
1.0 - 1.5	-0.44 ± 0.30	0.507 ± 0.093

It is of interest to use the SU_3 relationships described in Section 4.3 to relate the kaon beam data to the pion beam data. Equations (4.3.11-14) give the cross sections for π^0 and η production for the triple vertex diagrams with Pomerons on the bottom leg. To make use of these, an estimate of the ratio D'(t)/D(t) is needed and this was obtained from comparing η and η' production. The results from the NICE detector at Serpukhov (Ap79a) show that

$$\frac{d\sigma}{dt}(\pi^- p \to \eta' n) = (0.55 \pm 0.10)\frac{d\sigma}{dt}(\pi^- p \to \eta n), \qquad (7.1.9)$$

where the error in the ratio is composed of a 10% statistical error and a 15% error in the branching ratio. The result was obtained with 25 and 40 GeV beams and the ratio may fall slightly with t_m, but (7.1.9) is a good approximation for $t_m < 0.6$ GeV^2. Results from E111 summed over incident momenta between 20 and 200 GeV gave a ratio of 0.5 with a large error (Ba79). These results have both assumed a

branching ratio of 0.025 for $\eta' \to \gamma\gamma$ (PD78). Using SU_3, the cross sections for exclusive η and η' production are given by

$$\frac{d\sigma}{dt}(\pi^- p \to \eta n) \propto (\cos\theta D(t) - \sqrt{2}\sin\theta D'(t))^2 s^{2\alpha_{A_2}(t) - 2}, \quad (7.1.10a)$$

$$\frac{d\sigma}{dt}(\pi^- p \to \eta' n) \propto (\sin\theta D(t) + \sqrt{2}\cos\theta D'(t))^2 s^{2\alpha_{A_2}(t) - 2}, \quad (7.1.10b)$$

with the same constant of proportionality in the two cases. Using $\theta = -11^\circ$ (PD78), this gives

$$\frac{D'}{D} = -0.34 \pm 0.04 \text{ or } 0.77 \pm 0.07, \quad (7.1.11)$$

where the error includes the statistical error and the error in the branching ratio. The value used here is 0.77 since this solution is closer to the value of 1 given by the simple quark model (Al66). It also agrees with the value obtained at $s = 8$ GeV^2 and low t_m using $d\sigma/dt$ for the reactions $K^- p \to \pi^0\Lambda$, $\eta\Lambda$ and $\eta'\Lambda$ (Ma77).

Equations (4.3.11-14) can now be used to relate the kaon beam reactions to the pion beam reactions. Using the above values and assuming that the signature factors and couplings for members of the same octets are the same, so that $|\xi_{K^*}| = |\xi_\rho|$, $|\xi_{K^{**}}| = |\xi_{A_2}|$, $\gamma_{K^*K^*P} = \gamma_{\rho\rho P}$ and $\gamma_{K^{**}K^{**}P} = \gamma_{A_2A_2P}$, gives

$$G^{\pi}_{K^*K^*P}(t) = 0.25 G_{\rho\rho P}(t) + (0.53 \pm 0.02) G_{A_2A_2P}(t), \quad (7.1.12)$$

$$G^{\eta}_{K^*K^*P}(t) = 0.72 G_{\rho\rho P}(t) + (0.057 \pm 0.009) G_{A_2A_2P}(t), \quad (7.1.13)$$

where the error is due to the error in D'/D. The π^0 production from

kaon beams clearly comes more from K** exchange than from K* exchange whilst the η production is clearly dominated by K* exchange. On Figs. 7.3 and 7.6 are shown the predictions (7.1.12) and (7.1.13) respectively. It is seen that the agreement is fairly good for the π^0 production but poor for the η production. Also shown for comparison are the results for $\theta = 0^0$, that is, when the η is pure octet, η_8. In this case the result is independent of the value of D' and gives

$$G^{\pi}_{K^*K^*P}(t) = 0.25G_{\rho\rho P}(t) + 0.75G_{A_2A_2P}(t), \qquad (7.1.14)$$

$$G^{\eta}_{K^*K^*P}(t) = 0.75G_{\rho\rho P}(t) + 0.25G_{A_2A_2P}(t) \qquad (7.1.15)$$

These predictions clearly agree less well with the data in both cases. If the assumption from SU_3 that $\gamma_{K^*K^*P} = \gamma_{\rho\rho P}$ and $\gamma_{K^{**}K^{**}P} = \gamma_{A_2A_2P}$ is removed and instead it is assumed that

$$\frac{\gamma_{K^*K^*P}}{\gamma_{\rho\rho P}} = \frac{\gamma_{K^{**}K^{**}P}}{\gamma_{A_2A_2P}} = \frac{\sigma^P_{tot}(K^-p)}{\sigma^P_{tot}(\pi^-p)} \simeq 0.8, \qquad (7.1.16)$$

where just the total cross section due to Pomeron exchange (PD78) is used, then the predictions of (7.1.12,13) are reduced by 0.8 and agree better with the data. It should also be noted that the ratio D'/D depends on t and has only been determined at low values of t.

7.2 CROSS SECTIONS FROM KAON BEAMS

In this section, the data presented in Section 7.1 for π^0 and η production from kaon beams are shown as a function of t for various energy intervals. In Figs 7.7 and 7.8 are shown the cross sections for $K^- p \to \pi^0 X$ and $K^+ p \to \pi^0 X$ in 10 GeV energy bins. The cross sections fall exponentially for every energy interval. The ratios of the cross sections from the K^+ beam to those from the K^- beam integrated over t are 0.96 ± 0.04, 0.86 ± 0.04 and 0.60 ± 0.05 for the energy bins 70 - 80 GeV, 80 - 90 GeV and above 90 GeV respectively. The fall of the ratio with energy is due to the presence of the Reggeon exchange term and the low mass resonance term in the K^- beam cross section, as described in the previous section.

The ratio of the cross sections for the production of π^0 mesons with energies above 70 GeV from a K^- beam to that from a π^- beam is shown in Fig. 7.9. It is clearly harder to produce π^0 mesons from a kaon beam than from a pion beam. A ratio of 0.5 is predicted from the naïve quark model due to the presence of a strange quark in the kaon, whilst hard-scattering models such as the CIM model would predict a ratio below 0.5. The ratio clearly reflects the change in slope of the π^- beam cross section, since it rises rapidly from 0.1 to 0.5 at $t_m \simeq 0.5$ GeV^2 and then falls to 0.2 at $t_m \simeq 1.5$ GeV^2. The results for $t_m \simeq 1$ GeV^2 are in agreement with those of E268 in which the same detector was used but the trigger required the presence of a particle with high transverse momentum (Do78c).

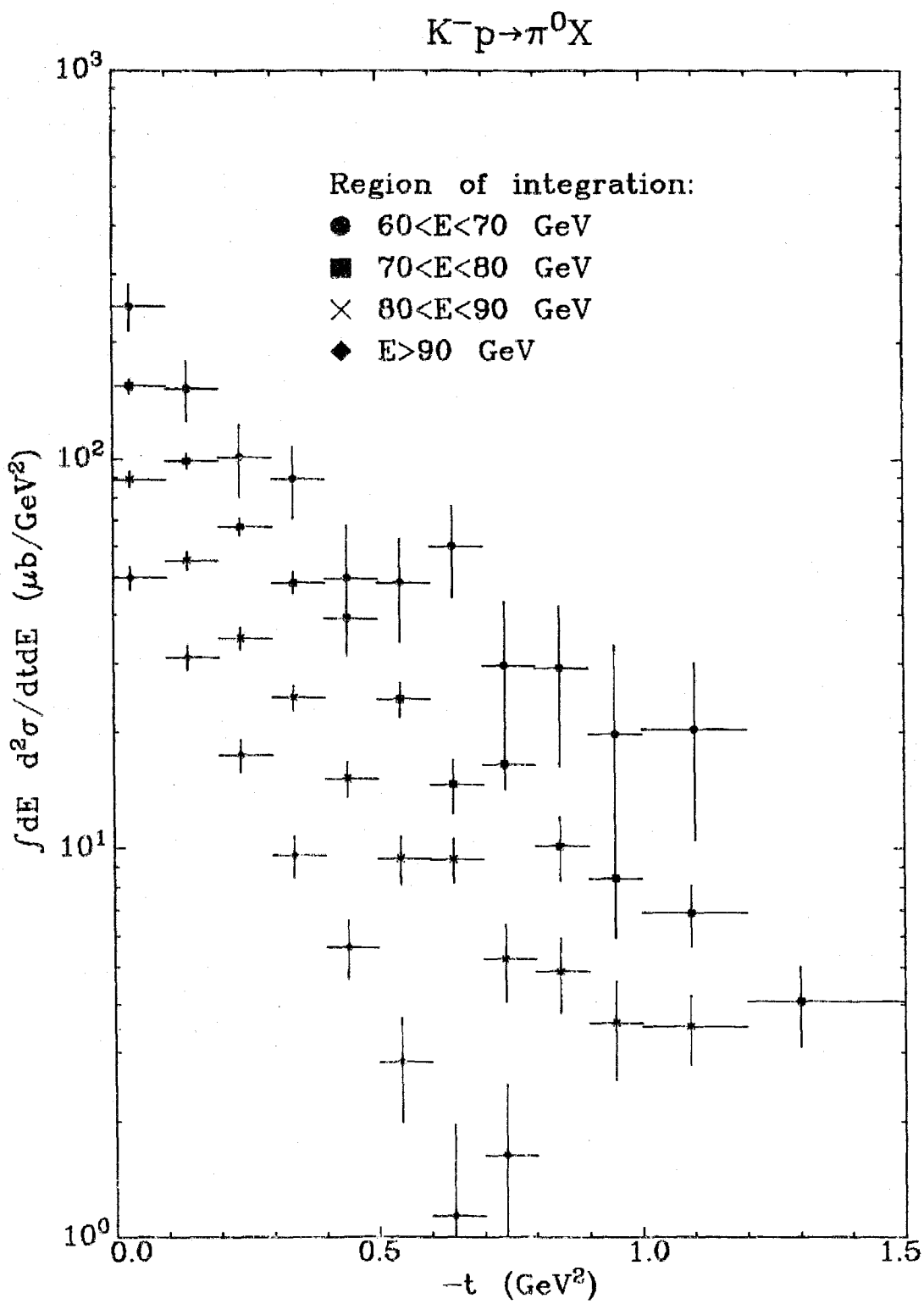

FIGURE 7.7 The t-dependence of the cross sections for $K^-p \to \pi^0 X$ integrated over 10 GeV ranges in the π^0 energy, E.

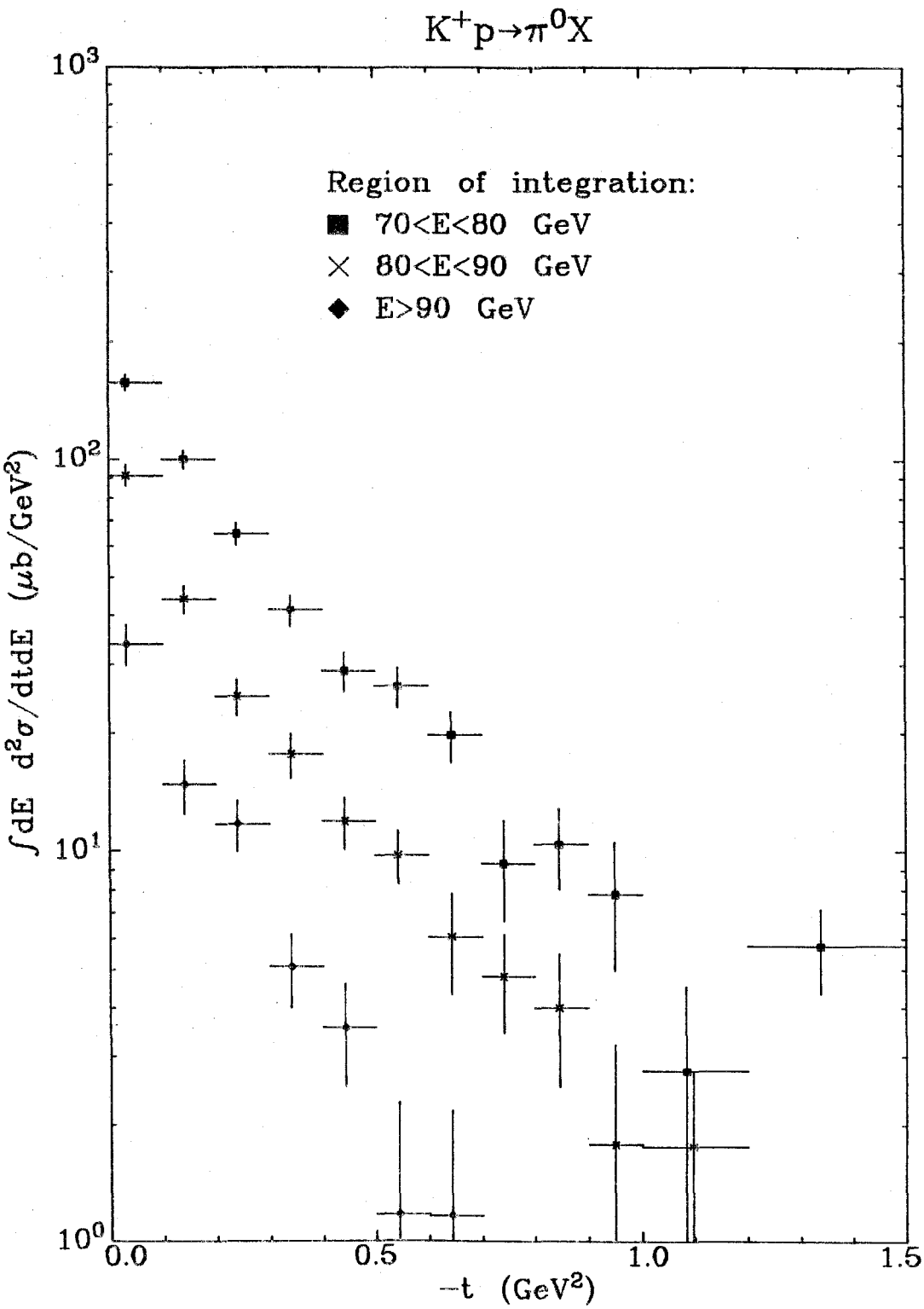

FIGURE 7.8 The t-dependence of the cross sections for $K^+p \to \pi^0 X$ integrated over 10 GeV ranges in the π^0 energy, E.

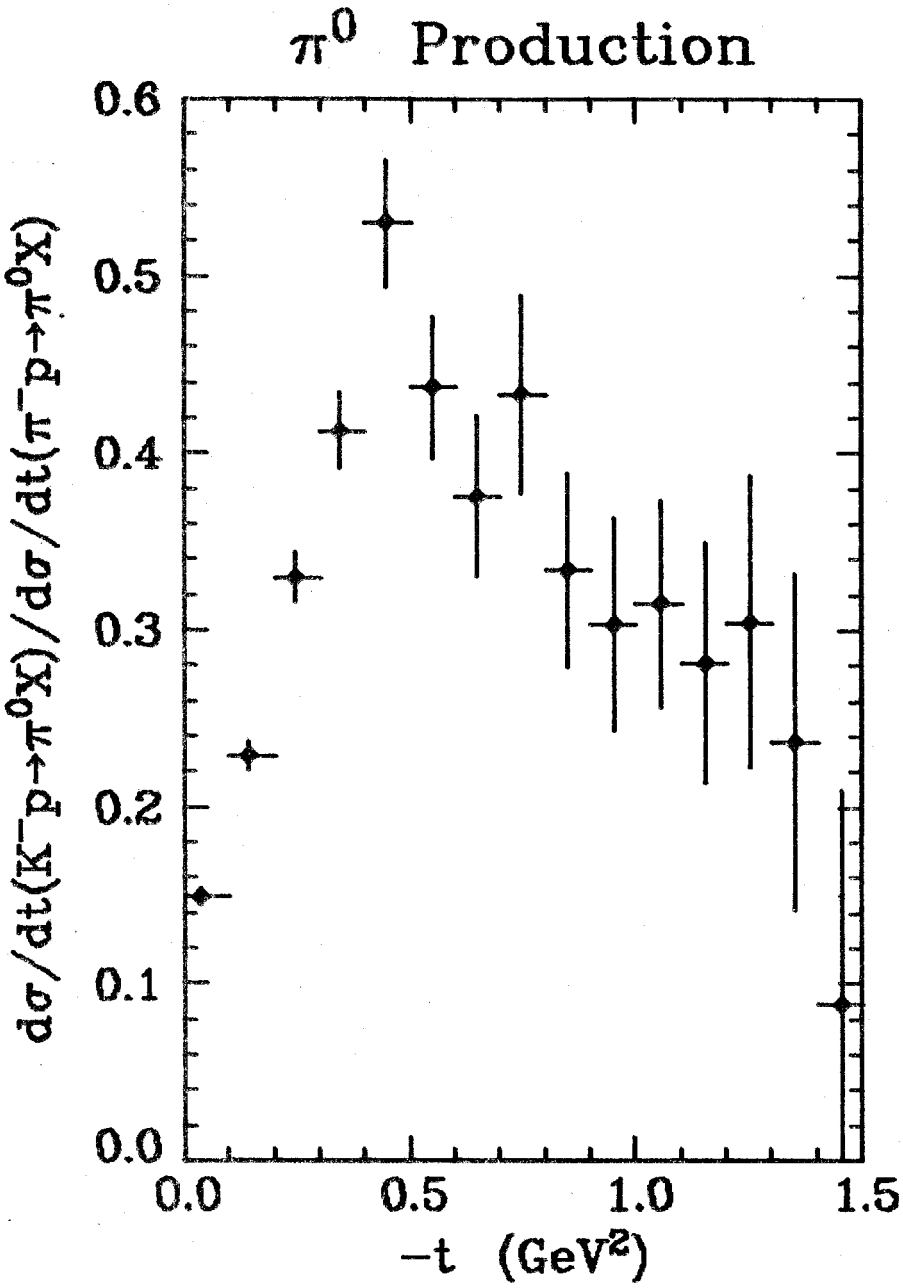

FIGURE 7.9 t-dependence of the ratio of the cross section for the production of π^0 mesons from a K^- beam to that from a π^- beam. Both cross sections are integrated over energies above 70 GeV.

The ratios of the cross sections for the production of η mesons with energies above 70 GeV to those for π^0 mesons are shown in Fig. 7.10 for both the K^- and the K^+ beam. This ratio is everywhere close to the value of 0.5 predicted by the naïve quark model, as discussed for pion beams in Section 5.3.

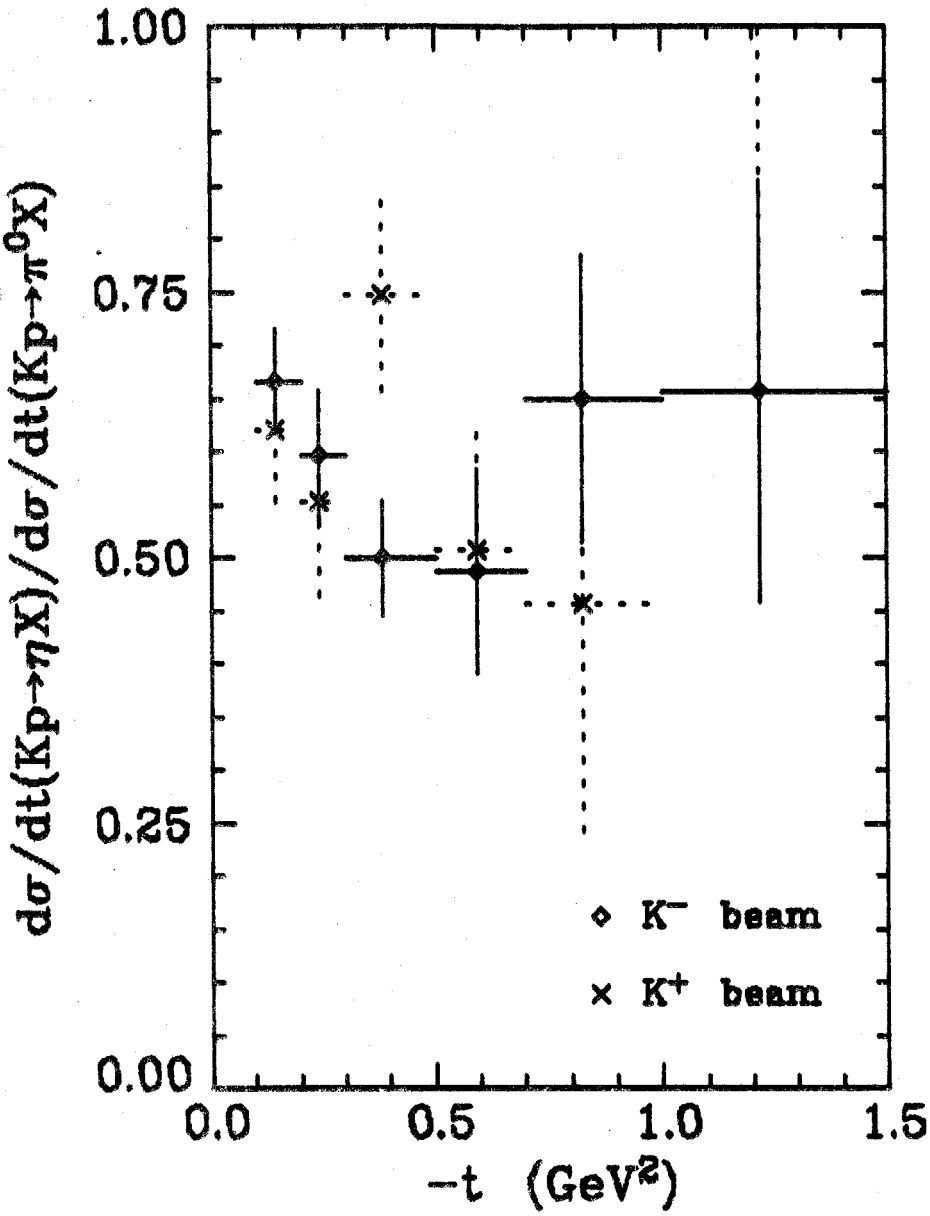

FIGURE 7.10 t-dependence of the ratios of the cross section for the inclusive production of η mesons to that for π^0 mesons from a K^- beam and from a K^+ beam. Both cross sections are integrated over energies above 70 GeV.

7.3 RESULTS FROM PROTON AND ANTIPROTON BEAMS

In this section, the results from the reactions,

$$p + p \rightarrow \pi^0 + X \tag{7.3.1}$$

and

$$\bar{p} + p \rightarrow \pi^0 + X, \tag{7.3.2}$$

are presented. The acceptance-corrected data for these reactions are shown on Fig. 7.11 as a function of the energy of the π^0, E, in different t bins. Large t bins were used because fewer data were collected for these reactions. Triple Regge theory predicts that the dominant terms in the cross section for reaction (7.3.1) are given by

$$\frac{d^2\sigma}{dtdx}(x,t,s)\Big|_{pp \rightarrow \pi^0 X} = G_{NNP}(t)(1 - x)^{1-2\alpha_N(t)} + G_{\Delta\Delta P}(t)(1 - x)^{1-2\alpha_\Delta(t)}, \tag{7.3.3}$$

where N denotes nucleon exchange, Δ denotes $\Delta(1232)$ exchange and P denotes Pomeron exchange on the bottom leg. There are other I = 1/2 and I = 3/2 exchanges besides the nucleon and the $\Delta(1232)$ respectively, as discussed in Section 4.3, but these are ignored here. These two trajectories are expected to dominate because they have the largest intercepts at t = 0 on the Chew-Frautschi plot.

The Chew-Frautschi plots for the three lightest N* and Δ baryons on the nucleon and $\Delta(1232)$ trajectories are presented in Fig. 1.3 and

two lines of slope 0.9 GeV^{-2} through the lowest mass particles are shown. It is clear that the $\Delta(1232)$ trajectory lies above the nucleon trajectory for $t > 0$. However it is clear from the statistics of the data presented on Fig. 7.11 that these trajectories are sufficiently close together that it was not possible to distinguish the difference in the energy-dependence and solve for the two trajectories separately. It is now shown that a good approximation is to ignore the $\Delta(1232)$ trajectory.

An experiment using a charged particle spectrometer at the CERN ISR (Si78) measured the reactions,

---

FIGURE 7.11 Data on $pp \to \pi^0 X$ and $\bar{p}p \to \pi^0 X$ as a function of the energy of the π^0, E, in different t bins. The results of fits to the proton data over the energy range 70 - 96 GeV are shown. The resulting values for α and G are shown on Figs. 7.12 and 7.13 and are listed in Table 7.3. The various curves on the antiproton data plots are discussed in the text.

KEY

—— Final fit for proton data; sum of contributions for antiproton.

--- NNP triple Regge contribution

— — NNR triple Regge contribution

—·— Contamination from pion beams

⬇ ⬇ Limits of fit

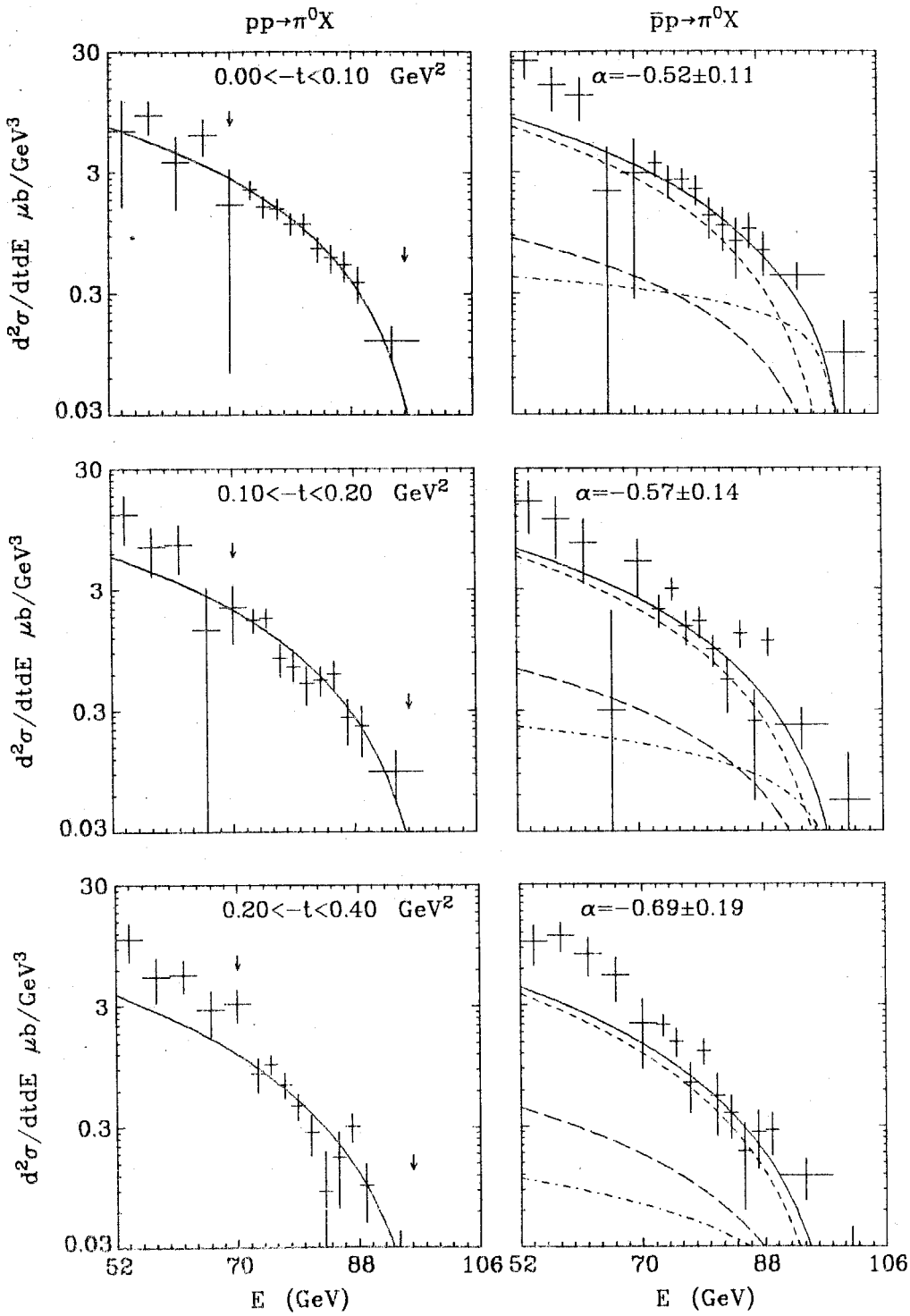
pp→π⁰X
p̄p→π⁰X
0.00<−t<0.10 GeV²
α=−0.52±0.11
0.10<−t<0.20 GeV²
α=−0.57±0.14
0.20<−t<0.40 GeV²
α=−0.69±0.19
d²σ/dtdE μb/GeV³
30
3
0.3
0.03
52
70
88
106
E (GeV)

FIGURE 7.11(a)

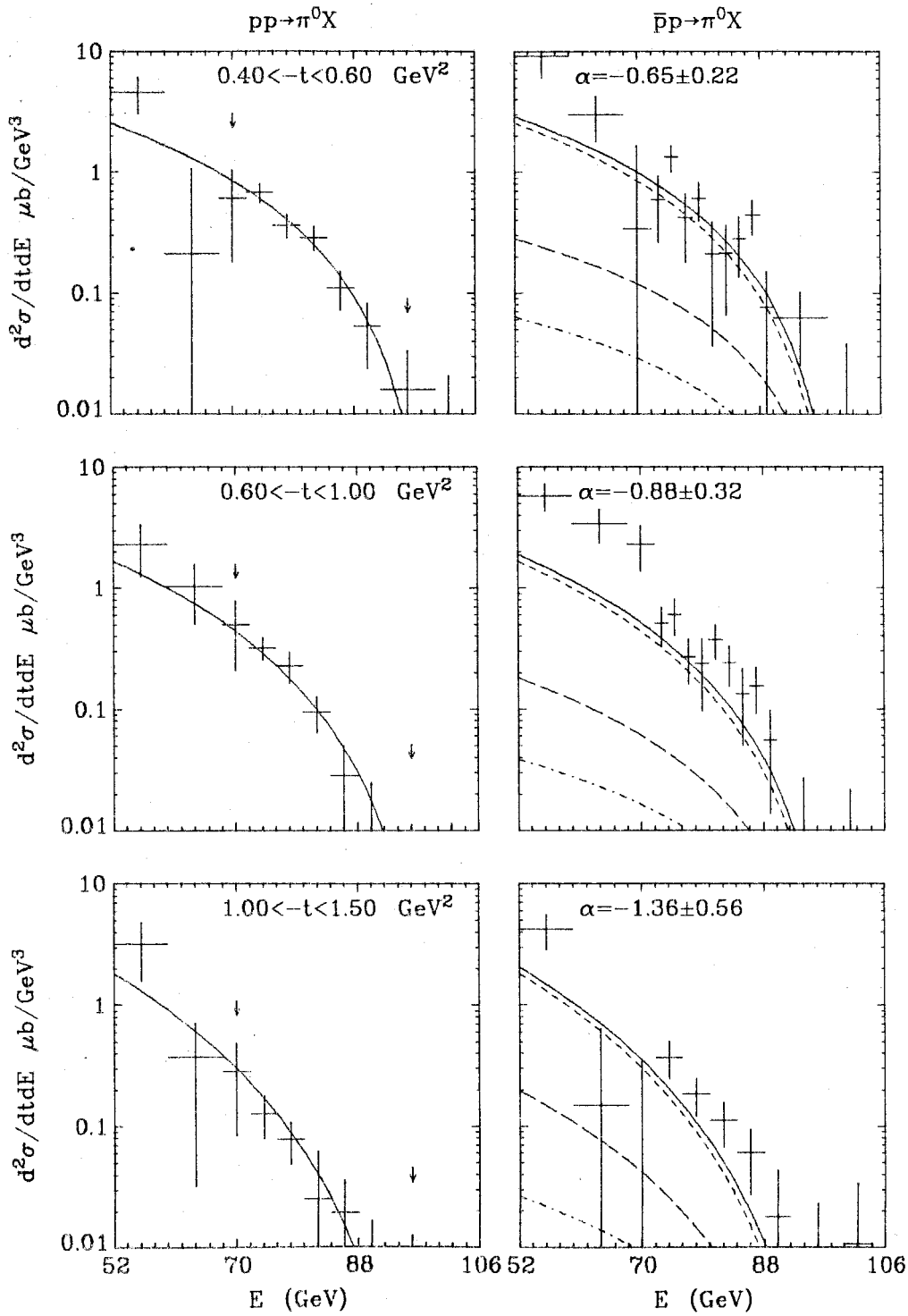
pp→π⁰X
p̄p→π⁰X
0.40<−t<0.60 GeV²
α=−0.65±0.22
0.60<−t<1.00 GeV²
α=−0.88±0.32
1.00<−t<1.50 GeV²
α=−1.36±0.56
d²σ/dtdE μb/GeV³
10
1
0.1
0.01
52
70
88
106
E (GeV)

FIGURE 7.11(b)

$$p + p \rightarrow \pi^+ + X \tag{7.3.4}$$

$$p + p \rightarrow \pi^- + X, \tag{7.3.5}$$

at $s = 2023\ \text{GeV}^2$ and $0.3 < -t < 1.5\ \text{GeV}^2$. The results for $0.7 < x < 0.95$ have been fitted to the form,

$$\frac{s}{\pi}\frac{d^2\sigma}{dtdM^2} = A(t)(M^2/s)^{1-2\alpha(t)}, \tag{7.3.6}$$

and the resulting trajectory, $\alpha(t)$, from each reaction is shown on Fig. 7.12. The cross sections for both reactions were also measured. Assuming that only the nucleon and $\Delta(1232)$ exchanges are important, the cross sections for reactions (7.3.4) and (7.3.5) are related to $G_{NNP}(t)$ and $G_{\Delta\Delta P}(t)$ in (7.3.3) by

$$\frac{d^2\sigma}{dtdx}(x,t,s)\Big|_{pp \rightarrow \pi^+X} = 2G_{NNP}(t)(1 - x)^{1-2\alpha_N(t)} + \frac{1}{2}G_{\Delta\Delta P}(t)(1 - x)^{1-2\alpha_\Delta(t)}, \tag{7.3.7}$$

$$\frac{d^2\sigma}{dtdx}(x,t,s)\Big|_{pp \rightarrow \pi^-X} = \frac{3}{2}G_{\Delta\Delta P}(t)(1 - x)^{1-2\alpha_\Delta(t)}. \tag{7.3.8}$$

The results showed that the cross section for reaction (7.3.5) is one-fourth that for reaction (7.3.4) for $0.7 < x < 0.95$ and hence the $\Delta(1232)$ exchange in reaction (7.3.1) contributes only about one-fourth of the cross section. Hence it was decided to solve for just one effective trajectory, which is referred to as the "nucleon trajectory" below.

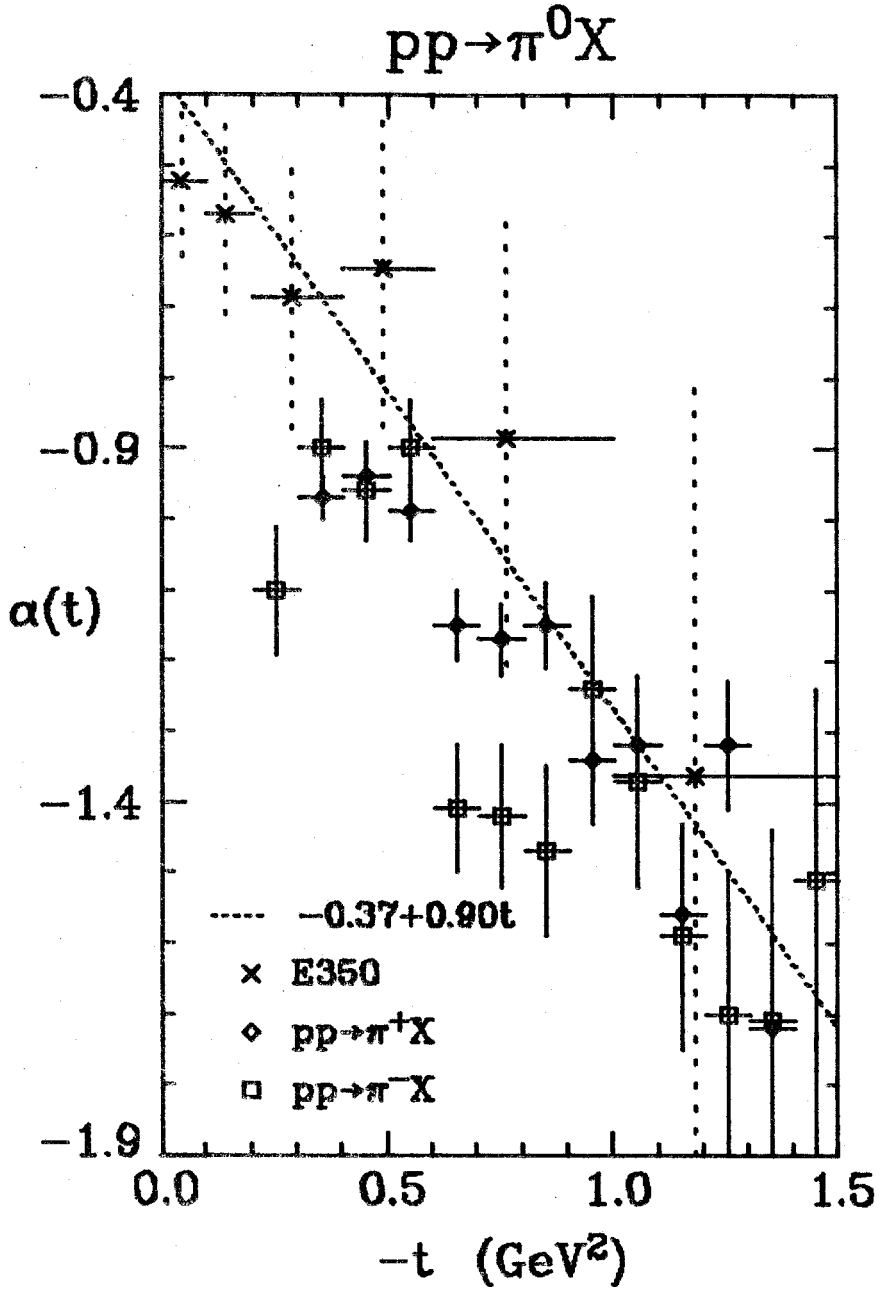

FIGURE 7.12 $\alpha_N(t)$ from the fits to $pp \to \pi^0 X$ over the range 70 - 96 GeV shown on Fig. 7.11. Also shown are the effective trajectories extracted from the reactions $pp \to \pi^+ X$ and $pp \to \pi^- X$ (Si78).

TABLE 7.3. Effective Regge trajectory, $\alpha(t)$, and residue function, $G(t)$, from fits to the $pp \to \pi^0 X$ data over the energy range 70 - 96 GeV.

-t range	α	G (mb/GeV^2)
0.0 - 0.1	-0.52 ± 0.11	3.27 ± 0.34
0.1 - 0.2	-0.57 ± 0.14	2.77 ± 0.36
0.2 - 0.4	-0.69 ± 0.19	2.15 ± 0.34
0.4 - 0.6	-0.65 ± 0.22	1.39 ± 0.28
0.6 - 1.0	-0.88 ± 0.32	1.29 ± 0.31
1.0 - 1.5	-1.36 ± 0.56	2.84 ± 0.84

The energy-dependence of just the proton beam data was fitted to the form (7.3.3) with the second term omitted. The resulting fits are shown by the solid curves on the proton data on Fig. 7.11 and were performed over the energy range 70 - 96 GeV. The resulting trajectory is shown on Fig. 7.12 and the residue function is shown on Fig. 7.13, and the values for both are listed in Table 7.3. The extracted trajectory is in good agreement with the straight line, $-0.37 + 0.90t$, which passes through the nucleon, and lies a little higher than the trajectory extracted from the $pp \to \pi^- X$ data. The residue function, $G_{NN\bar{P}}(t)$, falls with t_m for $t_m < 1$ GeV^2.

The antiproton beam data, reaction (7.3.2), were not as clean as the proton data and were not included in the fit, although they have been presented in Fig. 7.11. There were exchanges present with

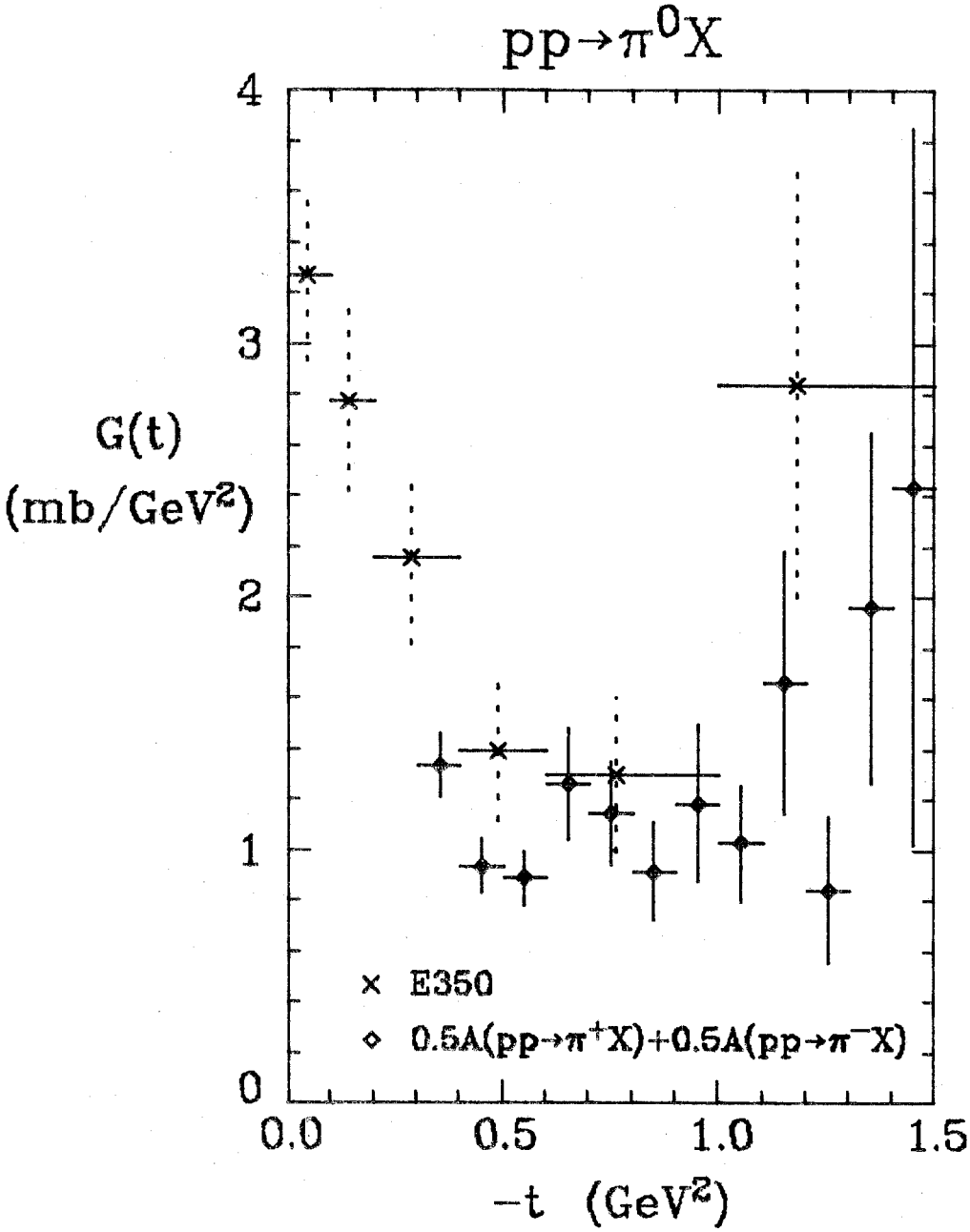

FIGURE 7.13 G(t) from the fits to the pp → π^0X data over the range 70 - 96 GeV as shown on Fig. 7.11. Results from charged pion production at the ISR (Si79) are shown for comparison.

Reggeon exchanges on the bottom leg and interference terms with an $I = 1/2$ exchange on one leg, an $I = 3/2$ exchange on the other leg and Reggeon exchange on the bottom leg. The Pomeron exchange terms had the same cross sections as in the proton beam case so these have been shown by the curves with small dashes on Fig. 7.11. The Reggeon term was then calculated using the result (4.I.41) in Appendix 4.I to give the Reggeon exchange cross section in terms of the Pomeron exchange cross section at $t = 0$. It was then assumed that the ratio of 0.9 held for all values of t. The results for the Reggeon exchange cross section are shown by the curves with large dashes on Fig. 7.11.

A second problem with the antiproton beam data was due to the presence of pions in the Cherenkov counter signal for antiprotons. It was estimated, using the results in Appendix 3.IX, that approximately 0.36% of the pion signal was present in the antiproton data. Due to the much larger cross section for the pion beam, this resulted in a substantial contribution to the cross section, which is shown by the dot-dashed curves on Fig. 7.11. The total estimated cross section for the antiproton data is shown by the solid curve and is seen to describe the data fairly well.

The t-dependence of the cross sections for reactions (7.3.1,2) integrated in 10 GeV energy bins starting at 60 GeV are shown in Figs. 7.14 and 7.15. The cross sections fall off exponentially with -t. The results of a parameterization to the cross section for reaction (7.3.4) from the ISR data are also shown. The cross sections for the

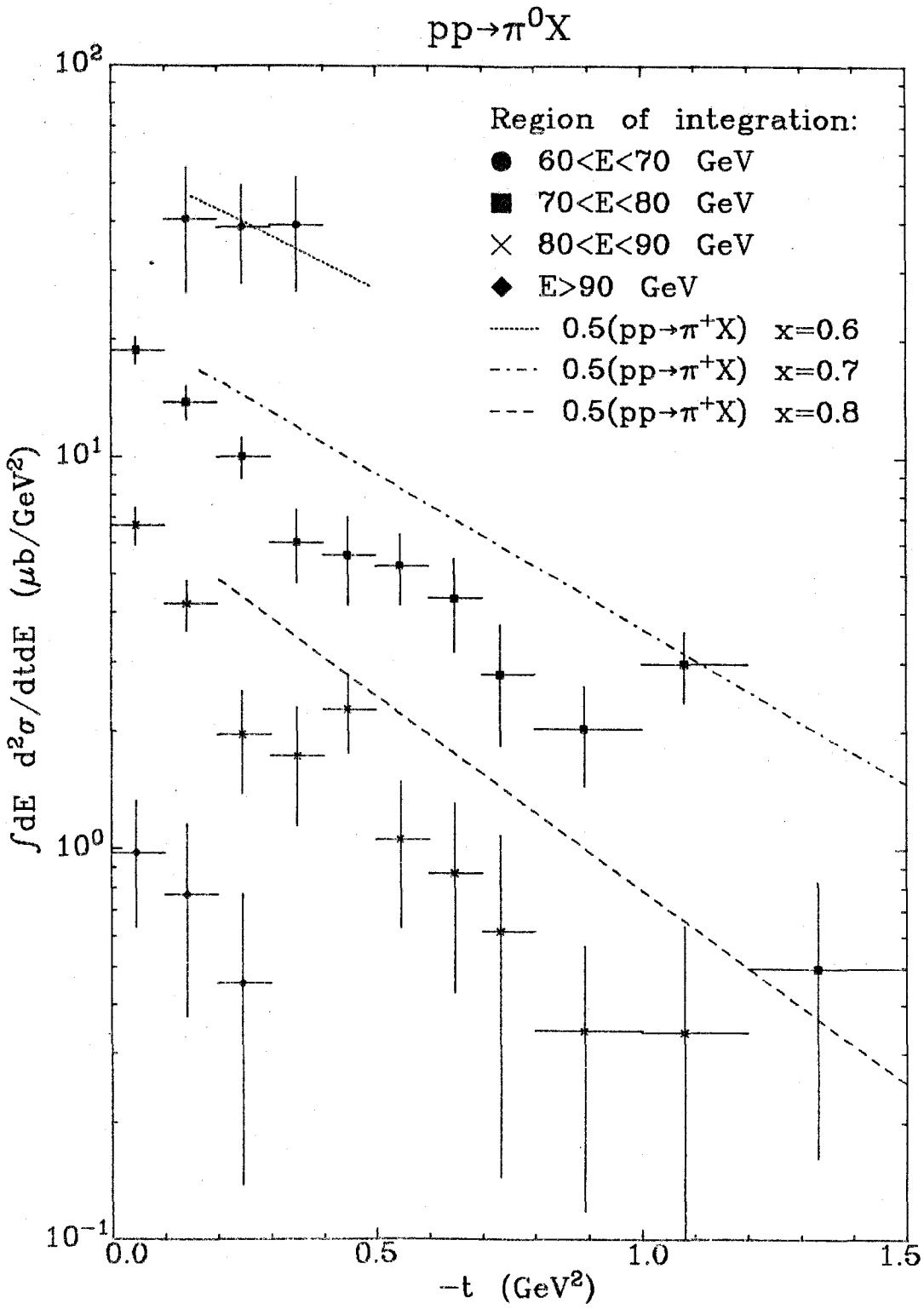

FIGURE 7.14 The t-dependence of the cross sections for pp → π^0X integrated over 10 GeV ranges in the π^0 energy, E.

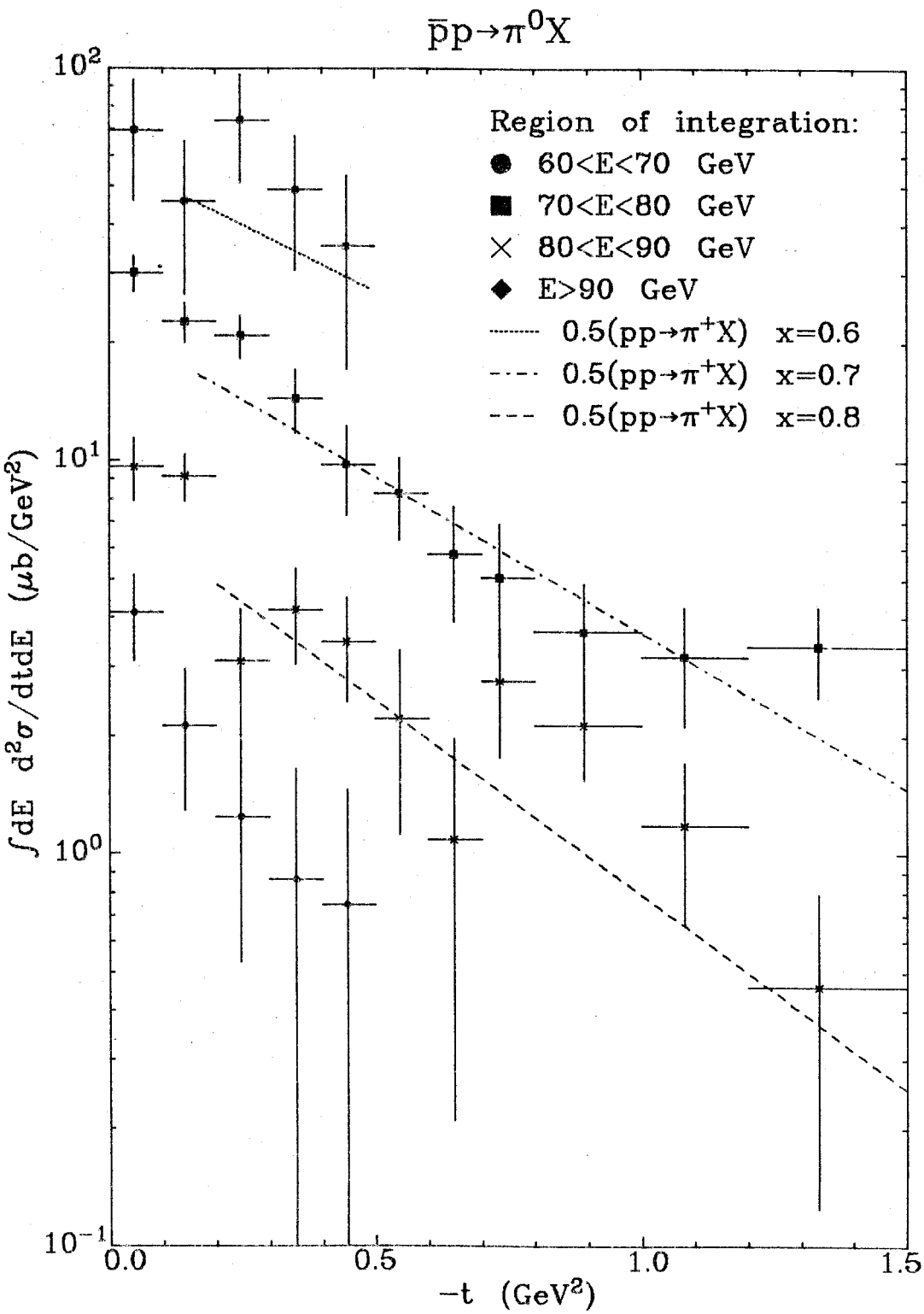

FIGURE 7.15 The t-dependence of the cross sections for $\bar{p}p \to \pi^0 X$ integrated over 10 GeV ranges in the π^0 energy, E.

reaction (7.3.4) for x = 0.6, 0.7 and 0.8 were fit to the form

$$\frac{d^3\sigma}{dp^3} = Ae^{-Cp_t^2}. \qquad (7.3.9)$$

Ignoring the Reggeon terms and the pion beam contamination, (7.3.3,7,8) show that the cross sections for π^0 production, reactions (7.3.1,2), are half the sum of the cross sections for π^+ and π^- production, reactions (7.3.4) and (7.3.5). Since the cross section for π^- production is about one-fourth that for π^+ production, the curves on Figs. 7.14,15 should be multiplied by 5/4 to give the prediction for π^0 production. It is seen that the proton beam data agree well with the ISR data whilst the antiproton beam data are a little higher, as expected from the discussion above.

A second comparison is shown on Fig. 7.13. Half the sum of A(t) from (7.3.6) for the π^+ and the π^- production cross sections is shown (Si79). It agrees fairly well with the π^0 production results, bearing in mind that different values of α (Fig. 7.12) have been used for extracting the residue functions in the three cases.

CHAPTER 8

CONCLUDING REMARKS

The 100 GeV data from E350 presented in this thesis are summarized well in terms of a parameterization of the form

$$\frac{d^2\sigma}{dtdx}(x,t) = B(t)(1 - x)^{A(t)}. \qquad (8.1)$$

Triple Regge theory predicts that $A(t) = 1 - 2\alpha(t)$, where $\alpha(t)$ is the trajectory of the exchanged particle, for the full inclusive data. An extension of this theory using the multiperipheral model predicts that $A(t) = -0.08 - 2\alpha(t)$ for the NFS data. It is found that the resulting trajectories for π^0 and η production from pion beams are similar and also that the trajectories extracted from the NFS data agree well with those from the full inclusive data. The Regge theory explanation is that π^0 production is due to the exchange of the ρ trajectory and η production is due to the A_2 trajectory. These trajectories are exchange-degenerate and the linear trajectories passing through the physical particles on these trajectories are almost equal. Thus it is not surprising that they agree for negative t and it is found that the extracted trajectories are the continuations of these straight lines to negative t.

The effective trajectories depart from their linear behavior at $t \simeq -1$ GeV^2 and start to flatten off. Unfortunately the statistics are too low to tell the value at which the trajectories level off, but the results indicate an α between -0.5 and -1.0. It is also

possible that the ρ and A_2 trajectories have different asymptotic behaviors although they are equal within statistics out to $t = -3$ GeV^2. The cross sections are also shown integrated in energy bins and these show a change of structure with t around -1 GeV^2. These phenomena suggest that a different physical mechanism from the triple Regge process is becoming dominant at high $-t$, such as some hard-scattering process.

It is not understood theoretically what is happening at large $-t$. The coherent exchange of a quark-antiquark pair (such as the CIM) as the dominant mechanism is ruled out by the data because the model predicts a cross section which is several orders of magnitude too low, even though this has to be the process responsible for exclusive scattering ($x = 1$) at high $-t$. Gluon exchange followed by the formation of a π^0 from the scattered quark predicts that α lies between 0 and -1 and could be the dominant process. Reliable calculations in this kinematic region have yet to be done. At low $-t$ there is no explanation yet of the triple Regge model by QCD. There is also no approach in QCD at present for calculating the NFS cross section.

The K* and nucleon trajectories are determined from the kaon, proton and antiproton beam data out to $t = -1$ GeV^2. They are consistent with the continuations of the corresponding linear trajectories in the physical m^2-J plane. The cross section and trajectory for π^0 production from protons agrees with the ISR data on π^+ and π^- production.

It is found that the cross sections are composed of more than one triple Regge contribution. The minor contributions were estimated and subtracted from the data before the trajectories were extracted from the dominant triple Regge term. Important contributions came from the $\dot{I} = 2$ and the $I = 3/2$ exchanges for π^0 production from pion and kaon beams respectively.

The normalization, $B(t)$, in (8.1) was also investigated and found to have dips at $t \simeq -0.5$ GeV^2 for π^0 production from pion beams for both the full inclusive and the NFS cases, but was fairly flat for η production in this region. This is expected from Regge theory because of the different signatures of the two trajectories. The normalizations for the two beam polarities were found to be equal for all the beam types, as expected for a dominant Pomeron exchange term, except at low -t, where other contributions were present.

In conclusion, it is seen that there are some interesting results from this experiment which are consistent with triple Regge theory at low -t and whose interpretations at high -t are not yet theoretically inderstood.

APPENDIX 2.I

DETAILS OF TRIGGERS

In this appendix, the details of the various triggers are explained. All triggers required that an acceptable beam particle be present. This was defined using the scintillation counters M1, M2, M3 and A0 shown on Fig. 2.1. M1, M2 and M3 were 6 mm, 3 mm and 1.6 mm thick respectively and each was viewed by one photomultiplier tube so that a charged particle passing through them would give minimum-ionizing pulse heights. M2 was the smallest counter in size, being 8 mm square, and thus it limited the aperture of the beam. M3 was close to the target to ensure that the particle reached the target. These three counters were discriminated just below the peak corresponding to one minimum-ionizing particle. A0 was a large counter with a 10 mm hole centered at the beamline and viewed by one photomultiplier tube whose output was discriminated at a level just below the one particle peak so as to work as a beam halo veto counter. The particles in the halo may have been scattered and lost momentum and so were not acceptable to the experiment.

The complete definition of an acceptable beam particle is shown on Fig. 2.I.1. "Beamgate" was a logic level set true whenever a spill reached the experiment. 2xMIN and DT were two signals defined by M1, whose output was fanned into four before being discriminated. The beam particles were in r.f. buckets spaced 20 ns apart and lasting for less than 1 ns. The resolution of much of the electronics was a few nanoseconds so it was important to veto buckets

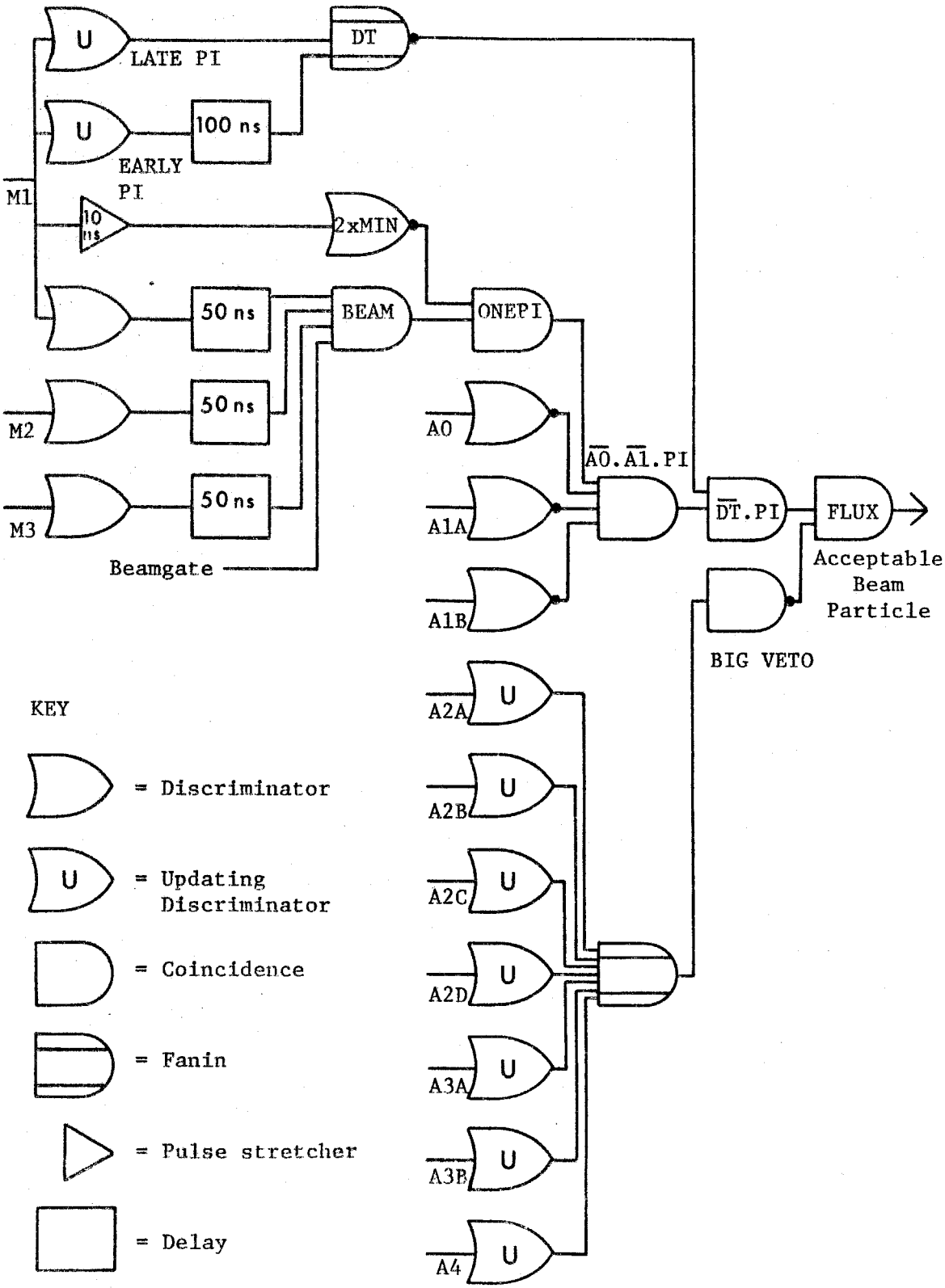

FIGURE 2.I.1 Definition of an acceptable beam particle.

with more than one particle present. This was done using one of the M1 outputs and integrating the signal over about 5 ns so that two particles in the same bucket would give a signal twice the size of that from one particle. The output was discriminated above the one particle peak and the result was called 2xMIN. It was also necessary to ensure that two particles were not present within the time resolution of the photon detector, which was about 50 ns. To do this, the basic signal from M1 was delayed by 50 ns, one output was discriminated with no delay (called "LATE PI") and one was discriminated with a 100 ns delay (called "EARLY PI"). These last two outputs were then passed through updating discriminators whose output pulses were 50 ns long and their outputs, called "DT" were placed in anticoincidence with M1. Then any particles present within 50 ns of each other would veto each other. The photomultiplier tubes had to recover after charged particles had hit them, since some beam halo particles which hit the A2 counters end on caused a large electromagnetic shower in them. Thus the experiment was turned off for a short time by the electronics whenever one of these counters fired. This signal was called "BIGVETO" and was formed by passing the signal from each of the charged particle veto counters through an updating discriminator and adding the total output. Three scalers counted the number of particles giving the BEAM, $\overline{A0}.\overline{A1}.PI$ and FLUX signals shown on Fig. 2.I.1.

To put an energy requirement in the trigger, the output from

each photomultiplier tube on the photon detector was fed into one of 14 mixers (To76). Each mixer was essentially a fanin which added up the total energy deposited in a group of up to 14 counters. These mixers could then be added up and discriminated. The basic trigger to obtain low t_m events, trigger A, just required that the total energy in either the x counters or the y counters be above one of three biases. The exact energies are described in Appendix 3.V but were approximately 40, 60 and 70 GeV. Trigger B was designed to accept only the high t_m data by removing the region of the detector near to the beamline from the trigger. This was accomplished by adding up the sum of counters 35 to 70 in the x view and the sum of counters 1 to 18 and 53 to 70 in the y view, as shown in the diagram below, and requiring that one of these two sums be above one of the three biases.

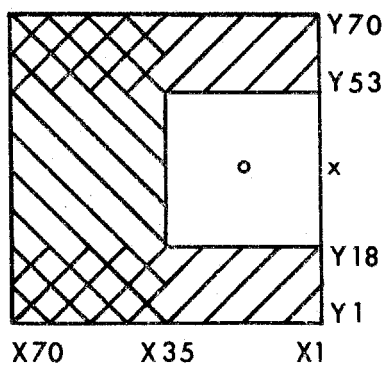

TRIGGER B

o = straight-through beam

x = bent beam

\ = triggered by x counters

/ = triggered by y counters

At any one time just one of the two geometry requirements and one bias level were enforced. A bit was set whenever a recorded event passed the imposed energy and geometry requirements.

Some of the data were collected by requiring a specific beam particle. Only the downstream Cherenkov counter could be used since the signal from the upstream counter arrived at the electronics too late to trigger the experiment. Trigger C required that there was no light seen by the outer photomultiplier tube, thus eliminating pions. Trigger K required that there was no light seen by the outer tube but light seen by the inner tube, thus requiring kaons. Both these triggers were run with the trigger A type energy requirements. A scaler counted the number of acceptable beam particles satisfying the imposed Cherenkov cut.

The NFS trigger used the signals recorded by the scintillation counters A1, A2, A3 and A4 shown on Fig. 2.1 and described in section 2.4. Its logic is shown in Fig. 2.I.2. The five photomultiplier tubes on each of the four counters of A2, called A, B, C and D, were added together electronically and discriminated at a level about two-thirds that of the one particle peak. The two A1 outputs (called A and B), the two A3 outputs (called A and B) and the A4 output were all discriminated at a similar level. The NFS trigger required that there be an acceptable beam particle and no signal from any of these scintillation counters. A bit was set whenever a recorded event satisfied the NFS requirement.

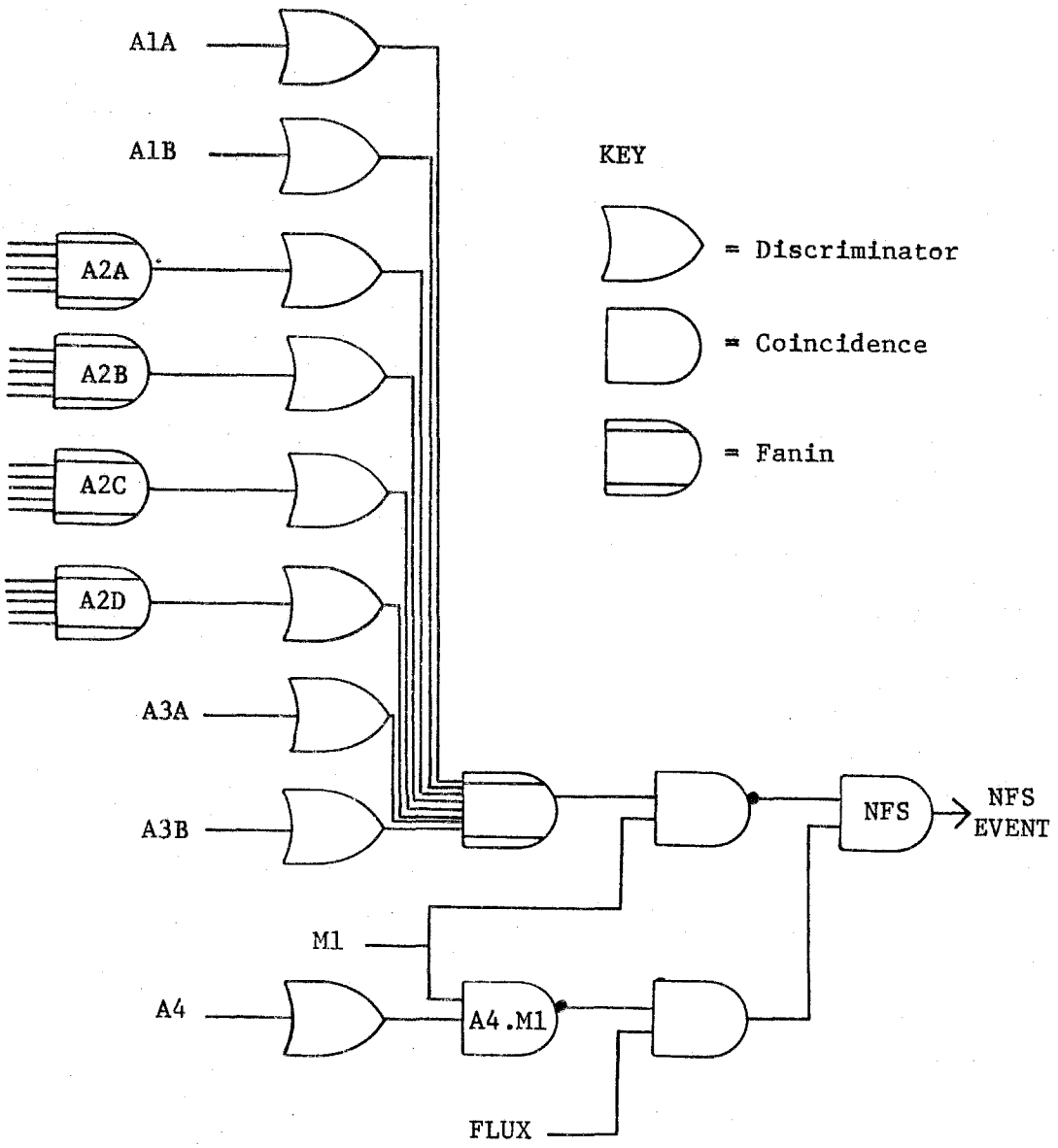

(Figure 2.I.1)

FIGURE 2.I.2 Definition of a Neutral Final State event

APPENDIX 3.I

DETERMINATION OF THE GAINS OF THE DETECTOR COUNTERS

The photomultiplier tubes and pulse height analyzers had to be set to give as uniform a response as possible. This was necessary in the hardware to make the energy cut-off of the trigger as sharp as possible since it was vetoing a cross section which fell with energy. Hence at the start of the data-taking run an "electron sweep" was done in which the beam was centered on the detector either horizontally or vertically. The detector was moved in the opposite direction so that the beam went through the center of each counter until about 200 events had been recorded. The beam consisted of 100 GeV electrons which were selected by setting up the downstream Cherenkov counter to act as a threshold counter to discriminate against particles with masses above that of the electron. A 3 mm scintillation finger was placed in the beam just in front of the detector to ensure that the beam went near to the center of the counter. The data from the 140 counters were analyzed on-line using a moments method (Ba75b) and the high voltages of the photomultiplier tubes were adjusted so as to equalize their responses. A second electron sweep was then done to check that their responses had been equalized.

To maintain the constancy of the counter gains throughout the experiment, Bi^{207} sources on each counter were monitored continuously as described in Section 2.5. An ideal value for the expected pulse

height of each source peak was found at the time of the electron sweep and at any time that a source measurement drifted away from this value the high voltage on the corresponding counter was adjusted accordingly.

For the off-line analysis, a second approach was used to obtain the counter gains. This method used the data itself and gave a more accurate determination. It was also necessary because the fitting method instead of the moments method was used for finding the π^0 energies and this treated such discrepancies as the differing sizes of the counters differently. It was also found that the results from electron sweeps taken at the start and the end of the run were in disagreement. For this determination, an iterative scheme was used with the first guess for the gains being obtained from the results of the electron sweep. Improved values were obtained by minimizing the χ^2 of fits to photons in π^0 and η mesons with respect to the gains. Clearly if the gain on a counter was too large then all the measured pulse heights were larger on average than those predicted by the shower shape. The determination of the gains was made using events in which a successful constrained fit to a π^0 or η meson had been made, as described in Appendix 3.IV. It was assumed that the shower shape was known.

Suppose that P_i is the measured pulse height in counter i and ES(d,E) is the expected pulse height at a distance d in a transverse direction from a photon of energy E. The determination of S is

described in Appendix 3.II. The multiplicative correction factor for the gain of counter i, γ_i, is then given by

$$\gamma_i = N/\sum_{k=1}^{N}\left(\sum_{j=1}^{n} E_j S(d_{ij},E_j)/P_i\right), \qquad (3.I.1)$$

where all the quantities in the summation over the events, k, refer to k. This sum is over N events in which one photon contributed at least three-quarters of the pulse height in counter i and there was no other photon centered within three counterwidths of its center. n is the number of photons in each event and d_{ij} is the distance from the j^{th} photon to the center of counter i. For each of the 140 counters the quantity γ_i was histogrammed and the means of Gaussian fits to these were used to correct the gains. It was found that this fitting technique gave the gains to 0.5%. The events should have been weighted according to their pulse heights but this was not done. Using the gains and the values of the sources on the tapes used to determine them, an "ideal" value for each source was determined. This in turn was used to determine the gains of the counters for other tapes.

APPENDIX 3.II

DETERMINATION OF THE ENERGY DEPENDENCE OF THE SHOWER SHAPE

The shower shape distribution is the average shape formed by the pulse heights in one view of the detector in response to a photon hitting it. Suppose that ES(d,E) is the pulse height in a counter whose center is a distance d in a transverse direction (either x or y) from a photon of energy E. The shape S was found iteratively. Initially the shape of a large number of isolated showers of 45 GeV photons from 50 GeV π^0 and η mesons was studied to obtain S as a function of d (Ba75a). The standard deviation at each point, $\sqrt{E}Q(d,E)$, was also measured as a function of d, giving the predicted deviation from the shower shape. A preliminary analysis of part of the data using this shape and deviation was carried out using the reconstruction analysis described in Section 3.3 with the mass of the particle constrained. S and Q were then refined by varying them about this first approximation and minimizing the χ^2 of fits to about 100,000 π^0 and η mesons, as described below.

Each photon was considered separately. For each counter covered by that photon let $E_jS(d_{ij},E_j)$ be the contribution to the pulse height in counter i from photon j of energy E_j at a distance d_{ij} from the center of the counter. This analysis used only counters i where the photon considered was the highest energy photon falling in the counter, denoted 1, and satisfied

$$E_1 S(d_{i1},E_1) > 0.75 \sum_{j=2}^{n} E_j S(d_{ij},E_j) \qquad (3.II.1)$$

where n was the total number of photons in the event. This requirement ensured that a substantial amount of the pulse height was due to the photon being considered and so any correction to the shower shape would affect just that photon. It was required that no other photon be within three counterwidths of its center. For any event, the measured pulse height in counter i, P_i, was expected to be about $\sum_j E_j S(d_{ij},E_j)$. The discrepancy gives the multiplicative correction factor, $\gamma(d,E)$, for the shower shape as follows:

$$\gamma(d,E) = \frac{1}{N} \sum_{k=1}^{N} \frac{P_i - \sum_{j=2}^{n} E_j S(d_{ij},E_j)}{E_1 S(d_{i1},E_1)} \qquad (3.II.2)$$

where the summation is over N events having $E - \Delta E < E_i < E + \Delta E$ and $d - \Delta d < d_{i1} < d + \Delta d$ for some counter $i = i(k)$. ΔE and Δd were energy and distance intervals chosen sufficiently large that γ could be histogrammed as a function of E and d. The means of Gaussian fits to these histograms were used to correct the shower shape. The resulting shower shape for 50 GeV photons is shown in Fig. 3.II.1. The shape was found to vary slightly with energy, becoming narrower as the energy increased. Fig. 3.II.2 shows the ratio of the 60 GeV shape to the 10 GeV shape, $S(d,60)/S(d,10)$, as a function of the distance d.

Another correction that was made was to look at the distribution of the center of the shower relative to the center of the nearest

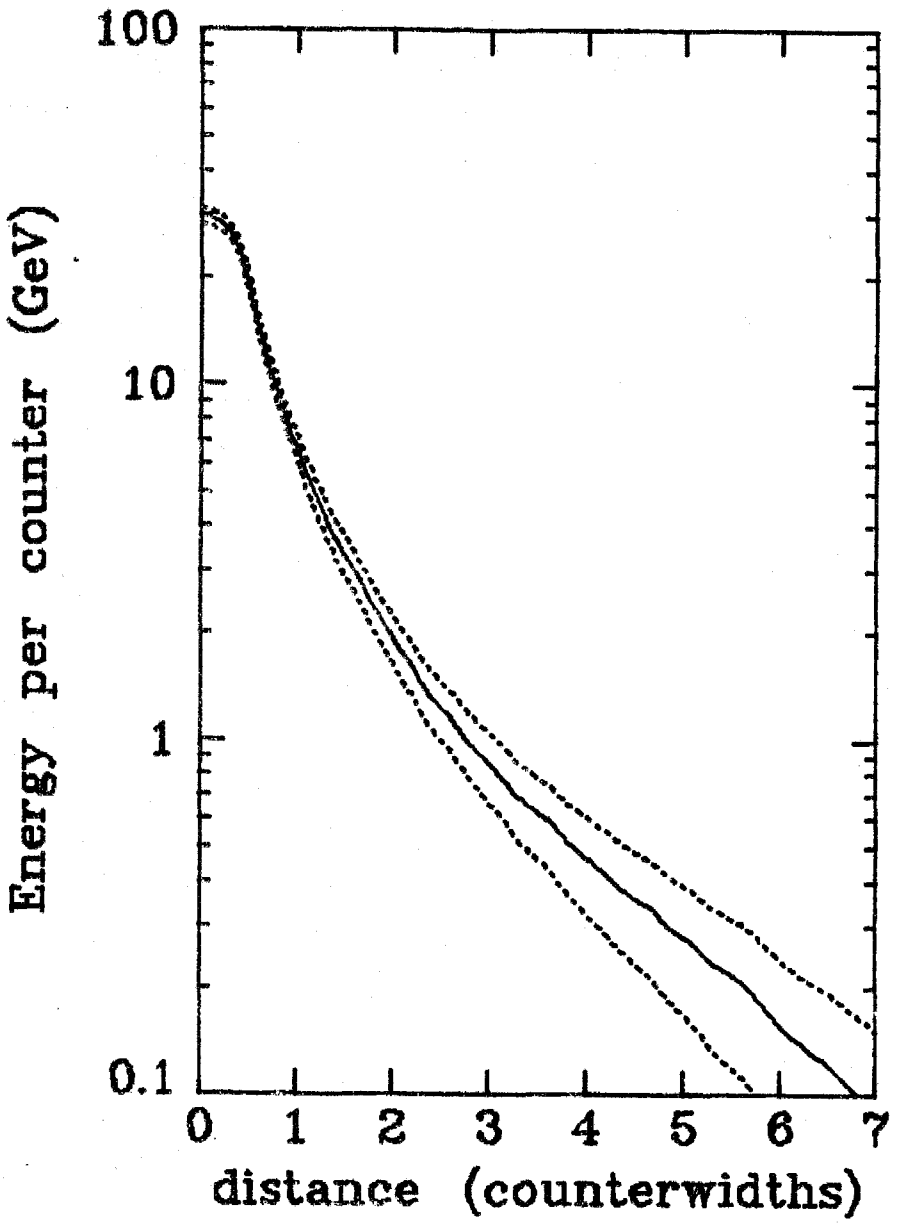

FIGURE 3.II.1 Shower shape for photon detector: the energy deposited in a counter by a 50 GeV photon as a function of its distance from the shower center (solid curve). The dotted curve shows the predicted fluctuation about this shape.

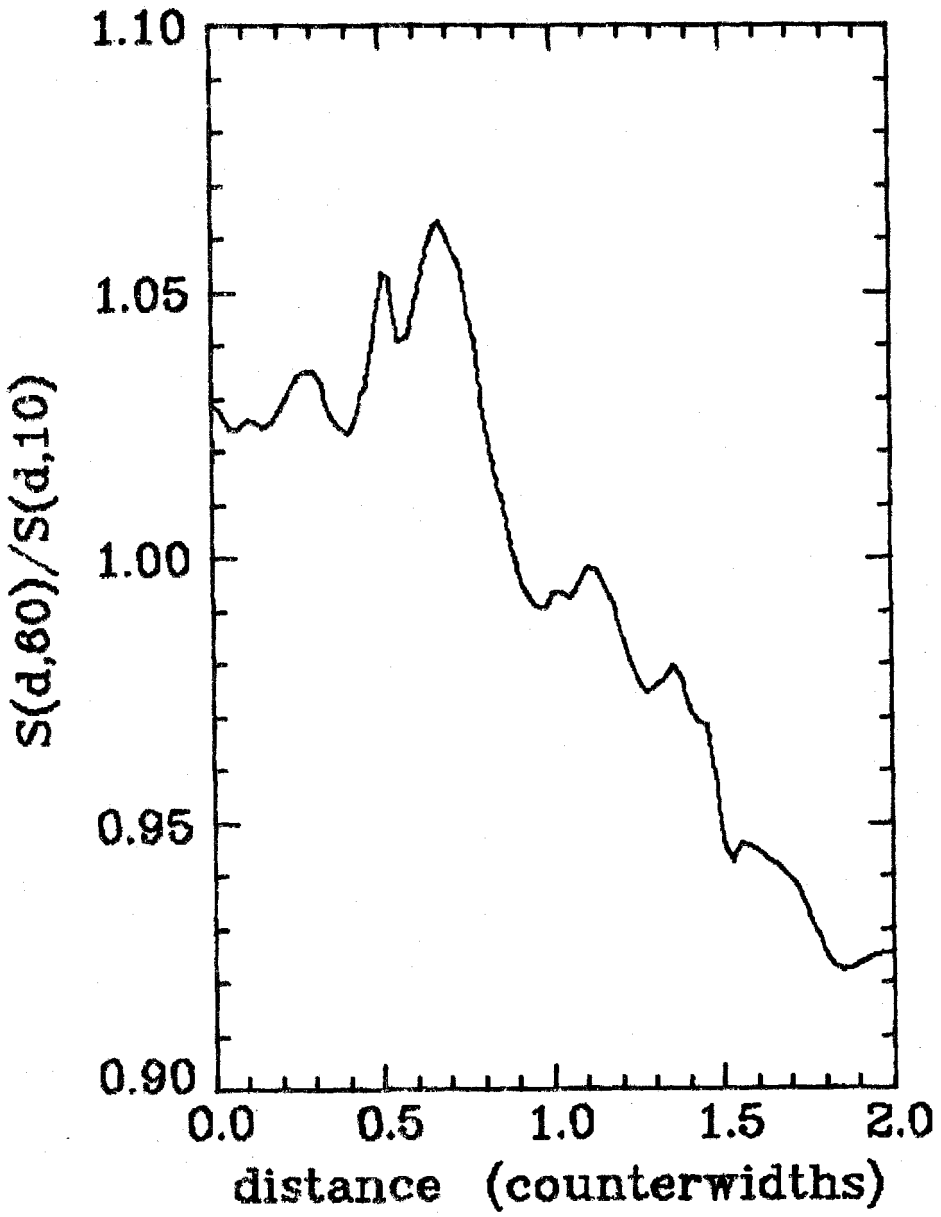

FIGURE 3.II.2 Ratio of 60 GeV shower shape to 10 GeV shower shape as a function of the distance from the shower center. The jagged nature is due to the interpolation used and is not real.

counter, Δ, and check that Δ was uniformly distributed between 0.0 and 0.5. The shower shape was adjusted accordingly. It was also noticed that the total energy in the shower, as given by the sum of points spaced one counterwidth apart along the shower shape, varied as a function of Δ, being 0.5% larger when $\Delta = 0$ and falling by 1% from $\Delta = 0.4$ to $\Delta = 0.5$. This effect may have been due to the wrapping between the counters together with a misalignment of the eight rods forming one counter.

It was also necessary to know the expected fluctuation about the shower shape, $\sqrt{E}Q(d,E)$, for use in the fit, as explained in Appendix 3.IV. This fit minimizes the χ^2 given by

$$\chi^2 = \sum_i [\{P_i - \sum_{j=1}^{n} E_j S(d_{ij},E_j)\}^2 / \sum_{j=1}^{n} E_j Q^2(d_{ij},E_j)], \qquad (3.II.3)$$

for any given event, where i runs over all the counters. To simplify this, let

$$Z_i = P_i \left(\sum_{j=1}^{n} E_j Q^2 \right)^{-1/2} \qquad (3.II.4a)$$

$$Y_{ji} = S \left(\sum_{j=1}^{n} E_j Q^2 \right)^{-1/2}. \qquad (3.II.4b)$$

Then

$$\chi^2 = \sum_j (Z_i - \sum_{j=1}^{n} E_j Y_{ji})^2. \qquad (3.II.5)$$

If the energy-dependence of Z_i and Y_{ji} are ignored, then the minimum

of (3.II.5) with respect to the energy of the m^{th} photon, E_m, is given by

$$\frac{\partial \chi^2}{\partial E_m} = 2\Big(\sum_{j=1}^{n} E_j M_{jm} - \sum_i Y_{mi} Z_i \Big) = 0, \qquad (3.II.6a)$$

where

$$M_{jm} = \sum_i Y_{ji} Y_{mi}. \qquad (3.II.6b)$$

The system (3.II.6) has the formal solution

$$E_j = \sum_p (M^{-1})_{jp} \sum_i Y_{pi} Z_i. \qquad (3.II.7)$$

The residual for counter i is

$$r_i = Z_i - \sum_{j=1}^{n} E_j Y_{ji}. \qquad (3.II.8)$$

Using the solution (3.II.7) gives the expected value of r_i^2 as

$$\langle r_i^2 \rangle = 1 - Y_i^T M^{-1} Y_i \qquad (3.II.9)$$

where $Y_i^T = (Y_{1i},\ldots,Y_{ni})$. The function Q was checked by calculating the theoretical value, $(1 - Y_i^T M^{-1} Y_i)_t$, from the shower shape as a function of d and E and then plotting the quantity

$$v = \langle r_i^2 \rangle / (1 - Y_i^T M^{-1} Y_i)_t \qquad (3.II.10)$$

as a function of d and E, as for the shower shape itself, and checking whether its mean was 1. If not, then the function Q was multiplied by $\sqrt{v}$.

When the shower shape was used in the analysis programs it was

calculated using quadratic interpolation over distance with points spaced 0.05 counterwidths apart and using linear interpolation over energy with points at 0, 20, 30, 50 and 80 GeV. It was found that the energy dependence of Q was negligible and so it was calculated in the analysis program using linear interpolation over distance.

APPENDIX 3.III

LEAKAGE CORRECTION

The backup counter, described in Section 2.5, was used to correct for the energy leakage from the back of the main photon detector. The amount of energy lost varied from event to event because it depended both on the energy of the photon and on the depth into the detector at which it first interacted. To understand how to correct for the leakage, the response of the backup counter to a monoenergetic beam of electrons was studied first. Consider a simple model for the energy deposited in a shower as a function of the depth, z, as shown on Fig. 3.III.1. Suppose that an electron of energy E_0 GeV loses energy E_1 in the main detector and energy E_2 in the backup counter and that the longitudinal dependence is given by

$$\frac{dE}{dz} = f(z - \ell; E_0), \qquad (3.III.1)$$

where z is the depth in radiation lengths and ℓ is the depth into the photon detector at which the shower starts. ℓ is very small for electrons due to the bremsstrahlung of soft photons (Wa79) but is considerable for photon showers. In the region of the backup counter the shower development may be assumed to be exponential of the form

$$f(z) = B(E_0)e^{-Az}. \qquad (3.III.2)$$

Some studies, such as those in Ref. (Mü72), have shown that this is only an approximation and that A varies slightly with E_0. The total energy deposited in the backup counter, between depths a and b, is

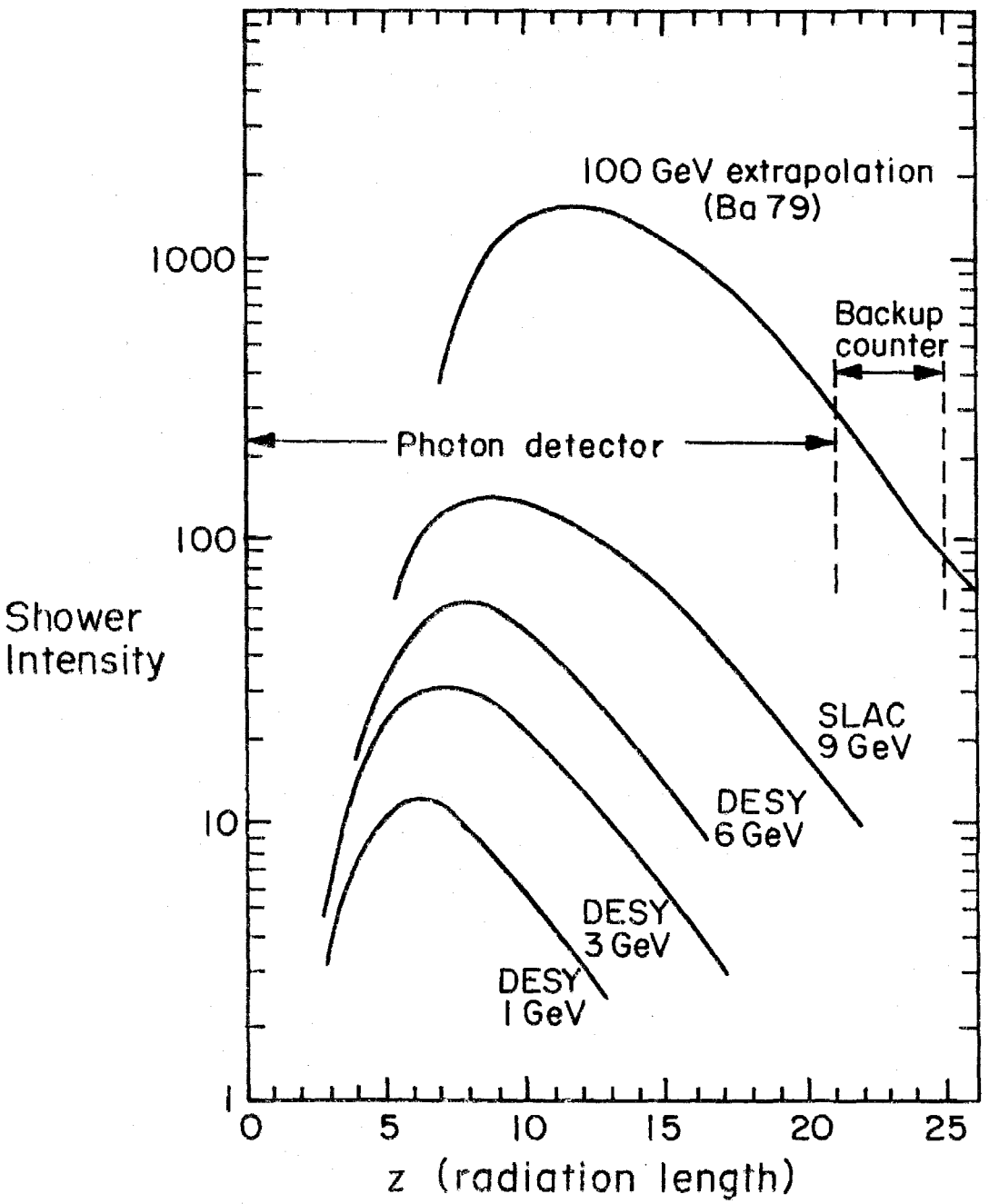

FIGURE 3.III.1 Longitudinal distribution of energy in an electromagnetic shower as a function of the depth of the shower, z (from Ref. (Ba79)).

$$E_2 = B(E_0)e^{A\ell}(e^{-Aa} - e^{-Ab})/A \qquad (3.III.3)$$

and the total energy in the shower is

$$E_0 = E_1 + \alpha_0 E_2 \qquad (3.III.4a)$$

where

$$\alpha_0 = 1/(1 - e^{A(a-b)}). \qquad (3.III.4b)$$

If it is assumed that the distribution of the starting point, ℓ, does not vary significantly with energy, then (3.III.3) shows that the mean energy deposited in the backup counter, $\langle E_2(E_0)\rangle$, is a function of E_0 only. As well as the 100 GeV electron sweep, in which the detector was moved across the electron beam as described in Appendix 3.I, some data were collected with electron beams of energies 20 and 50 GeV sent into a fixed spot on the detector. The response of the backup counter as a function of the electron energy is shown in Fig. 3.III.2. A good parameterization of the measured means at the three energies was found to be given by

$$\langle E_2(E_0)\rangle = 0.0118E_0^{1.316} \text{ pulse heights}, \qquad (3.III.5)$$

which is consistent with the calculation in ref. MU72 extrapolated to the depth of the photon detector.

To find the best estimate of the energy of an electron, (3.III.4) was first rewritten as

$$E_0 = \beta(P_D + \alpha P_B) \qquad (3.III.6)$$

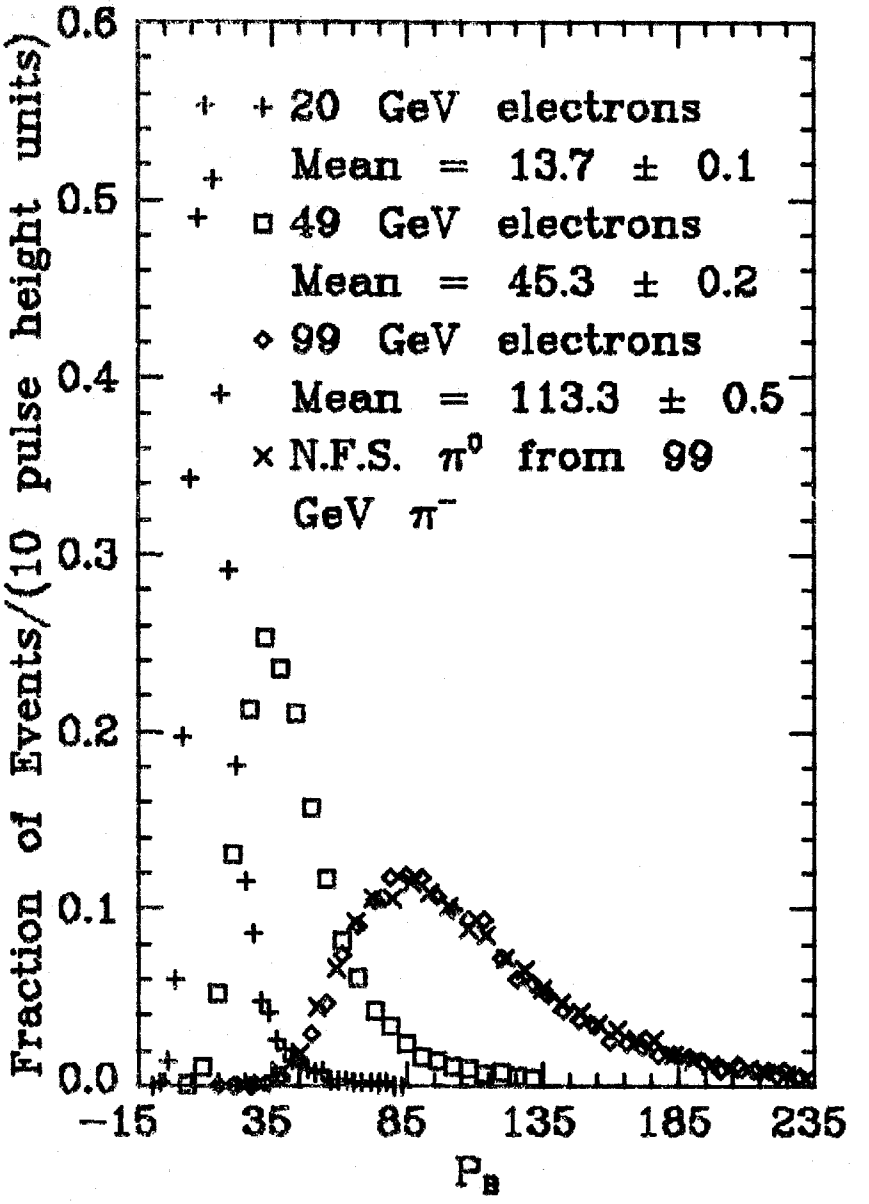

FIGURE 3.III.2 Distribution of the energy deposited in the backup counter, P_B, for electrons of energies 20, 49 and 99 GeV and for π^0 mesons from the NFS trigger with two photons in the detector and with $t_m < 0.1$ GeV^2 and energy above 90 GeV from a 99 GeV π^- beam.

where P_D and P_B are the total pulse heights in the photon detector and backup counter respectively, α is the leakage correction factor and β is the conversion factor from pulse height units into GeV. The quantity $P_D + \alpha P_B$ was histogrammed for various values of α as shown in Fig. 3.III.3 for $\alpha = 0.0$ and 1.1. The values of their standard deviation divided by the mean are shown on Fig. 3.III.4. There are minima at $\alpha \simeq 0.9$ for 49 GeV electrons and at $\alpha \simeq 1.2$ for 99 GeV electrons. The data at these two energies were not completely equivalent since the 99 GeV electrons were uniformly distributed among the backup counters whilst the 49 GeV electrons were concentrated in one place.

Since the main purpose of this experiment was to detect photons, not electrons, the leakage correction for photons was needed. There was no monoenergetic photon source, or even a monoenergetic π^0 meson source, available since, for example, the experiment had no neutral veto system or neutron detection system to detect π^0 mesons produced by charge-exchange processes. Hence the π^0 mesons with $t_m < 0.1$ GeV^2 from the NFS trigger, described in Section 2.6, having only two photons in the detector were used. Their uncorrected energy spectrum is shown on Fig. 3.III.5. On Fig. 3.III.2 is shown the distribution of the sum of the pulse heights in the backup counter, P_B, for such π^0 mesons having energy above 90 GeV coming from an incident 99 GeV π^- beam. It is almost identical to that for electrons at the same incident energy and so the required correction

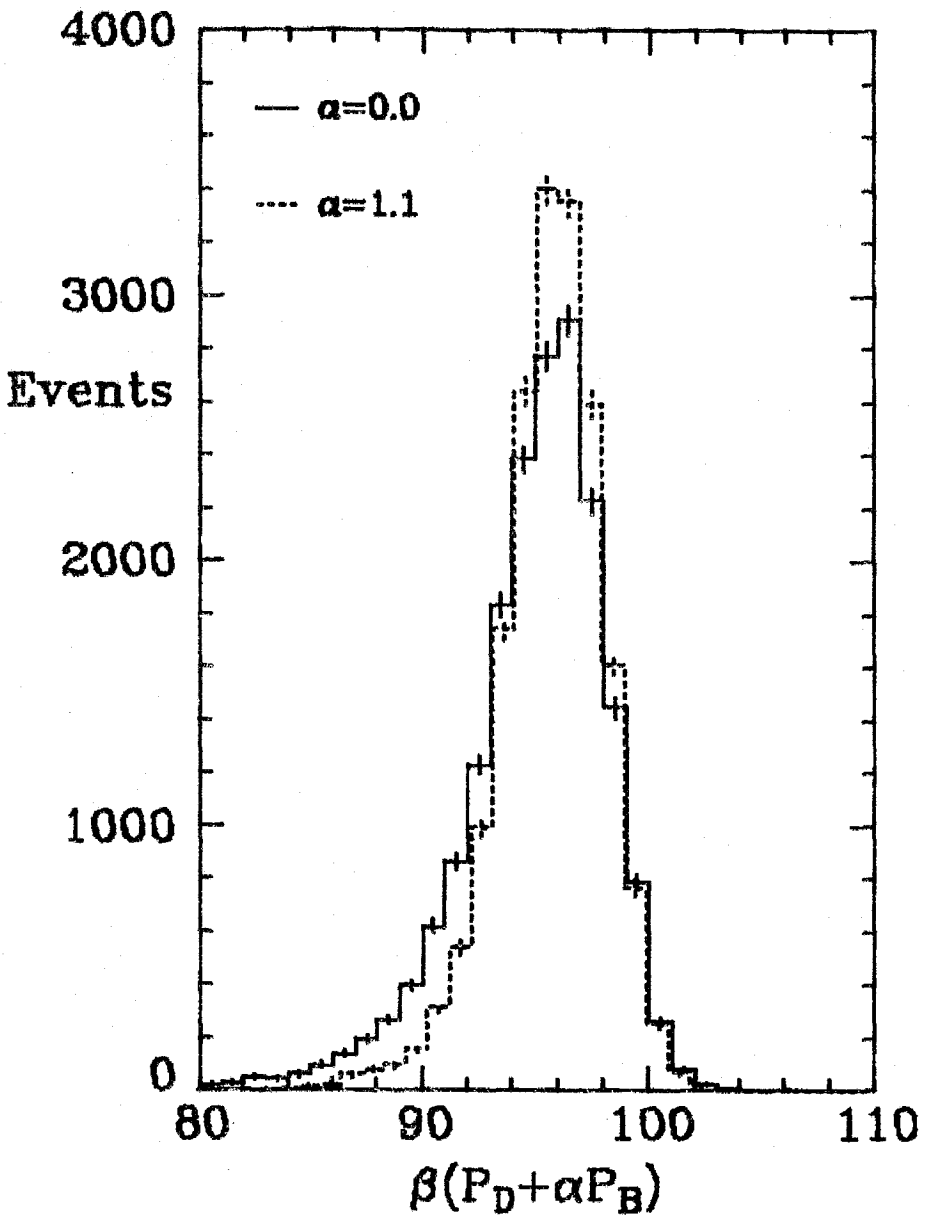

FIGURE 3.III.3 The uncorrected (α = 0.0) energy distribution for 99 GeV electrons compared to the distribution corrected using the backup counter with α = 1.1. The x-scale on the latter has been shifted so as to align the peaks.

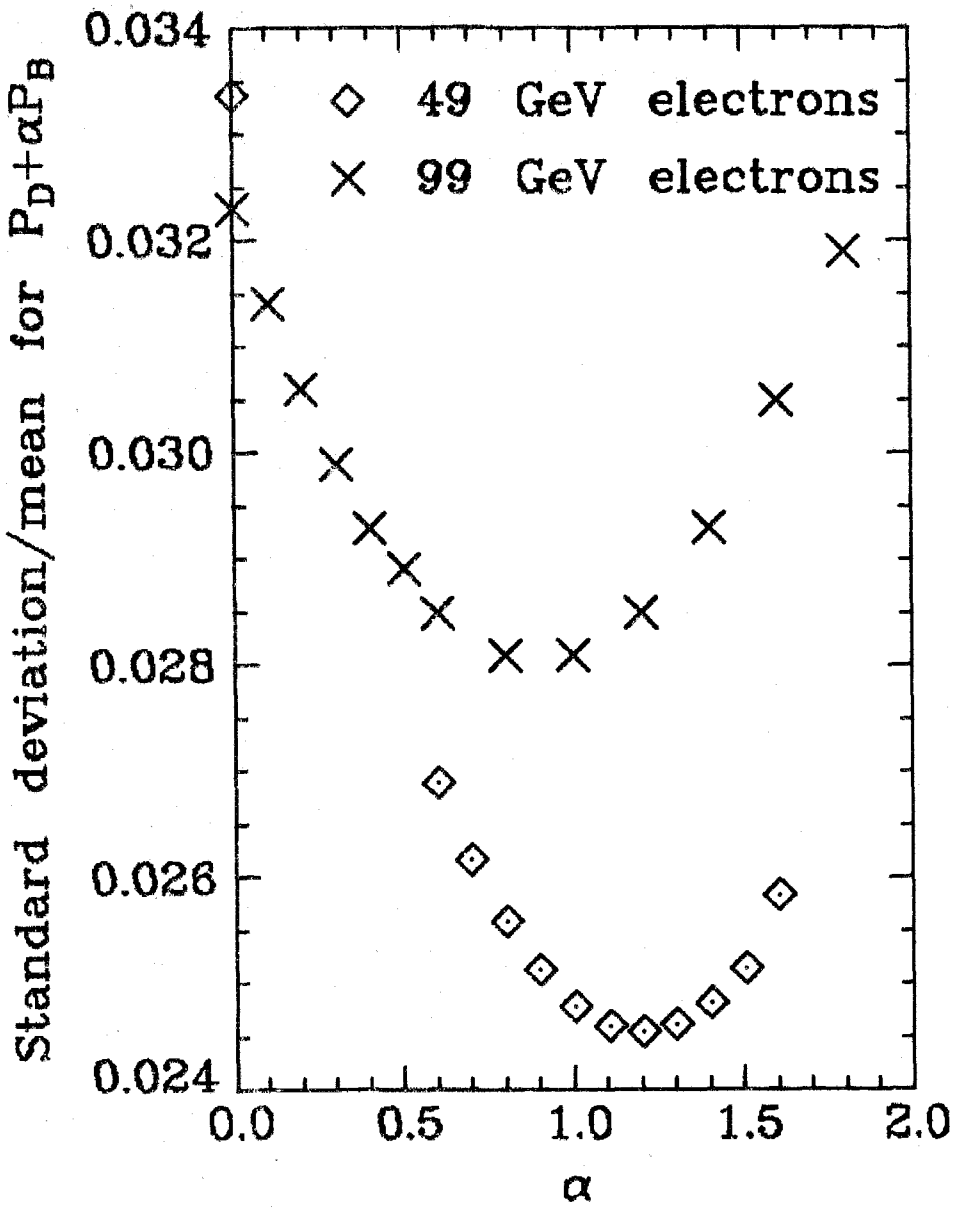

FIGURE 3.III.4 Standard deviation/mean of $P_D + \alpha P_B$ versus α for 49 and 99 GeV electrons.

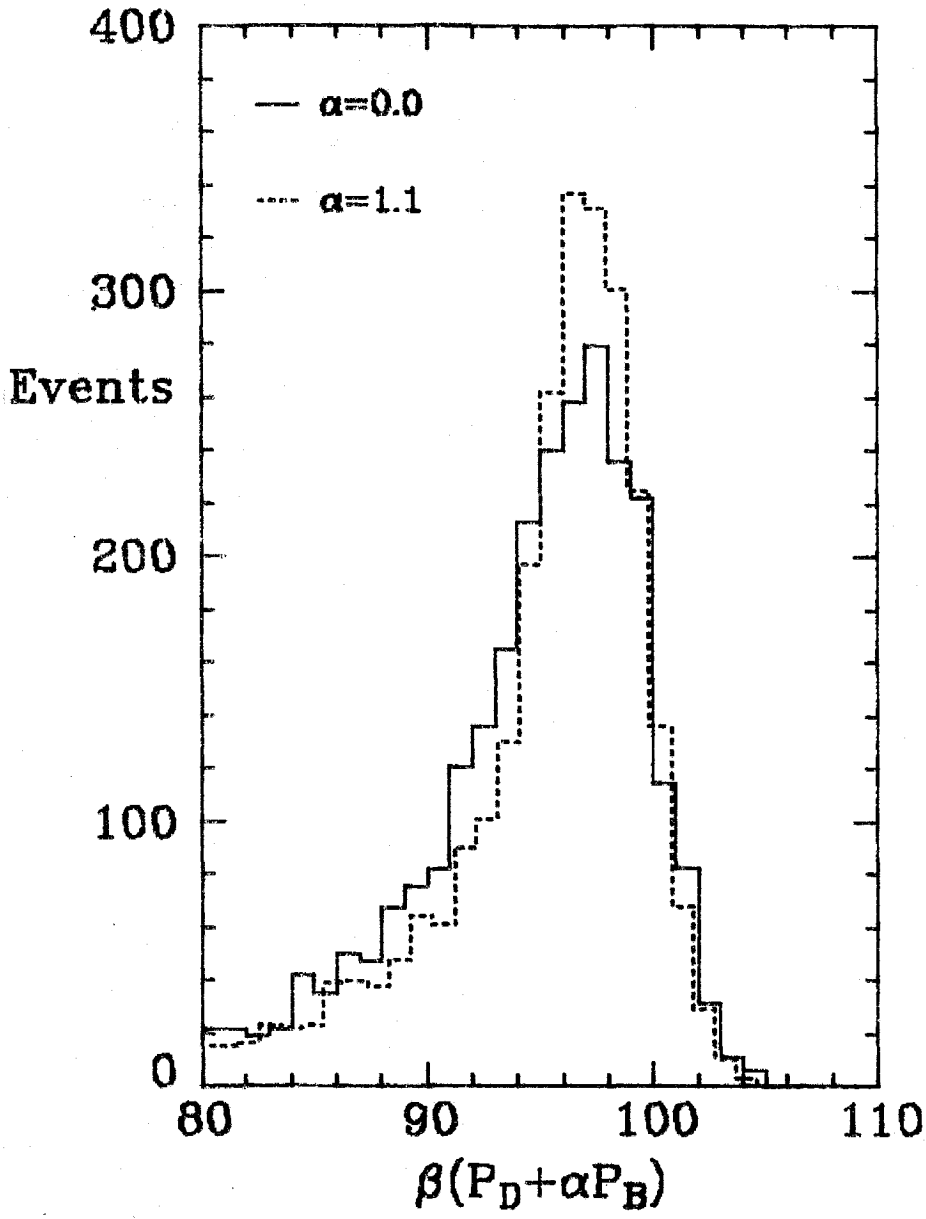

FIGURE 3.III.5 The uncorrected (α = 0.0) energy distribution for π^0 mesons from the NFS trigger with $t_m < 0.1$ GeV^2 and with the energy of the higher energy photon between 65 and 75 GeV for events with only two photons in the detector, compared with the energy distribution corrected for the backup counter with α = 1.1. The x-scale on the latter has been shifted so as to align the peaks.

factor, α, could be expected to be similar to that for electrons. However a 100 GeV π^0 is different from a 100 GeV electron in that it is composed of two showers instead of one, each of energy below 100 GeV. Since the photon showers generally commence with the production of electron-positron pairs, $\gamma + V \rightarrow e^- + e^+$ (where V denotes an external potential), whilst the electron showers generally start with the bremsstrahlung process, $e^- + V \rightarrow e^- + \gamma$, a π^0 might be expected to resemble four electron showers, with each electron shower starting deeper into the detector than the photon shower. So the value of α could differ between photons and electrons.

The quantity $P_D + \alpha P_B$ was histogrammed for various values of α and for different energy distributions among the two photons forming the π^0 meson. In Fig. 3.III.5 is shown the energy distribution for $\alpha = 1.1$ from π^0 mesons where the highest energy photon had an energy between 65 and 75 GeV. It is seen that the peak is narrower than for the uncorrected case and there is a smaller tail on the lower energy side of the peak. These results showed an improved resolution around the value $\alpha = 1.05$ which was finally used.

To correct for the leakage in the analysis of the data, it was decided for simplicity to use just the total energy deposited in the backup counter and to ignore its spatial distribution. From the results discussed above, the first correction tried was to multiply each pulse height from the photon detector by the factor

$$1 + \alpha P_B / P_D \qquad (3.III.7)$$

with $\alpha = 1.05$ and recalibrate accordingly to give the correct π^0 mass. When some events with two photons in the detector were refitted using this algorithm it was found that the response of the detector, that is, the variation of the mass obtained from the unconstrained fits with energy, became less linear than before. The algorithm was thus modified to give the correction factor

$$1 + \alpha(P_B - \sum_{i=1}^{n} \langle P_B(E_i) \rangle)/P_D. \qquad (3.III.8)$$

Here the mean pulse height expected in the backup counter from the energies, E_i, of the n photons present has been subtracted from the backup counter pulse height, P_B. It was assumed that this mean was the same as for the electrons which is given by (3.III.5).

In practice, the correction (3.III.8) could not be applied at the start of the event reconstruction process because the energy distribution among the photons was unknown. Hence a preliminary correction was made to each event by assuming that two photons were present with three-quarters and one-quarter of the total energy each. When the event had been analyzed up to the stage where the initial guesses for the energies were known, that is, just prior to fitting, then the pulse heights were recorrected. It was found that this method preserved the linearity of the detector response whilst improving the energy resolution.

Before making use of the backup counter in the analysis it was necessary to determine the relative gains of the ten photomultiplier

tubes. This was done in the off-line analysis by using the electron sweep to give the gains at the start of the data-taking run and then the source measurements were used to track the variation of the gains with time. Whilst sweeping over the 70 x counters of the photon detector, a fine scale sweep of the ten backup counters was being done simultaneously. Their pulse heights were recorded on tape and analyzed to obtain both the gains and the response of the detector to 100 GeV electrons as described above. From calculating the first moment,

$$\bar{x} = \sum_{j=1}^{10} x_j E_j / \sum_{j=1}^{10} E_j, \qquad (3.III.9)$$

for the central six counters and assuming that the counters were all of the same size, namely 7 counterwidths (1 counterwidth = 10.5 mm), it was found that the backup counters were displaced from the main detector by about 0.5 counterwidths, such that the first backup counter was approximately centered at the join of the third and fourth main detector counters.

The shape of the shower and the gains were found for the backup counters by minimizing the χ^2 given by

$$\chi^2 = \sum_{j=1}^{10} \sum_{i=-k}^{k} N_{ji}^2 (\overline{PH}_{ji} - g_j f_i)^2 / \overline{PH}_{ji} \qquad (3.III.10)$$

where g_j was the gain of the j^{th} backup counter, f_i was the expected pulse height in a backup counter when the electron beam was incident

at i counterwidths from its center, PH_{ji} was the recorded pulse height from the j^{th} backup counter and $\overline{PH}_{ji}$ was the mean of PH_{ji} over the number of events, N_{ji}, recorded in the j^{th} counter. k was chosen sufficiently large to include most of the shower shape. Minimizing this χ^2 resulted in the following expressions for f_i and g_j:

$$f_i = \sum_{j=1}^{10} (N_{ji}^2 g_j) / \sum_{j=1}^{10} (N_{ji}^2 g_j^2 / PH_{ji}) \qquad (3.III.11)$$

$$g_j = \sum_{i=-k}^{k} (N_{ji}^2 f_i) / \sum_{i=-k}^{k} (N_{ji}^2 f_i / \overline{PH}_{ji}). \qquad (3.III.12)$$

The final result for the backup counter shower shape, f_i, is shown in Fig 3.III.6.

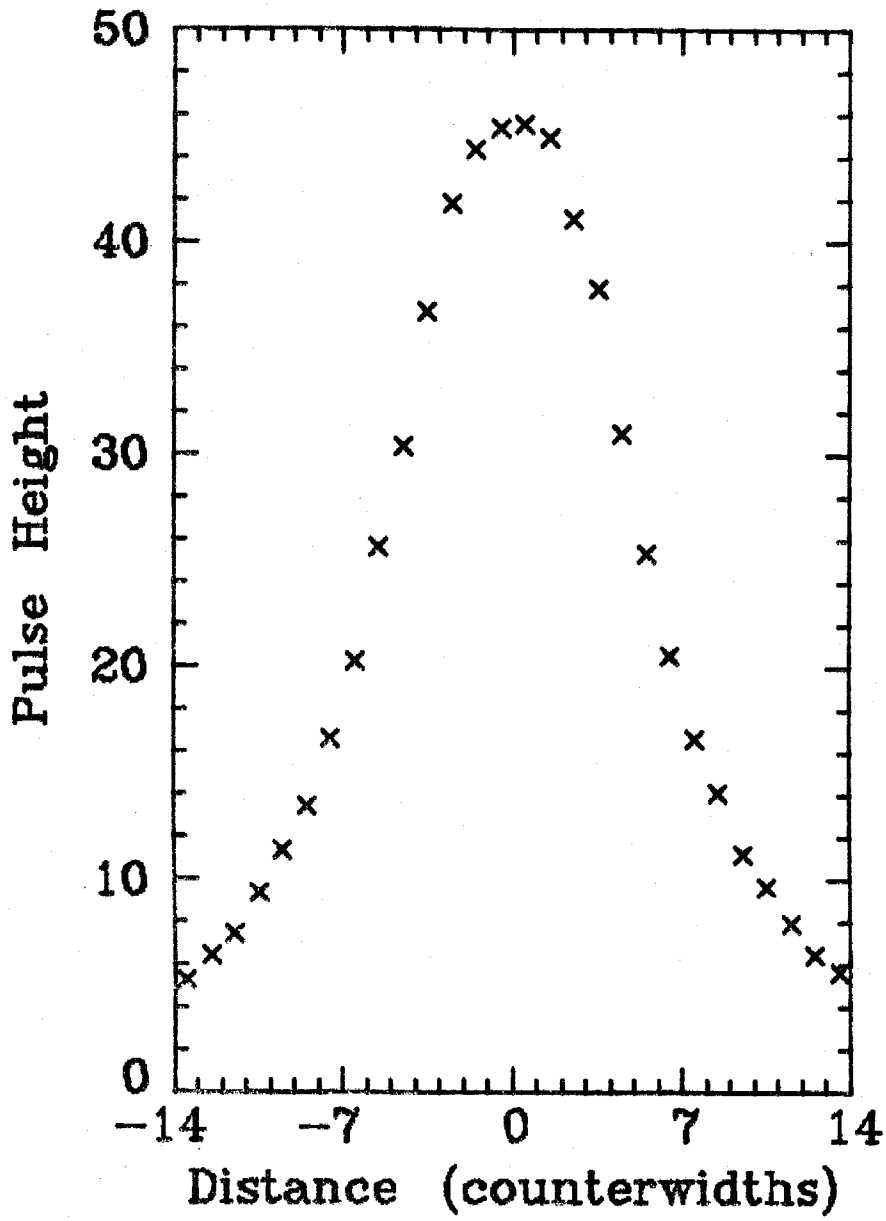

FIGURE 3.III.6 Backup counter shower shape: the distribution of pulse height with a 100 GeV electron beam incident at varying distances from it.

APPENDIX 3.IV

EVENT RECONSTRUCTION

The event reconstruction program used was called "TREAT" and its technical details are given in Ref. (Fo77a). A description of how it reconstructed events is given below. To start the search for photons, the counters in each view were first grouped into sectors. The pulse heights from counter 1 to counter 70 were scanned to find peaks where there was a maximum in the pulse height distribution and either one counter had a significant pulse height or two adjacent counters had a significant total pulse height. Then valleys were found between these peaks by finding which range of counters had low pulse heights and centering the valley at the middle of this range. When there were no counters with low pulse heights, the valley was centered at the counter with the minimum pulse height. Sectors were then defined which ran from one valley to the next, so that each sector contained one peak. Much of the remaining analysis used these sectors. They were later matched with sectors in the opposite view to form photons so that each sector contained between one and four photons. In the example shown in Fig. 3.1, four sectors labeled A, B, C and D have been found in the x view and three sectors labeled A, B and C in the y view. Hence this event would eventually be assigned at least four photons.

The range of each sector was now reduced by removing any counters with a very low pulse height. This would later lessen the range allowed for the positions of photons with centers in that sector and

the range used for fitting the shower shape. When only one counter remained in a sector, the event was rejected as this "spike" was probably from a charged particle interacting in the detector or from a photon hitting the light pipe of the counter. This cut out less than 0.1% of the events. It was the only analysis cut made to deal with charged particles since a visual scan of the events showed that they were not a problem.

A position was assigned to each sector by assuming that only one photon was present in it and using an empirically-determined algorithm based on the pulse height of the peak counter and the two adjacent counters. An energy was assigned by an iterative process using the predicted shower shape, which is described in Appendix 3.II. The first guess for each energy was obtained by adding up all the pulse heights of the counters in the sector. Then the tail of each photon outside its sector was calculated and added in and the tails of other photons which overlapped with this sector were subtracted. This was repeated with the improved energy guesses until the energies converged. For any sector with a peak at an edge counter (1 or 70) a position was assigned very near to the edge of the detector and the energy was assigned as the difference between the total energy and the energy of the other photons in the view. Events for which the energy so calculated was too negative or for which two or more peaks were at the edge were failed. This had little effect since a cut was later made to ensure that the photons

forming a particle were centered more than two counterwidths from any edge of the detector. The error in the energy of each photon was assigned along with the energy using the predicted deviation in the shower shape.

A secondary search of the sectors was now made to look for "shoulders" where a lower energy photon had its center near to another photon but was not separated by a distinct valley. These were found by using the sector positions and energies and the shower shape to predict the contributions of the highest energy photons to each sector. In each view, their predicted pulse heights were subtracted and the residual was searched for peaks. Tests were then made to check for the existence of secondary peaks and if one was found which was sufficiently separated from the original peaks then an extra sector was added for this sector by splitting one of the original sectors into two.

The two views were now paired together to find photons. This was done on the basis of a simple χ^2 formed from the sector energies and errors by assuming that the sectors corresponded to just one photon each. If an equal number of sectors, n, existed in the two views then pairings with n photons were tried. If the χ^2 was too large because the energies were not compatible between the views, a sector in each view was assigned two photons, giving a total of (n+1) photons. If there was one more sector in one view than in the other view, then two photons were assigned to just one sector in the

second view. If this was unsuccessful then two photons were assigned to one sector from the first view and either two photons each were assigned to two sectors or three photons were assigned to one sector in the second view. If there were three more sectors in one view than in the other view then only one algorithm was considered, namely that in which one sector in the second view was assigned four photons. The algorithm with the smallest number of photons having the least χ^2 from the sector energy pairing was tried first and a complete fit to the pulse heights, as described below, was made. Less likely algorithms were tried if this fit was unsuccessful until a successful fit had been made. Pairings with more photons were tried only if all pairings with fewer photons had failed. In the example shown on Fig. 3.1, the sectors have been paired together to give the photons at positions α, β, γ and δ.

After each pairing algorithm was chosen, guesses to the photon energies and the errors in them were assigned on the basis of the sector energies and errors. Initial guesses to the photon positions were also needed. When only one photon was present in a sector then the first guess for its position was just the center of the sector as determined when the peak was found. When more than one photon was present in a sector, the first guess for the position of the highest energy photon was again the peak position. The first guess for the position of the second highest energy photon was found by subtracting out the pulse heights from the highest energy photon

using the shower shape and taking the center of the counter with the highest remaining pulse height as its position. When no counters with significant pulse heights remained, its center was instead taken to be close to the peak counter. Further guesses at the positions were assigned using simple grids over the sector. For the third and fourth photons, a simple grid was again chosen, with the number of choices made depending on the width of the sector. The errors in the photon positions were also needed so that a χ^2 for the masses of photon pairs could be formed, as described below. When there were one or two photons assigned to a sector then the error in the photon position in this view was taken to be $0.26/\sqrt{E}$ counterwidths, where E was the guess to the photon energy in GeV. When there were three or more photons in a sector, the position error was taken to be half the number of consecutive counters with pulse heights greater than half that predicted at 0.6 counterwidths from the shower center.

The next stage in the analysis of an event was optional and involved looking for a particle in the event. Here only the two-photon decay modes of the π^0 and η mesons were considered. Fits to multi-photon particles such as K^0 mesons and $\pi^0\pi^0$ are also possible using TREAT and are described elsewhere (Co78). Using the energies, positions and their errors for the photons, the χ^2 for each pair of photons to have the mass of either a π^0 or an η was found. Fits were then tried for all pairs with a χ^2 below some value. In the example shown on Fig. 3.1, a π^0 was found formed from the photons at positions α and β.

The final stage was to fit the pulse heights to the predicted shower shape in order to find the best values for the energies and positions of the photons. This consisted of minimizing the χ^2 given by

$$\chi^2 = \sum_{v=1}^{2} \sum_{i=1}^{70} [\{P_i^v - \sum_{j=1}^{n} E_j S(d_{ij}^v, E_j)\}^2 / \sum_{j=1}^{n} E_j Q^2(d_{ij}^v)] \qquad (3.IV.1)$$

where P_i^v was the pulse height measured from counter i in view v, $E_j S(d_{ij}^v, E_j)$ was the predicted pulse height in counter i in view v from the j^{th} photon, of energy E_j, at distance d_{ij}^v from it, as described in Appendix 3.II, and $\sqrt{E_j} Q(d_{ij}^v)$ was the predicted deviation in this pulse height.

At this stage an option existed to constrain the mass, m, of the particle. In this case the energy of the lower energy photon, E_2, in the particle was taken to be

$$E_2 = m^2/(E_1 \theta_{lab}^2), \qquad (3.IV.2)$$

where E_1 was the energy of the other photon in the particle and the angular separation, θ_{lab}, was determined from the separation of the photons on the detector face by assuming that the interaction took place at the midpoint of the target. This approach reduced the number of parameters by one but did not take into account the inherent spread in the mass distribution due to the finite length of the target. Such a fit was called a "constrained fit" whereas one with no mass requirement was called an "unconstrained fit".

The nonlinear fit for the energies and positions of the photons was done using Marquardt's method (Ma63) with analytic derivatives, since this was found to be the fastest reliable method.

APPENDIX 3.V

DETERMINATION OF THE ENERGY THRESHOLD OF THE TRIGGER

The energy threshold of the trigger varied with the distance of a photon shower from the photomultiplier tubes. This happened because the discriminator cut on the peak pulse height instead of on the integral of the pulse height, and the shape of a pulse depended on the relative times of arrival at the phototube cathode of the light which traveled directly and that reflected from the end of the counter. The events which occurred near the phototubes required more energy to trigger than those further from them. The effect was noticed during the 100 GeV running period and a second discriminator was then used. The variation of the threshold energy with position was studied for each trigger type and the same cuts were applied to the data and to the events simulated by Monte Carlo techniques for the acceptance calculation (see Appendix 3.VII). An uniform energy cut could have been applied over the entire detector, but this would have eliminated too many events!

An experimental setup was designed to study the trigger response. The hydrogen was removed from the target and the beam was focused onto a piece of lead placed directly in front of the detector. The thickness of the lead (40 mm) was chosen so that electrons and pions were produced with a fairly flat energy spectrum and formed a localized spot on the detector. The detector was positioned with the spot centered on counter 35 in either the x or the y plane and events

were triggered on the energy in this plane. The detector was moved along this counter so that the pulse height spectrum could be measured at various distances along the counter. The results for both discriminators are shown on Fig. 3.V.1. The points correspond to the pulse height at which the triggering efficiency was 50%: the trigger was fully efficient about 20 pulse height units higher. The curves shown for the first discriminator correspond to the medium and high bias triggers used in this experiment, whilst the curves shown for the second discriminator do not correspond to particular biases as these data were collected before deciding where to set the bias levels for use with the second discriminator. The second discriminator was clearly much better than the first and the two planes of the first discriminator were also set at rather different levels. 1 GeV corresponds to approximately 27 pulse height units, so it is seen that the high bias x trigger required 90 GeV to trigger at the phototube end compared with only 70 GeV at the opposite end!

This experimental study did not cover all the biases used in this experiment but an extrapolation of these results to other biases could be made by assuming that the response was linear. A check on this extrapolation was made using the triple Regge data itself. Since the plane in which an event triggered was not recorded, this study used the data from trigger B with only one π^0 present in the detector which fell in one of the three regions: [$x > 35$, $18 < y < 53$], [$x < 35$, $y > 53$] or [$x < 35$, $y < 18$], where the positions

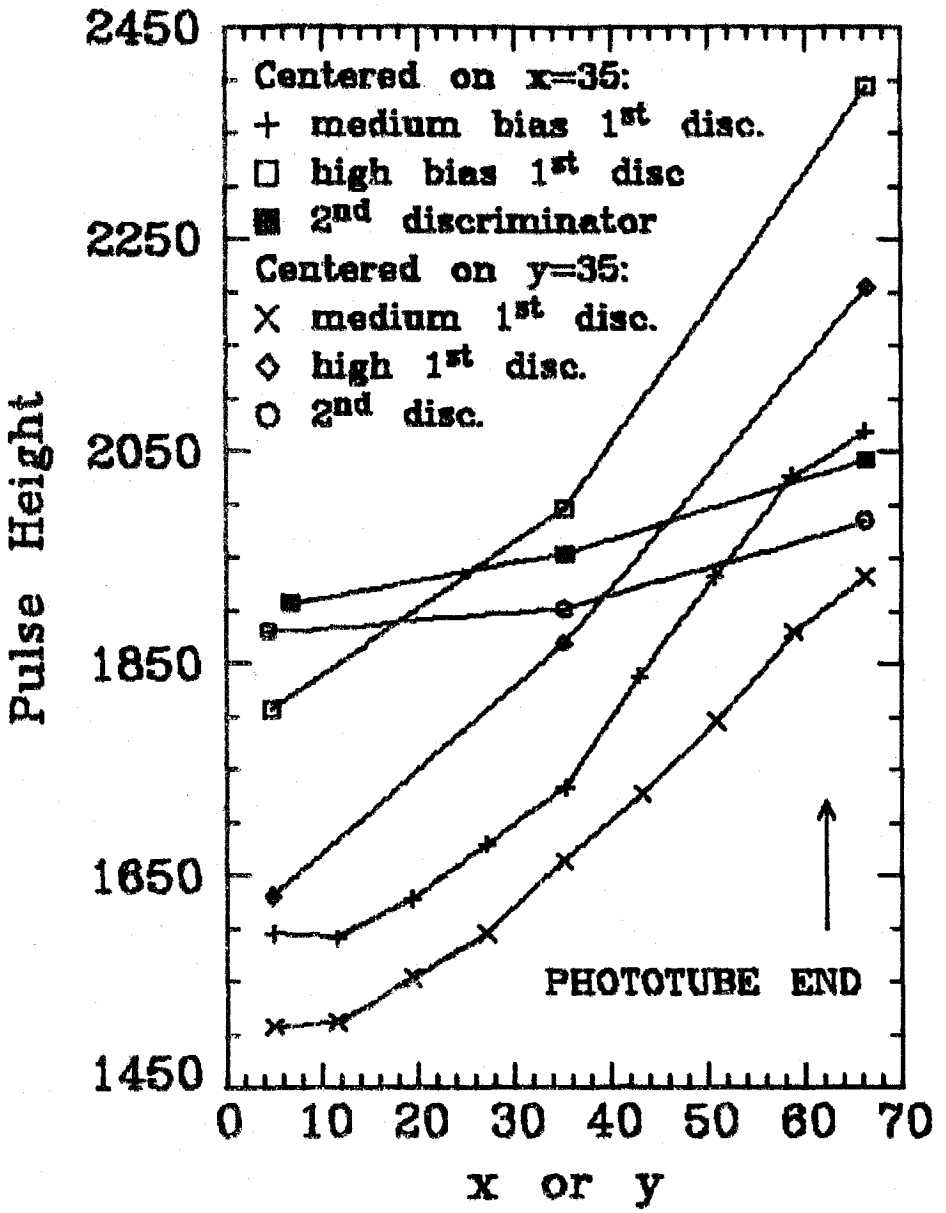

FIGURE 3.V.1 The pulse height required to trigger an event for the two discriminators used in this experiment.

refer to the center of the counters and one unit is the width of a counter. Because of the trigger B geometry, π^0 mesons falling in the first region were triggered by the x-view and those falling in the second and third regions were triggered by the y-view. During this study it was discovered that the mixer covering y counters 53 - 66 was faulty and photons in the second region often failed to trigger. The higher bias data were compared with the lower bias data, which gave the energy-dependence in the region of the cut-off. The results from this study agreed with those shown in Fig. 3.V.1 for the medium and high bias triggers taken with the first discriminator. The final cuts used for the high bias triggers with the two discriminators are shown in Fig. 3.V.2. The energy deposited was required to be at least 7.5% above these cuts. For the low bias trigger A, the medium bias trigger A and the medium bias trigger B taken with the first discriminator, the cuts were put at 72%, 94% and 88% of the high bias cut respectively. For the low and medium bias triggers taken with the second discriminator, the cuts were put at 66% and 89% of the high bias cut respectively.

A check that the triggers were fully efficient above these cuts is illustrated by Figs. 3.V.3-6. The quantity R is defined by

$$R = \max\left(\sum PH_x/C_x^1(y),\ \sum PH_y/C_y^1(x)\right), \qquad (3.V.1)$$

where the summation is over the photons in the event, PH_x and PH_y are the total pulse heights due to each photon in the x and y views

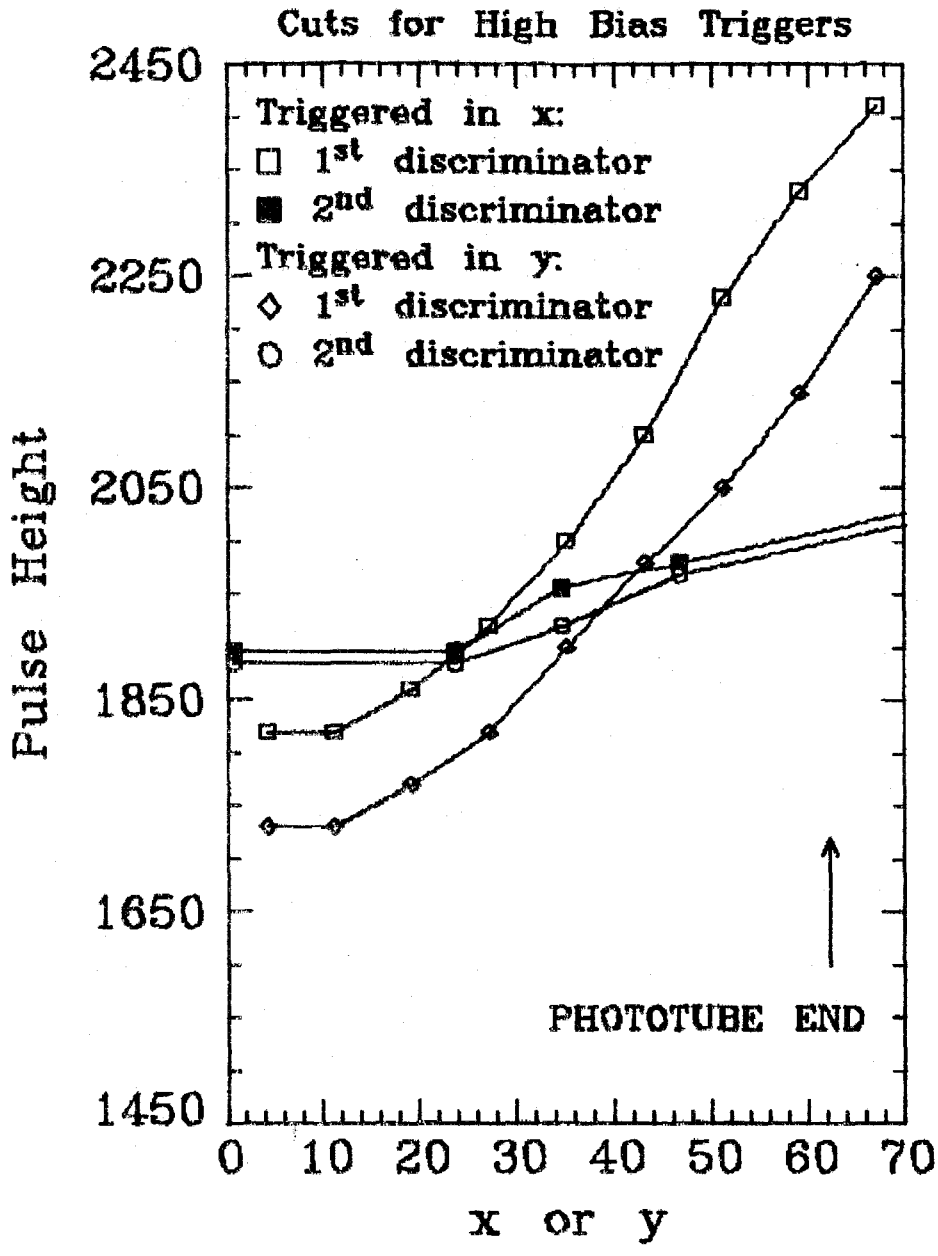

FIGURE 3.V.2 The cuts used in the data analysis for the high bias triggers for the two discriminators.

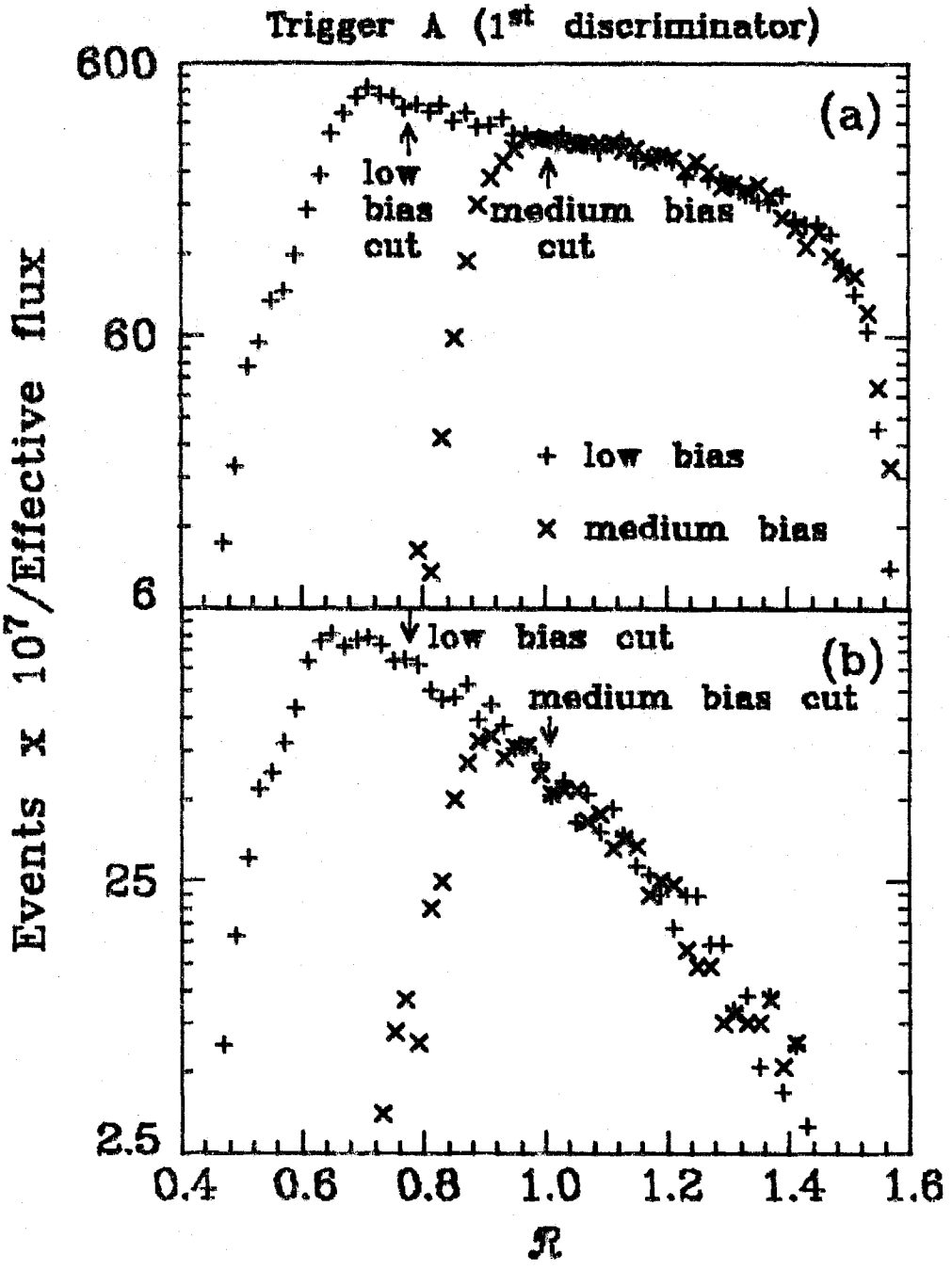

FIGURE 3.V.3 The distribution of R, defined by (3.V.1), for π^0 and η mesons produced from a π^+ beam with a full target using the first discriminator for (a) $-t < 0.5$ GeV^2 and (b) $-t > 0.5$ GeV^2.

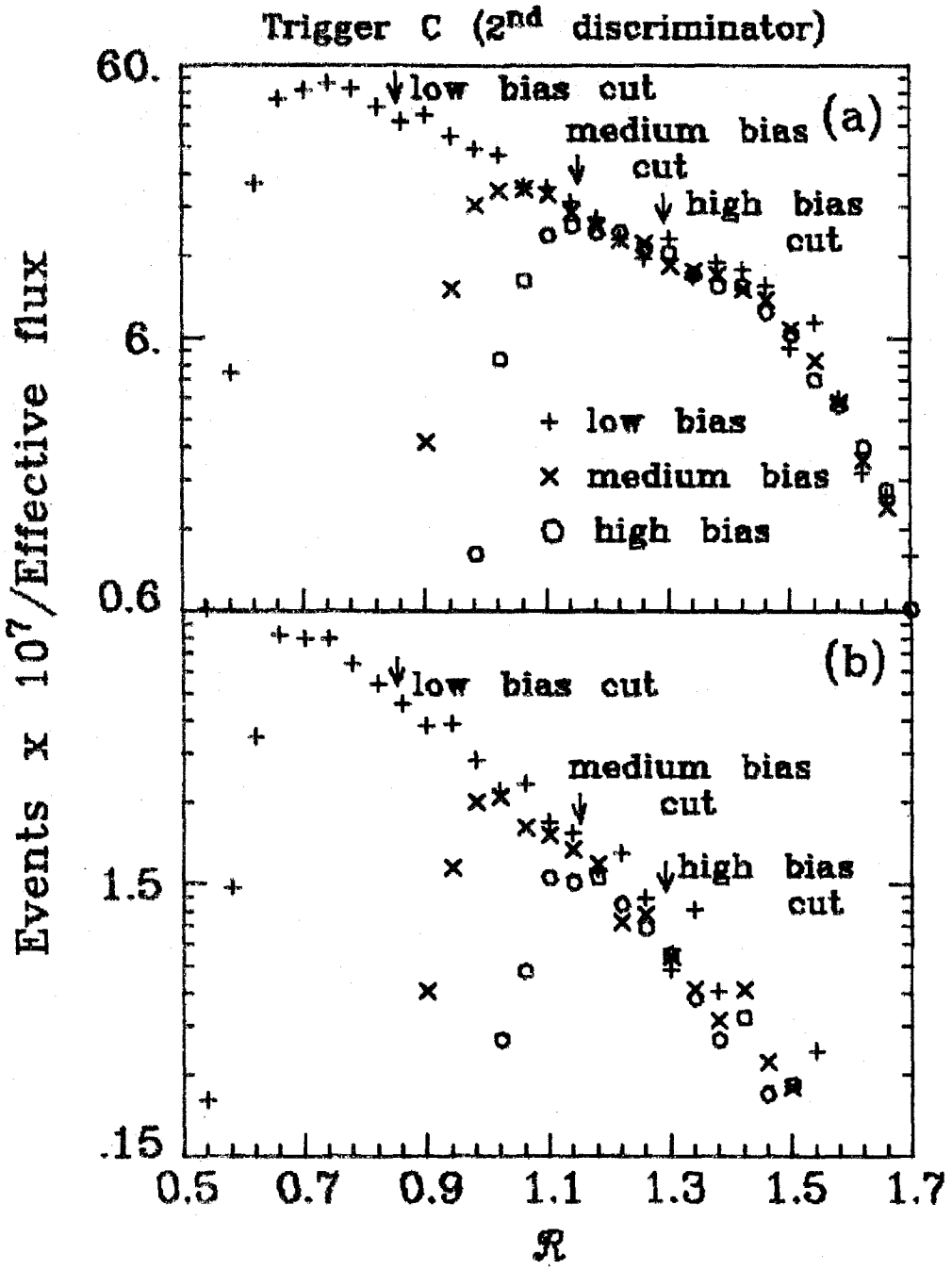

FIGURE 3.V.4 The distribution of R, defined by (3.V.1), for π^0 and η mesons produced from K^- and $\bar{p}$ beams with a full target using the second discriminator for (a) $-t < 0.5$ GeV^2 and (b) $-t > 0.5$ GeV^2.

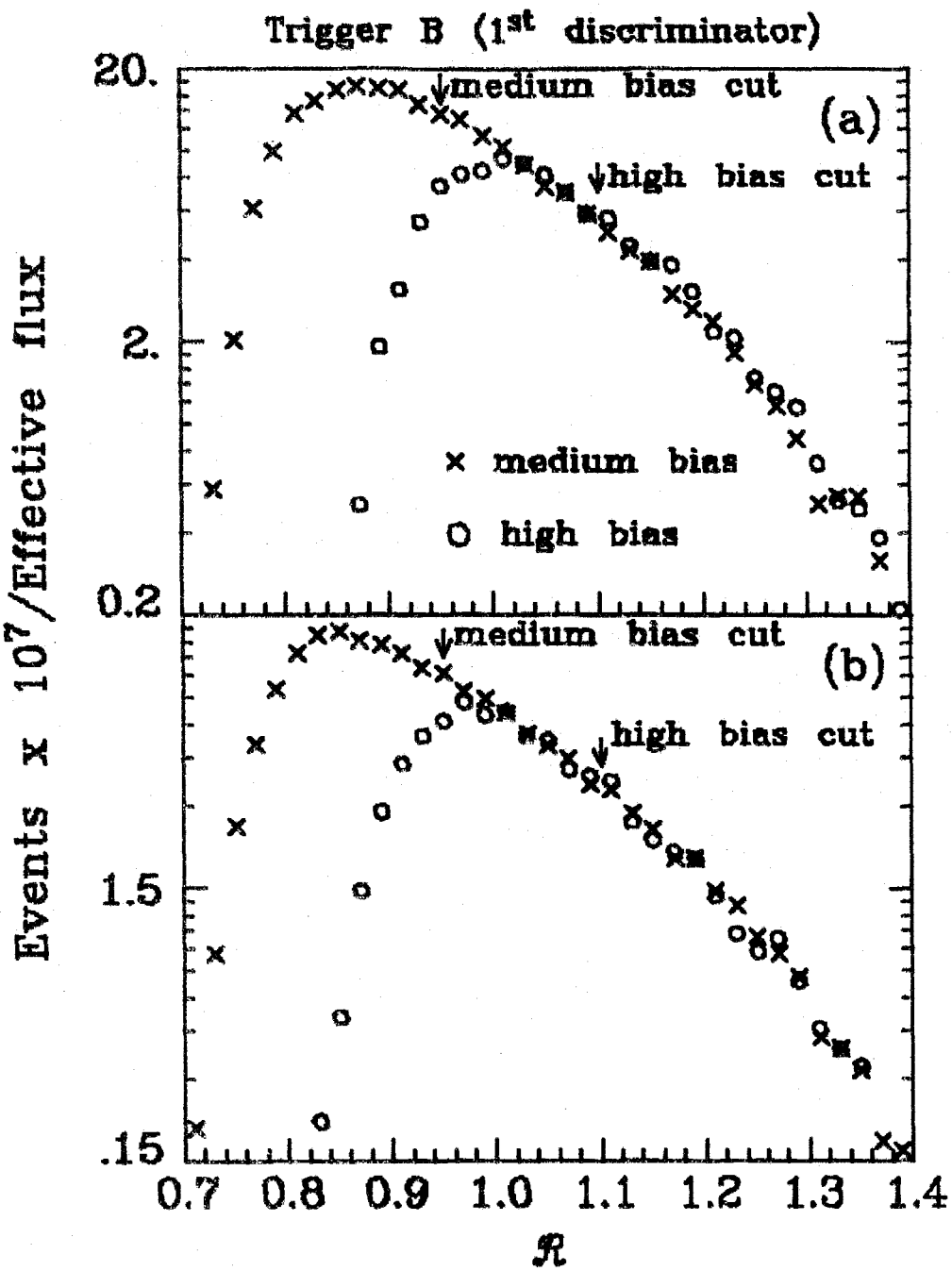

FIGURE 3.V.5 The distribution of R, defined by (3.V.1), for π^0 and η mesons produced from a π^- beam with a full target using the first discriminator for (a) $1.0 < -t < 1.5$ GeV^2 and (b) $-t > 1.5$ GeV^2.

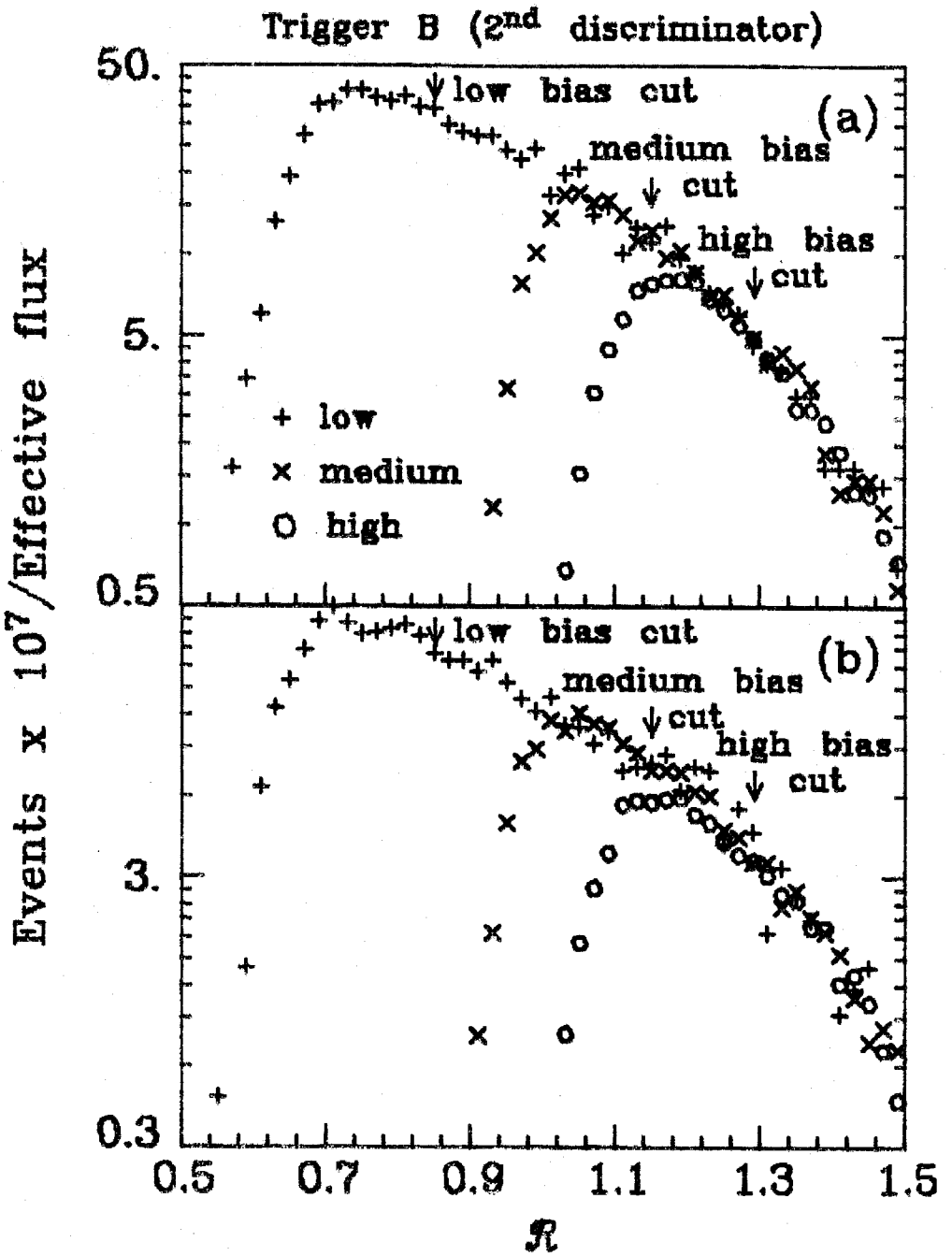

FIGURE 3.V.6 The distribution of R, defined by (3.V.1), for π^0 and η mesons produced from a π^- beam with a full target using the second discriminator for (a) $1.0 < -t < 1.5$ GeV^2 and (b) $-t > 1.5$ GeV^2.

and C_x^i and C_y^i are the cuts used for discriminator i for events triggered in the x and y views respectively. C_x^1 and C_y^1 are the cuts shown on Fig. 3.V.2 whilst C_x^2 and C_y^2 were set at 80% of the values shown on Fig. 3.V.2. For triggers A and C (Figs. 3.V.3,4) all events passing the analysis cuts with only two photons in the detector were used. For trigger B (Figs. 3.V.5,6) only events with two photons in the detector with the particle in the region [$y < 17$] or [$x > 36$, $y < 54$] were included. It is seen that all the trigger biases were fully efficient at the positions of the cuts.

APPENDIX 3.VI

CALCULATION OF THE π^0 AND η SIGNALS

The constrained fits (described in Chapter 3) did not distinguish the π^0 and η signals from the background in the same mass regions due to uncorrelated photons. The mass spectra from the unconstrained fits were therefore used to determine this background. The spectra for events with two photons in the detector are shown in Figs. 3.3 and 3.4. The π^0 and η signals were determined by subtracting smooth backgrounds, which were found by fitting polynomials to the mass regions on each side of the particle peaks. These were 0.060 - 0.104 GeV and 0.174 - 0.218 GeV for the π^0 and 0.400 - 0.475 and 0.625 - 0.700 for the η.

The π^0 and η signals were found as a function of the energy, E, and the laboratory production angle, $\Omega = p_t/E$, for various beams and triggers. Histograms were collected of the masses of the two-photon combinations from events with successful unconstrained fits for 10 GeV ranges in the energy of the two-photon combination and in 0.002 steradian ranges in Ω. The events with only two photons in the detector (called "2γ" in the tables) and those with more than two photons in the detector (called "$>2\gamma$") were considered separately as the backgrounds were much larger in the latter case, as shown in Tables 3.VI.1-3. About one-sixth of the events had more than two photons in the detector (see Table 3.2) and the lower energy data had higher multiplicities than the higher energy data. The

TABLE 3.VI.1 Background/signal for full inclusive reactions from a π^- beam.

			$\pi^- p \to \pi^0 X$		$\pi^- p \to \eta X$	
Trigger	Ω	Energy	2γ	$>2\gamma$	2γ	$>2\gamma$
A	all	60 - 65	0.002	0.04	0.14	6
A	all	65 - 75	0.001	0.03	0.08	3
A	all	75 - 85	0.001	0.03	0.05	6
A	all	> 85	0.000	0.01	0.02	4
A	0.000 - 0.002	> 60	0.001	0.04	0.08	no signal
A	0.002 - 0.004	> 60	0.001	0.03	0.06	3
A	0.004 - 0.006	> 60	0.001	0.03	0.05	3
A	0.006 - 0.008	> 60	0.003	0.04	0.05	2
A	0.008 - 0.010	> 60	0.002	0.02	0.05	4
A	0.010 - 0.014	> 60	0.001	0.02	0.09	2
A	> 0.014	> 60	0.001	0.01	0.29	3
B	> 0.012	60 - 65	0.0010	0.017	0.10	3
B	> 0.012	65 - 75	0.0007	0.013	0.09	1
B	> 0.010	75 - 85	0.0006	0.011	0.09	2
B	> 0.010	> 85	0.0004	0.006	0.15	1
B	0.012 - 0.014	> 60	0.0011	0.015	0.09	2
B	0.014 - 0.016	> 60	0.0010	0.016	0.10	1
B	0.016 - 0.018	> 60	0.0012	0.019	0.17	2
B	> 0.018	> 60	0.0017	0.027	0.18	2

TABLE 3.VI.2 Background/signal for NFS reactions from a π^- beam.

			$\pi^- p \to \pi^0 X^0$		$\pi^- p \to \eta X^0$	
Trigger	Ω	Energy	2γ	>2γ	2γ	>2γ
NFS	all	15 - 25	0.05	0.23	no signals	
NFS	all	25 - 35	0.02	0.18	no signals	
NFS	all	35 - 45	0.006	0.15	no signals	
NFS	all	45 - 55	0.002	0.10	1.1	5
NFS	all	55 - 65	0.002	0.06	0.19	4
NFS	all	65 - 75	0.001	0.04	0.11	3
NFS	all	75 - 85	0.0005	0.02	0.04	1
NFS	all	85 - 95	0.0002	0.009	0.03	1
NFS	all	> 95	0.0001	0.004	0.007	0.4
NFS	0.000 - 0.002	> 15	0.0004	0.14	0.03	9
NFS	0.002 - 0.004	> 15	0.0004	0.13	0.02	4
NFS	0.004 - 0.006	> 15	0.0009	0.13	0.02	20
NFS	0.006 - 0.008	> 15	0.002	0.13	0.04	14
NFS	0.008 - 0.010	> 15	0.003	0.13	0.09	14
NFS	0.010 - 0.014	> 15	0.005	0.10	0.23	11
NFS	> 0.014	> 15	0.007	0.07	0.13	14
NFS	0.000 - 0.002	> 55	0.0002	0.06	0.02	6
NFS	0.002 - 0.004	> 55	0.0002	0.04	0.01	5
NFS	0.004 - 0.006	> 55	0.0006	0.04	0.02	9
NFS	0.006 - 0.008	> 55	0.0007	0.04	0.02	3
NFS	0.008 - 0.010	> 55	0.0010	0.04	0.02	2
NFS	0.010 - 0.014	> 55	0.0008	0.02	0.13	1
NFS	> 0.014	> 55	0.0005	0.02	0.03	1

TABLE 3.VI.3 Background/signal for K^- and $\bar{p}$ beams. No signal was present for the multi-photon η events from the K^- beam.

		$K^-p \to \pi^0 X$		$K^-p \to \eta X$	$\bar{p}p \to \pi^0 X$	
Ω	Energy	2γ	$>2\gamma$	2γ	2γ	$>2\gamma$
all	55 - 65	0.003	0.15	0.11	0.001	0.04
all	65 - 75	0.004	0.13	0.04	0.002	0.02
all	75 - 85	0.002	0.07	0.04	0.000	0.06
all	> 85	0.001	0.06	0.01	0.000	0.05
0.000 - 0.002	> 55	0.002	0.30	0.02	0.000	0.04
0.002 - 0.004	> 55	0.002	0.15	0.02	0.001	0.02
0.004 - 0.006	> 55	0.001	0.09	0.03	0.001	0.02
0.006 - 0.008	> 55	0.002	0.14	0.01	0.000	0.04
0.008 - 0.010	> 55	0.003	0.14	0.04	0.000	0.03
0.010 - 0.014	> 55	0.003	0.04	0.06	0.002	0.03
> 0.014	> 55	0.005	0.06	0.32	0.000	no data

histograms were collected for the full and empty target data separately and then the empty target data, divided by the effective flux, were subtracted from the full target data, divided by the effective flux, as in (3.4.1). A linear background of the form, A + B x mass, described most of the bins. The ratios of the background in the mass region 0.12 - 0.15 GeV to the π^0 signal and of the background in the mass region 0.5 - 0.6 GeV to the η signal are shown in Tables 3.VI.1-3. The ratio of the background to the signal was larger for

TABLE 3.VI.4 Coefficients, a, b and c, for the weighting function, (3.VI.1) for the various triggers.

	Trigger:		A	B	NFS	NFS	C	C
	Beam:		π^-	π^-	π^-	π^-	K^-	$\bar{p}$
	Energy:		> 60	> 60	> 55	> 15	> 55	> 55
particle	# γ	coeff						
π^0	2	a	0.388	1.08	-0.285	0.111	-8.77	-3.91
		b	1.000	0.983	0.995	1.007	1.395	1.123
		c	0.033	0.039	0.0368	0.0017	-0.392	-0.067
	> 2	a	5.9	-3.2	-2.97	6.334	15.5	8.4
		b	1.34	1.337	0.805	0.818	1.15	5.4
		c	-0.340	-0.168	0.235	0.205	-0.297	-6.57
η	2	a	-1.37	-12.1	-4.28		-6.68	
		b	0.764	1.022	1.465		0.808	
		c	0.267	0.119	-0.393		0.244	
	> 2	a	-812.5	-22.0	1133.		0	
		b	0.34	-0.088	0.06		0	
		c	-0.59	1.25	0		0	

the multiphoton events than for the two photon events because the background was larger due to the many pairings possible for the multiphoton events. It was larger for the η than for the π^0 since the η signal was reduced by its small acceptance and its lower cross section.

The number of events with successful constrained fits was found for each bin. The ratios of the signal to the number of constrained events gave weights which were then expressed as functions of Ω and E of the form,

$$\text{weight}(\Omega,E) = \max[(1 + a\Omega)(b + 0.01cE),0]. \quad (3.VI.1)$$

The coefficients, a, b and c, found using the above approach are summarized in Table 3.VI.4. Each constrained event used in the cross section determination was weighted accordingly. For the lower bias data, extrapolations of (3.VI.1) were made since there were insufficient data to warrant a detailed study of the background below 60 GeV. The weights for the positive polarity beam data were assumed to be the same as those for the negative polarity beam data.

APPENDIX 3.VII

ACCEPTANCE CALCULATION

The acceptance is the probability for an event to be included in the final selection of events used for the cross section determinations. In this experiment, the acceptance was a function of the energy, E, the transverse momentum, p_t, and the mass of the particle. The acceptance was calculated by simulating events by Monte Carlo techniques. It was found separately for the π^0 and η mesons and as a function of E and the angle, $\Omega = p_t/E$, at which the particle was produced in the laboratory frame. These variables were chosen because the discriminator cut was largely a function of E and the geometrical cuts were mainly functions of Ω. The procedure used for applying the acceptance correction to the data is summarized on Fig. 3.2.

The acceptance was calculated in two parts, which were later multiplied together to give the total acceptance. The first part was the probability for both photons from a particle to hit the detector. A grid was chosen with 43 points in Ω between 0 and 0.027 and with energy points at 5 GeV intervals between 25 and 100 GeV for π^0 mesons and between 45 and 100 GeV for η mesons. 20,000 decays of π^0 and η mesons were generated at each grid point. The direction of the incident particle was generated using an empirical distribution of the beam intersection point at the detector, determined using the beam hodoscopes described in Section 2.2, as this was found to

provide an adequate description of the beam direction. The interaction was assumed to occur uniformly along the length of the target. The decay of the π^0 or η into two photons was generated isotropically in the center of momentum frame. The photons were then Lorentz-transformed to the laboratory frame and the positions where the photons hit the plane of the detector were calculated. The fraction of events with both photons hitting the detector gave the desired probability.

The second part of the acceptance calculation involved finding the probability of particles with both photons in the detector passing the cuts to be accepted for inclusion in the cross section determination. For this part of the calculation, a coarser grid of points in Ω was chosen with a finer grid where the acceptance varied most. The energy grid for π^0 mesons was 20, 30, 40, 45, 50, 55, 60, 65, 70, 75, 80, 90 and 100 GeV. The energy grid for η mesons was 40, 50, 55, 60, 65, 70, 72, 75, 80, 85 and 100 GeV, with 90 GeV for trigger B only. Events were again simulated by Monte Carlo techniques but now pulse heights were generated for those events with both photons falling within the detector. The contribution to the pulse height at each counter from a photon was generated using a Gaussian distribution with mean given by the shower shape and σ given by the predicted fluctuation about the shower shape (described in Appendix 3.II). It was found that photons simulated using Poisson distributions for the fluctuations gave similar results and so it was concluded that the results did not depend on the assumed

distribution.

About 5000 events were thrown for each value of Ω and E. The pulse heights were recorded on tape so as to look just like a data summary tape. They were then fitted to find the energies and positions of the photons using the same analysis program, TREAT, as used for analyzing the data (see Appendix 3.IV), with the requirement that a 2-photon particle be present, whose mass was then constrained in the fit. Most of the events were fitted successfully at low Ω and medium energies. The largest failure rate, about 2% for π^0 mesons, occurred at high energy at the values of $\Omega \simeq 0.02$ corresponding to the top and bottom edges of the detector. About two-thirds of this was due to photons landing near to the edge of the detector and failing the sector-finding algorithm and about one-third was due to the two photons having a mass significantly different from the π^0 mass. The overall failure rate was about 0.2%. Most of these events would have been failed later by the secondary set of cuts imposed on the positions of the photons forming a π^0 and on the χ^2 of the fit. There may however have been a bias in that the Monte Carlo events were generated without the background photons which are present in real events and which would increase the failure rate.

The same cuts were now applied to the results of these fits as to the data, as described in Section 3.4. Each event was considered eleven times over so that the cuts for each trigger could be applied. Several of the trigger types were repeated as two different discriminators (Appendix 3.V) had been used to apply the hardware energy cut.

The discriminator cut was applied to the energy with which the particles had been generated instead of the energy resulting from the fit. This was done by scaling the fitted energies of both photons by the ratio of the energy at which the event was generated to the fitted energy. In addition it was required that the energy of the particle found by the fit was not more than 5 GeV less than that at which it was thrown. This eliminated any three-photon events found by TREAT. Such misfits cause a "feeddown" effect from the higher to the lower energies. However only 0.1% of the Monte Carlo events failed on this cut and so the effect is not likely to form an important bias for the full inclusive cross sections, which fall with energy, but it may cause a bias in the low t_m NFS cross sections, which rise with energy.

The acceptance found from the second part of the calculation was largely flat as a function of Ω except at those values corresponding to an edge of the detector being hit. It also varied little with energy except in the region of the trigger bias, where it varied sharply in a region of a few GeV. Extra energy points were added by using the events generated at the closest energies to the new grid points and multiplying the pulse heights by the ratio of these energies. This technique was used to generate points at 22 additional energies for π^0 mesons for selected triggers.

In Figs. 3.VII.1 and 2 are shown the total acceptance for π^0 mesons produced from a 99.2 GeV pion beam as a function of their energy and four-momentum-transfer-squared, t, from three different

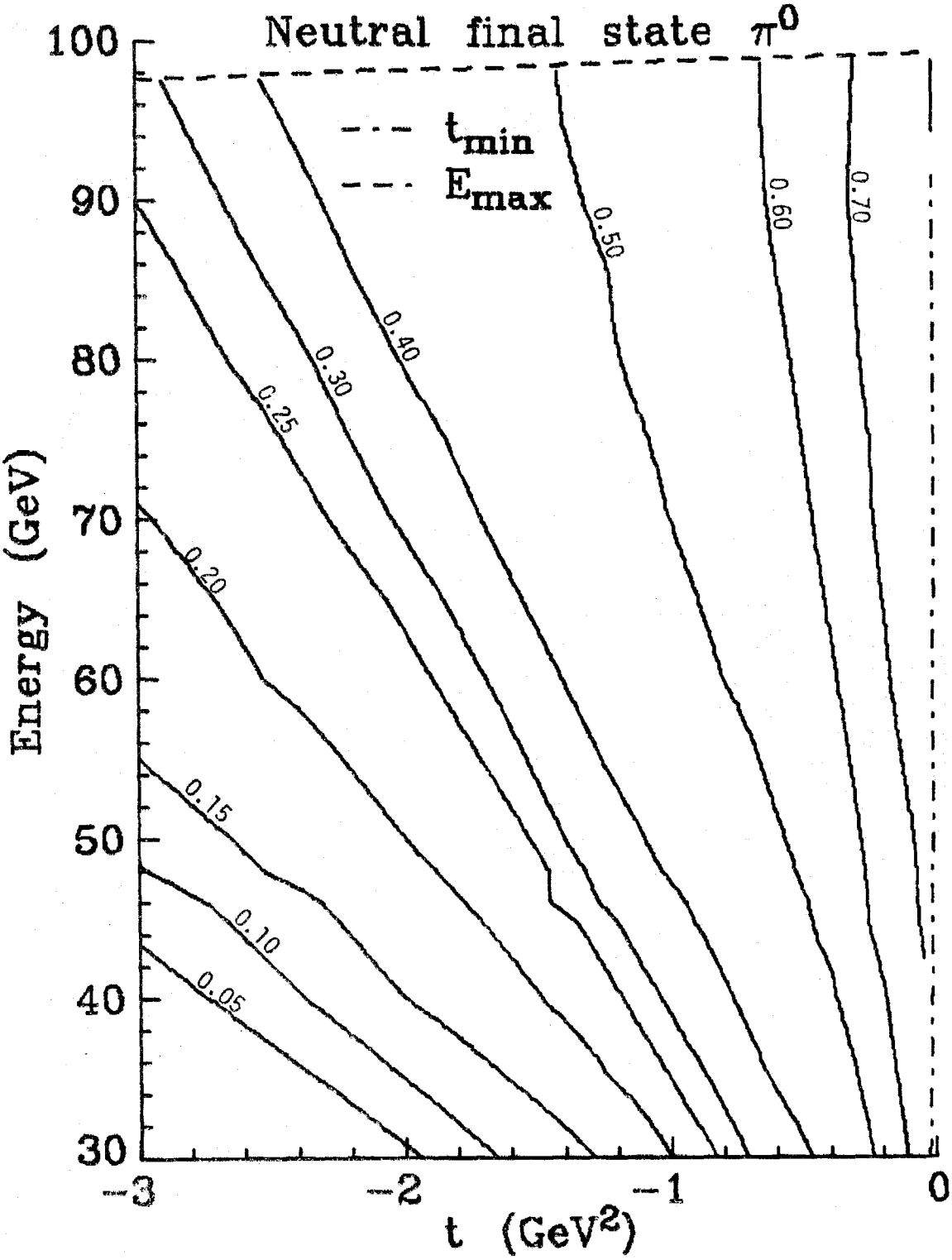

FIGURE 3.VII.1 Acceptance for π^0 mesons from a 99.2 GeV pion beam for the NFS trigger.

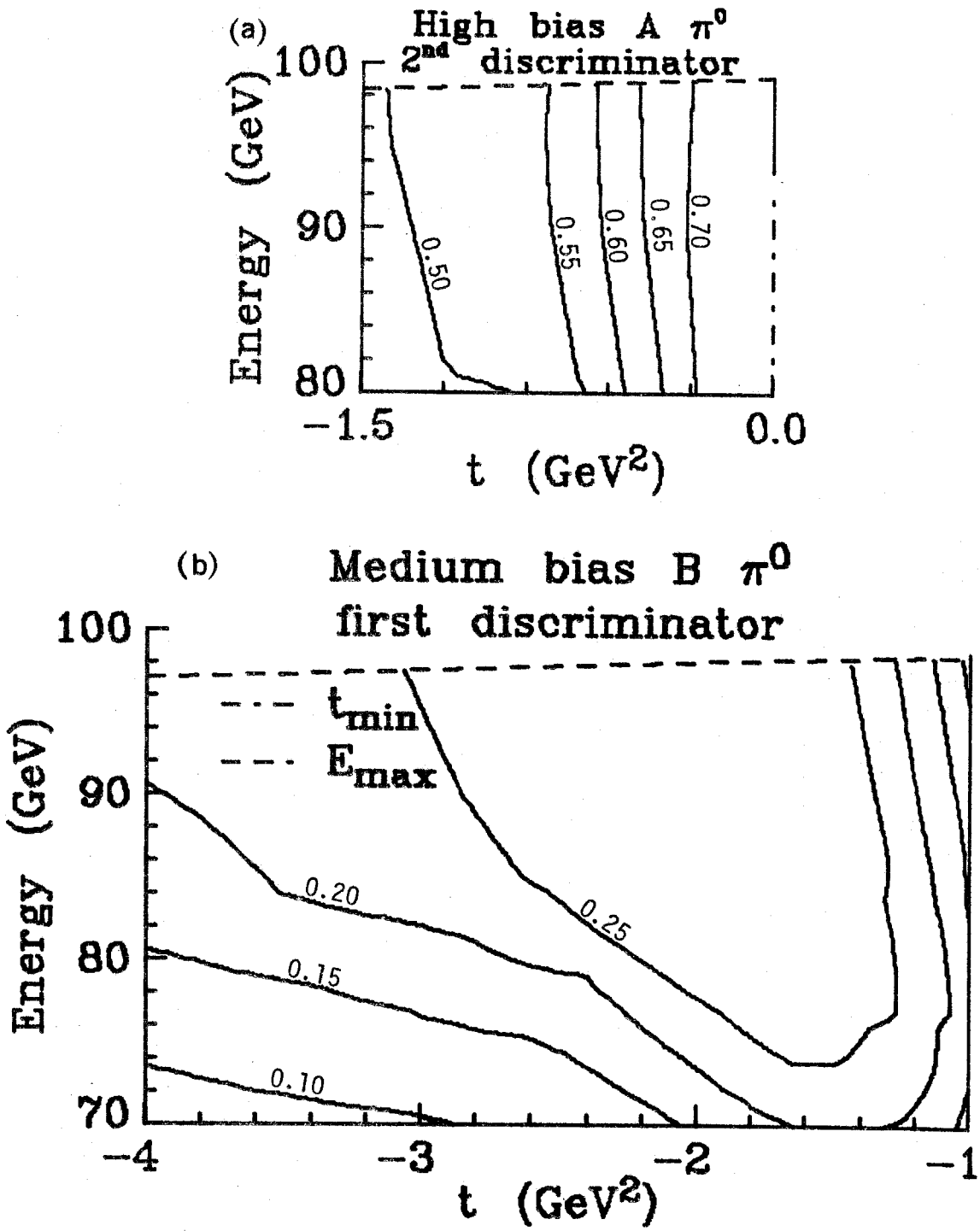

FIGURE 3.VII.2 Acceptance for π^0 mesons from a 99.2 GeV pion beam for (a) the high bias trigger A using the second discriminator and (b) the medium bias trigger B using the first discriminator.

triggers. In Fig. 3.VII.1 is shown the basic acceptance with no energy cuts as used for the NFS trigger. The acceptance is nowhere greater than 0.75 because of the cut on the decay cosine of the π^0. It increases with energy because the separation between the two photons from the π^0 decreases and so they are closer together and more likely to both hit the detector. For any given value of t, the acceptance does not change too dramatically with energy. The dot-dashed line on the figures shows the kinematic cut-off due to t_{min} and the dashed line shows the kinematic cut-off due to the energy of the beam particle.

In Fig. 3.VII.2(a) is shown the acceptance for trigger A with the highest energy bias and using the second discriminator (described in Appendix 3.V). Again the acceptance varies with energy and t over the energy range (E > 80 GeV) presented). It falls off rapidly below 80 GeV due to the cut-off of the discriminator. In Fig. 3.VII.2(b) is shown the acceptance for trigger B with the medium energy bias using the first discriminator. This trigger was used for the pion beam data with $t_m > 1$ GeV^2 presented in Chapter 5. In Figs. 3.VII.3 and 4 are shown the total acceptances for η mesons from the same three triggers. In these cases the acceptance is further reduced by the branching ratio of η mesons into two photons (0.38) and by the higher mass of the η, which causes the separation of the photons to be larger. However the acceptance does vary smoothly with energy and t in all cases.

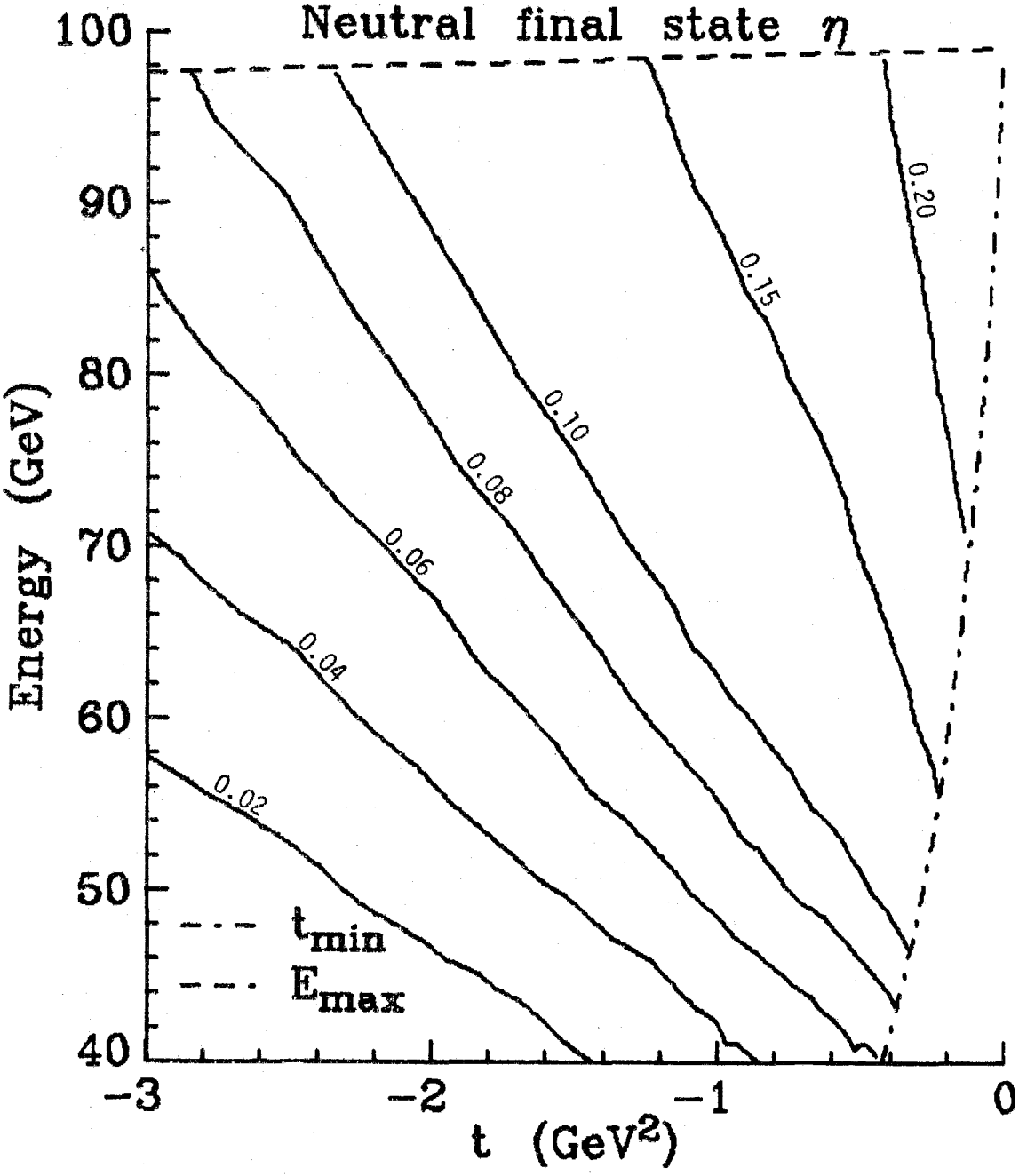

FIGURE 3.VII.3 Acceptance for η mesons from a 99.2 GeV pion beam for the NFS trigger.

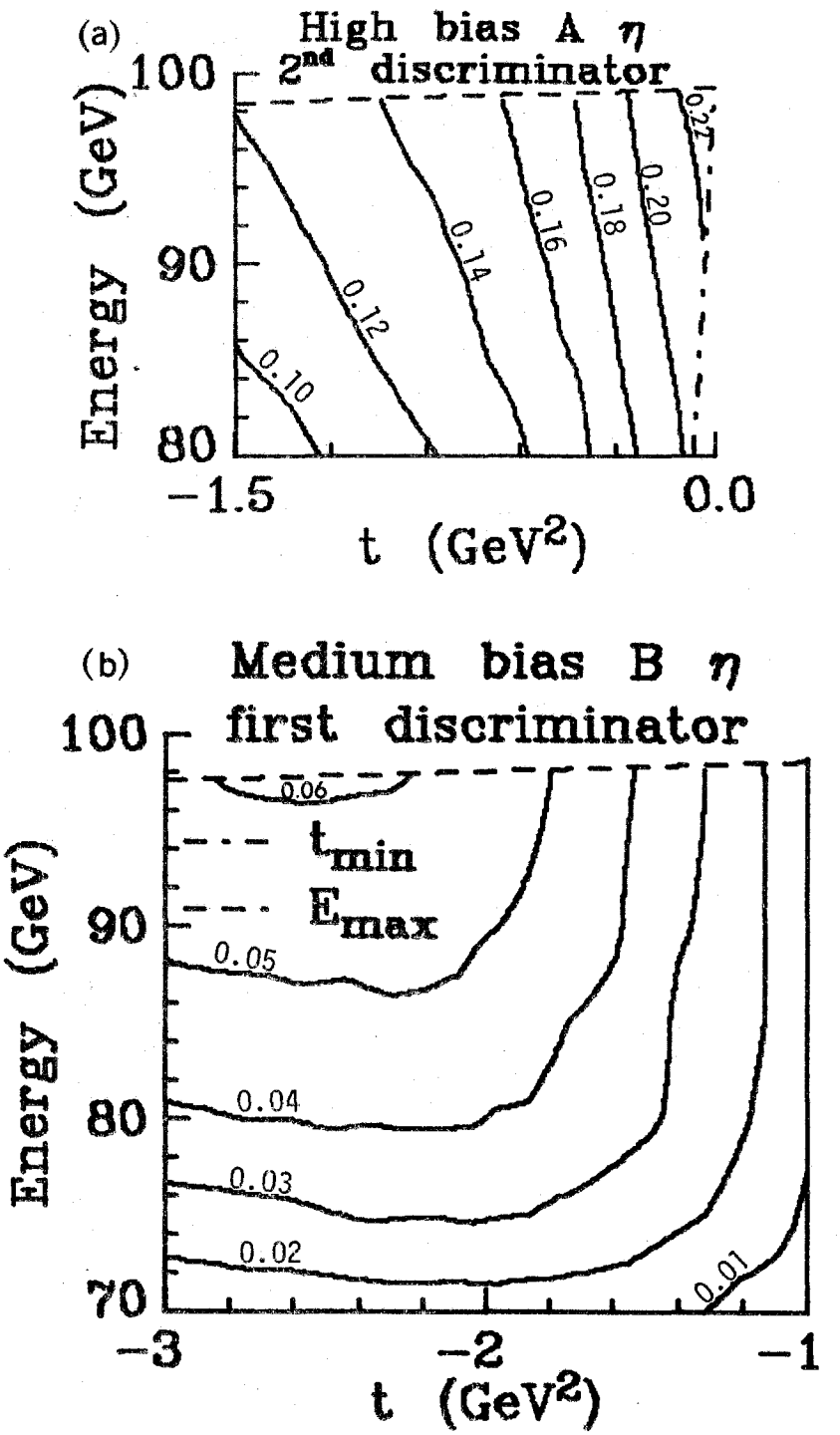

FIGURE 3.VII.4 Acceptance for η mesons from a 99.2 GeV pion beam for (a) the high bias trigger A using the second discriminator and (b) the medium bias trigger B using the first discriminator.

APPENDIX 3.VIII

MULTIPLE INTERACTIONS AND BEAM ATTENUATION

The hydrogen target was one-tenth of an interaction length long and so π^0 and η mesons may have been produced as a result of two or more interactions and also the flux was reduced by interactions which did not produce π^0 or η mesons. Both these effects produce a correction of a few percent to the data but they act in opposite directions and so roughly cancel out over most of the kinematic region of this experiment, except at high p_t where the cross section extracted from the data has to be reduced due to the multiple scattering effects.

The multiple scattering cross section is dominated by the double scattering cross section with one of the scatters being diffractive. The second interaction cannot be diffractive as it would have to be of the form $\pi^0 p \to \pi^0 X$ or $\eta p \to \eta X$ and any π^0 or η produced will usually decay electromagnetically before it can interact with the hydrogen. Hence the multiple scattering cross section was calculated by supposing that at most two scatters were involved and that the correction for an interaction $ap \to bX$ was due only to the processes:

$$a + p \to \begin{cases} a' + p \\ a' + X \end{cases}, \qquad a' + p \to b + X, \tag{3.VIII.1}$$

where a' is a particle of the same type and charge as a. The data were multiplied by the factor C where

$$C(x,t) = \frac{1}{1 + A(x,t)} \frac{B(x)}{1 - \exp(-B(x))}. \qquad (3.VIII.2)$$

A(x,t) is due to the double scattering and is given by

$$A(x,t) = 2.57 \times 10^{-3} \int_{t'} dt' \int_{\theta'} d\theta' \left(\frac{d\sigma}{dt}(ap \to a'p) \frac{d^2\sigma}{dt''dx}(a'p \to bX) + \right.$$

$$\left. \int_{x'} dx' \frac{d^2\sigma}{dt'dx'}(ap \to a'X) \frac{d^2\sigma}{dt''dx''}(a'p \to bX) \right) \Big/ \frac{d^2\sigma}{dtdx}(ap \to bX), \qquad (3.VIII.3)$$

where x'' and t'' are chosen so that b is produced at x and t with respect to a and the cross sections are in millibarns. B is due to the beam attenuation and is defined so that the beam loss in distance dx along the target at point x is given by

$$\text{Beam}(x) - \text{Beam}(x + dx) = \frac{B(x)}{L} \text{Beam}(x) dx \qquad (3.VIII.4)$$

where L is the length of the target and Beam(x) is the beam intensity at point x. Since the elastic and diffractive scatterings have already been included in the calculation of A, B is given by

$$B(x) = 2.57 \times 10^{-3} [\sigma_{tot}(ap) - \int_t dt \frac{d\sigma}{dt}(ap \to ap) -$$

$$\int_t dt \int_{x'>x} dx' \frac{d^2\sigma}{dtdx'}(ap \to aX)], \qquad (3.VIII.5)$$

where the cross sections are in millibarns. More details of the calculation are given in Ref. (Fo77b).

Only three reactions were considered, namely $\pi^- p \to \pi^0 X$, $\pi^- p \to \eta X$ and $pp \to \pi^0 X$. It was assumed that the corrections for the π^+ and

kaon beams were the same as those for the π^- beam and the corrections for the antiproton beam were the same as those for the proton beam. The denominator in A(x,t) [Eqn. (3.VIII.3)] was calculated using the results from this experiment parameterized in the form

$$\frac{d^2\sigma}{dtdx}(t,x) = G(t)(1 - x)^{H(t)}. \qquad (3.VIII.6)$$

This was also used for calculating the cross section for the second process in (3.VIII.1). The parameterizations of the πp and pp elastic cross sections from the Fermilab Single Arm Spectrometer (Fe75) were used for $t_m < 1$ GeV^2 and $t_m < 0.4$ GeV^2 respectively and those from Ref. (Ak76) were used for higher t_m. The parameterization of the inelastic $\pi^- p \to \pi^- X$ cross section in Ref. (Ay76) was used for $t_m < 1$ GeV^2 and a parameterization (Fo77b) based on the results from similar reactions (Al76, An77) and on theoretical predictions was used for $t_m > 1$ GeV^2. The parameterization of the $pp \to pX$ cross section from Ref. (Ta76) was used.

The correction factor, C, for selected values of the energy, E, of the detected particle and its four-momentum transfer-squared, t, is presented in Table 3.VIII.1. It is seen that the higher t_m data have to be decreased relative to the lower t_m data for all these reactions. At a fixed value of t the correction varies little with energy and so any error in its determination will have little effect on the trajectory, α.

No correction was made for the multiple scattering in the NFS

TABLE 3.VIII.1. Correction factor, C, for the multiple scattering and beam attenuation evaluated at selected values of the energy, E, and four-momentum-transfer-squared, t, of the detected particle for an incident particle of momentum 99 GeV.

E (GeV)	$-t$ (GeV^2)	C for $\pi^- p \to \pi^0 X$	C for $\pi^- p \to \eta X$	C for $pp \to \pi^0 X$
50	0.5	1.008	1.011	1.023
50	1.0	1.007	1.008	1.020
50	2.0	1.005	1.002	0.995
50	3.0	0.992	0.970	-
50	4.0	0.980	-	-
70	0.5	1.009	1.016	1.025
70	1.0	1.011	1.013	1.026
70	2.0	1.009	1.005	1.000
70	3.0	1.001	0.980	-
70	4.0	0.997	-	-
90	0.5	1.002	1.017	1.025
90	1.0	1.007	1.012	1.023
90	2.0	1.004	1.004	1.009
90	3.0	0.998	0.979	-
90	4.0	1.000	-	-

data. Its effect was negligible because every interaction has to produce neutral particles. The π^- flux was reduced by 3% for the NFS data to account for the beam attenuation.

APPENDIX 3.IX

CHERENKOV COUNTER ANALYSIS

The secondary beam, M2, from the Fermilab meson laboratory target was composed of pions, kaons, (anti)protons and electrons (or positrons) and so Cherenkov counters were used to distinguish the beam particles. The outputs from the four photomultiplier tubes were discriminated so as to set bits and were also pulse height analyzed. The pulse height distributions from FLUX runs with a negative polarity beam are shown in Figs. 3.IX.1-4 (solid curves). These FLUX runs were sandwiched between the 20-60 minute long triple Regge data-taking runs using triggers A, B, C, K and NFS. The trigger just required a successful beam particle, as defined in Appendix 2.I, and so the data collected reflected the true beam composition. Only about 2000 events were collected on each FLUX run compared with about 20000 events on each triple Regge data run, so all the FLUX runs have been summed together for the different beam conditions.

Also shown on Figs. 3.IX.1-4 are the pulse height distributions for the cases when the corresponding bit was set (dotted curve) or not set (dot-dashed curve). These bits are denoted DO, DI, UO and UI for the outer (O) and inner (I) photomultiplier tubes on the downstream (D) and upstream (U) counters, respectively. It is seen that these bits were set at a level just below the one photoelectron peak. The bits and the pulse heights were recorded on tape for every event. A bit pattern, called a CERBIT, was defined as

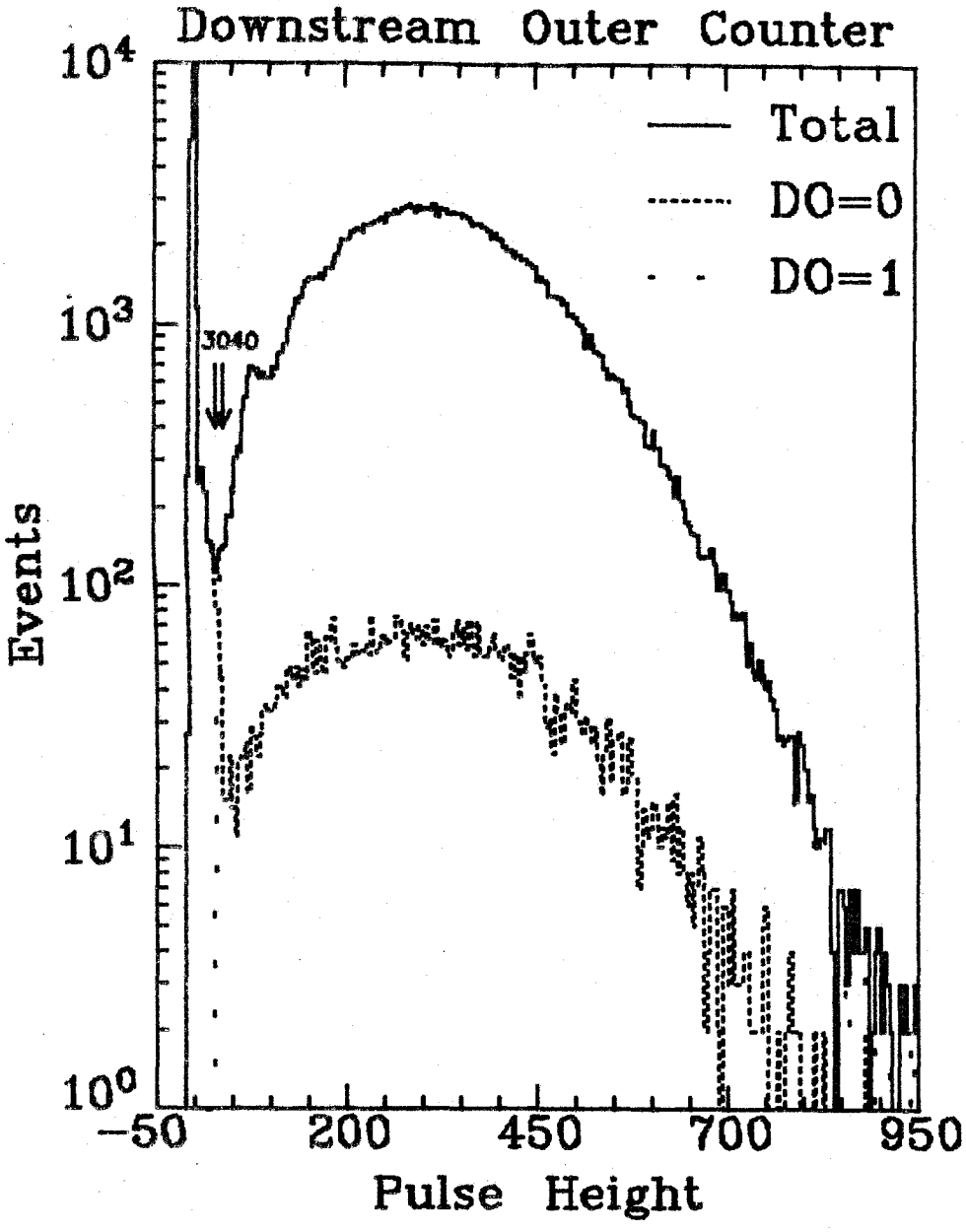

FIGURE 3.IX.1 Distribution of pulse height from outer photomultiplier tube of downstream Cherenkov counter for the negative polarity beam FLUX data. The cuts used for DOPION (40) and DOPROT (30) are indicated by the arrows.

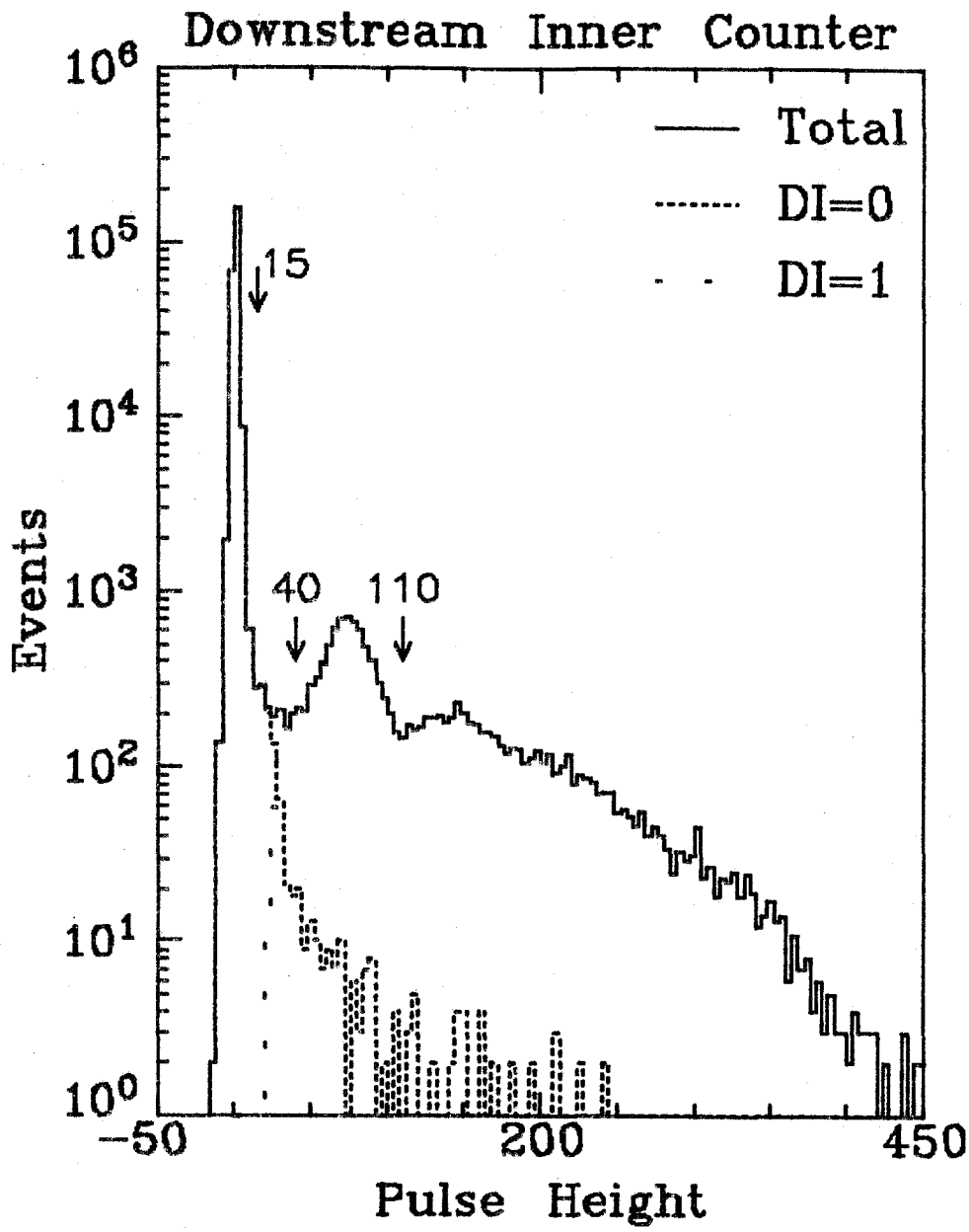

FIGURE 3.IX.2 Distribution of pulse height from inner photomultiplier tube of downstream Cherenkov counter for the negative polarity beam FLUX data. The cuts used for DIPION (40), DIPROT (15) and DIKAON (110) are indicated by the arrows.

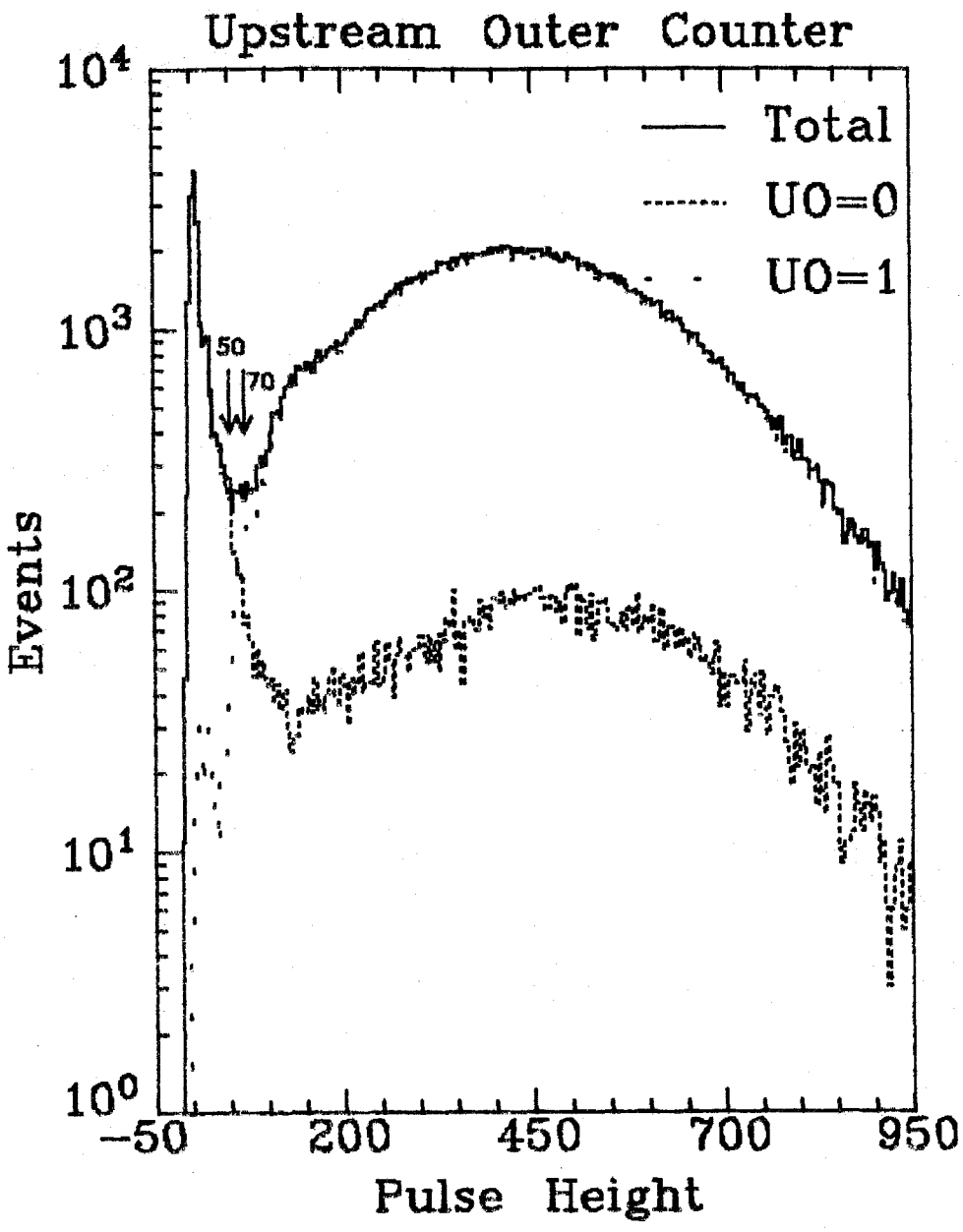

FIGURE 3.IX.3 Distribution of pulse height from outer photomultiplier tube of upstream Cherenkov counter for the negative polarity beam FLUX data. The cuts used for UOPION (70) and UOPROT (50) are indicated by the arrows.

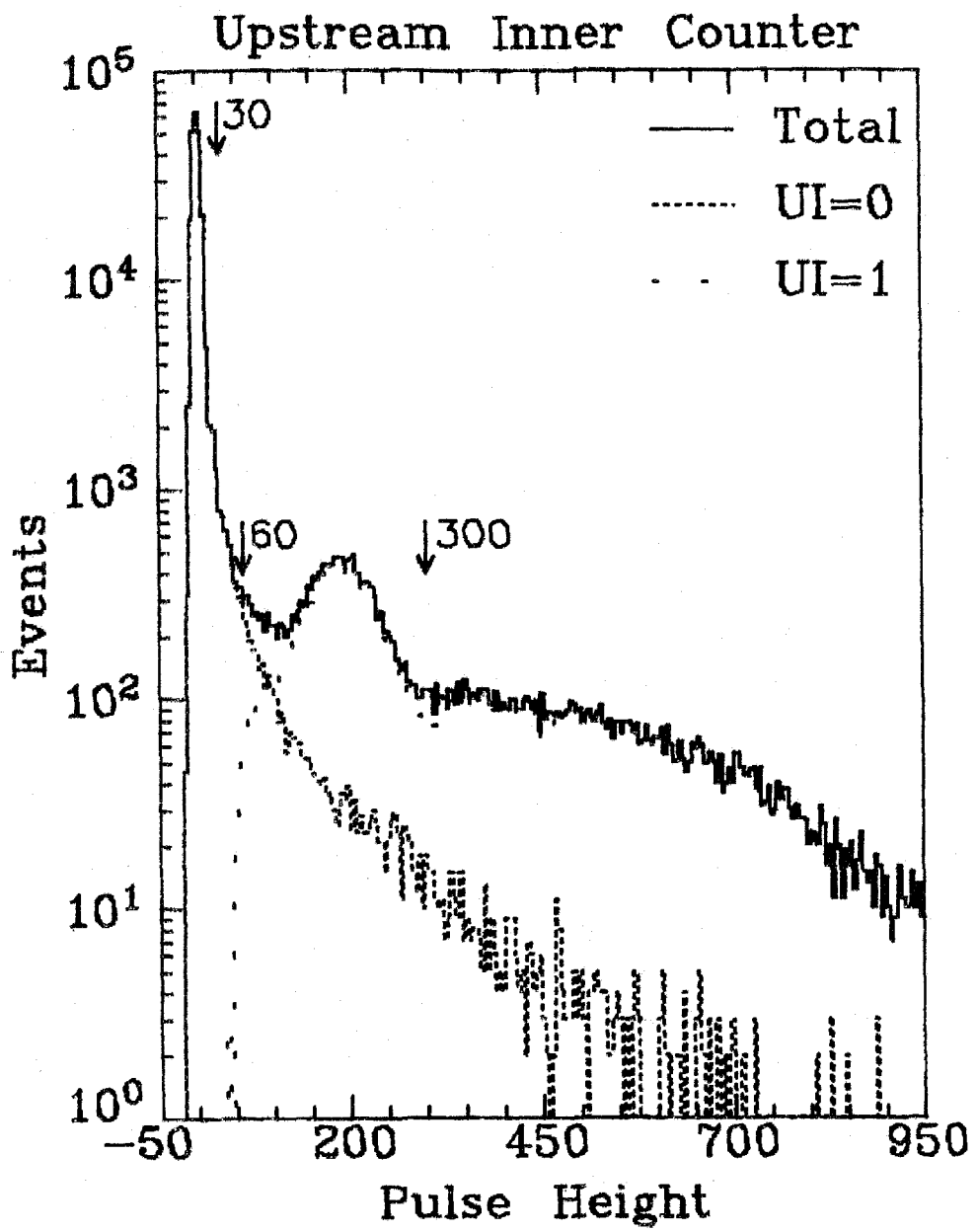

FIGURE 3.IX.4 Distribution of pulse height from inner photomultiplier tube of upstream Cherenkov counter for the negative polarity beam FLUX data. The cuts used for UIPION (30), UIPROT (60) and UIKAON (300) are indicated by the arrows.

$$CERBIT = 8 \times DO + 4 \times DI + 2 \times UO + UI. \qquad (3.IX.1)$$

Three scalers, called π^*, p* and K*, counted the triggers with CERBIT values of 10, 0 and 5 respectively. These scalers counted every time that an acceptable beam particle reached the experiment, regardless of whether the event was recorded, and the accumulated scalers were written out for each event. Another scaler, called the FLUX scaler, added up the total number of acceptable beam particles, denoted N below.

The bit patterns for the scalers, π^*, p* and K*, were most often set by pions (and electrons), (anti)protons and kaons, respectively. But not every pion gave the pattern π^*, for sometimes, due to the spread of the beam, the pion would be off-axis and the ring of light would miss the outer counter or give light which hit both counters. The photomultiplier tubes were not fully efficient and thus did not always see the light. The opposite effect also occurred with noise or spurious light causing a spurious bit to be set. Hence the π^*, p* and K* scalers did not count the true number of their corresponding beam particles. A method is now described which shows how the fraction of beam particles can be calculated (Ba77, Ke79).

This method used the bit patterns recorded on tape to calculate the true pion, proton and kaon fluxes by finding the probabilities for the various particles to set bits. Suppose that the probabilities for pions (or electrons), protons (or antiprotons) and kaons to set the bit DO are DOPI, DOP and DOK respectively. Let DIPI, DIP, DIK,

UOPI, UOP, UOK, UIPI, UIP and UIK be defined similarly. The scalers may be expressed in terms of these probabilities. For example, the fraction of π^* triggers is given by

$$N_{\pi^*}/N = F_\pi \times DOPI \times \overline{DIPI} \times UOPI \times \overline{UIPI} + F_p \times DOP \times \overline{DIP} \times UOP \times \overline{UIP} + F_K \times DOK \times \overline{DIK} \times UOK \times \overline{UIK}, \qquad (3.IX.2)$$

where F_π, F_p and F_K are the fractions of pions (or electrons), (anti)protons and kaons in the beam.

For a particular trigger type, the fractions of beam particles in the events recorded on tape, f_π, f_p and f_K, differ from those in the beam because the particles have different cross sections. The fraction of events, F_{CERBIT}, recorded on tape with each of the sixteen bit patterns, giving CERBIT values ranging from 0 to 15, can be expressed in terms of the fractions f and the probabilities. For example, F_{10} is given by

$$F_{10} = f_\pi \times DOPI \times \overline{DIPI} \times UOPI \times \overline{UIPI} + f_p \times DOP \times \overline{DIP} \times UOP \times \overline{UIP} + f_K \times DOK \times \overline{DIK} \times UOK \times \overline{UIK}, \qquad (3.IX.3)$$

which is dominated by the contribution from pions since each of DOPI, $\overline{DIPI}$, UOPI and $\overline{UIPI}$ is expected to be close to unity whereas DOP, UOP, DOK, $\overline{DIK}$, UOK and $\overline{UIK}$ are all expected to be near to zero. The system of sixteen equations of the form (3.IX.3) can be solved to find the fractions f and the twelve probabilities. There are only fourteen variables to solve for since the constraint,

$$f_\pi + f_p + f_K = 1, \qquad (3.IX.4)$$

is applied. The system of three scaler equations of the form (3.IX.2) can then be inverted to find the fractions F in terms of the known scaler fractions, $N_{\pi*}/N$, N_{p*}/N and N_{K*}/N, and the constraint,

$$F_\pi + F_p + F_K = 1, \qquad (3.IX.5)$$

is then applied. The system was solved by a minimization technique using a χ^2 formed from the equations of the form (3.IX.3) and the constraint (3.IX.5). The constraint (3.IX.4) was included by substituting f_π into (3.IX.3).

This method only holds if the probabilities are the same for the scalers as for the bits since they are determined from the bits and then applied to the scalers. There was available an easy check as to whether this assumption was true. This used the FLUX runs, for which $f_\pi = F_\pi$, $f_p = F_p$ and $f_K = F_K$. If N_π^b, N_p^b and N_K^b are the number of events having bit patterns with CERBIT values of 10, 0 and 5 respectively, and if N_e is the total number of events, then one expects that

$$\frac{N_\pi^b N}{N_e N_{\pi*}} = \frac{N_p^b N}{N_e N_{p*}} = \frac{N_K^b N}{N_e N_{K*}} = 1. \qquad (3.IX.6)$$

Unfortunately, this was not the case, as shown in Table 3.IX.1, where the FLUX runs have been divided into categories depending on the beam conditions. The - and + denote the negative and positive

TABLE 3.IX.1. Comparison between bits and scalers using FLUX runs. Ratios differing by more than four standard deviations from unity are starred.

FLUX run type	$(N_{\pi}^{b}N)/(N_{e}N_{\pi*})$	$(N_{p}^{b}N)/(N_{e}N_{p*})$	$(N_{K}^{b}N)/(N_{e}N_{K*})$
a^-	1.0105 ± 0.0022*	1.023 ± 0.032	1.034 ± 0.026
b^-	1.0253 ± 0.0016*	0.971 ± 0.018	1.006 ± 0.017
c^-	1.0034 ± 0.0018	0.955 ± 0.021	1.014 ± 0.021
a^+	1.0044 ± 0.0058	0.989 ± 0.011	1.003 ± 0.041
b^+	1.0296 ± 0.0060*	0.9818 ± 0.0080	0.937 ± 0.038
c^+	1.0171 ± 0.0080	0.948 ± 0.014	0.929 ± 0.053

polarity beams. The types a, b and c correspond to the beam conditions for the triggers A, B and C (or K). The chief differences between the FLUX runs were the thickness of the lead placed at the first focus, which was 9.5 mm and 3.2 mm for a and b whilst no lead was used for c, and the beam intensity, which was typically 10^5, 2×10^6 and 10^6 particles per spill for a, b and c respectively.

It is seen that, in general, the ratios all differ from unity and sometimes are more than four standard deviations above unity, as shown by the starred numbers. One explanation is that the bits were at fault and may not have been gated correctly. It is then seen from Figs. 3.IX.1-4 that the downstream counter bits were not set about 2% of the time when the pulse height corresponded to one photoelectron or more and the upstream counter bits failed to be set about 4% of the time. A second explanation is that the pulse height

analyzers had too long a gate and were seeing light from another beam particle. When the pulse height distribution was examined for the case of type a FLUX runs (Ke79), for which a lower beam rate was used, it was found that a lower fraction of events gave a significant pulse height when no bit was set, so making the second explanation more likely. The beam fractions listed in Table 2.1 were obtained from the FLUX runs with the best agreement for (3.IX.6). It is shown below that it was not necessary to know these beam fractions in order to normalize the data although it would have allowed a better determination of the normalizations had it been feasible to determine how the beam fractions depended on the beam conditions.

To determine the cross sections, it was necessary to know the beam particle, preferably on an event-by-event basis. Even though the pulse heights were misleading because light from previous events was sometimes seen, the beam particles were defined in terms of the pulse heights instead of the bit patterns for the analyses presented in this thesis. This definition allowed more freedom of choice as the cuts could be varied for the different particles, as shown in Table 3.IX.2. The positions of these cuts are shown in Figs. 3.IX.1-4. A PION was defined as a beam particle which satisfied one of the $PION_1$, $PION_2$ or $PION_3$ cuts and a KAON was one which satisfied one of the $KAON_1$, $KAON_2$ or $KAON_3$ cuts. The three definitions used for a PION and for a KAON were chosen to be mutually exclusive and thus no event satisfied more than one definition.

TABLE 3.IX.2. Definition of software beam particles.

	Pulse Height Cut				
	DO	DI	UO	UI	Bit pattern
$PION_1$	> 40	< 40	> 70	< 30	PIONBIT = 10
$PION_2$	> 40	< 40	> 70	> 30	PIONBIT = 11
$PION_3$	> 40	> 40	> 70	< 30	PIONBIT = 15
PROTON	< 30	< 15	< 50	< 60	PROTBIT = 0
$KAON_1$	< 40	> 15	< 70	> 60	KAONBIT1 = 5
$KAON_2$	< 40	< 15	< 70	> 300	KAONBIT2 = 1
$KAON_3$	< 40	> 110	< 70	< 60	KAONBIT3 = 4

It was necessary to understand how close the distributions of PIONs, PROTONs and KAONs came to the true distributions of pions, protons and kaons. The method used was similar to that described above for obtaining the beam fractions from the CERBIT distributions. New distributions were defined as follows:

$$\begin{aligned}
&\text{PIONBIT} = 8 \times \text{DOPION} + 4 \times \text{DIPION} + 2 \times \text{UOPION} + \text{UIPION},\\
&\text{PROTBIT} = 8 \times \text{DOPROT} + 4 \times \text{DIPROT} + 2 \times \text{UOPROT} + \text{UIPROT},\\
&\text{KAONBIT1} = 8 \times \text{DOPION} + 4 \times \text{DIPROT} + 2 \times \text{UOPION} + \text{UIPROT},\\
&\text{KAONBIT2} = 8 \times \text{DOPION} + 4 \times \text{DIPROT} + 2 \times \text{UOPION} + \text{UIKAON},\\
&\text{KAONBIT3} = 8 \times \text{DOPION} + 4 \times \text{DIKAON} + 2 \times \text{UOPION} + \text{UIPROT},
\end{aligned} \tag{3.IX.7}$$

where DOPION, DOPROT, DIPION, DIPROT, DIKAON, UOPION, UOPROT, UIPION, UIPROT and UIKAON are 1 for DO > 40, DO > 30, DI > 40, DI > 15,

DI > 110, UO > 70, UO > 50, UI > 30, UI > 60 and UI > 300 respectively and 0 otherwise. Equations similar to (3.IX.3) were set up for each of the five distributions defined in (3.IX.7) and, as before, the probabilities and beam particle fractions were solved for (without the constraint (3.IX.5)). The probability of a signal from a proton could not be larger than that for pions or kaons since the proton produced no Cherenkov light itself whereas the pions and kaons produced light. Hence the additional constraints,

$$\text{DOP} \leq \text{DOK}; \quad \text{DIP} \leq \text{DIPI}; \quad \text{UOP} \leq \text{UOK}; \quad \text{UIP} \leq \text{UIPI}, \qquad (3.IX.8)$$

were imposed. It was assumed that there were no correlations.

Consider now just the PIONBIT distribution. The fraction of events from true pions, kaons and protons can be expressed in terms of the fractions of events with PIONBIT values of PION, 0 and 5, where PION is the sum of PION_1 (= 10), PION_2 (= 11) and PION_3 (= 15) as follows:

$$\begin{bmatrix} f_\pi \\ f_p \\ f_K \end{bmatrix} = \begin{bmatrix} P(\text{PION}/\pi) & P(\text{PION}/p) & P(\text{PION}/K) \\ P(0/\pi) & P(0/p) & P(0/K) \\ P(5/\pi) & P(5/p) & P(5/K) \end{bmatrix}^{-1} \begin{bmatrix} f_{\text{PION}} \\ f_0 \\ f_5 \end{bmatrix} \qquad (3.IX.9)$$

where P(B/A) is the probability that beam particle A gives a PIONBIT value of B. Hence, for example,

$$P(\text{PION}/\pi) = \text{DOPI}.\overline{\text{DIPI}}.\text{UOPI}.\overline{\text{UIPI}} + \text{DOPI}.\overline{\text{DIPI}}.\text{UOPI}.\text{UIPI} + \text{DOPI}.\text{DIPI}.\text{UOPI}.\overline{\text{UIPI}}. \qquad (3.IX.10)$$

Hence it is possible to find the coefficients, a, in the following expressions:

$$f_{\pi} = a_{\pi}^{PION} f_{PION} + a_{\pi}^{0} f_{0} + a_{\pi}^{5} f_{5}, \qquad (3.IX.11)$$

$$f_{p} = a_{p}^{10} f_{10} + a_{p}^{PROTON} f_{PROTON} + a_{p}^{5} f_{5}, \qquad (3.IX.12)$$

$$f_{K} = a_{K}^{10} f_{10} + a_{K}^{0} f_{0} + a_{K}^{KAON} f_{KAON}, \qquad (3.IX.13)$$

where 0 and 5 in (3.IX.11) refer to the value of PIONBIT, 10 and 5 in (3.IX.12) refer to the value of PROTBIT and 10 and 0 in (3.IX.13) refer to the value of KAONBIT. The resulting values for the coefficients are presented in Table 3.IX.3 for the various FLUX run types. For the negative polarity beam, it is seen that the contamination in the PION definition is very small - about 0.1% of the kaons contribute - and that only 2.5% of the pions are omitted. The PROTON definition is not as clean, with a 0.01% contamination from pions and a 1% contamination from kaons, and about 6% of the antiprotons are omitted. The KAON definition is also not clean, with a 0.001% contamination from pions and a 1% contamination from protons and 20% of the kaons are omitted. Considering the beam fractions listed in Table 2.1, these results show that the contamination in the PION and KAON signals can be neglected but also show that 0.5% of the PROTON signal is due to pions and 2% is due to kaons. The latter number may be lower in fact and a result of fitting low statistics data since the solution for the positive polarity beam shows no

TABLE 3.IX.3. Normalization and contamination results: the coefficients defined in (3.IX.10-12).

Particle	FLUX run	a_π^{PION}	a_π^0 (x 10^5)	a_π^5 (x 10^5)
PION	a^-	1.0256 ± 0.0020	0 ± 1	-41 ± 7
PION	b^-	1.02492 ± 0.00071	-225 ± 64	-169 ± 16
PION	c^-	1.0256 ± 0.0016	0 ± 1	-144 ± 18
PION	a^+	1.0341 ± 0.0043	0 ± 0	-84 ± 23
PION	b^+	1.0767 ± 0.0119	-50 ± 53	-708 ± 177
PION	c^+	1.0694 ± 0.0067	0 ± 0	-984 ± 236
		a_p^{10} (x 10^5)	a_p^{PROTON}	a_p^5 (x 10^5)
PROTON	a^-	-7 ± 1	1.097 ± 0.067	-953 ± 49
PROTON	b^-	-10 ± 0	1.045 ± 0.037	-878 ± 56
PROTON	c^-	-9 ± 0	1.072 ± 0.045	-665 ± 84
PROTON	a^+	-19 ± 7	1.020 ± 0.010	0 ± 11
PROTON	b^+	-64 ± 22	1.099 ± 0.034	0 ± 0
PROTON	c^+	-8 ± 18	1.044 ± 0.010	0 ± 0
		a_K^{10} (x 10^5)	a_K^0 (x 10^5)	a_K^{KAON}
KAON	a^-	-1 ± 0	-605 ± 395	1.13 ± 0.11
KAON	b^-	-4 ± 0	-792 ± 654	1.28 ± 0.14
KAON	c^-	-3 ± 0	-27 ± 31	1.25 ± 0.13
KAON	a^+	0 ± 0	0 ± 0	1.17 ± 0.21
KAON	b^+	0 ± 2	-116 ± 82	1.50 ± 0.40
KAON	c^+	0 ± 0	0 ± 0	1.47 ± 0.30

contamination from kaons in the PROTON signal. There is still, in the positive data, a 0.01% pion contamination in the PROTON signal but this is negligible because of the large proton content of the positive polarity beam. The contamination in the PION and KAON signals are again shown to be small.

The beam particles, as defined by the software cuts on the pulse heights, thus did not fully agree with the true beam particles. It was necessary to normalize the data to obtain the cross sections. Ignoring the contaminations for the present, the pion cross section is given by

$$\left.\frac{d\sigma(E,t)}{dtdE}\right|_{\pi} = \frac{N_{PION}(E,t)a_{\pi}^{PION}x2.57 \times 10^{-3}}{\text{Effective flux}.F_{\pi} \times dtdE}, \quad (3.IX.14)$$

where $N_{PION}(E,t)$ is the number of events with energies between $E - dE/2$ and $E + dE/2$ and four-momentum-transfer-squared between $t - dt/2$ and $t + dt/2$ which satisfy all the analysis cuts as described in Chapter 3. The number 2.57×10^{-3} describes the amount of hydrogen in the target. The effective flux is defined as

$$\text{Effective flux} = \frac{\text{No. of events x Flux}}{\text{No. of triggers}}, \quad (3.IX.15)$$

where the "events" are those recorded on tape except for any which failed to hit any plane of the beam hodoscope counters and the "triggers" are those events which satisfy the trigger requirements, as recorded by a scaler. This takes into account the dead time of the experiment, due to the electronics and computer, which caused

some triggers not to be recorded on tape. It was not possible to use (3.IX.14) since F_π could not be found for all beam conditions, as discussed earlier. Consequently, the following definition was used for the pion cross section:

$$\left.\frac{d\sigma}{dtdE}(E,t)\right|_\pi = \frac{N_{PION}(E,t) \times 2.57\times10^{-3}}{\text{Effective flux}.F^{FLUX}_{PION}.dEdt} \qquad (3.IX.16)$$

where F^{FLUX}_{PION} is the fraction of events on a FLUX run satisfying the PION definition. The proton and kaon cross sections are defined likewise. The values of F_{PION}, F_{PROTON} and F_{KAON} for the various FLUX run types are given in Table 3.IX.4. In applying (3.IX.16), the form of the Cherenkov counter trigger had to be considered. Trigger C was taken with the requirement that DO = 0 but putting this constraint into the definition of PROTONs and KAONs made no difference to the results from the FLUX runs. However trigger K

TABLE 3.IX.4. Fraction of PIONs, PROTONs and KAONs on FLUX runs.

FLUX run type	F_{PION}	F_{PROTON}	F_{KAON}
a^-	0.9095 ± 0.0014	0.02152 ± 0.00068	0.03914 ± 0.00091
b^-	0.91122 ± 0.00084	0.02023 ± 0.00042	0.03287 ± 0.00058
c^-	0.91509 ± 0.00097	0.01945 ± 0.00048	0.03165 ± 0.00061
a^+	0.6585 ± 0.0032	0.2675 ± 0.0030	0.0345 ± 0.0012
b^+	0.6794 ± 0.0029	0.2399 ± 0.0026	0.0282 ± 0.0010
c^+	0.6534 ± 0.0040	0.2379 ± 0.0036	0.0277 ± 0.0014
$c^{+}*$			0.0221 ± 0.0012

was taken with the additional requirement that DI = 1 and many of the KAONs failed to satisfy this constraint. The last line of Table 3.IX.4 shows the KAON content with this constraint imposed.

From the numbers in Table 3.IX.4, a crude estimate of the electron and positron content of the beam can be made. The FLUX runs of type a and b were taken with sufficient lead in the beam so as to eliminate the electrons and positrons of the required momenta, whereas type c was taken with no lead in the beam and so both the "pion" content of the beam, as defined by the Cherenkov counters, and the total flux were enhanced. Averaging together the values of F_{PION} for types a and b and comparing this to type c shows that the negative polarity beam contains 5 ± 1% electrons and 87 ± 2% pions and the positive polarity beam contains 2 ± 1% positrons and 64 ± 1% pions. For the negative polarity beam a more precise determination of the electron content was made as follows. On both the negative polarity trigger B and trigger C data runs, the NFS trigger was included along with the triple Regge trigger. The electrons only produce neutral final states through the weak interaction and thus the contribution to the NFS triggers from their interactions is negligible. The ratio of the NFS triggers to the flux on the trigger B runs was larger than on the trigger C runs because the lead removed the electrons from the total flux counted. Thus the fraction of electrons in the beam could be calculated and the result was 0.081 ± 0.002. Since π^- mesons and protons are produced in equal numbers

and about twice this number of π^+ mesons are produced at the meson laboratory target at 100 GeV with a 400 GeV incident proton beam and since the electrons and positrons are produced at about the same rate as they come mainly from π^0 decays, the fraction of positrons in the positive beam should be about one-third times the fraction of electrons in the negative beam. Thus about 2-3% of the positive beam should be positrons and this agrees fairly well with the above results.

APPENDIX 4.I

ESTIMATION OF REGGEON EXCHANGE CROSS SECTIONS

As described in Section 4.3, there are triple Regge contributions from terms with Reggeon (R) exchanges on the bottom leg of the triple vertex diagram as well as the dominant contributions with Pomeron (P) exchanges. These two terms differ both in their s-dependence and in their x-dependence. Since the data presented here come from only one beam momentum, it was not possible to use the s-dependence to isolate these terms. The difference in the x-dependence was only 0.5 in the exponent of $(1 - x)$ and, since the overall exponent had to be determined anyway, it was decided that this term could not be isolated using the x-dependence alone, although the data did show that its contribution was small. Thus some theoretical arguments were used to estimate its magnitude.

It was possible to estimate the ratio of the contributions of the Reggeon exchanges to the two beam polarities. For the reactions with incident pion beams and detected π^0 mesons, the ratio of the residue functions, $G_{\rho\rho f_\pm}$, in (4.3.4) is given by

$$\frac{G_{\rho\rho f_+}}{G_{\rho\rho f_-}} = \frac{A^R(\rho^+ p \to \rho^+ p)\big|_{t=0}}{A^R(\rho^- p \to \rho^- p)\big|_{t=0}} = \frac{\sigma^R_{tot}(\rho^+ p)}{\sigma^R_{tot}(\rho^- p)} \qquad (4.I.1)$$

where $f_\pm$ are the linear combinations $f_\pm = (\sqrt{2}f \mp \sqrt{3}\rho)/\sqrt{5}$ and the f' has been ignored. The superscript R means that only the Reggeon exchange part of the amplitude or cross section is required. In

(4.I.1) the ρ mesons are virtual and so it cannot be used directly because neither the virtual nor the real $\rho^{\pm}p$ total cross section has been measured. It is now shown that their ratio may be approximated by the ratio of the $\pi^{+}p$ to the $\pi^{-}p$ total cross section.

Since the f is a combination of the f and the ρ, it is necessary to check that the f and the ρ contribute in the same proportion to the πp cross section as to the ρp cross section. SU_3 may be used to derive the following relationships:

$$\frac{\gamma(V_1 \to V_1 V_1)}{\gamma(V_1 \to P_1 P_1)} = \frac{\gamma(V_1 \to V_{1/2} V_{1/2})}{\gamma(V_1 \to P_{1/2} P_{1/2})} \qquad (4.I.2)$$

$$\frac{\gamma(T_0 \to V_1 V_1)}{\gamma(T_0 \to P_1 P_1)} = \frac{\gamma(T_1 \to V_{1/2} V_{1/2})}{\gamma(T_1 \to P_{1/2} P_{1/2})}, \qquad (4.I.3)$$

where P_I, V_I and T_I denote the members of the pseudoscalar, vector and tensor octets respectively with isospin I. Thus, ignoring mass effects, it is found that

$$\frac{\gamma(\rho \to \rho\bar{\rho})}{\gamma(\rho \to \pi\bar{\pi})} = \frac{\gamma(\rho \to K^*\bar{K}^*)}{\gamma(\rho \to K\bar{K})} \qquad (4.I.4)$$

$$\frac{\gamma(f_8 \to \rho\bar{\rho})}{\gamma(f_8 \to \pi\bar{\pi})} = \frac{\gamma(A_2 \to K^*\bar{K}^*)}{\gamma(A_2 \to K\bar{K})}, \qquad (4.I.5)$$

where f_8 denotes the octet particle formed from the f and the f'. To relate the left-hand sides of (4.I.4) and (4.I.5), a relationship is now deduced between the right-hand sides.

Consider the reaction,

$$K^+ + n \to K^0 + p, \tag{4.I.6}$$

which has no resonances, as there are no strangeness S = 1 baryons in the quark model, and so, by duality, its amplitude has a vanishing imaginary part. The t-channel exchange is pure I = 1 and due to the ρ and A_2 exchanges and so the imaginary parts of these must cancel, giving

$$\gamma(\rho \to K\bar{K})\gamma(\rho \to n\bar{p}) = \gamma(A_2 \to K\bar{K})\gamma(A_2 \to n\bar{p}). \tag{4.I.7}$$

The same argument applied to the reaction,

$$K^{*+} + n \to K^{*0} + p, \tag{4.I.8}$$

where K* denotes the K*(892), gives

$$\gamma(\rho \to K^*\bar{K}^*)\gamma(\rho \to n\bar{p}) = \gamma(A_2 \to K^*\bar{K}^*)\gamma(A_2 \to n\bar{p}). \tag{4.I.9}$$

Combining (4.I.7) and (4.I.9) gives

$$\frac{\gamma(\rho \to K^*\bar{K}^*)}{\gamma(\rho \to K\bar{K})} = \frac{\gamma(A_2 \to K^*\bar{K}^*)}{\gamma(A_2 \to K\bar{K})}, \tag{4.I.10}$$

and this, together with (4.I.4) and (4.I.5), provides the required relationship,

$$\frac{\gamma(f_8 \to p\bar{p})}{\gamma(\rho \to p\bar{p})} = \frac{\gamma(f_8 \to \pi\bar{\pi})}{\gamma(\rho \to \pi\bar{\pi})}. \tag{4.I.11}$$

Hence the ratio of the ρ and the f_8 couplings to the $\pi\bar{\pi}$ are the same as to the $\rho\bar{\rho}$ and, if the simple quark model is assumed, the same is true for the singlet particle, f_1. Thus (4.I.1) gives, within the context of the approximations made,

$$\frac{G_{\rho\rho f_+}}{G_{\rho\rho f_-}} = \frac{\sigma^R_{tot}(\pi^+ p)}{\sigma^R_{tot}(\pi^- p)}. \qquad (4.I.12)$$

To find σ^R_{tot}, the cross sections are expressed as

$$\sigma_{tot}(s) = \sigma^P_{tot} + \sigma^R_{tot}(s), \qquad (4.I.13)$$

where the cross section due to Pomeron exchange is assumed to be independent of s and that due to Reggeon exchange is assumed to vanish as $s \to \infty$. The measured cross sections with $10 < s < 70$ GeV^2 (De71,De73,Ca76) then gave

$$G_{\rho\rho f_+}/G_{\rho\rho f_-} = 0.65 \pm 0.04. \qquad (4.I.14)$$

It was noticed however that $\sigma_R(s)$ did not behave quite like $s^{-0.5}$, as predicted for Reggeon exchange. This may be due to the Pomeron cross section not being flat, as indicated by the rise of the total cross section for $s > 200$ GeV^2. It is clear that the Pomeron is a more complicated singularity than a simple pole. A second parameterization of the total cross section is discussed later in this Appendix.

When fits to the data with the constraint (4.I.14) were tried, it

was found that the normalization of the $\rho\rho f$ term was still undetermined. Hence an estimate was made of the size of $G_{\rho\rho f_-}$. Its value at t = 0 was obtained using results from a previous analysis of the reaction pp → pX (Fi74) and its t-dependence was obtained from the Fixed Mass Sum Rules, described in Section 4.2 and (Co77). For this reaction, either the Pomeron or Reggeons (ρ, A_2, ω, ϕ, f and f') may be exchanged on any of the three legs. The analysis assumed that only the PPP, PPR, RRP and RRR exchanges were present and ignored the interference terms. The t-dependence of these terms were parameterized and found from fitting the data. The normalization of the RRR term in pp → pX, G_{RRR}, can be compared to the normalization of the $\rho\rho f_-$ term in $\pi^- p \to \pi^0 X$, $G_{\rho\rho f_-}$, by

$$\frac{G_{\rho\rho f_-}}{G_{RRR}} = \frac{|\gamma_{\pi\pi\rho}\xi_\rho|^2}{|\gamma_{pp\rho}\xi_\rho|^2 + |\gamma_{ppA_2}\xi_{A_2}|^2 + |\gamma_{pp\omega}\xi_\omega|^2 + |\gamma_{ppf}\xi_f|^2} \quad (4.I.15)$$

where the ϕ and f' exchanges have been ignored because of their small couplings. Here γ_{abc} denotes the coupling at the abc vertex and ξ_a denotes the signature factor of particle a as defined by (4.1.14). All the quantities in (4.I.15) are functions of t but here just the values at t = 0 will be used because the value of G_{RRR} was only determined well at t near 0. It is now assumed that all these Reggeons have the same trajectory, that is, $\alpha_\rho = \alpha_{A_2} = \alpha_\omega = \alpha_f = \alpha$, say. Also the lack of resonances in both the elastic scattering reactions, pp → pp and pn → pn, shows that the vector and tensor couplings for both isospin 0 and 1 are equal, that is,

$\gamma(\rho \to p\bar{p}) = \gamma(A_2 \to p\bar{p})$ and $\gamma(\omega \to p\bar{p}) = \gamma(f \to p\bar{p})$ by an argument analogous to that resulting in (4.I.7). Then, since the ρ has odd signature, (4.I.15) gives

$$\frac{G_{\rho\rho f_-}}{G_{RRR}} = \frac{|\gamma_{\pi\pi\rho}|^2 \sin^2(\pi\alpha/2)}{|\gamma_{pp\rho}|^2 + |\gamma_{pp\omega}|^2} . \qquad (4.I.16)$$

Using the measured values of these couplings at $t = 0$, it was found that (Fo77c)

$$G_{\rho\rho f_-}/G_{RRR} = 0.18, \qquad (4.I.17)$$

whilst the compilation of couplings (Na79) gave both the values 0.175 and 0.46. The latter was probably a miscalculation. Since it was found that $G_{RRR}(0) = 18.1$ mb/GeV^2 (Fi74), (4.I.17) gives

$$G_{\rho\rho f_-}(0) = 3.3 \text{ mb/GeV}^2. \qquad (4.I.18)$$

To check this normalization and to estimate the t-dependence of the data, the FMSR were used in the form of relation (4.2.9). For the reactions, $\pi^{\pm}p \to \pi^0 X$, odd n corresponds to the P and f exchanges on the bottom leg whilst even n corresponds to ρ exchange. Now (4.I.14) gives

$$\sqrt{2}G_{\rho\rho\rho}/\sqrt{5}G_{\rho\rho f_-} = 0.18 \pm 0.02 \qquad (4.I.19)$$

and so, if $G_{\rho\rho\rho}$ can be found, then (4.I.19) gives $G_{\rho\rho f}$. To find $G_{\rho\rho\rho}$, (4.2.9) was used with $n = 0$ and $N = 2$ GeV^2 to give

$$\int_0^2 d\nu \left[\frac{d^2\sigma}{dtdM^2}(\pi^- p \to \pi^0 X) - \frac{d^2\sigma}{dtdM^2}(\pi^0 p \to \pi^- X) \right] =$$

$$\frac{G_{\rho\rho\rho}(t)(s/2)^{2\alpha_\rho(t) - 2\alpha_\rho(0)}}{64\pi^2(\alpha_\rho(0) - 2\alpha_\rho(t) + 1)} . \qquad (4.I.20)$$

where the I = 2 exchange has been ignored on the right-hand side. The cross section for $\pi^0 p \to \pi^- X$ was obtained by assuming that it was dominated by ρ^+ exchange and so

$$\frac{d^2\sigma}{dtdM^2}(\pi^0 p \to \pi^- X) = \frac{d^2\sigma}{dtdM^2}(\pi^+ p \to \pi^0 X) . \qquad (4.I.21)$$

Hence $G_{\rho\rho\rho}$ could be obtained using the data measured in this experiment. However the large energy resolution of 1.6 GeV smeared out the resonance contributions and so it was not possible to make a good determination of G. The result obtained was

$$G_{\rho\rho f_-}(t) \simeq 3 \pm 3 \text{ mb/GeV}^2 . \qquad (4.I.22)$$

It is seen from (4.I.20) and from the discussion in Appendix 4.II on low mass resonance production that $G_{\rho\rho\rho}(t)$ will have a t-dependence similar to the charge exchange reaction, $\pi^- p \to \pi^0 n$. Hence the cross assumed was

$$\frac{d^2\sigma}{dtdx}(\pi^- p \to \pi^0 X)\Big|_{\rho\rho f_-} = \frac{3}{\sqrt{s}} \frac{\frac{d\sigma}{dt}(\pi^- p \to \pi^0 n)(t)}{\frac{d\sigma}{dt}(\pi^- p \to \pi^0 n)(0)} (1 - x)^{0.5 - 2\alpha_\rho(t)} . \qquad (4.I.23)$$

A similar approach was used to estimate the contribution of the $A_2A_2f_\pm$ triple Regge terms to the production of η mesons from $\pi^\pm$ beams, so just the differences will be noted here. The relation (4.I.1) holds with the ρ replaced by the A_2. Then (4.I.2,3) may be used with T_1 replacing V_1 on the left-hand side and (4.I.4,5) become

$$\frac{\gamma(\rho \to A_2\bar{A}_2)}{\gamma(\rho \to \pi\bar{\pi})} = \frac{\gamma(\rho \to K^{**}\bar{K}^{**})}{\gamma(\rho \to K\bar{K})} \qquad (4.I.24)$$

$$\frac{\gamma(f_8 \to A_2A_2)}{\gamma(f_8 \to \pi\bar{\pi})} = \frac{\gamma(A_2 \to K^{**}\bar{K}^{**})}{\gamma(A_2 \to K\bar{K})}, \qquad (4.I.25)$$

where K** denotes the K*(1430). Using reaction (4.I.6) together with the reaction,

$$K^{**+} + n \to K^{**0} + p, \qquad (4.I.26)$$

gives (4.I.10) with the K* replaced by the K** and (4.I.11) with the ρ replaced by the A_2 and thus

$$G_{A_2A_2f_+}/G_{A_2A_2f_-} = 0.65 \pm 0.04. \qquad (4.I.27)$$

The comparison with the RRR term of the pp → pX analysis is similar, with (4.I.16) replaced by

$$\frac{G_{A_2A_2f_-}}{G_{RRR}} = \frac{|\gamma_{\pi\eta A_2}|^2 \cos^2(\pi\alpha/2)}{|\gamma_{pp\rho}|^2 + |\gamma_{pp\omega}|^2}. \qquad (4.I.28)$$

Now the ratio of the coupling $|\gamma_{\pi\eta A_2}(t)|^2$ to the coupling $|\gamma_{\pi\pi\rho}(t)|^2$ in (4.I.16) is just the ratio of the cross section for $\pi^- p \to \eta n$ to that for $\pi^- p \to \pi^0 n$, and hence the cross section used was

$$\frac{d^2\sigma}{dtdx}(\pi^- p \to \eta X)\Big|_{A_2 A_2 \not P} = \frac{3}{\sqrt{s}} \frac{\frac{d\sigma}{dt}(\pi^- p \to \eta n)(t)}{\frac{d\sigma}{dt}(\pi^- p \to \pi^0 n)(0)} (1 - x)^{0.5-2\alpha_{A_2}(t)} . \tag{4.I.29}$$

For the estimation of the Reggeon exchange terms in $K^- p \to \pi^0 X$ and $K^- p \to \eta X$, a different approach was used which obtained the ratio of the Reggeon exchange terms to the Pomeron exchange terms by supposing that

$$\frac{d^2\sigma^{RRR}}{dtdx}(t=0) \Big/ \frac{d^2\sigma^{RRP}}{dtdx}(t=0) = \frac{\sigma^R_{tot}(K^- p)}{\sigma^P_{tot}(K^- p)} . \tag{4.I.30}$$

Since the s-dependence of the Pomeron exchange term is not understood, two different approaches were used in applying (4.I.30). The first approach was to suppose that the Pomeron exchange cross section was flat, as in (4.I.13), with a magnitude given by the cross section for s between 100 and 200 GeV^2, and that the Reggeon exchange cross section was given by the difference. Using the $K^- p$ cross section (De71,De73,Ca76) for $20 \leqslant s \leqslant 60$ GeV^2 gave

$$G_{RRR}(0)/G_{RRP}(0) \simeq 0.5. \tag{4.I.31}$$

A second approach was to suppose that the s-dependence of the Pomeron cross section was given by the $K^+ p$ total cross section, which

has no Reggeon exchange contributions, and to subtract this from the K^-p total cross section to give the Reggeon exchange cross section. This approach gave

$$G_{RRR}(0)/G_{RRP}(0) \simeq 0.9, \tag{4.I.32}$$

which is clearly larger than (4.I.31) since the Pomeron cross section rises with s. Thus it was estimated that

$$G_{RRR}(0)/G_{RRP}(0) = 0.7 \pm 0.3. \tag{4.I.33}$$

The error estimated in (4.I.33) is due to the lack of understanding of the s-dependence of the total cross sections and not to the statistics. It was assumed that the t-dependence of the Reggeon cross sections were similar to those of the corresponding low mass resonance terms, discussed in Appendix 4.II.

To judge the reliability of this approach, it was applied also to the pion beam reactions by assuming that

$$\frac{d^2\sigma^{\rho\rho f_\pm}}{dtdx}(t=0) \Big/ \frac{d^2\sigma^{\rho\rho P}}{dtdx}(t=0) = \frac{\sigma^R_{tot}(\pi^\pm p)}{\sigma^P_{tot}(\pi^\pm p)} \tag{4.I.34}$$

Assuming that the Pomeron exchange gave a flat total cross section resulted in the values,

$$G_{\rho\rho f_-}(0)/G_{\rho\rho P}(0) \simeq 0.66, \tag{4.I.35}$$

$$G_{\rho\rho f_+}(0)/G_{\rho\rho P}(0) \simeq 0.44, \tag{4.I.36}$$

whilst assuming that the s-dependence of the Pomeron exchange cross section was given by the K^+p total cross section gave

$$G_{\rho\rho f_-}(0)/G_{\rho\rho P}(0) \simeq 1.0, \tag{4.I.37}$$

$$G_{\rho\rho f_+}(0)/G_{\rho\rho P}(0) \simeq 0.8. \tag{4.I.38}$$

The ratio of the value of $G_{\rho\rho f_-}$ estimated in (4.I.18) to the measured normalization of the $\rho\rho P$ term, $G_{\rho\rho P}$, at low t was about 0.45, in better agreement with the value obtained with a flat cross section for the Pomeron exchange than with the rising cross section.

For the $\bar{p}p \to \pi^0 X$ Reggeon exchange cross sections, this method could be applied with only a few assumptions, since the top legs are dominantly antiproton exchange. Hence it was assumed that

$$\frac{d^2\sigma^{NNR}}{dtdx}(t=0) \Big/ \frac{d^2\sigma^{NNP}}{dtdx}(t=0) = \frac{\sigma^R_{tot}(\bar{p}p)}{\sigma^P_{tot}(\bar{p}p)} \tag{4.I.39}$$

Assuming that the Pomeron exchange cross section was flat gave

$$G_{NNR}(0)/G_{NNP}(0) \simeq 0.6, \tag{4.I.40}$$

whilst assuming that the s-dependence of the Pomeron cross section was given by the pp total cross section, which does not allow Reggeon exchange, gave

$$G_{NNR}(0)/G_{NNP}(0) \simeq 0.9. \tag{4.I.41}$$

Thus the Reggeon contribution relative to the Pomeron contribution is about the same for the antiproton beam as for the K^- beam.

APPENDIX 4.II

ESTIMATION OF CROSS SECTIONS FOR LOW MASS RESONANCE PRODUCTION

Triple Regge theory is not valid at x near unity since M^2 is not large there, as shown by relation (4.2.3). For pion beams, this is the region of resonance production of Δ and N* baryons through reactions of the form,

$$\pi^{\pm} + p \rightarrow \pi^0 + \Delta, N^*, \tag{4.II.1}$$

$$\pi^{\pm} + p \rightarrow \eta + \Delta, N^*. \tag{4.II.2}$$

Since the energy resolution of the experiment for π^0 and η mesons is about 1.6 GeV at high x, some of the low energy tail from the resonance production will overlap the triple Regge region. As the cross section for these resonances is comparable to the triple Regge cross sections in this overlap region, it was necessary to include the cross section for these resonances explicitly when fitting the data to find the triple Regge contributions.

For neutron production, the Elll results on the reactions

$$\pi^- + p \rightarrow \pi^0, \eta + n \tag{4.II.3}$$

were used (Ba76, Da76). A model based on the Regge theory prediction,

$$\frac{d\sigma}{dt}(s,t) = \beta(t)\nu^{2\alpha(t)-2} \tag{4.II.4a}$$

where

$$\nu = \frac{s - u}{4m_p}, \tag{4.II.4b}$$

with $\alpha(t)$ and $\beta(t)$ parameterized as functions of t, describes all their cross sections from 20 GeV to 200 GeV satisfactorily and so this was used. The resulting curves for α and β for the ρ and A_2 trajectories are shown on Figs. 1.1, 4.II.1 and 4.II.2.

There are no high energy measurements on $\Delta(1232)$ production and so the results on the reactions (B174b),

$$\pi^+ + p \to \pi^0 + \Delta^{++}(1232) \qquad (4.II.5)$$

$$\pi^+ + p \to \eta + \Delta^{++}(1232), \qquad (4.II.6)$$

with a beam of momentum 5.45 GeV, were used. Considering the isospin of the t-channel for (4.II.5) shows that its amplitude is given by

$$A(\pi^+\pi^0 \to \bar{p}\Delta^{++}) = (\sqrt{3}T_1 + T_2)/\sqrt{8}, \qquad (4.II.7)$$

where T_1 and T_2 are the amplitudes for isospin, I, = 1 and 2 exchanges in the t-channel. For $\Delta(1232)$ production from a π^- beam,

$$\pi^- + p \to \pi^0 + \Delta(1232), \qquad (4.II.8)$$

the t-channel amplitude is

$$A(\pi^-\pi^0 \to \bar{p}\Delta^0) = (T_1 - \sqrt{3}T_2)/\sqrt{8}. \qquad (4.II.9)$$

The reactions (4.II.5,8) are known to be dominated by ρ exchange, with I = 1, and thus the approximation $T_2 = 0$ may be used in (4.II.7) and (4.II.9) to give

$$\frac{d\sigma}{dt}(\pi^-p \to \pi^0\Delta^0) \simeq \frac{1}{3}\frac{d\sigma}{dt}(\pi^+p \to \pi^0\Delta^{++}) \qquad (4.II.10)$$

and thus the contribution to both the π^- and π^+ beams can be found

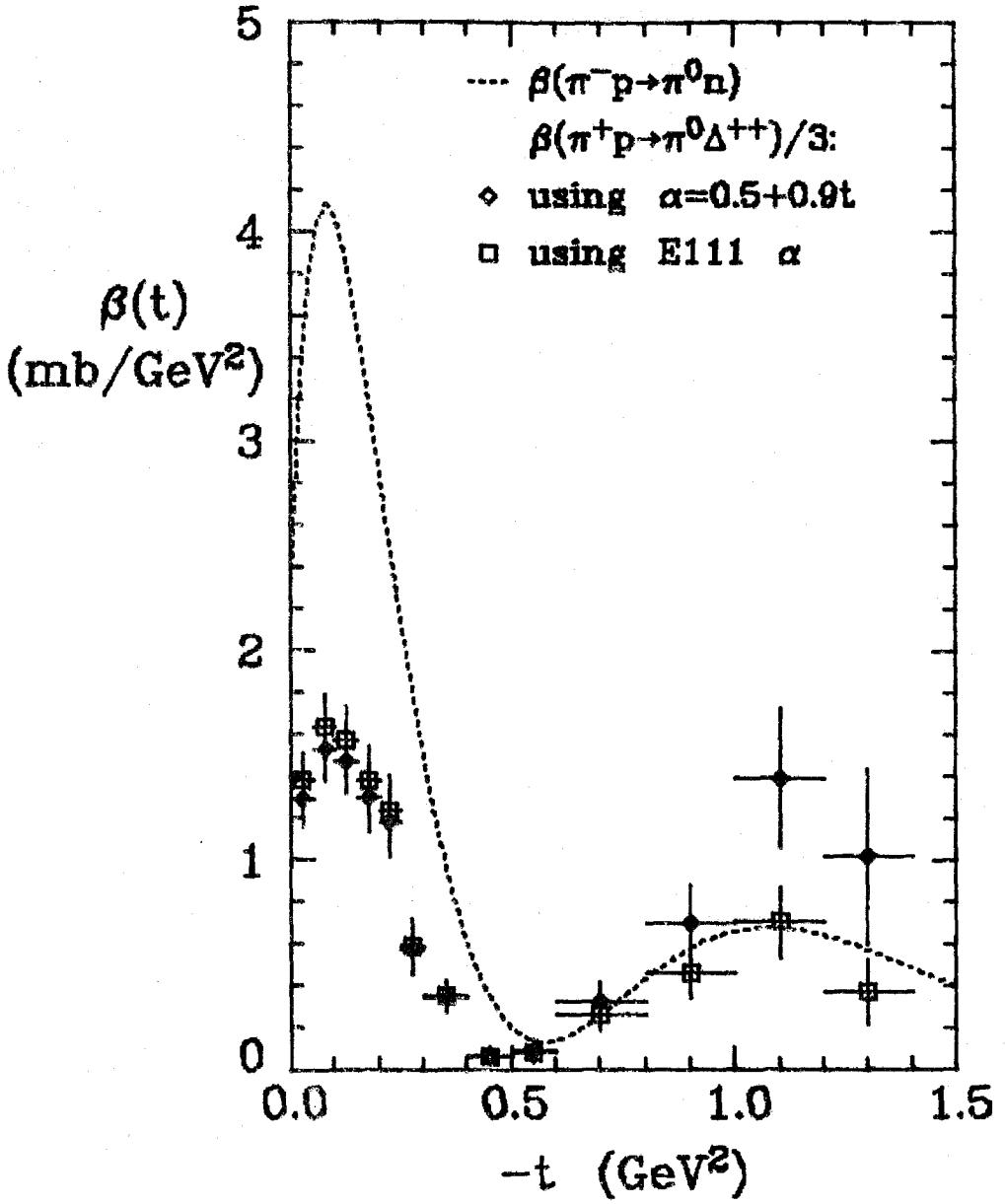

FIGURE 4.II.1 Parameterization of low mass resonance production in conjunction with a π^0 in terms of $\beta(t)$ as defined by (4.II.4). The curve for neutron production is taken from the E111 results (Ba76) and the points for $\Delta(1232)$ production are from Ref. (Bl74b) and are derived for two different parameterizations of α.

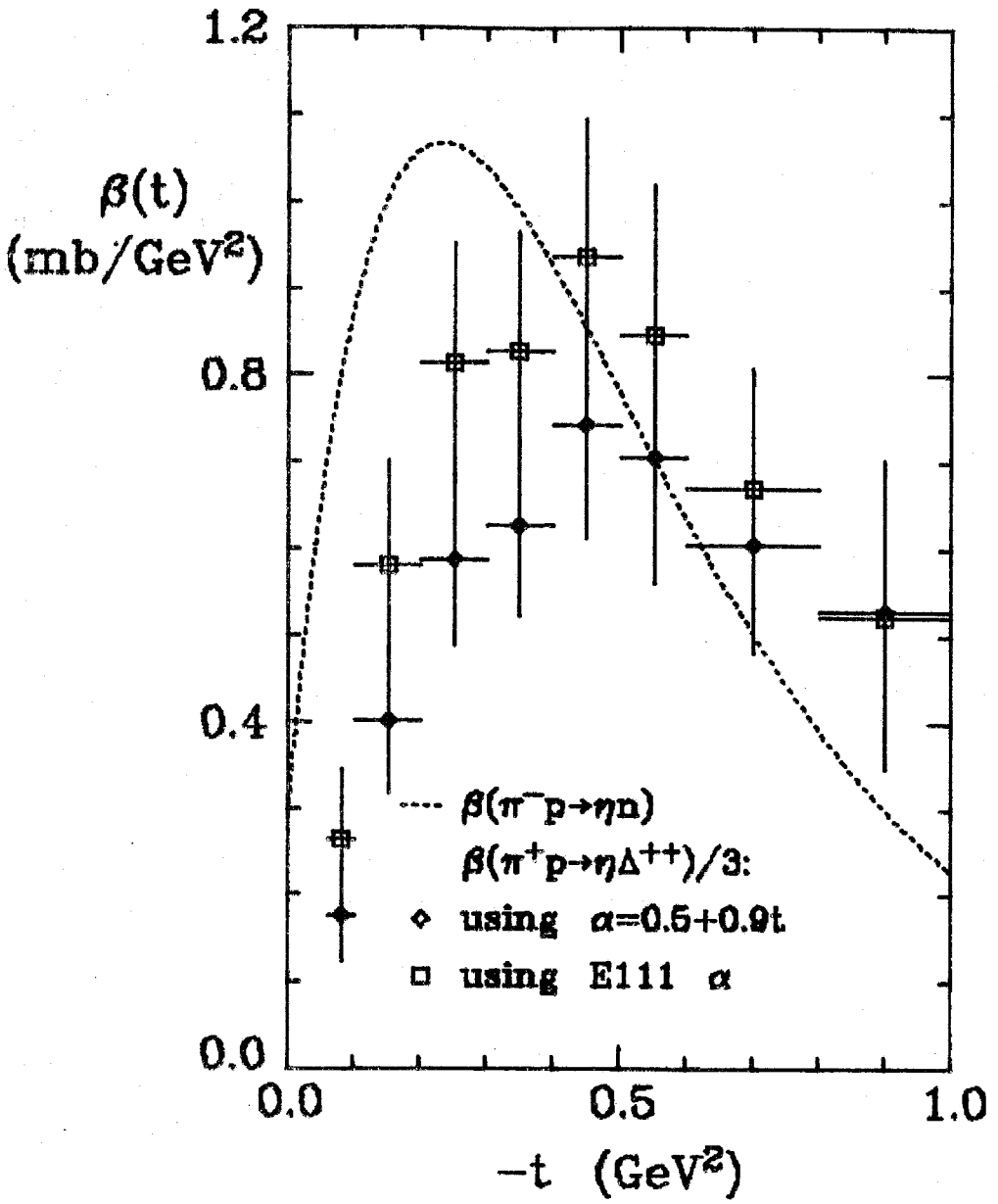

FIGURE 4.II.2 Parameterization of low mass resonance production in conjunction with an η in terms of β(t) as defined by (4.II.4). The curve for neutron production is taken from the E111 results (Da76) and the points for Δ(1232) production are from Ref. (B174b) and are derived for two different parameterizations of α.

using their results. For η production, only the I = 1 exchange is allowed and so in this case

$$\frac{d\sigma}{dt}(\pi^- p \to \eta\Delta^0) = \frac{1}{3}\frac{d\sigma}{dt}(\pi^+ p \to \eta\Delta^{++}). \qquad (4.II.11)$$

To extrapolate these results to the beam momentum used in this experiment, β(t) was first extracted from the Δ^{++} data using (4.II.4) and the results are shown in Figs. 4.II.1,2 for two different parameterizations of the trajectories, namely the Elll results and the linear approximation, α(t) = 0.5 + 0.9t. β(t) was parameterized by supposing that

$$\frac{1}{3}\beta(\pi^+ p \to \pi^0\Delta^{++}) = (a_1 + a_2 t + a_3 t^2)\beta(\pi^- p \to \pi^0 n) \qquad (4.II.12)$$

$$\frac{1}{3}\beta(\pi^+ p \to \eta\Delta^{++}) = (b_1 + b_2 t + b_3 t^2)\beta(\pi^- p \to \eta n), \qquad (4.II.13)$$

and, using α from the Elll results, it was found that

$$a_1 = 0.42, \quad a_2 = 0.23\ \text{GeV}^{-2}, \quad a_3 = 0.51\ \text{GeV}^{-4};$$
$$b_1 = 0.18, \quad b_2 = -2.42\ \text{GeV}^{-2}, \quad b_3 = -0.98\ \text{GeV}^{-4}. \qquad (4.II.14)$$

The cross section for Δ production was then calculated at the value of s appropriate for this experiment using (4.II.4).

There have been few measurements of the production of higher mass N* and Δ resonances from pion beams. Hence it was decided to include explicitly just the neutron and the $\pi^0 n$ decay mode of the Δ(1232) for the NFS production of low mass resonances. As shown in Chapter 6, this gave successful results. In the full inclusive case, the cross

section for resonance production from the π^- beam is larger than for the NFS case because many N* baryons will decay into several charged pions. Thus the cross section was calculated by supposing that the π^+ beam resonance production was due only to the production of $\Delta^{++}(1232)$ baryons and using two-component duality arguments to say that the ratio of π^- to π^+ resonance production is the same as the ratio of the $\rho\rho R$ exchanges (R = Reggeon) from the two beams. In Appendix 4.I, it was shown that this ratio is about 1.5 and hence, integrating over all masses, it was supposed that

$$\frac{d\sigma}{dt}(\pi^- p \to \pi^0,\eta + \text{resonances}) \simeq 1.5\frac{d\sigma}{dt}(\pi^+ p \to \pi^0,\eta + \Delta^{++}). \quad (4.II.15)$$

For K^- beams, resonances also occur at low masses where strange baryons are produced. For π^0 production, the Λ, $\Sigma^0(1192)$ and the $\Sigma^0(1385)$ were included and for η production just the Λ was included. To find the cross sections for their production, the results from Ref. (Ch76) on the following reactions from a K^- beam of momentum 14.3 GeV were used:

$$K^- + p \to \pi^0 + \Lambda, \quad (4.II.16)$$

$$K^- + p \to \pi^- + \Sigma^+(1192), \quad (4.II.17)$$

$$K^- + p \to \pi^- + \Sigma^+(1385), \quad (4.II.18)$$

$$K^- + p \to \eta + \Lambda. \quad (4.II.19)$$

The cross sections for producing a π^0 together with a Σ^0 are related to (4.II.17,18) by

$$\frac{d\sigma}{dt}(K^- p \to \pi^0 \Sigma^0) = 0.5 \frac{d\sigma}{dt}(K^- p \to \pi^- \Sigma^+) \qquad (4.II.20)$$

if it is assumed that the I = 3/2 exchange amplitude is negligible. To obtain the cross sections at the energies of this experiment, (4.II.4) was again assumed. The cross sections for π^0 production were then added together and fitted to an exponential, giving

$$\frac{d\sigma}{dt}(K^- p \to \pi^0 + \text{low mass resonances}) = 9.2e^{9.7t} \ \mu b/GeV^2. \quad (4.II.21)$$

For the $\eta\Lambda$ production, the cross section fitted to

$$\frac{d\sigma}{dt}(K^- p \to \eta\Lambda) = 2.2e^{12t} \ \mu b/GeV^2. \qquad (4.II.22)$$

APPENDIX 4.III

CALCULATION OF THE ISOSPIN = 2 AND ISOSPIN = 3/2 π EXCHANGE CROSS SECTIONS

The calculation of the triple Regge diagrams where at least one of the top two legs is either an isospin, I, = 2 cut or an I = 3/2 cut is described in this appendix. The I = 2 exchange arises in the production of π^0 mesons from $\pi^{\pm}$ beams and the I = 3/2 exchange arises in π^0 production from $K^{\pm}$ beams, as described in section 4.3.

The triple vertex diagrams for $\pi^{\pm}p \to \pi^0 X$ not represented by the $\rho\rho P$ and $\rho\rho f$ exchanges are shown below:

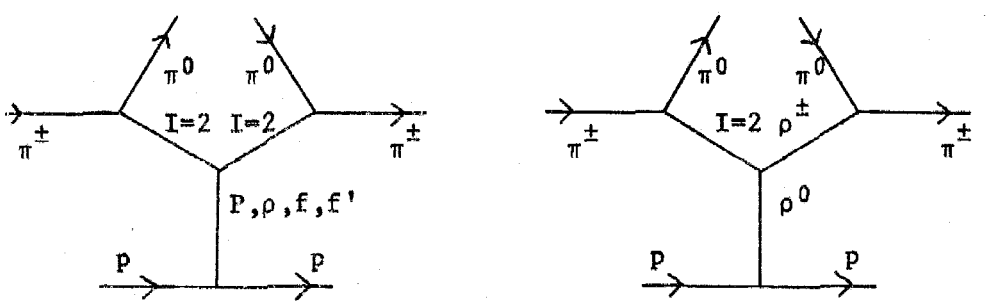

The calculation described here just considers the case in which a pion is specifically produced as part of the X, as shown schematically below:

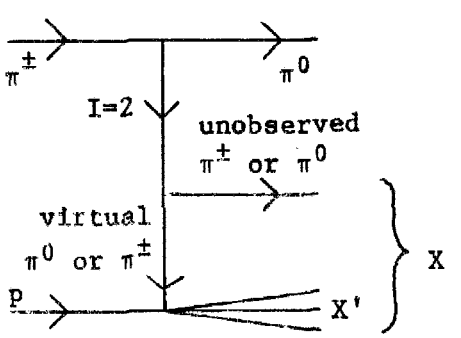

It assumes that the I = 2 exchange becomes two pions combined in a state with I = 2, one of which is unobserved. The other pion is virtual and interacts with the target proton. There are other processes, such as $\rho\rho$ production instead of $\pi\pi$ production from the I = 2 exchange, which should also be included. It is assumed here that the term considered here dominates at low t and high x because of the low pion mass.

The process was modeled by supposing that the incident pion scattered off the virtual pion which then interacted with the proton:

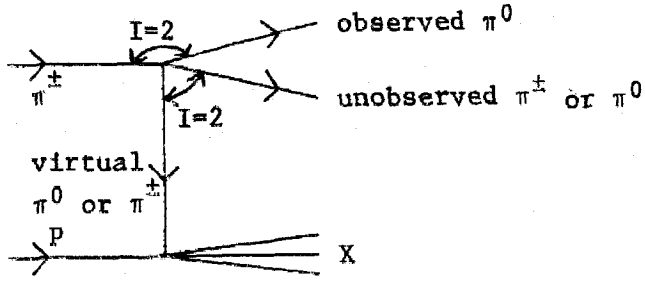

The $\pi\pi$ scattering part of this process was calculated from the known scattering amplitudes and the $\pi p \to X$ part was calculated from the total cross section. The cross section for π^0 production was obtained by integrating over the momenta of the unobserved pion.

The cross section for the production of a π^0 of 3-momentum p_ξ and energy E_ξ by $\pi^\pm$ beams is given by

$$E_\xi \frac{d^3\sigma^\pm}{dp_\xi^3} = \frac{1}{4(2\pi)^6 p_{lab}} \int \frac{d^3p_\zeta}{E_\zeta} \frac{\sum A^\pm_{\xi\zeta} \sigma^\pm_{tot}(s_{\chi p})}{(t_\chi - m_\pi^2)^2} p_{\chi_{lab}} \qquad (4.III.1)$$

where ζ denotes the undetected real pion and χ denotes the virtual

exchanged pion. p_{lab} and $p_{\chi lab}$ are the scalar momenta of the incident and exchanged pions in the laboratory frame. $A^{\pm}_{\xi\zeta}$ is the amplitude-squared for the incident pion to scatter off χ to produce ξ and ζ when the $\chi\zeta$ system has I = 2. The summation is over the two terms due to a neutral pion or a charged pion being exchanged. Calculating this in terms of isospin amplitudes gives

$$\sum A^{\pm}_{\xi\zeta}\sigma^{\pm}_{tot} = \frac{1}{8}|T^1_2|^2[3\sigma_{tot}(\pi^{\pm}p) + \sigma_{tot}(\pi^{\mp}p)] + \frac{1}{4}\,\mathrm{Re}(T^1_1{}^*T^1_2) \times [\sigma_{tot}(\pi^{\pm}p) - \sigma_{tot}(\pi^{\mp}p)] \qquad (4.III.2)$$

where T^1_1 and T^1_2 are the amplitudes for I = 1 and 2 scattering in the $\chi\zeta$ system. To calculate these, they are reexpressed in terms of the measured amplitudes, T_0, T_1 and T_2, for I = 0, 1 and 2 scattering in the $\xi\zeta$ system by

$$\begin{aligned} T^1_1 &= T_0/3 + T_1/2 - 5T_2/6 \\ T^1_2 &= T_0/3 - T_1/2 + T_2/6. \end{aligned} \qquad (4.III.3)$$

These amplitudes were obtained from ref. (Hy75) for the higher masses, $m_{\xi\zeta} \gtrsim 0.8$ GeV/c^2 and from ref. (No78) for the lower masses. The s and d waves were included for T_0, the p and f waves were included for T_1 and just the s wave was included for T_2.

The $\pi p \to X$ vertex was calculated by supposing that the pion was real, but using the c.m. energy of the virtual pion - proton system, $\sqrt{s_{\chi p}}$. A parameterization of the measured πp total cross sections was used (PD78). The integration over the undetected pion

was done using Monte Carlo techniques.

To check this calculation, the cross section for the reaction $\pi^+ p \to \pi^- X$ was calculated using the same approach. This reaction is pure I = 2 exchange in the triple Regge model and is represented by

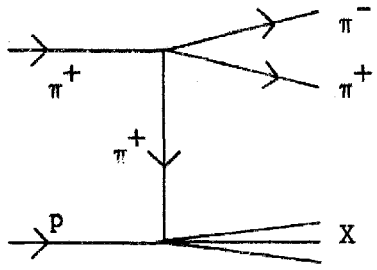

so that

$$\sum A_{\xi\zeta}\sigma_{tot} = |T_2^1|^2\sigma_{tot}(\pi^+ p). \qquad (4.III.4)$$

The results of this calculation were compared with measurements made with the Fermilab Single Arm Spectrometer using an incident 100 GeV pion beam and with the detected π^- having a transverse momentum, p_t, of 0.3 or 0.5 GeV (Cu78). The comparison is shown in Fig. 4.III.1 and the agreement is seen to be good at high x, but not perfect. At low x the I = 2 term is much lower than the data as expected since other physics may be dominating this region as -t is not small here. The calculated cross section for p_t = 0.3 GeV lies above the data whilst that for 0.5 GeV lies below the data at high x. This disagreement was investigated by putting an additional form factor depending on the mass of the virtual pion into (4.III.1) to represent the coupling of the virtual pion to the proton. The best result was obtained with its value being unity everywhere, which is the value it has for a

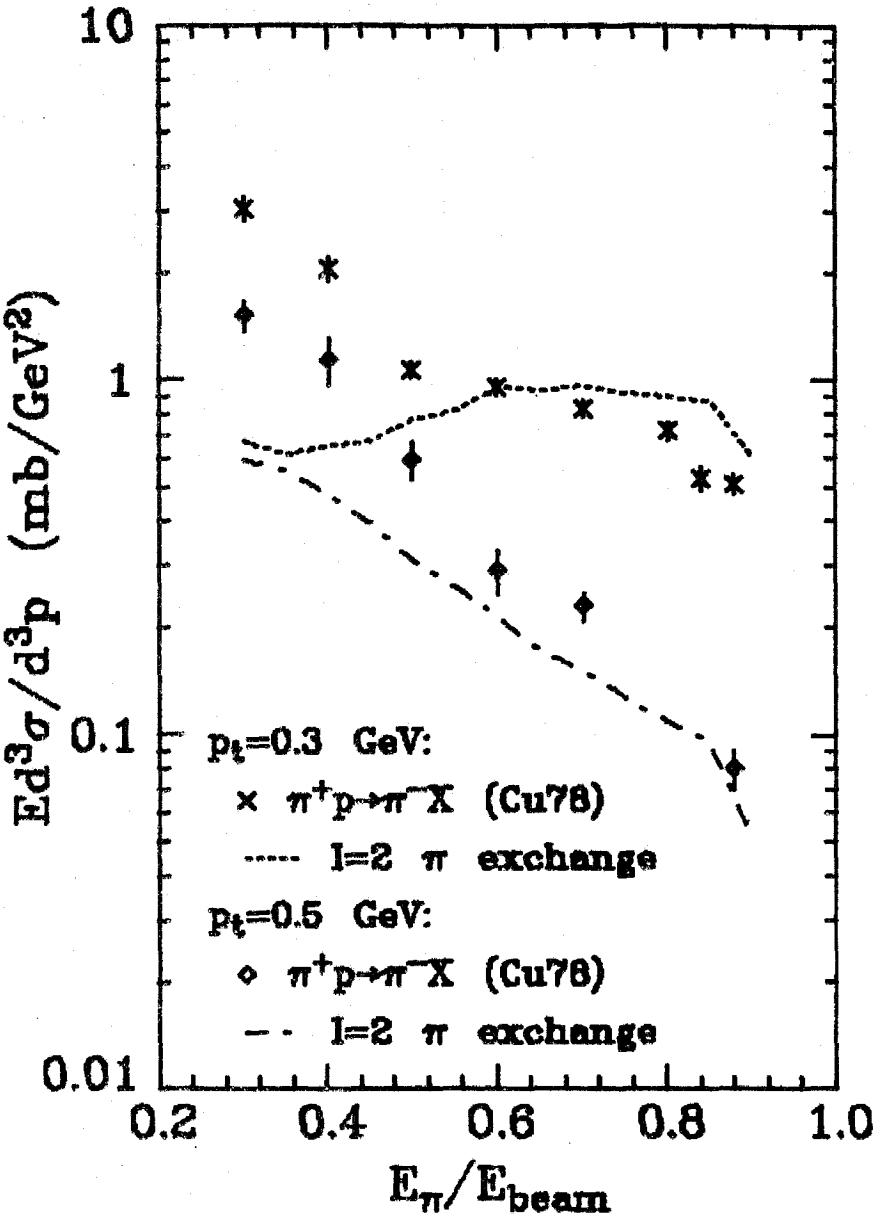

FIGURE 4.III.1 Comparison of measurements of the reaction $\pi^+p \to \pi^-X$ at 100 GeV with transverse momentum, p_t, of 0.3 and 0.5 GeV from Ref. (Cu78) with a calculation assuming only isospin = 2 pion exchange. The data have an overall normalization error of 15%.

real pion. Comparisons with $\pi^0\pi^0$ inclusive production would be worthwhile, but the analysis from this reaction is incomplete (Co78). The resulting I = 2 cross sections are discussed in section 5.1.

The calculation for the I = 3/2 exchange is similar and based on the reaction shown diagramatically below:

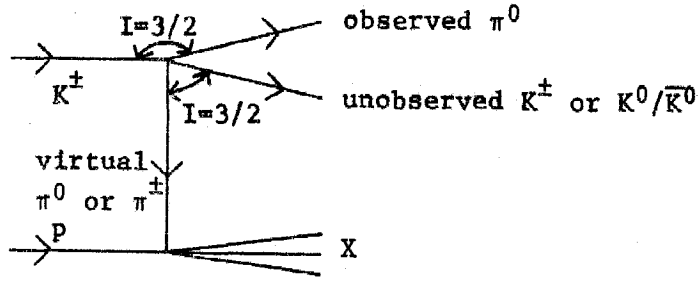

It assumes that the exchange is due to a pion and a kaon in a state with I = 3/2, with the kaon unobserved and the pion virtual, so this reaction is again due to pion exchange. The cross section is given by (4.III.1) with

$$\sum A^{\pm}_{\xi\zeta}\sigma^{\pm}_{tot} = \frac{2}{9}|T'_{3/2}|^2[2\sigma_{tot}(\pi^{\pm}p) + \sigma_{tot}(\pi^{\mp}p)] + \frac{2}{9}\,\mathrm{Re}(T'^{*}_{1/2}T'_{3/2}) \times [\sigma_{tot}(\pi^{\mp}p) - \sigma_{tot}(\pi^{\pm}p)] \qquad (4.III.5)$$

where $T'_{1/2}$ and $T'_{3/2}$ are the amplitudes for I = 1/2 and 3/2 scattering in the $\chi\zeta$ system. These are related to the amplitudes, $T_{1/2}$ and $T_{3/2}$ in the $\xi\zeta$ system by

$$\begin{aligned} T'_{1/2} &= -T_{1/2}/3 + 4T_{3/2}/3 \\ T'_{3/2} &= 2T_{1/2}/3 + T_{3/2}/3. \end{aligned} \qquad (4.III.6)$$

These amplitudes were obtained from Ref. (Es79) and the rest of the calculation followed just as for the I = 2 case. The resulting

cross section is discussed in section 7.1. Figure 4.III.2 shows a calculation made by the same approach for the process $K^+p \to \pi^-X$, which is pure $I = 3/2$ exchange at high x, compared to measurements of this reaction (Cu78). It is seen that the calculation agrees favorably.

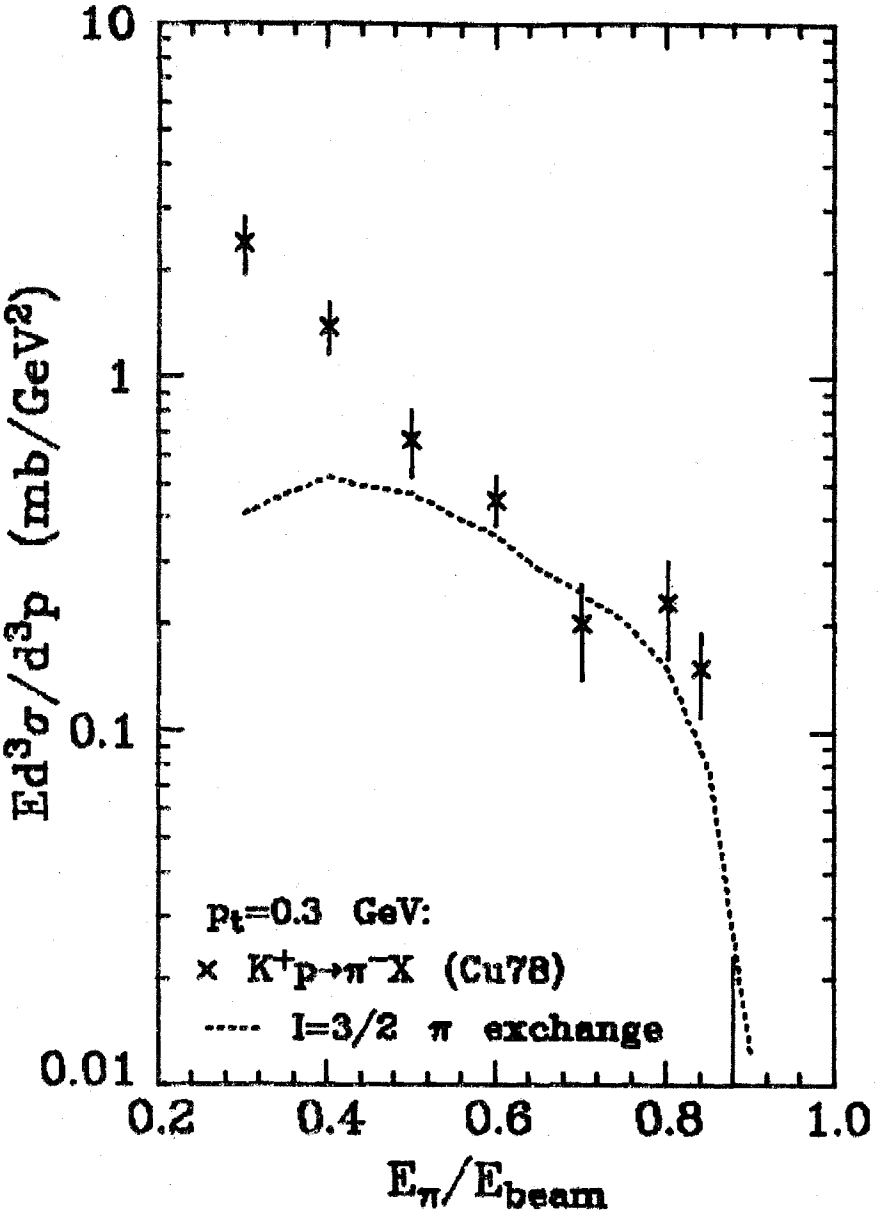

FIGURE 4.III.2 Comparison of measurements of the reaction $K^+p \to \pi^-X$ at 100 GeV with p_t = 0.3 GeV from Ref. (Cu78) with a calculation assuming only isospin = 3/2 pion exchange. The data have an overall normalization error of 15%.

APPENDIX 5.I

ENERGY RESOLUTION

The measured energy, E_m, of a particle was different from its real energy, E. A response function, $f(E_m;E)$, which represents the distribution of E_m for a particle of energy E, had to be determined so that any theoretical prediction for the cross section, T(E), could be smeared with the response function to give the prediction for the measured cross section, $T_m(E_m)$:

$$T_m(E_m) = \int T(E) f(E_m;E) dE. \qquad (5.I.1)$$

It was important in this experiment to minimize the width, σ, of the response function, which is given by

$$\sigma^2(E) = \int (E - E_m)^2 f(E_m;E) dE_m. \qquad (5.I.2)$$

This was because the value of σ determined what structure could be seen in the energy spectrum and the reliability of the contents of each energy bin. Many factors determined the size of σ, most of which were discussed in Chapter 3 and in earlier appendices.

The detector was originally designed for use in E111, for which the energy resolution was less important because the energies of the detected particles produced in exclusive reactions are fixed by the beam momentum and their p_t. Two important additions were made to improve the energy resolution for E350. The backup counter, described in Appendix 3.III, was added to sample the energy in depth

and its use both reduced σ and eliminated the tail on the lower energy side of the response curve, thus making f more Gaussian. There was also an improved scheme for monitoring the gains of the photomultiplier tubes by recording the pulse heights of the sources during the data-taking runs (between beam spills) instead of recording their pulse heights during special runs.

In the off-line software, a large initial effort was made to decrease σ. The raw energy resolution, determined from the sum of the pulse heights of the photons in the particle and supposing that the gains were exactly known, was 2% at 100 GeV. The gains of all 140 counters were determined by a preliminary analysis of part of the data sample, as described in Appendix 3.I. It was not possible to determine these exactly, both because of statistics and time-dependent effects and also because each counter consisted of eight rods in depth, whose relative gains were unknown (for example, their sizes may have varied) and so the gain of a counter would depend on the relative amounts of energy deposited in each rod. There was also the effect of light attenuation along the rods. Before the detector was constructed, numerous tests were made to investigate this effect (Wa72) and the final result was that each rod was wrapped with aluminized mylar silk-screened with a black dot pattern which was solid black at the near end and pure mylar at the far end and varied in blackness between the two ends. There remained a rather irregular response at the 1% level. These attenuation effects have now been investigated

and are being incorporated into the analysis of the second data set (200 GeV incident momentum). Since the attenuation curves for each counter were different and it was also necessary to know the positions in the opposite plane, this correction was not easy.

The fitting approach to the analysis, described in Appendix 3.IV, also helped to decrease σ. An improved determination of the shower shape was made which incorporated its energy dependence, as described in Appendix 3.II. Effects such as the planar nature of the detector, which meant that showers near the edge saw more lead than those near the straight-through beam intersection point, were not important since the distant showers saw only 0.05% more material as the detector was far from the target. The effect of the varying widths of the counters was studied for the 200 GeV data set and found to be a small correction compared with the attenuation effects. There was also an edge effect, which caused showers formed near the edge of the detector to have a different shape. Consequently it was required that both photons in the triple Regge particle were at least two counterwidths from every edge of the detector. However no cut was imposed on the other photons in the event so any change in their shape would affect the results as all the photons in an event were included in the fit.

The fits which determined the energy of the particles constrained the energy of the lowest energy photon in the particle using (3.IV.2). The separation, θ_{lab}, of the two photons was calculated by assuming

that the interaction took place at the mid-point of the target. Thus the finite length of the target (0.6 m) gave a 0.9% contribution to the energy resolution at 100 GeV. θ_{lab} also depended on the positions of the photons, which were only determined to 0.5 mm. The value of σ increased with the decay cosine, cos θ, of the particle. For each photon shower, the relative error was proportional to $E_\gamma^{-1/2}$, which increases as the energy decreases. Hence a cut requiring that cos be less than 0.75 was imposed.

It was assumed that the energy response function, f, was Gaussian with a width, σ, given by

$$\sigma^2 = \sigma_A^2 E^2 + \sigma_B^2 E. \qquad (5.I.3)$$

The contribution to σ which depends on the square-root of the energy, $\sigma_B\sqrt{E}$, was due to the energy resolution of the detector for the case of perfect gains and zero target length. This resolution at 100 GeV was 0.55% for cos θ = 0 and 1.35% for cos θ = 0.75 and so the average value of σ_B = 0.09 $GeV^{-1/2}$ was used. To find σ_A, the low -t NFS data, presented in Section 6.2, were used and the value of σ_A allowed to vary in fits to the data above energies of 80 GeV. The best fits gave $\sigma_A = 1.5 \times 10^{-4}$. In Section 5.1, it is shown that the results for the ρ trajectory were not sensitive to the knowledge of the energy resolution (see Table 5.3).

APPENDIX 5.II

BEAM MOMENTUM DETERMINATION

This experiment used a secondary meson beam at Fermilab. The proton beam of momentum 400 GeV was extracted from the main ring and directed onto a tungsten target about two-thirds of an interaction length long. A series of dipole bending magnets selected the secondary particles with the desired momenta and a series of quadrupole magnets focussed the particles along the beamline, as described in Ref. (Og78). The beam was modeled using the TRANSPORT computer program and the magnet currents were determined for use in running the experiment. These currents were reduced by about 2% midway through the 100 GeV run and the data from the two incident momenta have been added together. The quoted values for the beam momentum refer to the first one. Approximate excitation curves were used for the magnets and so the TRANSPORT program only determined the beam momentum to 3%. It was necessary to know it better because the quantity relevant for the triple Regge analysis was $x \simeq E_{\pi^0}/E_{beam}$ at values close to unity. The π^0 energy was measured in pulse height units and so the beam momentum only had to be well-determined in pulse height units.

There were several methods which could be used for determining the beam momentum in the off-line analysis. One simple approach was to look at the average pulse heights of the electrons used to determine the gains of the counters (see Appendix 3.I). Using the calibration determined from fixing the π^0 mass gave a beam momentum of about 100 GeV. Due to effects such as the light attenuation along

the counters, the error in this determination was about 1 GeV.

A second method was to look at the energy spectra of NFS events at low t_m (Fig. 6.2). For this study the data were accumulated in t bins of size 0.1 GeV^2 for $t_m \leq 0.4$ GeV^2. It is clear from the statistics of the data presented on Fig. 6.2 that if the theory were fully understood then there would be no problem in determining the beam momentum. However neither was the low mass resonance cross section completely known at these energies nor was the triple Regge prediction well-defined at x near 1 and so the beam momentum was not well-determined. This is shown by the results from the fits which are listed in Table 5.II.1. For a given t bin the beam momentum varies little with the cuts but it does vary with t. It was therefore concluded that the beam momentum was 99.2 GeV with an error relative to the energies measured by the detector varying from 0.2 GeV at t near 0 to 0.5 GeV at large t after taking into account the error in the calibration and attenuation effects. This approach was also used to determine that the second beam momentum was 1.65% lower than the first beam momentum. This number was well-determined since it came from comparing the shapes of the energy spectra. When the low t_m NFS η production data were compared with the π^0 data they appeared to give the same beam momentum.

A third approach was to look at the decays of non-interacting K^- and K^+ beam particles into π^0 mesons which were detected. The chief decay is

TABLE 5.II.1. Beam momentum determined from the low t_m NFS data with the following different cuts:

(a) fitting above 80 GeV and allowing the energy resolution to vary;

(b) fitting above 80 GeV with $\sigma_A^2 = 1.5 \times 10^{-4}$ in (5.I.1);

(c) fitting above 90 GeV with $\sigma_A^2 = 1.5 \times 10^{-4}$;

(d) as in (c) with the normalization of the low mass resonance terms increased by 2%.

-t range	(a)	(b)	(c)	(d)
0.0 - 0.1	99.07 ± 0.02	99.08 ± 0.01	99.09 ± 0.01	99.08 ± 0.01
0.1 - 0.2	99.27 ± 0.03	99.25 ± 0.02	99.23 ± 0.02	99.22 ± 0.02
0.2 - 0.3	99.34 ± 0.05	99.33 ± 0.05	99.30 ± 0.05	99.28 ± 0.05
0.3 - 0.4	99.50 ± 0.10	99.43 ± 0.11	99.40 ± 0.10	99.39 ± 0.10

$$K^{\pm} \to \pi^{\pm} + \pi^0, \qquad (5.II.1)$$

which has a branching ratio of 21.2%. For such a two-body decay, the beam momentum can be determined from the measured energy and transverse momentum of the π^0 meson. Cuts were made to ensure that the kaon decayed before being bent by the magnet. This gave a result of about 100 GeV for the beam momentum. However the errors were large. The three-body decays, $K^{\pm} \to e^{\pm}\nu\pi^0$, $\mu^{\pm}\nu\pi^0$ and $\pi^0\pi^{\pm}\pi^0$, have branching ratios of 4.8%, 3.2% and 1.7% respectively, and so they had to be modeled and their contributions subtracted before looking at the decay (5.II.1). There was also an error due to the lack of

knowledge of the gains of the few counters near the beam intersection point used for this determination. It was decided to use the NFS determination of 99.2 GeV for the trajectories presented here.

APPENDIX 6.I

DEFINITION OF THE NEUTRAL FINAL STATE

In this Appendix, the software cuts defining the Neutral Final State (NFS) events and the corrections due to missing NFS events are described. The hardware cuts used in the NFS trigger are described in Section 2.6 and Appendix 2.I. The scintillation counters, A2, A3 and A4, shown on Fig. 2.1 and described in Section 2.4, were pulse height analyzed. This allowed a higher hardware cut to be used and a cleaner software cut to be applied later using the pulse heights. Since charge is conserved, there were at least two charged particles present in any non-NFS event and so a fairly clean cut could be made.

The response of the counters to charged particles was determined from the interactions of positively charged beam particles and from cosmic rays. This gave the relative gains of the twenty phototubes on the A2 counter and of the two phototubes on the A3 counter. The total pulse heights of the A2, A3 and A4 counters were then histogrammed and the one-particle peak identified for each case. They were then weighted according to the position of the one-particle peak and all the counters were summed together. A cut was applied to the sum well below the one-particle peak to define the NFS events. This cut was applied in the off-line analysis and was found to be clean as most of the events vetoed by it had several charged particles present.

The neutral final state was defined to refer to the final products resulting from the strong interactions. Thus if a Δ^0 was

TABLE 6.I.1 Efficiency for detecting neutral final state events

	$\pi^-p \to X^0$ at 50 & 100 GeV		$\pi^-p \to (\pi^0,\eta)n$ at 100 GeV	
Correction	Full tgt	Empty tgt	Full target	Empty target
Photon conversion	0.86±0.07	0.99±0.01	0.893±0.002	0.958±0.002
Charged particle decays	0.98±0.01	0.98±0.01	Included in acceptance	
Strange particle veto	0.90±0.03	0.90±0.03	1	1
Neutron veto	0.98±0.01	0.98±0.01	0.97 ±0.01	0.97 ±0.01
Delta rays	0.90±0.04	1.00±0.01	0.90 ±0.04	1.00 ±0.01
Total	0.67±0.07	0.86±0.03	0.78 ±0.04	0.93 ±0.01

produced, together with other neutral particles, and it decayed to $\pi^0 n$ then the event was classified as a NFS event whilst if it decayed to $\pi^- p$ then the event was excluded. If a Λ was produced, together with other neutral particles, then the event was classified as NFS regardless of whether it decayed to $\pi^- p$ or $\pi^0 n$ since these are weak decays. However some NFS events were excluded by the trigger due to the secondary production of charged particles by weak and electromagnetic processes, as listed in Table 6.I.1. The efficiencies for detecting the total neutral final state cross section at 50 and 100 GeV and for detecting the exclusive reactions, $\pi^- p \to \pi^0 n$ and $\pi^- p \to \eta n$, are listed. The corrections for the data taken with no hydrogen in the target are listed separately (as "empty target") since these were different from those with the hydrogen (listed as "full target"). The neutral final state corrections for the reactions $\pi^- p \to \pi^0 X^0$ and $\pi^- p \to \eta X^0$ were made using the calculable corrections when the X^0 is

just the neutron, since the particle content of the X^0 was unknown. This approach led to a systematic error in the trajectory, α, and in the cross sections.

Some of the photons produced converted into electron-positron pairs in the hydrogen, the target walls, the beam exit windows, the A4 counter, the canvas tent around the target cart and in the air before the magnet. Photons converting in the air after the magnet produced electron-positron pairs which had showers resembling photon showers in the detector. This effect was corrected for using the radiation lengths from Ref. (PD78). Since most of the conversions occurred in the hydrogen, the correction for the full target data is different from that for the empty target data, which was taken with the target evacuated of all but 0.5% of the hydrogen (Jo75). The correction of 0.893 for the photons from the π^0 and η mesons converting had to be applied to the full inclusive data also.

For correcting the total neutral final state cross section, only the conversions which produced electrons detectable in the veto counters had to be considered. The probability of a π^0 or η meson decaying through the 2γ decay mode having a photon convert in this case is 0.928 for the full target data and 0.994 for the empty target data. Also 1.15% of the π^0 mesons decay through the Dalitz pair decay, $\pi^0 \rightarrow e^+e^-$, and 29% of the η mesons decay electromagnetically or weakly into final states with charged particles present (PD78). For the π^0 or η production, these decays were included in the acceptance calculation (see Appendix 3.VII). For the total NFS cross

section, the vetoing of events by charged particles from weak and electromagnetic decays of neutral particles has to be considered. This will be dominated by the electrons and positrons from π^0 and η decays and by the weak decays of the lighter strange particles. It was thus necessary to estimate the particle content of the NFS events, which has not been measured.

To estimate the number of π^0 mesons present in NFS events, the structure of pion production in inclusive events was studied. Table 6.I.2 is taken from Ref. (Wh76) and gives the mean multiplicities of all charged particles, $\langle n_c \rangle$, of negatively-charged particles, $\langle n_- \rangle$, and of π^0 mesons, $\langle n_o \rangle$, in $\pi^{\pm}p$ collisions.

TABLE 6.I.2 Measured multiplicities in $\pi^{\pm}p$ collisions at 100 GeV

	π^-p	π^+p
$\langle n_c \rangle$	6.8	6.8
$\langle n_- \rangle$	3.4	2.4
$\langle n_o \rangle$	3.0	2.8

These multiplicities suggest that the average structures of the final states are given by

$$\pi^-p \longrightarrow 1 \text{ leading } \pi^- + 2.4\ \pi^- + 2.4\ \pi^+ + 1 \text{ neutron} + 3.0\ \pi^0,$$

$$\pi^+p \longrightarrow 1 \text{ leading } \pi^+ + 2.4\ \pi^- + 2.4\ \pi^+ + 1 \text{ proton} + 2.8\ \pi^0.$$

Thus, on the average, 2.4 charged pions of each polarity from the central region are produced, together with one leading pion of the

same polarity as the incident pion coming from its fragmentation. In NFS events, it may be supposed that there is one leading π^0 produced together with some number, N, of other pions. N is probably less than 2.4 and is zero for the 10% contribution to the NFS cross section from $\pi^- p \rightarrow \pi^0 n$. Hence it is estimated that $N = 1 \pm 1$ and so an average NFS event will have 2 ± 1 π^0 mesons. Since the average number of η mesons in full inclusive events is small (An76), it is assumed here that η production may be ignored. This gives the quoted values of 0.86 ± 0.07 and 0.99 ± 0.01 for the corrections due to photon conversions for the full and empty target data respectively and 0.98 ± 0.01 for the correction due to the charged particle decays. The data were corrected by dividing by the values in Table 6.I.1.

The lighter strange particles decay weakly as they cannot conserve strangeness. 64% of the decays of the Λ produce charged particles, mainly $\pi^- p$, whilst 69% of the decays of the K^0_S produce charged particles, mainly through the $\pi^+\pi^-$ decay mode (PD78). To conserve baryon number, either a neutron or a Λ will be present in almost all NFS events. The relative amounts of neutron and Λ present were estimated from the results in (Da73, Da74, En75, Wh76) on inclusive neutron and Λ production from pp collisions at high energies. It was found that Λ baryons were present in $15 \pm 5\%$ of the NFS events. Assuming an average transverse momentum of 0.3 GeV, the Λ will be produced at about 45^o in the laboratory. It has a characteristic decay length ($c\tau$) of 80 mm and so a typical Λ will travel a distance of 30 mm in the laboratory. Thus almost all of the Λ baryons will

decay before reaching the A2 counter, a 0.18 m box surrounding the target. Hence 10 ± 3% of the NFS events are lost by Λ decays. The number of slow K^0 mesons produced in NFS events is assumed to be negligible.

In the E111 analysis (Jo75), the effect of neutrons interacting in the scintillation counters and vetoing the event was studied. From their results and from assuming that 85% of the events contained one neutron, as discussed above, it was found that 2% of the total NFS events were vetoed. Another correction, which was also studied in detail in Ref. (Jo75), was due to the production of delta rays by the pion beam on passing through the target. The correction of 0.90 has been estimated using these studies and the large error of 0.04 comes from having different hardware cuts from E111.

For correcting π^0 and η NFS production, it is necessary to know how the various corrections depend on the kinematical region of the produced meson. Clearly all the corrections except that due to delta rays will differ. Since it has been fairly hard to estimate the corrections even for the total cross section, it was decided to normalize the π^0 and η data by applying the correction for $\pi^- p \rightarrow (\pi^0,\eta)n$ to all the data. This approach probably underestimated the cross section by less than 10% at $x = 0.5$.

REFERENCES

Ak76 ... C. W. Akerlof et al., Phys. Rev. D14, 2864 (1976).

Al66 ... G. Alexander et al., Phys. Rev. Lett. 17, 412 (1966).

Al76 ... M. G. Albrow et al., Nucl. Phys. B108, 1 (1976).

An76 ... K. J. Anderson et al., Phys. Rev. Lett. 37, 799 (1976).

An77 ... R. L. Anderson et al., Phys. Rev. Lett. 38, 880 (1977).

Ar78 ... M. W. Arenton et al., "Measurement of Exclusive Hypercharge-Exchange Reactions at 35 to 140 GeV/c", ANL-HEP-PR-78-24 (1978).

Ap73 ... W. D. Apel et al., Phys. Lett. 46B, 459 (1973).

Ap79a... W. D. Apel et al., Phys. Lett. 83B, 131 (1979).

Ap79b... W. D. Apel et al., Nucl. Phys. B154, 189 (1979).

Ay76 ... D. S. Ayres et al., Phys. Rev. Lett. 37, 1724 (1976).

Ba75a... A. V. Barnes, "Measurement of Single Photon Showers in the Detector", CIT internal memo (1975).

Ba75b... A. V. Barnes, "Online Scheme for Determining the Gain of the CIT Shower Detector using Electrons in the Beam as a Mono-energetic Shower Source", CIT internal memo (1975).

Ba75c... A. V. Barnes, "Detector Gains", CIT internal memo (1975).

Ba76 ... A. V. Barnes et al., Phys. Rev. Lett. 37, 76 (1976).

Ba77 ... A. V. Barnes, "Handling of Cherenkov Counter Data", CIT internal memo (1977).

Ba78a... A. V. Barnes et al., Nucl. Phys. B145, 45 (1978).

Ba78b... A. V. Barnes et al., Nucl. Phys. B145, 67 (1978).

Ba78c... A. V. Barnes et al., Phys. Rev. Lett. 41, 1260 (1978).

Ba79 ... A. V. Barnes, private communication (1979).

Be71 ... E. L. Berger and G. C. Fox, Nucl. Phys. B26, 1 (1971).

Bl74a... R. Blankenbecler and S. J. Brodsky, Phys. Rev. D9, 2973 (1974).

Bl74b... I. J. Bloodworth et al., Nucl. Phys. B81, 231 (1974).

Bl78 ... R. Blankenbecler, S. J. Brodsky and J. F. Gunion, Phys. Rev. D18, 900 (1978).

Bø74 ... H. Bøggild and T. Ferbel, Ann. Rev. Nucl. Sci. 24, 451 (1974).

Br72 ... E. Bracci et al., "Compilation of Cross Sections I - π^- and π^+ Induced Reactions", CERN/HERA 72-1 (1972).

Br79a... C. Bromberg et al., Phys. Rev. Lett. 43, 561 (1979).

Br79b... S. J. Brodsky and G. P. Lepage, "Exclusive Processes and the Exclusive-Inclusive Connection in Quantum Chromodynamics", SLAC-PUB-2294 (1979)

Bu76a... J. Butler, in BNL Report No. BNL-50598, edited by H. Gordon and R. F. Peierls, Proceedings of the American Physical Society Meeting, Division of Particles and Fields, Upton, New York (1976).

Bu76b... F. W. Busser et al., Nucl. Phys. B106, 1 (1976).

Ca76 ... A. S. Carroll et al., Phys. Lett. 61B, 303 (1976).

Ch61 ... G. F. Chew and S. C. Frautschi, Phys. Rev. Lett. 7, 394 (1961).

Ch76 ... B. Chaurand et al., Nucl. Phys. B117, 1 (1976).

Ch78 ... M. K. Chase and W. J. Stirling, Nucl. Phys. B133, 157 (1978).

Co77 ... P. D. B. Collins, "An Introduction to Regge Theory and High Energy Physics", published by Cambridge University Press (1977).

Co78 ... B. G. Cortez, "Analysis of the Inclusive Reaction $\pi^{\pm}p \to \pi^0\pi^0X$ using Triple Regge Formalism", Senior Thesis, CIT (1978).

Cr68 ... H. R. Crouch et al., Phys. Rev. Lett. 21, 845 (1968).

Cu78 ... D. Cutts et al., Phys. Rev. Lett. 40, 141 (1978).

Da73 ... F. T. Dao et al., Phys. Rev. Lett. 30, 1151 (1973).

Da74 ... F. T. Dao et al., Phys. Rev. D10, 3588 (1974).

Da76 ... O. I. Dahl et al., Phys. Rev. Lett. 37, 80 (1976).

Da77 ... O. I. Dahl et al., Phys. Rev. Lett. 38, 54 (1977).

De71 ... S. P. Denisov et al., Phys. Lett. 36B, 528 (1971).

De73 ... S. P. Denisov et al., Nucl. Phys. B65, 1 (1973).

Do78a... G. J. Donaldson et al., Phys. Rev. Lett. 40, 684 (1978).

Do78b... G. J. Donaldson et al., "A Compilation of Invariant Cross Sections for the Reactions $\pi^{\pm}$, $K^{\pm}$ and $p^{\pm} + p \to \pi^0 + X$ at 100, 200 and 300 GeV/c", BNL-23844 (1978).

Do78c... G. J. Donaldson et al., Phys. Rev. Lett. 40, 917 (1978).

Ed60 ... A. R. Edmonds, "Angular Momentum in Quantum Mechanics", published by Princeton University Press (1960).

En75 ... J. Engler et al., Nucl. Phys. B84, 70 (1975).

Es78 ... P. Estabrooks et al., Nucl. Phys. B133, 490 (1978).

E374 ... E350 Proposal, "A Proposal to Study π^0 and η Inclusive Production with incident π^- in the Triple Regge Region", CALT-68-472 (1974).

Fa79 ... G. R. Farrar and G. C. Fox, "Calculation of the CIM Model for $\pi^-p \to \pi^0X$", CIT internal memo (1979).

Fe69 ... R. P. Feynman, Phys. Rev. Lett. 23, 1415 (1969).

Fe75 ... Fermilab Single Arm Spectrometer Group, Phys. Rev. Lett. 35, 1195 (1975).

Fi74 ... R. D. Field and G. C. Fox, Nucl. Phys. B80, 367 (1974).

Fi77 ... R. D. Field and R. P. Feynman, Phys. Rev. D15, 2590 (1977).

Fi79 ... R. D. Field, in Proc. 19th Int. Conf. High Energy Physics, edited by S. Homma, M. Kawaguchi and H. Miyazawa, published by Physical Society of Japan (1979).

Fo71 ... G. C. Fox, in "Phenomenology in Particle Physics 1971", edited by C. B. Chiu, G. C. Fox and A. J. G. Hey, Caltech (1971).

Fo72 ... G. C. Fox, "A Picture Book of High-Energy Scattering", CIT internal memo (1972).

Fo74 ... G. C. Fox and D. J. Mellema, "Physics and Feasibility Study for Analysis of Inclusive π^0 and η Production in π^-p and pp Interactions", CALT-68-475 (1974).

Fo77a... G. C. Fox and R. G. Kennett, "TREAT - An Analysis Program for the CEX Detector", CIT internal memo (1977).

Fo77b... G. C. Fox, "E350 Memo: Double Interactions in Target", CIT internal memo (1977).

Fo77c... G. C. Fox and R. D. Field, private communication (1977).

Gu65 ... O. Guisan, Phys. Lett. 18, 200 (1965).

Ho73 ... D. Horn and F. Zachariasen, "Hadron Physics at Very High Energies", published by Benjamin (1973).

Hy73 ... B. Hyams et al., Nucl. Phys. B64, 134 (1973).

Ja78 ... M. Jacob and P. V. Landshoff, Phys. Reports, 48C, 285 (1978).

Jo75 ... R. A. Johnson, "Measurement of the $\pi^- p \to \pi^0 n$ and $\pi^- p \to \eta n$ Differential Cross Sections at Beam Momenta from 20 to 200 GeV/c", Ph. D. thesis, Lawrence Berkeley Laboratory Report No. LBL-4610 (1975).

Ka76 ... G. L. Kane and A. Seidl, Rev. Mod. Phys. 48, 309 (1976).

Ke77 ... R. G. Kennett, "Files GIANT - E350", CIT internal memo (1977).

Ke79 ... R. G. Kennett, "Cherenkov Counter Analysis of the E350 100 GeV Data", CIT internal memo (1979).

Ko79 ... C. Kourkoumelis et al., Phys. Lett. 84B, 277 (1979).

Ma63 ... D. W. Marquardt, J. Soc. Indust. Appl. Math. 11, 431 (1963).

Ma77 ... F. Marzano et al., Nucl. Phys. B123, 203 (1977).

Mu70 ... A. H. Mueller, Phys. Rev. D2, 2963 (1970).

Mü72 ... D. Müller, Phys. Rev. D5, 11 (1972)

Na76 ... H. Navelet and P. R. Stevens, Nucl. Phys. B104, 171 (1976).

Na79 ... M. M. Nagels, Nucl. Phys. B147, 189 (1979).

No78 ... D. Novoseller, Nucl. Phys. B137, 445 (1978).

Og78 ... A. Ogawa, "Measurement of Inclusive Production of Neutral Pions at High Transverse Momentum", Ph. D. thesis, Lawrence Berkeley Laboratory Report No. LBL-8305 (1978).

PD78 ... Particle Data Group, Phys. Lett. 75B, i (1978).

Po75 ... V. Polychronakis et al., Phys. Rev. D11, 2400 (1975).

Sh76 ... M. H. Shaevitz et al., Phys. Rev. Lett. 36, 5 (1976).

Si76 ... D. Sivers et al., Phys. Reports 23C, 1 (1976).

Si78 ... J. Singh et al., Nucl. Phys. B140, 189 (1978).

Si79 ... J. Singh, private communication (1979).

So66 ... P. Sonderegger et al., Phys. Lett. 20, 75 (1966).

St65 ... A. V. Stirling et al., Phys. Rev. Lett. 14, 763 (1965).

St75 ... J. K. Storrow and G. A. Winbow, J. Phys. G; Nucl. Phys. 1, 263 (1975).

Ta76 ... F. E. Taylor et al., Phys. Rev. D14, 1217 (1976).

To76 ... A. V. Tollestrup, notes on CEX detector (1976).

Wa68 ... M. A. Wahlig, Phys. Rev. 168, 1515 (1968).

Wa71 ... R. L. Walker, "Identification of π^0, η and X^0", CALT-68-330, CIT internal memo (1971).

Wa72 ... R. L. Walker, "Attenuation of Light in Long Scintillators", Calt-68-348, CIT internal memo (1972).

Wa79 ... R. L. Walker, private communication (1979).

Wh76 ... J. Whitmore, Phys. Reports 27C, 187 (1976).